

# 博士論文

## Design and Functionalization of Fullerenes for High-Performance Perovskite Solar Cells

(高性能ペロブスカイト太陽電池のためのフラーレンの設計と機能化)

Hao-Sheng LIN

林 昊升



Doctoral Dissertation

**Design and Functionalization of Fullerenes for  
High-Performance Perovskite Solar Cells**

by

**Hao-Sheng LIN**

Presented to

GRADUATE SCHOOL OF ENGINEERING, THE UNIVERSITY OF TOKYO

in Partial Fulfillment of the Requirements for the Degree of

**Doctoral of Philosophy**

in the Field of Mechanical Engineering

May 2020



## **Abstract**

Buckminsterfullerene (C<sub>60</sub>), a perfectly symmetric soccer ball shape molecule, has been widely investigated in multiple disciplines since the successful gram-scale production achieved in 1990. In the past several decades, thanks to the rapid development of organic chemistry, tremendous methodologies have been well demonstrated for the functionalization. Then, versatile fullerene materials have been synthesized and presented in a wide range of applications, including biomedicine, cosmetics, and photovoltaic. Among these applications, fullerene materials have been mostly demonstrated in the photovoltaic field, thanks to their remarkably excellent electric properties such as ultrafast photo-induced charge transfer, the low reorganization energy, *etc.* Accordingly, considerable efforts have devoted to developing fullerene materials in both organic solar cells (OSCs) and perovskite solar cells (PSCs). The first fullerene-utilized OSC was reported in 1995 using fullerene as an electron-acceptor in the active layer, which obtained a power conversion efficiency (PCE) of 3.5%. Since that, the energy level and solubility were elucidated to be the key for the design and functionalization of fullerenes, owing to fullerenes take the role in the active layer of OSCs. Different from fullerenes in OSCs, fullerenes are commonly used as electron-transport layers (ETLs) in PSC. So, merely transferring the strategies of fullerenes in OSCs to PSCs understandably results in poor performance. Although fullerene-applied PSC achieved an impressively excellent PCE of 21.3% compared with the first device in a PCE of 3.9% in 2013, most examples were obtained by a try-and-error method, which typically exhibited difficult in reproducibility. Consequently, the design and functionalization of fullerenes for high-performance PSCs remain unclear.

Herein, this thesis mainly discussed how fullerenes influence the performance of PSCs and how to design a good fullerene material for high-performance PSCs. Unlike

to fullerene materials in OSCs, this thesis found that fullerene materials in PSCs should be more concerned regarding the electron-carrier mobility, interlayer morphology, and passivation effect, as fullerene materials were utilized as the ETLs or dopant instead the electron-acceptors in OSCs.

- **Interlayer morphology:** fullerene materials that can form a uniformly amorphous ETL film improve the perovskite film quality. Accordingly, thermal-deposited C<sub>60</sub> and mixed C<sub>60</sub>/C<sub>70</sub> ETLs exhibited a higher PCE than solution-processed fullerene ETLs’.
- **Electron-carrier mobility:** there are more pristine C<sub>60</sub> and fullerene derivatives with 1,2-addition pattern applied in PSCs, as multi-adducts have poor electron mobility because of the large molecular size, and thusly discrete molecule packing.
- **Passivation effect:** fullerene materials that installed alkoxy (RO-), amine (RNH<sub>2</sub>-), carbonyl (C=O) groups can function as the Lewis base to passivate the Pb<sup>2+</sup> to improve the stability and performance by reducing the defects in perovskite cell.

However, conventional fullerene-anion and fullerene-radical chemistry produced fullerene materials failed to achieve fullerene molecules that having all the demands mentioned above. Accordingly, this thesis developed fullerene-cation chemistry to obtain the designed fullerene materials, which achieved the up-to-date highest PCE of 20.7% in an NH<sub>3</sub>PbI<sub>3</sub>-type PSC.

In short, this thesis deeply discussed the design of fullerene materials applied in PSCs, and the functionalization of fullerene materials through fullerene-cation chemistry. Moreover, this thesis is anticipated to afford the comprehensive understanding and the advanced knowledge for not only the scholars and scientists that currently engaged in this field but also the prospective researchers.

**Keywords:** *Fullerenes; Fullerene-cation chemistry; Perovskite solar cells; Electron-transport layer; Electron-carrier mobility; Interlayer morphology; Passivation effect.*

## **Acknowledgment**

First and foremost, I would like to express my special appreciation to my supervisors, Prof. Shigeo Maruyama and Prof. Yutaka Matsuo. They not only gave me great advice on my academic research but also have always been supporting me both financially and psychologically.

To Prof. Shigeo Maruyama, I sincerely thank you for broadening my horizons and providing tremendous opportunities that accessing me to the real industrial world. Most impressively, I will never forget what you said when you encouraged me to participate in the GSDM program. “A qualified Ph.D. is not simply recognized by how many papers you can, is by how much contribution you can do for the world.” Thanks to the GSDM program, I got to improve my communication skills and be more inclusive when collaborating with people from different backgrounds.

To Prof. Yutaka Matsuo, I earnestly thank you for patiently advising me on advanced research skills and deep understandings of chemistry. Since the first time I met you at the University of Science and Technology, I could never imagine my Ph.D. would achieve such productive and satisfactory. Your sagacious suggestions and passion always encourage me to persevere in my Ph.D. and spiring me up when I was in the tough periods. Most importantly, I learned how critical tiny things in research as even now I can recall you keep saying, “God is in the detail.”

I felt extremely fortunate that I could under the supervisor by Prof. Maruyama and Prof. Matsuo, which allows me to get both horizontal and vertical promotion in my abilities. And I holy appreciate for the most excellent example both of you have showcased as successful scientists and principal investigators.

Meanwhile, I would like to express my holy thanks to Dr. Il Jeon. If without your genius vision, I could never achieve so much and start a different research topic compared with my previous background. Also, your passion for chasing for challenges

## *Acknowledgement*

---

profoundly influence me so that I can be more confident to face the difficulties and challenges.

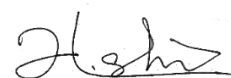
I would also like to thank the members of the Maruyama group, Prof. Rong Xiang and Dr. Ming Liu for teaching me the electrical microscopy; Mr. Seungju Seo and Mr. Shunhei Okawa for collaborative research of carbon nanotubes in solar cell application. Ms. Maiko Terao and Mr. Makoto Watanabe for administrative and financial supports.

In particular, the members of the Matsuo group have contributed immensely to my research and personal life in Tokyo. Dr. Takafumi Nakgawa and Dr. Yuki Itabashi in Miraikan not only gave me fruitful advice but also being as grateful Japanese teachers for me. Mr. Yue Ma, Dr. Xiao-Yu Yang, Mr. Yun Yu, and Dr. Huan Wang at the University of Science and Technology of China gave me great supports in material synthesis and characterization.

Thanks to my friends in Japan, my time in Tokyo was delightful even I did poorly in Japanese. Although I could not spend much time together because of my busy schedule, I regard them extremely special: Jiawei Yang, Xiangkun Yin, Na Li, Xiaolei Guo, Yao Li, Xufangqiuzi Song, and now they are part of my life.

Above all, I would like to thank my family for all their love and support. Super-duper thanks to my mother and father. Your taking care and encouragement give me great spiritual supports. And my true love, Zhimiao Murong, your faithful support and care give me infinite power to overcome all difficulties and obstacles no matter how tough they are.

Finally, I would like to express my appreciation again and wish you all the best. At this unusual historical timing that the whole world is suffering from the Coronavirus-19, I cross my fingers for all nations that they could recover from this disaster as soon as possible. Besides, I would like to tell myself whatever I will do in the future, act with integrity, competence, diligence, respect, and in an ethical manner.



@UTokyo, March 7, 2020



## Scientific Achievements

### (a) Publications

#### 2020

---

- 1 **H.-S. Lin**, Y. Ma, R. Xiang, S. Manzhos, I. Jeon, S. Maruyama, Y. Matsuo, A One-step Direct Oxidation of Alkoxy to Ketone: Oxidation of Alkoxy Indano[60]fullerenes to [60]Fullerene-fused Ketones via Weak Copper Oxidant, *to be submitted*.
- 2 **H.-S. Lin**, J.-M. Lee, J. Han, C. Lee, S. Seo, S. Tan, H. M. Lee, E. J. Choi, M. S. Strano, Y. Yang, S. Maruyama, I. Jeon, Y. Matsuo, J.-W. Oh, Denatured M13 Bacteriophage-Templated Perovskite Solar Cells Exhibiting High Efficiency. *Adv. Sci.* **2020**, accepted.
- 3 **H.-S. Lin**, S. Okawa, Y. Ma, S. Yotsumoto, C. Lee, S. Tan, S. Manzhos, M. Yoshizawa, S. Chiashi, H. M. Lee, T. Tanaka, H. Kataura, I. Jeon, Y. Matsuo, S. Maruyama, Polyaromatic Anthracene Nano-tweezer on Semiconducting Carbon Nanotubes for Growth and Bridging of Perovskite Crystal Grains in Solar Cells, *Chem. Mater.* **2020**, *Chem. Mater.* 2020, 32, 5125-5133.
- 4 **H.-S. Lin**, Y. Matsuo, Fullerenes in Photovoltaics, *Handbook of Fullerene Science and Technology*, Springer, **2020**, *in press*.
- 5 X.-X. Yan, B. Li, **H.-S. Lin**, F. Jin, C. Niu, K.-Q. Liu, G.-W. Wang, S. Yang, Successively Regioselective Electrosynthesis and Electron Transport Property of Stable Multiply Functionalized [60]Fullerene Derivatives, *Research* **2020**, 2059190. (IST Cited Times: 0)

#### 2019

---

- 6 X.-Y. Yang<sup>‡</sup>, **H.-S. Lin**<sup>‡</sup>, Y. Matsuo, Highly Selective Synthesis of Tetrahydronaphthaleno[60]fullerenes via Fullerene-Cation-Mediated

- Intramolecular Cyclization, *J. Org. Chem.* **2019**, *84*, 16314-16322. (IST Cited Times: 0)
- 7 **H.-S. Lin**, I. Jeon, Y. Chen, X.-Y. Yang, T. Nakagawa, S. Maruyama, S. Manzhos, Y. Matsuo, Highly selective and Scalable Fullerene-Cation-Mediated Synthesis Accessing Cyclo[60]fullerenes with Five-Membered Carbon Ring and Their Application to Perovskite Solar Cells, *Chem. Mater.* **2019**, *31*, 8432-8439. (IST Cited Times: 4)
- 8 I. Jeon, A. Shawky, **H.-S. Lin**, S. Seo, H. Okada, J.-W. Lee, A. Pal, S. Tan, A. Anisimov, E. I. Kauppinen, Y. Yang, S. Manzhos, S. Maruyama, Y. Matsuo, Controlled Redox of Lithium-Ion Endohedral Fullerene for Efficient and Stable Metal Electrode-Free Perovskite Solar Cells, *J. Am. Chem. Soc.* **2019**, *141*, 16553-16558. (IST Cited Times: 1)
- 9 J.-W. Lee, I. Jeon, **H.-S. Lin**, S. Seo, T.-H. Han, A. Anisimov, E. I. Kauppinen, Y. Matsuo, S. Maruyama, Y. Yang, Vapor-Assisted Ex-Situ Doping of Carbon Nanotube toward Efficient and Stable Perovskite Solar Cells, *Nano Lett.* **2019**, *19*, 2223-2230. (IST Cited Times: 8)
- 10 H. Ueno, I. Jeon, **H.-S. Lin**, A. Thote, T. Nakagawa, H. Okada, S. Izawa, M. Hiramoto, H. Daiguji, S. Maruyama, Y. Matsuo, Li@C<sub>60</sub> Endohedral Fullerene as a Supraatomic Dopant for C<sub>60</sub> Electron-transporting Layers Promoting the Efficiency of Perovskite Solar Cells, *Chem. Commun.* **2019**, *55*, 11837-11839. (IST Cited Times: 1)
- 11 A. Thote, I. Jeon, **H.-S. Lin**, S. Manzhos, T. Nakagawa, D. Suh, J. Hwang, M. Kashiwagi, J. Shiomi, S. Maruyama, H. Daiguji, Y. Matsuo, High-Working-Pressure Sputtering of ZnO for Stable and Efficient Perovskite Solar Cells, *ACS Appl. Electron. Mater.* **2019**, *1*, 389-396. (IST Cited Times: 1)
- 12 A. Thote, I. Jeon, J.-W. Lee, S. Seo, **H.-S. Lin**, Y. Yang, H. Daiguji, S. Maruyama, Y. Matsuo, Stable and Reproducible 2D/3D Formamidinium-Lead-Iodide Perovskite Solar Cells. *ACS Appl. Electron. Mater.* **2019**, *2*, 2486-2493. (IST Cited Times: 7)

**2018**

---

- 13 **H.-S. Lin**, I. Jeon, R. Xiang, S. Seo, J.-W. Lee, C. Li, A. Pal, S. Manzhos, M. S. Goorsky, Y. Yang, S. Maruyama, Y. Matsuo, Achieving High Efficiency in Solution-Processed Perovskite Solar Cells Using C<sub>60</sub>/C<sub>70</sub> Mixed Fullerenes. *ACS Appl. Mater. Interfaces* **2018**, *10*, 39590-39598. (IST Cited Times: 10)
- 14 **H.-S. Lin**, Y. Matsuo, Functionalization of [60]Fullerene through Fullerene Cation Intermediates, *Chem. Commun.* **2018**, *54*, 11244-11259. (IST Cited Times: 12)
- 15 X.-Y. Yang, **H.-S. Lin**, I. Jeon, Y. Matsuo, Fullerene-Cation-Mediated Noble-Metal-Free Direct Introduction of Functionalized Aryl Groups onto [60]Fullerene, *Org. Lett.* **2018**, *20*, 3372-3376. (IST Cited Times: 14)

**(b) Oral Presentations at Conferences**

- 1 **H.-S. Lin**, I. Jeon, Y. Matsuo, S. Maruyama, Polyaromatic Anthracene Nanotweezer on Semiconducting Carbon Nanotubes for Growth and Bridging of Perovskite Crystal Grains in Solar Cells, **The 58<sup>th</sup> Fullerene, Carbon Nanotubes, Graphene Symposium**, Tokyo, Japan, March 20-24, 2020.
- 2 **H.-S. Lin**, I. Jeon, S. Maruyama, Y. Matsuo, Fullerene-Cation-Mediated Synthesis of Cyclo[60]fullerene with 5-Membered-Rings and their Application to Perovskite Solar Cells, **The 99<sup>th</sup> Annual Meeting of Chemical Society of Japan**, Kobe, Japan, March 12-19, 2019.
- 3 **H.-S. Lin**, I. Jeon, S. Maruyama, Y. Matsuo, Fullerene-Cation-Mediated Synthesis of Cyclo[60]fullerene with 5-Membered-Rings and their Application to Perovskite Solar Cells, **The 56<sup>th</sup> Fullerene, Carbon Nanotubes, Graphene Symposium**, Tokyo, Japan, March 1-5, 2019.
- 4 **H.-S. Lin**, I. Jeon, S. Maruyama, Y. Matsuo, Achieving High Efficiency in Solution-Processed Perovskite Solar Cells using C<sub>60</sub>/C<sub>70</sub> Mixed Fullerenes, **The 55<sup>th</sup> Fullerene, Carbon Nanotubes, Graphene Symposium**, Sendai, Japan, September 9-12, 2018.
- 5 **H.-S. Lin**, X.-Y. Yang, I. Jeon, Y. Matsuo, Fullerene-Cation-Mediated Noble-

Metal-Free Direct Introduction of Functionalized Aryl Groups onto [60]Fullerene, **Annual Meeting of Physical Organic Chemistry**, Tokyo, Japan, September 6-8, 2018.

- 6 **H.-S. Lin**, Y. Matsuo, G.-W. Wang, Electrochemical Synthesis of Carbonyl[60]fullerene Derivatives, **The 98<sup>th</sup> Annual Meeting of Chemical Society of Japan**, Chiba, Japan, March 19-22, 2018.

**(c) Poster Presentations at Conferences**

- 1 **H.-S. Lin**, I. Jeon, S. Maruyama, Y. Matsuo, Highly selective and Scalable Fullerene-Cation-Mediated Synthesis Accessing Cyclo[60]fullerenes with Five-Membered Carbon Ring and Their Application to Perovskite Solar Cells, **The 58<sup>th</sup> Fullerene, Carbon Nanotubes, Graphene Symposium**, Tokyo, Japan, March 20-24, 2020.
- 2 **H.-S. Lin**, I. Jeon, S. Maruyama, Y. Matsuo, Highly selective and Scalable Fullerene-Cation-Mediated Synthesis Accessing Cyclo[60]fullerenes with Five-Membered Carbon Ring and Their Application to Perovskite Solar Cells, **CIAiS International Symposium**, Tokyo, Japan, February 28, 2020.
- 3 **H.-S. Lin**, I. Jeon, S. Maruyama, Y. Matsuo, Achieving High Efficiency in Solution-Processed Perovskite Solar Cells using C<sub>60</sub>/C<sub>70</sub> Mixed Fullerenes, **CIAiS International Symposium**, Tokyo, Japan, Mar 1, 2019.
- 4 **H.-S. Lin**, I. Jeon, S. Maruyama, Y. Matsuo, Achieving High Efficiency in Solution-Processed Perovskite Solar Cells using C<sub>60</sub>/C<sub>70</sub> Mixed Fullerenes, **CIAiS International Symposium**, Tokyo, Japan, Mar 8, 2018.

# Contents

<b>Abstract</b>	<b>i</b>
<b>Acknowledgment</b>	<b>iii</b>
<b>Scientific Achievements</b>	<b>v</b>
(a) Publications	v
(b) Oral Presentations at Conferences	vii
(c) Poster Presentations at Conferences	viii
<b>Contents</b>	<b>ix</b>
<b>List of Figures</b>	<b>xiii</b>
<b>List of Tables</b>	<b>xix</b>
<b>Nomenclature</b>	<b>xxi</b>
<b>Preface</b>	<b>1</b>
<b>Chapter 1. Introduction</b>	<b>5</b>
1.1. Research background	5
1.2. Fullerene chemistry	6
1.2.1. Conventional fullerene chemistry	7
1.2.2. Fullerene cation chemistry	13
1.3. Fullerenes in photovoltaics	21
1.3.1. Fundamentals of photovoltaics	22
1.3.2. Fullerenes in organic solar cells	26
1.3.3. Fullerenes in perovskite solar cells	43
<b>Chapter 2. Purpose, Challenges and Structure of the Thesis</b>	<b>61</b>
2.1 How to design fullerenes for high-performance PSCs	61
2.2 Challenges of designing and functionalizing fullerenes	63
2.3 Structure of the thesis	63

<b>Chapter 3. Interlayer morphology of fullerenes</b>	<b>65</b>
<b>3.1 Research background</b>	<b>65</b>
<b>3.2 Mixed C<sub>60</sub>/C<sub>70</sub> ETL for high-performance PSCs</b>	<b>67</b>
3.2.1 Investigation of pristine fullerene ETLs in PSCs	67
3.2.2 Investigation of mixed fullerenes ETLs in PSCs	70
3.2.3 Investigation of vacuum-dry process for fullerene ETLs in PSCs	75
<b>3.3 Materials and methods</b>	<b>78</b>
3.3.1 Materials preparation	78
3.3.2 Device fabrication	79
3.3.3 Performance evaluation and characterization	80
<b>3.4 Summary</b>	<b>81</b>
 <b>Chapter 4. Electron-transport mobility of fullerenes</b>	 <b>83</b>
<b>4.1 Research background</b>	<b>83</b>
<b>4.2 Fullerene-cation-mediated synthesis of FIFs</b>	<b>86</b>
4.2.1 Synthesis of arylhydro[60]fullerenes	86
4.2.2 Synthesis of aryl[60]fullerenyl dimer precursors	87
4.2.3 Optimization for reaction conditions	88
4.2.4 Substrate scope of FIFs	89
4.2.5 Mechanistic studies of fullerene-cation mediated synthesis	91
<b>4.3 PSCs performance and electron mobility of FIFs</b>	<b>92</b>
4.3.1 Photovoltaic performance of FIFs applied PSCs	92
4.3.2 Energy levels of FIFs	94
4.3.3 Charge dynamics of FIF	96
4.3.4 Hysteresis of FIF-applied PSCs	97
4.3.5 Computational studies of electron-transport ability of FIFs	98
<b>4.4 Materials and methods</b>	<b>101</b>
4.4.1 Materials preparation	101
4.4.2 Synthesis of full-carbon indano[60]fullerenes	102
4.4.3 Device fabrication and evaluation	105
<b>4.5 Summary</b>	<b>107</b>
 <b>Chapter 5. Passivation effect of fullerenes</b>	 <b>109</b>
<b>5.1 Research background</b>	<b>109</b>
<b>5.2 FIFs as passivation layer in PSCs</b>	<b>111</b>
5.2.1 Influence of molecular hindrance	111
5.2.2 Exciton quenching by passivation layer	113
5.2.3 Film quality of perovskite layer	114
5.2.4 Large-size crystal growth of perovskite cell	115
5.2.5 Trap density and trap-filling limit voltage	117
5.2.6 Reproducibility of fullerene passivation layer applied PSCs	118

<b>5.3</b>	<b>Amino[60]fullerene as passivation dopant in PSCs</b>	<b>119</b>
5.3.1	Fullerene-cation-mediate synthesis of amino[60]fullerene	119
5.3.2	Amino[60]fullerene doped perovskite for PSCs	121
<b>5.4</b>	<b>Materials and methods</b>	<b>122</b>
5.4.1	Fullerene-cation-mediated synthesis of 1,4-diaryl[60]fullerenes	122
5.4.2	Fabrication procedures of inverted PSCs	124
<b>5.5</b>	<b>Summary</b>	<b>125</b>
<b>Chapter 6.</b>	<b>Evaporable fullerene-fused ketone as ETL</b>	<b>127</b>
<b>6.1</b>	<b>Research background</b>	<b>127</b>
<b>6.2</b>	<b>Synthesis of fullerene-fused ketones</b>	<b>129</b>
6.2.1	Optimization of reaction conditions	129
6.2.2	Mechanistic studies for the synthesis of fullerene-fused ketones	130
6.2.3	Extension of substrate scope	139
<b>6.3</b>	<b>Evaporable fullerene-fused ketone as ETL in PSCs</b>	<b>140</b>
6.3.1	Thermal stability of fullerene-fused ketone	140
6.3.2	Thermal-deposition of FIF and fullerene-fused ketone	141
6.3.3	Device performance	142
<b>6.4</b>	<b>Materials and methods</b>	<b>143</b>
6.4.1	Synthesis of fullerene-fused ketone	143
6.4.2	Device fabrication	144
<b>6.5</b>	<b>Summary</b>	<b>145</b>
<b>Chapter 7.</b>	<b>Conclusions</b>	<b>147</b>
<b>7.1</b>	<b>Conclusions</b>	<b>147</b>
<b>7.2</b>	<b>Prospects</b>	<b>149</b>
<b>Appendix</b>		<b>151</b>
<b>A.1</b>	<b>M13 bacteriophage-template for perovskite growth</b>	<b>151</b>
<b>A.2</b>	<b>s-SWNT for growth and bridging perovskite crystals</b>	<b>153</b>
<b>Bibliography</b>		<b>157</b>

## *Contents*

---



## List of Figures

<b>Figure 0.1.</b> Amount of papers published and indexed by IST Web of Science™ with different keywords as: (a) fullerene; (b) carbon nanotubes; (c) graphene.	2
<b>Figure 0.2.</b> The expectations and big history news related to fullerene integrated with the Hype Cycle curve.	3
<b>Figure 1.2.1.1.</b> Examples for fullerene-anion mediated reactions.	7
<b>Figure 1.2.1.2.</b> Examples for fullerene-radical mediated reactions.	9
<b>Figure 1.2.1.3.</b> Examples for fullerene cycloaddition reactions.	11
<b>Figure 1.2.2.</b> Generation of [60]fullerene cation intermediates.	13
<b>Figure 1.2.2.1.</b> Early-stage studies on fullerene-cation chemistry.	14
<b>Figure 1.2.2.2.</b> Recent studies on fullerene-cation chemistry.	16
<b>Figure 1.2.2.3.</b> FeCl <sub>3</sub> -mediated fullerene radical cation generation.	19
<b>Figure 1.2.2.4.</b> Cu[II]-mediated fullerene cations generation.	20
<b>Figure 1.3.1.1.</b> Illustrations of the structure and the working principle of photovoltaics.	22
<b>Figure 1.3.1.2.</b> Illustrations of the $J$ - $V$ curve with related photovoltaic parameters.	24
<b>Figure 1.3.2.1.</b> Illustrations of photoelectric conversion mechanism inside active layer.	26
<b>Figure 1.3.2.2.</b> The first fullerene-applied OSCs with an illustration of device structure.	28
<b>Figure 1.3.2.3.</b> Fullerene electron acceptors with a 58- $\pi$ system.	29
<b>Figure 1.3.2.4.</b> Fullerene electron acceptors with a 56- $\pi$ system.	34
<b>Figure 1.3.2.5.</b> Fullerene electron acceptors with other $\pi$ system.	37

## *List of Figures*

---

<b>Figure 1.3.2.6.</b> PCE record plot of OSCs with P3HT:fullerenes as active layer.	42
<b>Figure 1.3.3.1.</b> (a) The graphic illustration of octahedra structure of the perovskite material. (b) A summarize energy level diagram of representative organometal perovskite materials.	43
<b>Figure 1.3.3.2.</b> Fullerenes applied as electron-transport layer in PSCs.	46
<b>Figure 1.3.3.3.</b> Fullerenes applied as over-coat on top of metal oxide layer in PSCs.	51
<b>Figure 1.3.3.4.</b> Fullerenes applied as dopant in PSCs.	56
<b>Figure 1.3.3.5.</b> PCE record plot of fullerenes utilized MAPbI <sub>3</sub> -PSCs with different application methods.	60
<b>Figure 2.1.</b> Principles for designing the fullerene materials for OSCs and PSCs.	62
<b>Figure 3.2.1.1.</b> Illustration and cross-section SEM observations of PSC architectures used in this work.	67
<b>Figure 3.2.1.2.</b> Computed energy band diagrams of pristine fullerenes and mixed C <sub>60</sub> /C <sub>70</sub> .	68
<b>Figure 3.2.1.3.</b> Photoluminescence of MAPbI <sub>3</sub> on different fullerene ETL films with glass substrates.	69
<b>Figure 3.2.2.1.</b> <i>J-V</i> curves of the normal-type PSCs using a) thermal-deposited C <sub>60</sub> - (black) and C <sub>70</sub> - (red) as ETLs; b) spin-coated C <sub>60</sub> - (black) and C <sub>70</sub> - (red) as ETLs.	70
<b>Figure 3.2.2.2.</b> a) GIXRD 2θ scan of thermal-deposited C <sub>60</sub> film (blue line), spin-coated C <sub>60</sub> film (black line), and spin-coated mixed C <sub>60</sub> /C <sub>70</sub> film (red line). TEM images of b), c) thermal-deposited C <sub>60</sub> film; d), e) spin-coated C <sub>60</sub> film with an SAED as an inset; and f), g) spin-coated mixed C <sub>60</sub> /C <sub>70</sub> film with an SAED as an inset.	71
<b>Figure 3.2.2.3.</b> AFM topographic images of spin-coated a) C <sub>60</sub> film and b) mixed C <sub>60</sub> /C <sub>70</sub> film with roughness average values. AFM adhesion images of spin-coated c) C <sub>60</sub> film and d) mixed C <sub>60</sub> /C <sub>70</sub> film with the 3D images. e) Transmittance of fullerene ETL films with different C <sub>60</sub> /C <sub>70</sub> ratios along with their pictures.	73
<b>Figure 3.2.2.4.</b> Photovoltaic parameters and statistical analysis of thermal-deposited	

## List of Figures

---

- C<sub>60</sub>-applied PSCs (black circles), spin-coated C<sub>60</sub>-applied PSCs (red triangles), spin-coated mixed C<sub>60</sub>/C<sub>70</sub>-applied PSCs (blue diamonds), and vacuum-dried mixed C<sub>60</sub>/C<sub>70</sub>-applied PSCs (purple squares), showing a)  $J_{SC}$ , b)  $V_{OC}$ , c) FF, and d) PCE. 74
- Figure 3.2.3.1.** a)  $J$ - $V$  curves of PSCs with mixed C<sub>60</sub>/C<sub>70</sub> ETL by different post treatment. AFM images of spin-coated C<sub>60</sub>/C<sub>70</sub> films by b) 200 °C TA, and b) 100 °C vacuum-dry. 76
- Figure 4.2.5.** Mechanism of Cu[II]-promoted fullerene-cation-mediated synthesis for FIFs. 91
- Figure 4.3.1.1** (a) Illustration of a normal-type planar PSC structure in this study with fullerenes as passivation layers. (b)  $J$ - $V$  curves of the selected best-performing examples: control device on bare SnO<sub>2</sub> (black line), SnO<sub>2</sub>/C<sub>60</sub> (blue line) and SnO<sub>2</sub>/FIF **5a** (red line). 92
- Figure 4.3.2.** Potentials in eV vs a ferrocene/ferrocenium (Fc/Fc<sup>+</sup>) couple were recorded by cyclic voltammetry in *o*-DCB solution containing Bu<sub>4</sub>N<sup>+</sup>(CF<sub>3</sub>SO<sub>2</sub>)<sub>2</sub>N<sup>-</sup> (0.1 M) as supporting electrolyte at 25 °C with a scan rate of 0.05 V/s. Platinum disk, platinum wire, and Ag/Ag<sup>+</sup> electrodes were used as the working, counter, and reference electrodes, respectively. <sup>a</sup> Estimated LUMO levels using the following equation: LUMO level = – (4.8 +  $E_1$ ) eV [154]. \* Irreversible wave. 94
- Figure 4.3.3.** Electron mobility measurements based on space-charge limited current. 96
- Figure 4.3.4.**  $J$ - $V$  curves with hysteresis illustration of perovskite coated on (a) bare SnO<sub>2</sub> and (b) on FIF **5a**/SnO<sub>2</sub>. 97
- Figure 4.3.5.** (a) Molecular orbitals of **5a** visualized by VESTA with isosurfaces at 0.01 e<sup>1/2</sup>Å<sup>-3</sup>. (b) Solid state packing from molecular dynamic simulations. 98
- Figure 5.1.** Molecular structure of FIF and the schematic mechanism of methoxy passivation. 110
- Figure 5.2.1.** FTIR spectra of FIFs **5a** (red line) for (a)  $\nu_{(C-H)}$  and (c)  $\nu_{(C-O)}$ , **5f** (blue line) for (b)  $\nu_{(C-H)}$  and (d)  $\nu_{(C-O)}$  with and without the presence of PbI<sub>2</sub>. 112
- Figure 5.2.2.** (a) UV-Vis spectra of glass/SnO<sub>2</sub>/MAPbI<sub>3</sub> (blue), glass/SnO<sub>2</sub>/C<sub>60</sub>/MAPbI<sub>3</sub> (green), glass/SnO<sub>2</sub>/**5a**/MAPbI<sub>3</sub> (red); (b) Steady-state PL spectra of glass/MAPbI<sub>3</sub> (black), glass/SnO<sub>2</sub>/MAPbI<sub>3</sub> (blue), glass/SnO<sub>2</sub>/C<sub>60</sub>/MAPbI<sub>3</sub>

## List of Figures

---

- (green), and glass/SnO<sub>2</sub>/**5a**/MAPbI<sub>3</sub> (red) excited by a light source with a wavelength of 550 nm. 113
- Figure 5.2.3.** (a) Water contact angles of DMF on the C<sub>60</sub>, PC<sub>61</sub>BM, FIF (**5a**), respectively. (b) Coverage images of corresponding fullerenes on the top of SnO<sub>2</sub>. (c) The images of perovskite film on C<sub>60</sub>, PC<sub>61</sub>BM, and FIF (**5a**), respectively. 114
- Figure 5.2.4.1.** Top-view and cross-sectional SEM images of the perovskite films on **5a**-passivated and bare SnO<sub>2</sub> substrates. 115
- Figure 5.2.4.2.** (a) XRD spectra of the reference ITO/SnO<sub>2</sub>/MAPbI<sub>3</sub> (blue), ITO/SnO<sub>2</sub>/C<sub>60</sub>/MAPbI<sub>3</sub> (green), ITO/SnO<sub>2</sub>/**5a**/MAPbI<sub>3</sub> (red). (b) (110) Peak showing the FWHM trend. 116
- Figure 5.2.5.** Trap density and trap-filling limit voltage measurement through SCLC curves. 117
- Figure 5.2.6.** Statistical analyses and distribution of 20 devices in the same batch: (a) PCE, (b)  $V_{OC}$ , (c) FF, and (d)  $J_{SC}$ . 118
- Figure 5.3.1.1.** Fullerene-cation-mediated intermolecular coupling between fullerene-cation and weak nucleophiles. 120
- Figure 5.3.1.1.** Fullerenyl-cation-mediated coupling reactions with functional aryl groups to obtain functionalized diaryl[60]fullerenes. 120
- Figure 5.3.2.** Amino[60]fullerene as an dopant for passivating the perovskite at grain boundaries. 121
- Figure 6.1.1.** Concept of one-step direct oxidation of alkoxy group to ketones. 128
- Figure 6.2.2.1.** <sup>18</sup>O isotope-labeled experiments. Reaction conditions: **1a** (3.0 mg, 3.6 μmol), CuBr<sub>2</sub> (4.0 equiv.), *o*-DCB (3.0 mL) at 100 °C for 1.5 hours in a sealed tube. (a) Absence of H<sub>2</sub><sup>18</sup>O. (b) 20.0 equiv. of H<sub>2</sub><sup>18</sup>O. 130
- Figure 6.2.2.2.** Reaction conditions: **1a** (3.0 mg, 3.6 μmol), CuBr<sub>2</sub> (4.0 equiv.), *o*-DCB (3.0 mL). (a) Concentration of **1a** varies over time at different temperature. (b) Concentration of **2a** varies over time at different temperatures. (c) Plots of  $\ln([1a]_0/[1a])$  varies over time at different temperature, where  $[1a]_0$  and  $[1a]$  stands for an initial concentration and the concentration at the time of **1a**, respectively. Reaction concentration varies over time at different temperature. (d) Arrhenius (black) and Eyring plots (blue) in this one-step

## *List of Figures*

---

oxidation reaction.	132
<b>Figure 6.2.2.4.</b> TEMPO experiments. Conditions: <b>1a</b> (3.0 mg, 3.6 $\mu\text{mol}$ ), $\text{CuBr}_2$ (4.0 equiv.), <i>o</i> -DCB (3.0 mL) at 100 $^\circ\text{C}$ for 1.5 hours. (a) Absence of TEMPO. (b) 4.0 equiv. of TEMPO. (c) 10.0 equiv. of TEMPO.	135
<b>Figure 6.2.2.5.1.</b> Plausible mechanism for $\text{CuBr}_2$ promoted one-step direct oxidation of alkoxy to ketone.	136
<b>Figure 6.2.2.5.2.</b> Plausible mechanism for $\text{H}_2\text{O}$ involved cycle. $^1\text{H}$ NMR with $\text{H}_2\text{O}$ as internal reference ( $\delta = 1.560$ ppm).	137
<b>Figure 6.2.2.5.3.</b> DFT computed energy change from <b>III</b> to <b>2a</b> in the presence of $\text{Br}^-$ .	137
<b>Figure 6.2.2.5.4.</b> DFT computed energy change from <b>I</b> to <b>II</b> in the presence of $\text{Br}^-$ .	138
<b>Figure 6.3.1.</b> TGA analyses of (a) FIF <b>5a</b> and $\text{PC}_{61}\text{BM}$ , and (b) $\text{C}_{60}$ under the nitrogen atmosphere.	140
<b>Figure 6.3.2.</b> HPLC analyses of the fullerenes (a) before thermal deposition, and (b) after thermal-deposition under a vacuum chamber.	141
<b>Figure 6.3.3.</b> $J$ - $V$ curves of (a) $\text{C}_{60}$ as thermal-deposited ETL, and (b) Fullerene-fused ketone as thermal-deposited ETL.	142
<b>Figure 6.5.</b> Graphic summary of one-step oxidation of alkoxy indano[60]fullerenes to [60]fullerene-fused ketones.	145
<b>Figure A.1.</b> The concept of applying denatured M13 bacteriophage for high-performance PSCs.	152
<b>Figure A.2.</b> The concept of applying denatured M13 bacteriophage for high-performance PSCs.	154

## *List of Figures*

---

# List of Tables

<b>Table 3.2.1.1.</b> Photovoltaic parameters of the PSCs using thermal-deposited fullerenes as ETLs under one sun (AM 1.5 G, 100 mW cm <sup>-2</sup> ).	67
<b>Table 3.2.2.1.</b> Photovoltaic parameters of the normal-type PSCs using spin-coated fullerenes as the ETLs under one sun (AM 1.5 G, 100 mW cm <sup>-2</sup> ).	71
<b>3.2.3 Investigation of vacuum-dry process for fullerene ETLs in PSCs</b>	75
<b>Table 3.2.3.1.</b> Photovoltaic parameters of the normal-type PSCs using mixed C <sub>60</sub> /C <sub>70</sub> as the ETL with different post treatments under one sun (AM 1.5 G, 100 mW cm <sup>-2</sup> ).	75
<b>Table 4.2.1.</b> Synthesis of arylhydro[60]fullerenes <b>3a–g<sup>a</sup></b> .	86
<b>Table 4.2.2.</b> Synthesis of arylhydro[60]fullerenes <b>4a–g<sup>a</sup></b> .	87
<b>Table 4.2.3.</b> Optimization for reaction conditions for <b>5a<sup>a</sup></b> .	88
<b>Table 4.2.4.</b> Fullerene-cation-mediated intramolecular cyclization with versatile substrates <sup>a</sup> .	90
<b>Table 4.3.1.1.</b> Photovoltaic parameters of the normal-type perovskite solar cells using fullerenes as the over-coating layer of ETL under 1 sun (AM 1.5 G, 100 mW cm <sup>-2</sup> ). Average values with standard deviation are obtained from 20 devices in the same batch.	93
<b>Table 4.3.3.</b> Electron mobility of C <sub>60</sub> and <b>5a</b> .	96
<b>Table 5.2.4.1.</b> XRD peak characterization and information.	116
<b>Table 6.2.1.</b> Optimization of the reaction conditions. <sup>[a]</sup>	129
<b>Table 6.2.2.1.1.</b> HRMS data of non- <sup>18</sup> O labeled <b>2a</b> .	131
<b>Table 6.2.2.1.2.</b> HRMS data of <sup>18</sup> O labeled <b>2a-(<sup>18</sup>O)</b> .	131
<b>Table 6.2.2.2.</b> Activation parameters for the one-step direct oxidation of alkoxy indano[60]fullerene <b>1a</b> .	133

## *List of Tables*

---

<b>Table 6.2.2.3.</b> $^1\text{H}$ NMR with $\text{H}_2\text{O}$ as internal reference ( $\delta = 1.560$ ppm) of (a) <b>1a</b> . (b) Reaction mixture. (c) Methanol.	134
---	-----

<b>Table 6.2.3.</b> $\text{CuBr}_2$ promoted one-step direct oxidation of alkoxy to ketone with versatile substrates <sup>[a]</sup> .	139
---	-----



## **Nomenclature**

OSC	Organic solar cell
PSC	Perovskite solar cell
$J$ – $V$ characteristic	Current density–voltage characteristic
$V_{OC}$	Open circuit voltage
$J_{SC}$	Short circuit current density
FF	Fill factor
$R_s$	Serial resistance
$R_{SH}$	Shunt resistance
PCE	Power conversion efficiency
AFM	Atomic force microscopy
PL	Photoluminescence
SEM	Scanning electron microscopy
TEM	Transmission electron microscopy
SAED	Selected-area electron diffraction
XPS	X-ray photoelectron spectroscopy
XRD	X-ray diffraction spectroscopy
FT-IR	Fourier transforms infrared spectroscopy
NMR	Nuclear magnetic resonance
HRMS	High-resolution mass spectrum
HPLC	High-performance liquid chromatography
DFT	Density function theory
HOMO	Highest occupied molecular orbital
LUMO	Lowest unoccupied molecular orbital
SCLC	Space-charge-limited current

## *Nomenclature*

---

## **Preface**

A person, who was born between the 1980s and 1990s, not only can witness the occurrence of The Fourth Industrial Revolution but also can feel the fundamental changes in the way we live, work and relate to another. I, the author of this thesis, feel extremely honored that God brings my life to this era so that I could also become a contributor to this historical moment. Different from The Third Industrial Revolution, where most silicon-based high-tech devices have emerged, Moore's law has reached its end when stepping in the Fourth Industrial Revolution. Consequently, the development pace of human society is highly probable to decelerate if kept following the trend of the silicon-based industry, which is compelling the human to discover a new growth engine to switch on the next-stage development.

Very intriguingly, the major economies around the world coincidentally announced the same target at the same time to discover and develop the new materials, which are mainly related to the carbon-based semiconducting materials. Although the discovery of carbon is as old as the homo sapiens, the discovery of first carbon-based semiconducting material was in the 1950s. Since 1985, the year when fullerene was discovered, human strides to the new era of nanoscience and nanotechnology. Within the next decade, the other two carbon allotropes carbon nanotubes and graphene were also found. Compared with the most popular silicon-based products in the semiconducting industry, the carbon-based semiconducting materials exhibit more superiors such as flexibility, transparency, and portability, which perfectly meets the requirement of wearable devices in contemporary life. On the other hand, compared with chemical modifying methods for silicon materials, there are more methods have been developed to functionalize the carbon materials. Thanks to those versatile chemical methods, carbon semiconducting materials can be customized to possess more unique properties for use in different purposes. Accordingly, considerable efforts have

been devoted to the research and development of carbon cluster materials, especially in academic research, there are more than 10,000 papers published per year. However, excluding the academic interests in graphene still keeps growing, both fullerene and carbon nanotubes encountered a decrease in academic interests, yet lots of publications achieved per year according to the up-to-date index by ISI Web of Science™ (**Figure 0.1**).

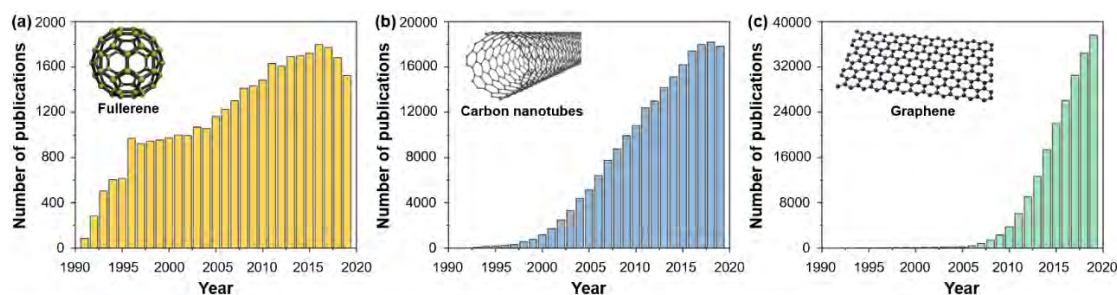


**Figure 0.1.** Amount of papers published and indexed by IST Web of Science™ with different keywords as: (a) fullerene; (b) carbon nanotubes; (c) graphene.

“Structure determined the property,” which perfectly explains the different properties that fullerene, carbon nanotubes, and graphene have. Graphene, a sheet-shaped molecule that structure by  $sp^2$  hybridized orbitals, exhibits its dominant conductivity among all carbon cluster materials. Differently, fullerene and carbon nanotubes can present the semi-conductivity, which is thanks to they are formed by a combination of  $sp^2$  and  $sp^3$  hybridized orbitals. As fullerene has more components of  $sp^3$  hybridization, it only shows the semiconducting ability. But fullerene demonstrates its most strong chemical modifiability among those materials so that it benefits tremendously from the development of related organic chemistry.

Although fullerene was the earliest carbon cluster material indicating the decreased academic interest in 2016, it is supposed to be the most industry-suitable semiconducting carbon material. This academic interest decrease could be reasonably attributed to the bottleneck that the fullerene chemistry faced, as fullerene material development much relies on its chemistry development. According to the trend of technology development illustrated by the Hype Cycle curve, fullerene is now

undergoing its downside movement (**Figure 0.2**).

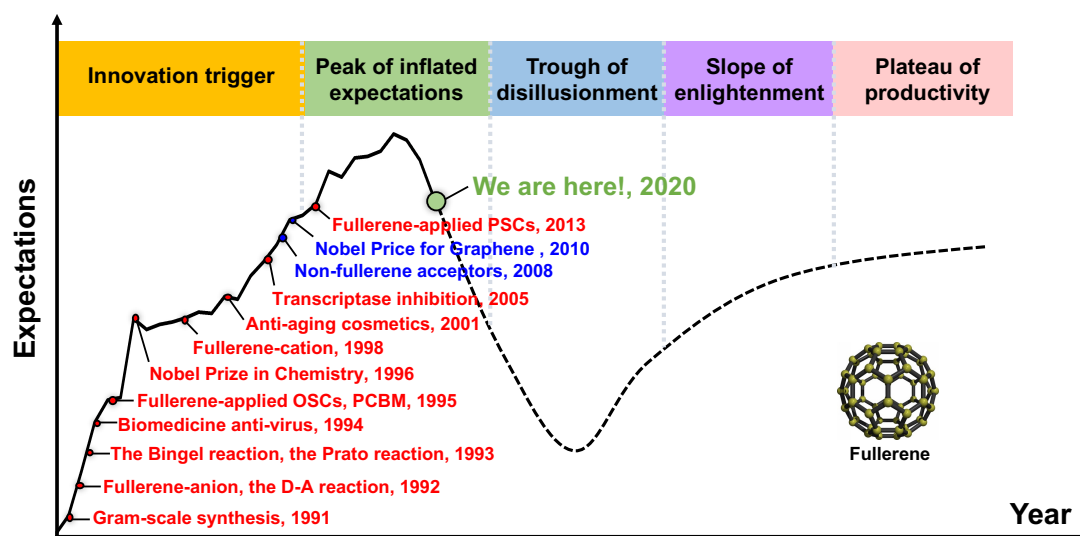


**Figure 0.2.** The expectations and big history news related to fullerene integrated with the Hype Cycle curve.

Since the gram-scale synthesis achieved in 1991, the investigation on fullerene chemistry became accessible. Therefore, sorts of chemistry synthetic methods including, anionic reaction, radical reaction, cycloaddition reaction and cationic reactions, have been successfully put forwarded. Then, versatile applications such as photovoltaic, biomedicine, and cosmetics have been achieved. Nevertheless, there is no further innovation occurred on neither fullerene chemistry nor the applications since 2014, the year that first fullerene-applied perovskite solar cell was fulfilled.

Typical Hype Cycle consists of five stages as innovation trigger, peak of inflated expectations, trough of disillusionment, slope of enlightenment and plateau of productivity. Apparently, fullerene is now at the peak of inflated stage and on the way to the trough of disillusionment. Therefore, rather than being pessimistic about the fullerene industry, I am more optimistic about fullerene's future coming profitable market if we can have a different understanding to lead our research and development of fullerene.

Herein, considered the fullerene materials rely much on the development of

## *Preface*

---

chemistry, my Ph.D. course was devoted most part to the development of fullerene cation chemistry, which is the youngest specie among fullerene chemistry. Subsequently, a series of novel functionalized fullerene materials have been successfully obtained and then investigated in photovoltaics. This thesis aims to provide the fullerene industry with a better understanding and method to design and functionalize the fullerene materials, especially for the people who are working in fullerene-applied perovskite solar cells.

Science is fascinating because of its unpredictable nature. What we can do is keep hungry and humble towards nature, and discover as much as we can. Therefore, there are still many unexplored areas in science, which is calling for further research to make them come true.

Hao-Sheng Lin  
@the University of Tokyo  
March 12, 2020

## Chapter 1.

# Introduction

### 1.1. Research background

Buckminsterfullerene ( $C_{60}$ ), an allotrope of carbon whose molecule consists of 60 carbon atoms in a fully symmetric spherical shape, was first discovered in 1985 by H. W. Kroto, R. F. Curl, and R. E. Smalley *et al.* [1]. Since the first gram-scale was reported by W. Krätschmer and co-workers in 1990, tremendous efforts have been devoted to investigating the properties and applications of fullerenes [2]. Accordingly, fullerene related disciplines including chemistry, physics, biology got rapid development within decades so that fullerene materials have been achieved and evaluated in sorts of areas such as photovoltaics [3,4], biomedicines [5,6], cosmetics [7], and field-electric transistors [8,9]. However, among that wide range of tested applications, fullerene materials have been mostly demonstrated in the photovoltaic field thanks to their remarkably excellent electrical properties such as ultrafast photo-induced charge transfer property [10], and the low reorganization energy [11]. Thus, fullerene materials present a superior performance in both organic solar cells (OSCs) and perovskite solar cells (PSCs), although different roles that fullerene materials play. So far, the fullerene applied photovoltaics have achieved a PCE up to 21.3% [12], dramatically promoted from the first fullerene-utilized photovoltaics with a PCE of 3.2% in 1995 [13].

However, fullerene materials happened to the bottleneck in 1996, shifting substantial interests to non-fullerene materials [14], although fullerene-applied PSCs just boosted as a promising field [15]. Back in history, once a breakthrough occurred in materials science, there must have progress that happened in fundamental chemistry methodology in advance. Consequently, the current severe situation in fullerene

materials profoundly relates to the shortage of breakthrough among fullerene chemistry methodologies. Herein, this thesis aims to provide a comprehensive strategy for the high-performance fullerene-applied PSCs through the design and functionalization of fullerenes by advanced fullerene chemistry methodologies.

## **1.2. Fullerene chemistry**

Based on the critical active species that the chemical reaction involves in, the chemistry is typically classified as anion chemistry, radical chemistry, cation chemistry, and cycloaddition chemistry. It is well accepted that  $C_{60}$  generally performs similarly as an electron-deficient olefin because of its unique bond configuration formed by a mixture of  $sp^2$  and  $sp^3$  hybridized orbitals [16]. Accordingly, most studies were carried on the fullerene anion and radical species. Besides, thanks to the unique lowest unoccupied molecular orbital (LUMO) level of  $C_{60}$ , it can easily behave as the dienophile to undergo the cycloaddition reactions [17]. So, the abovementioned reactions are now commonly categorized as conventional fullerene chemistry. Although the most amount of materials were born of classical fullerene chemistry, the conventional fullerene chemistry now seems to be stuck, and no more updated fullerene materials could be obtained anymore. Therefore, faced with the bottleneck met in the conventional fullerene chemistry, scientists started to attempt the most challenge fullerene cation chemistry, expecting that fullerene cation could provide a new access for discovering novel materials using in fullerene applications. Herein, this section will separately introduce the conventional fullerene chemistry and fullerene cation chemistry. But more attention will be concentrated on fullerene cation chemistry, as this is the major breakthrough that this thesis achieved.



### 1.2.1. Conventional fullerene chemistry

Owing to fullerene behaving as an electron-olefin and its impressively low LUMO level, it easily reacts through an anionic pathway, a radical pathway, or a cycloaddition pathway. Accordingly, much research and considerable efforts have been devoted to investigating conventional fullerene chemistry.

#### 1.2.1.1. Fullerene anion chemistry

As fullerene shows its extraordinary electron-deficiency, it can readily react with all sorts of nucleophilic reagents through the fullerene-anion mediated reactions (Figure 1.2.1.1).

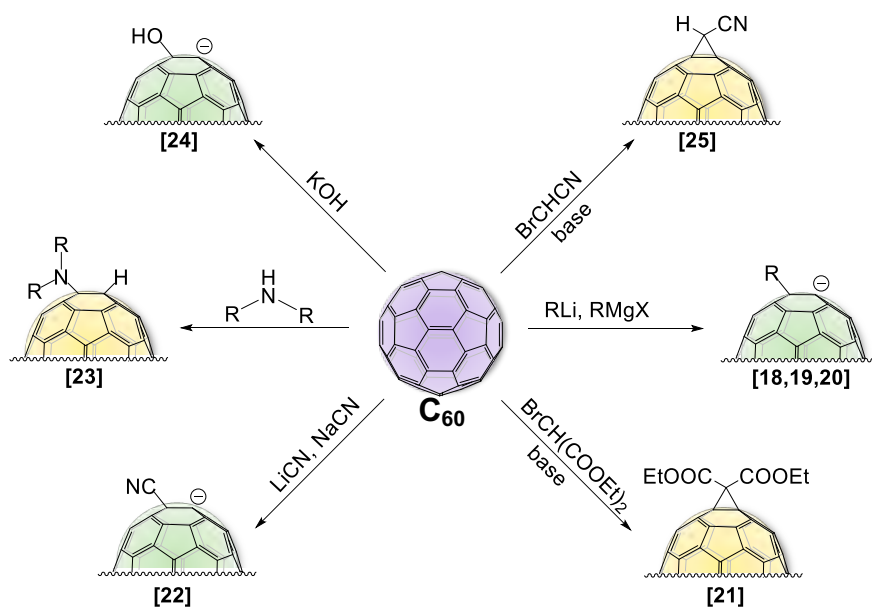


**Figure 1.2.1.1.** Examples for fullerene-anion mediated reactions.

$C_{60}$  can easily react with organometallics such as organolithium [18], and Grignard reagents to form the organo[60]fullerene anion  $RC_{60}^-$  as primary intermediates [19]. Then, generated  $RC_{60}^-$  can quickly react with the electrophile to form the fullerene 1,2-adducts [20]. In 1993, the Bingel group presented an elegant method for the cyclopropanation of fullerenes by using  $\alpha$ -halo esters or  $\alpha$ -halo ketones as nucleophiles in the presence of a base [21]. Notably, the Bingel reaction is now well recognized as

one of the most useful strategies for the efficient production of cyclopropano[60]fullerene derivatives. Apart from the introduction of alkyl or phenyl moieties, the addition of cyanide also undergoes a fullerene-anion mediated pathway. For instance,  $C_{60}$  can react with LiCN or NaCN at room temperature to produce the cyano[60]fullerene anion and then followed by quenching with various electrophiles [22]. Also, the molecules that contain the Lewis base elements such as amines and hydroxyls can correspondingly produce the amino[60]fullerenes [23], and hydroxyl[60]fullerenes [24], respectively. Similar to the Bingel reaction,  $C_{60}$  can also easily react with the  $\alpha$ -halocarbanions to form the cyanocyclopropano[60]fullerene [25].

In addition to the directly react with the nucleophiles to form the fullerene-anion intermediates, fullerene-anions can also be generated by chemical reduction or electrochemical reduction. For instance, the electrochemical reduction can selectively reduce the  $C_{60}$  to a variety of fullerene anions (e.g.,  $C_{60}^{n-}$ ,  $n = 1-6$ ) [26]. In contrast, the chemical reduction by alkali metals (e.g., Li [27], K [28], Cs, Rb [29] ), alkaline earth metals (e.g., Ca, Ba) typically reduced  $C_{60}$  to its monoanionic stage [30].

In short, owing to the remarkable electron-deficiency of  $C_{60}$ , it can smoothly undergo various nucleophilic additions to form the fullerene-anion intermediate ( $NuC_{60}^-$ ). Subsequently, generated fullerene-anion intermediate is neutralized by (a) the addition of electrophiles to form  $C_{60}E_nNu_n$ ; (b) an internal nucleophilic substitution to give cyclo[60]fullerene derivatives; (c) an oxidation to afford  $C_{60}Nu_2$ .

### 1.2.1.2. Fullerene radical chemistry

Owing to the excellent electron-deficiency of  $C_{60}$ , it can easily convert to the anion by directly reduction or nucleophilic addition. Unlike the formation of fullerene-anion, fullerene-radical is generated from the accepting single electron, which has been intensively investigated by electron spin resonance (ESR) spectroscopy [31]. Consequently, since the successful characterization of the fullerene-radical, a large variety of radicals have been attempted to add to fullerenes, producing diamagnetic or paramagnetic adducts (Figure 1.2.1.2).

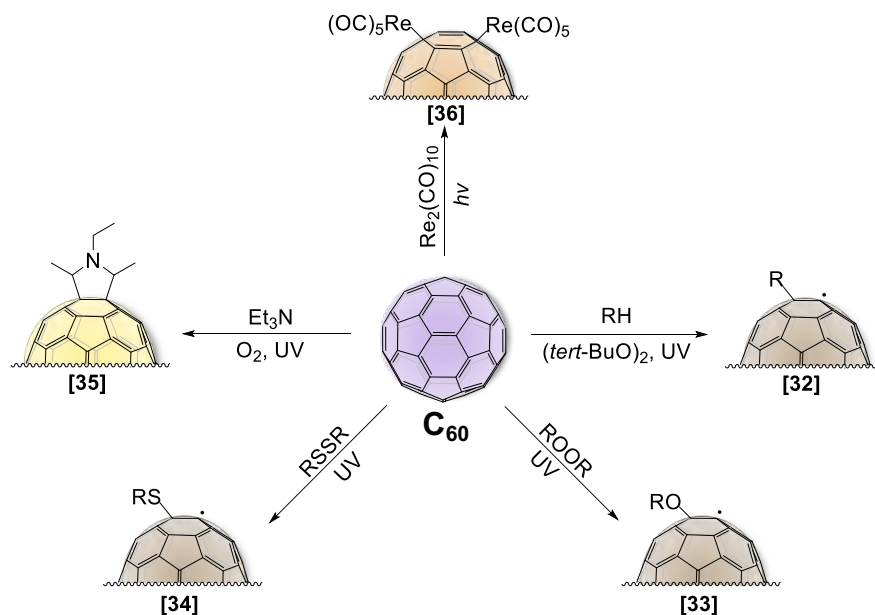


**Figure 1.2.1.2.** Examples for fullerene-radical mediated reactions.

Using peroxide reagents to initiate radical addition is one of the most popular synthetic strategies applied in radical-mediated synthesis. For example, when  $C_{60}$  reacted with hydrocarbons (RH) in the presence of di-*tert*-butylperoxide, the reaction proceeded through a fullerene-radical-mediated pathway affording alkyl[60]fullerene radicals  $RC_{60}^{\bullet}$  [32]. If the reaction was conducted in the absence of RH, the dialkylperoxides (ROOR) could react with  $C_{60}$  upon irradiation, producing the alkoxy[60]fullerene-radical  $ROC_{60}^{\bullet}$  [33]. Expectedly, the alkyl-disulfides (RSSR) can also effectively generate  $RS^{\bullet}$  upon irradiation and then immediately added to  $C_{60}$  to

provide the corresponding alkylthio radical intermediate [34]. Although tertiary amines cannot directly add to the  $C_{60}$  through nucleophilic addition, tertiary amines can react with  $C_{60}$  *via* a photochemical reaction, efficiently producing [60]fullerene-pyrroline derivatives [35]. Interestingly, the metalation of  $C_{60}$  also can be achieved by the fullerene-radical-mediated reactions. For instance,  $(CO)_5Re^{\bullet}$ , generated by photodissociation of Re–Re bond, can easily add to  $C_{60}$  to form  $C_{60}[Re(CO)_5]_2$  with a 1,4-addition pattern [36]. Generally, although fullerene mono-adduct has a 1,2-addition structure, fullerene 1,4-adduct is formed owing to the bulky substitution group. In addition to metalation of  $C_{60}$  by transition metals, transition metals, including rhodium (Rh) [37], and Tungsten (W) [38] are also widely applied for the functionalization of fullerenes through fullerene-radical intermediates.

Briefly sum up, the high electron-affinity of  $C_{60}$  and its derivatives allows fullerenes can functionalize as the radical sponge, which enables them utilized as a potential radical scavenger. Moreover, some fullerene derivatives designed for trapping the peroxide radical or hydroxyl radical, opening a new gate for curing the neurodegenerative diseases.

### 1.2.1.3. Fullerene cycloaddition chemistry

$C_{60}$  typically has two kinds of bonds, one is called [6,6]-bond, and the other is [5,6] bond. Notably, the [6,6]-bond is a double-bond, which exhibits a dienophilic character so that it can easily react with diene through cycloaddition reactions. Generally, the cycloaddition of dienes to  $C_{60}$  mainly produces the monoadducts, yet multi-addends can also be found but in a low yield. In the cycloaddition of  $C_{60}$ ,  $C_{60}$  always provides its LUMO for diene because of its remarkably low LUMO energy level. However, monoaddition brakes down the pristine 60  $\pi$ -conjugate system to 58  $\pi$ , which significantly increases the LUMO energy level so that further cycloaddition is prohibited. Although the cycloaddition reaction shows poor regioselectivity compared with fullerene-anion- or radical-mediated reactions, it is still the most utilized method for synthesizing fullerene materials because of its simple procedures (Figure 1.2.1.3).

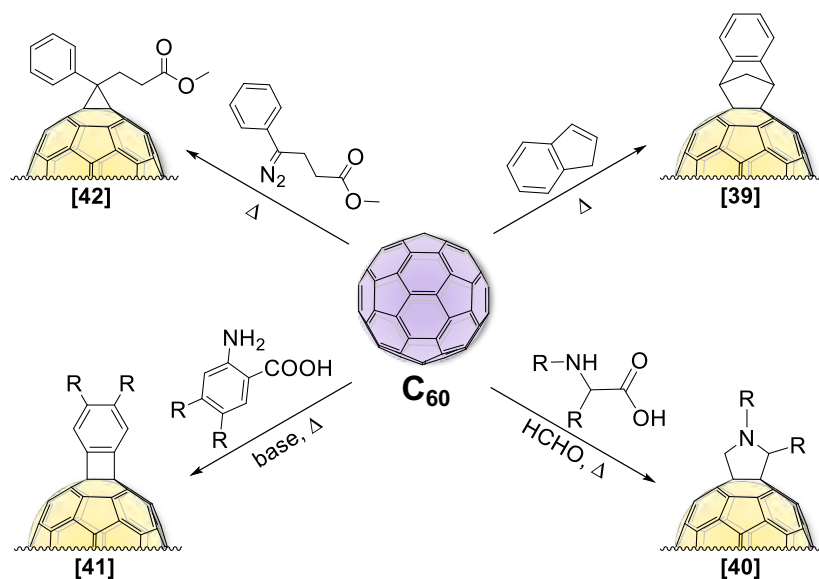


**Figure 1.2.1.3.** Examples for fullerene cycloaddition reactions.

Most cycloaddition cases were presented in [4+2] reactions, usually known as the Diels-Alder reaction,  $C_{60}$  using its [6,6] double bonds as dienophile to react with dienes. For instance, fullerene organic electron-acceptors indene- $C_{60}$  monoadduct (ICMA) and indene- $C_{60}$  bisadduct (ICBA) were synthesized from the cycloaddition of indene to  $C_{60}$  [39]. Apart from [4+2] cycloaddition,  $C_{60}$  can also react with 1,3-dipoles to undergo

[3+2] cycloadditions. The Prato reaction, the milestone reaction among [3+2] cycloadditions, using *in situ* 1,3-dipoles, generated from  $\alpha$ -amino acids with aldehydes or ketones, to react with C<sub>60</sub> producing a set of fullerene pyrroline derivatives [40]. Intriguingly, C<sub>60</sub> can also undergo the [2+2] cycloaddition with the *in situ* generated benzyne to form the cyclo[60]fullerene with a four-membered-carbon-ring [41]. Carbene, a highly reactive specie, can selectively react with the [6,6] double bonds of C<sub>60</sub> by a [2+1] cycloaddition. Through the [2+1] cycloaddition, the commercially available fullerene electron-acceptor, phenyl-C<sub>61</sub>-butyric acid methyl ester (PC<sub>61</sub>BM), produced from the reaction of C<sub>60</sub> with diazo derivatives [42].

So far, a variety of cycloadditions have applied to C<sub>60</sub> and provide a powerful tool for the efficient functionalization of fullerenes. Accordingly, versatile fullerene materials using in photovoltaics, biomedicines were derived from the cycloaddition synthesis.

Although tons of fullerene reactions mediated by anion, radical intermediates, or through a pericyclic transition state, only limited examples were presented here because of the restricted pages of this thesis. On the other hand, the main purpose of this thesis is to demonstrate a new methodology for developing new fullerene materials. Such new methods have nothing to do with the classical fullerene chemistry. Instead, novel fullerene cation chemistry will be discussed how it promotes the development of fullerene materials. Therefore, the following section will exclusively present the history of fullerene-cation chemistry and its related materials development.

### 1.2.2. Fullerene cation chemistry

Although fullerene cations abundantly exist in space as a significant interstellar molecular ion [43], lab-scale generation of fullerene-cation is extremely difficult compared with the production of fullerene-anion and fullerene-radical and fullerene-cation. This is also due mainly to the natural electro-deficiency of fullerene, which prohibits the formation of fullerene-cation directly from electrochemical oxidation or addition by electrophiles. Currently, we have successfully established a facile synthesis to provide organo[60]fullerenyl cations ( $\text{RC}_{60}^+$ ) and [60]fullerene radical cations ( $\text{C}_{60}^{\bullet+}$ ), respectively (Figure 1.2.2) [44]. It should be noted that  $\text{RC}_{60}^+$  has a newly formed LUMO with a much low LUMO energy level compared to the LUMO of pristine  $\text{C}_{60}$ . Then, the new LUMO provides further possibilities for the chemical functionalization onto the [60]fullerene cage, such as (a) nucleophilic addition reaction with a high yield and selectivity [45], (b) intramolecular rearrangement reaction to form the [60]fullerene derivatives with unique structure [46], (c) the intramolecular cyclization to produce the special fullerene derivatives [47].

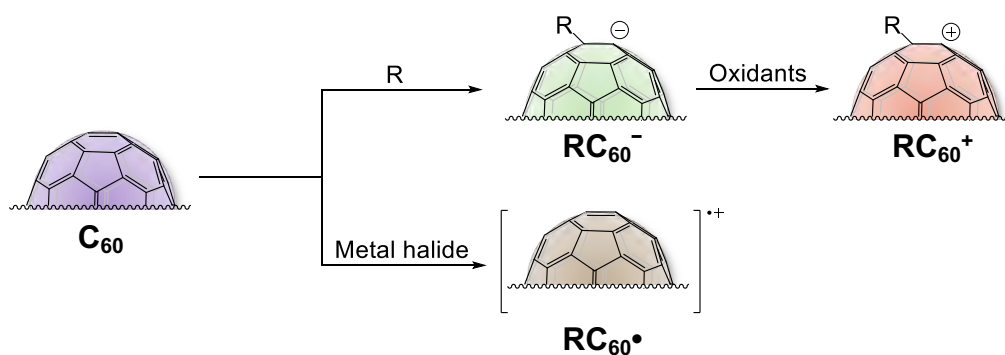


**Figure 1.2.2.** Generation of [60]fullerene cation intermediates.

Herein, this section is about to discuss the [60]fullerene derivatization methodologies based on the fullerene-cation chemistry, which is also one of the crucial points for this thesis. During the discussion, the fullerene-cation mediated reactions and produced materials will be demonstrated, which is expected to benefit the scientists who work in fullerene chemistry and materials science with a new understanding of fullerene design and functionalization.

### 1.2.2.1. Early-stage studies on fullerene cations

Although fullerene cation species are known to be unfavorable in production because of the intrinsic electron-deficiency of fullerene, many pioneering scientists contributed to early-stage studies on fullerene cation species. Thanks to their persistent efforts, several protocols have been developed to generate the fullerene cation intermediates with the production of bundles of fullerene derivatives (Figure 1.2.2.1). Herein, this section will present the early research and examples for the fullerene cation chemistry.

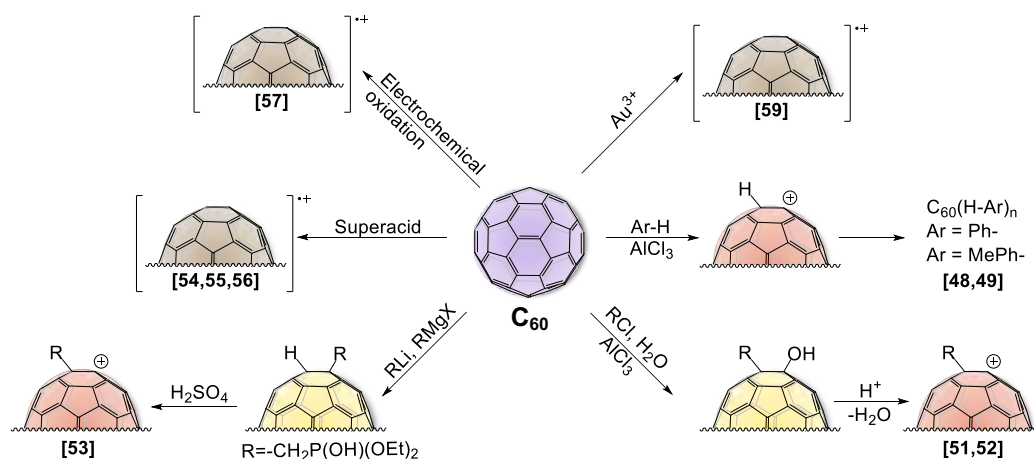


**Figure 1.2.2.1.** Early-stage studies on fullerene-cation chemistry.

First organo[60]fullerenyl cation ( $RC_{60}^+$ ) mediated reaction was reported by Olah's group in 1991, using aluminum chloride ( $AlCl_3$ ) as the Lewis acid to trigger Friedel-Crafts (F-C) reaction between benzenes and  $C_{60}$  [48,49]. Similar to classical F-C alkylation, the key intermediate of the reaction on  $C_{60}$  was the hydro[60]fullerenyl cation ( $HC_{60}^+$ ), which immediately underwent an electrophilic arylation by benzene to afford the corresponding arylated [60]fullerene derivatives  $C_{60}Ar_nH_n$  ( $Ar = C_6H_5-$ ,  $MeC_6H_4-$ ;  $n = 1-3, 6, 12, 16$ ). However, the first long-lived fullerene-cation was not fulfilled and unambiguously characterized until 1998 by treating penta-aryl[60]fullerene derivatives  $C_{60}Ar_5Cl$  ( $Ar = C_6H_5-$ ,  $4-FC_6H_4-$ ) in the presence of  $AlCl_3$  to form the *in situ* penta-aryl[60]fullerenyl cations,  $Ar_5C_{60}^+$  [50]. Although the first  $AlCl_3$  promoted F-C failed to produce an excellent result, the high reactivity of



fullerene-cation attracted considerable attention. Later on, Kitagawa and Komatsu *et al.* optimized the  $\text{AlCl}_3$ -promoted F-C reaction of  $\text{C}_{60}$ , achieving the highly selective synthesis of alkyl[60]fullerols, which could be subsequently transformed to fullerene-cation and produce alkyl[60]fullerene derivatives with broad functional groups in high yields [51,52]. To further improve the synthesis of fullerene-cation intermediate, Komatsu's group utilized the hydro[60]fullerenes ( $\text{RC}_{60}\text{H}$ ) as precursors to produce the fullerene cation intermediates [53]. Through the hydro[60]fullerenes generated fullerene-cation intermediate process, the reaction proceeded much efficiently with improved yields and selectivity.

Besides  $\text{RC}_{60}^+$  intermediates, [60]fullerenyl radical cation ( $\text{C}_{60}^{\bullet+}$ ) has also been preliminarily investigated. The first  $\text{C}_{60}^{\bullet+}$  was produced from the  $\text{C}_{60}$  in a solution of concentrated sulphuric acid and observed through the electron paramagnetic resonance (EPR) spectra in 1991 [54]. Since then, much research was successfully conducted by using superacid to oxidize  $\text{C}_{60}$  to  $\text{C}_{60}^{\bullet+}$  [55,56]. Although  $\text{C}_{60}$  can be easily achieved its  $\text{C}_{60}^{6-}$  form via electrochemical reduction, the first electrochemical oxidation generated  $\text{C}_{60}^{\bullet+}$  was not completed until 1993 under an extremely harsh condition by Echegoyen's group [57]. Later on, enlightened by this pioneering work, plenty of attempts were conducted by modifying the reaction conditions, including high-vacuum, de-gas, de-water, *etc.*, which even successfully afforded  $\text{C}_{60}^{3+}$  [58]. Apart from the electrochemical oxidation, the chemical oxidation was also investigated after that. The Choi group elegantly reported a facile production of  $\text{C}_{60}^{\bullet+}$  using  $\text{Au}^{3+}$  to oxidize the pristine  $\text{C}_{60}$  through a single electron transfer (SET) pathway [59]. Unfortunately, none of the early studies on  $\text{C}_{60}^{\bullet+}$  demonstrated useful in synthesis, which was ascribed to their high reactivity.

In short, although the above presented early-stage studies on fullerene cation intermediates failed to produce fullerene derivatives in high yields or even gave a much poor performance than the reaction mediated by fullerene-anions or radicals, these studies doubtlessly pictured the vision for the later research and development of fullerene-cation mediates.

### 1.2.2.2. Recent studies on fullerene cations

Thanks to high-pace development of chemistry and advanced fullerene techniques, recent studies unveiled considerable superiors of fullerene-cation mediated reactions. Compared with early-stage studies, recent studies presented more promising and practical methodologies for fullerene-cation mediated synthesis (Figure 1.2.2.2). Herein, this section will present recent progress and cases on fullerene-cation mediated chemistry, which is expected to afford readers an understanding of where this thesis begins.

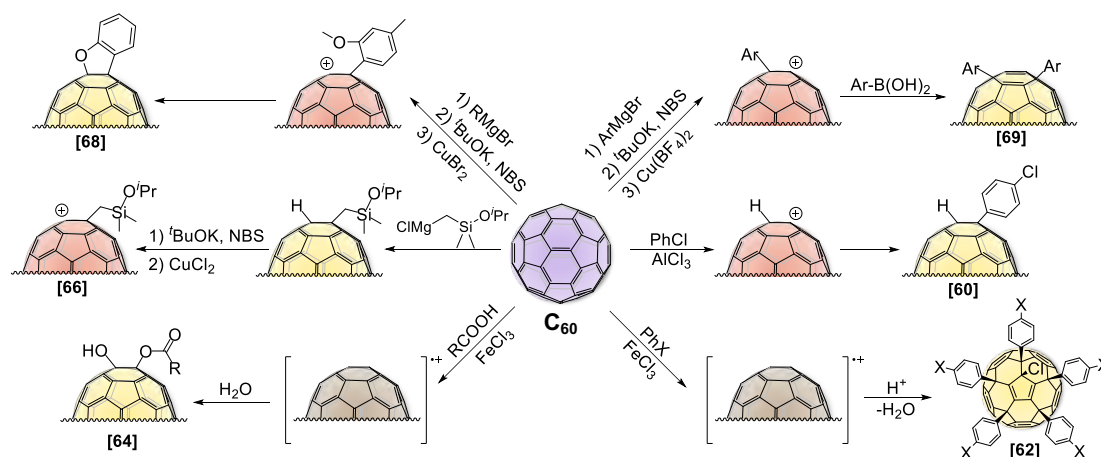


**Figure 1.2.2.2.** Recent studies on fullerene-cation chemistry.

Intriguingly, although the first  $\text{AlCl}_3$ -mediated F-C reactions of  $\text{C}_{60}$  failed to give the fullerene derivatives with high selectivity, the first applicable fullerene-cation mediated synthetic method was again found to be F-C reaction. In 2007, the Nakamura group deeply investigated previous  $\text{AlCl}_3$ -mediated F-C reaction, and conclusively confirmed that the proton source for  $\text{HC}_{60}^+$  was from the hydrolysis of  $\text{AlCl}_3$  [60]. Accordingly, through controlling the electronegativity of the benzene source, they successfully synthesized the aryl[60]fullerene derivatives with broad substrate scope in delighted yields. Different from the  $\text{AlCl}_3$ -mediated reaction,  $\text{FeCl}_3$  promoted a fullerene-radical-cation mediated reaction yet play a similar role as the Lewis acid. Compared with the  $\text{AlCl}_3$ -mediated F-C reaction,  $\text{FeCl}_3$ -mediated F-C reaction can avoid unwanted production of hydrogen[60]fullerene structure as fullerenylium proton is

well-accepted that it is detrimental to the stability. Although Cooks's group reported the first  $\text{FeCl}_3$ -mediated generation of  $\text{C}_{60}^{*+}$  in 1991 [61], the first applicable  $\text{FeCl}_3$ -mediated synthesis was presented by the Matsuo Group in 2011 [62]. They successfully synthesized versatile halogenated benzene functionalized fullerene derivatives by reacting to  $\text{C}_{60}$  with halogenated benzene substrates in the presence of  $\text{FeCl}_3$ . Next, Matsuo's group further developed the  $\text{FeCl}_3$ -mediated  $\text{C}_{60}^{*+}$  reaction so that it achieved the first fullerenyl ester derivatives [63]. More interestingly,  $\text{FeCl}_3$ -generated  $\text{C}_{60}^{*+}$  not only can efficiently synthesize the fullerene dimer ( $\text{C}_{120}$ ) [64], but it also can convert the cyclo[60]fullerene derivatives including ICMA,  $\text{PC}_{61}\text{BM}$  backward to the pristine  $\text{C}_{60}$  through a retro Diels-Alder reaction [65]. In general, despite  $\text{FeCl}_3$ -mediated reactions that can reliably generate  $\text{C}_{60}^{*+}$  to functionalize the fullerene cage with versatile substituents, the mechanism of some reactions was still unclear.

Compared to the  $\text{FeCl}_3$  and  $\text{AlCl}_3$  mediated fullerene-cation reactions, the  $\text{Cu}[\text{II}]$ -mediated fullerene-cation reactions played a dominant role in recent fullerene-cation mediated synthesis. For instance,  $\text{CuCl}_2$ -mediated fullerene-cation reactions rendered a most applicable method for synthesizing methano[60]fullerene ( $\text{C}_{60}\text{CH}_2$ ) [66], which is an essential precursor for many fullerene electron-acceptor materials such as methano indene fullerenes (MIFs) [67]. Although many groups reported the synthesis of  $\text{C}_{60}\text{CH}_2$ , the obvious drawbacks such as low yield, difficulties in purification, severely limited their utilization in the industry. Nakamura's group elegantly designed an *iso*-propoxyl silane substrate to produce the silyl-methyl fullerene precursor, whose polarity was different from those of both pristine  $\text{C}_{60}$  and  $\text{C}_{61}\text{CH}_2$ , which thusly enabled a facile separation. Intriguingly, when the *iso*-propoxyl in silane was replaced by aryl, 1,2-di(organo)fullerene derivatives were obtained from the migration of aryl onto the fullerene cage, which suggested that fullerene-cation mediated reaction also have the potential for the intramolecular migration [46]. Besides the production of methano[60]fullerene derivatives, heterocyclo[60]fullerene derivatives can also be fulfilled through  $\text{Cu}[\text{II}]$ -mediated fullerene-cation synthesis. Matsuo and Nakamura *et al.* reported  $\text{Cu}[\text{II}]$  cyclization reactions to obtain the oxygen-containing 5- and 7-

membered cyclo[60]fullerene derivatives [68]. They used versatile oxygen-containing substrates in the presence of  $\text{CuBr}_2$ , successfully affording sorts of functionalized oxygen-contain 5- and 7-membered cyclo[60]fullerenes. Notably, apart from  $\text{Cu[II]}$ -mediated intra-molecular cyclization reactions, the inter-molecular coupling reactions were also investigated through a  $\text{Cu[II]}$ -mediated reaction. Instead of heterogenous  $\text{CuX}_2$  salts, homogeneous  $\text{Cu}(\text{BF}_4)_2$  was applied as the copper source for the synthesis of 1,4-diaryl[60]fullerene derivatives thorough an inter-molecular coupling reaction [69]. This  $\text{Cu[II]}$ -mediated inter-molecular reaction showed its impressively high yields regardless of under a water-containing system.

In short, recent studies established several protocols for efficient production of fullerene-cation and fullerenyl radical cation intermediates in the presence of the Lewis acid. Among these Lewis acids,  $\text{Cu[II]}$  salts demonstrated their remarkable superiors in the geriaction of  $\text{C}_{60}^+$  because of the excellent selectivity and the high yields. More notably,  $\text{Cu[II]}$ -mediated synthesis impressively enabled the unique structure and derivatives that were unachievable when processed under a fullerenyl anion or radical-mediated reaction. Accordingly, fullerene-cation mediated synthesis undoubtedly provides excellent potentials in the fullerene materials. Therefore, all fullerene materials designed and functionalized in this thesis are derived from the fullerene-cation or fullerenyl-radical-cation mediated protocols.

### 1.2.2.3. Strategy for generation of fullerene radical cation

Recent studies successfully demonstrated an efficient *in situ* generation of  $C_{60}^{\bullet+}$  intermediate by using metal halides such as  $FeCl_3$ . If the generation of  $C_{60}^{\bullet+}$  was simply considered on the basis of oxidation/reduction potential,  $FeCl_3$  was impossible to access  $C_{60}^{\bullet+}$  intermediate as  $C_{60}^{\bullet+}/C_{60}$  showed a much positive potential (+ 2.03 V) [57] than that of  $Fe^{3+}/Fe^{2+}$  (+ 0.77 V) refer to the standard hydrogen electrode [55]. Consequently, the successful oxidation of  $C_{60}$  by  $FeCl_3$  should also be benefited from halogen. Thanks to the deep investigation on  $C_{60}^{\bullet+}$ ,  $FeCl_3$ -promoted generation of  $C_{60}^{\bullet+}$  has now been accepted as a facile method through two plausible pathways (Figure 1.2.2.3). a) Electrochemical properties of  $C_{60}$  was changed by the coordination between the chlorine atom of  $FeCl_3$  and  $C_{60}$  cage, which triggers electron transfer from  $C_{60}$  to  $FeCl_3$ , generating the  $C_{60}^{\bullet+}$  with loss of  $FeCl_2$  and  $Cl^-$ . Then,  $C_{60}^{\bullet+}$  and  $Cl^-$  form a resting state radical ( $C_{60}Cl^{\bullet}$ ), allowing  $FeCl_3$  molecule to drag the Cl from  $C_{60}Cl^{\bullet}$  to produce  $C_{60}^{\bullet+}$ . Notably, the counter anion  $FeCl_4^-$  can significantly stabilize  $C_{60}^{\bullet+}$  so that allow its further derivatization. b)  $Cl^-$ , generated from the decomposition of  $FeCl_3$ , firstly attaches onto  $C_{60}$  to generated the chloro[60]fullerene anion ( $C_{60}Cl^-$ ). Next,  $C_{60}Cl^-$  is immediately oxidized by  $FeCl_3$  to produce  $C_{60}Cl^{\bullet}$ , which can then undergo a C–Cl bond cleavage to afford  $C_{60}^{\bullet+}$  with loss of  $Cl^-$ . Finally, generated  $C_{60}^{\bullet+}$  can further go through the Friedel-Crafts reaction [62], directly react with other nucleophiles [63], or even proceed a fullerene dimerization [64].

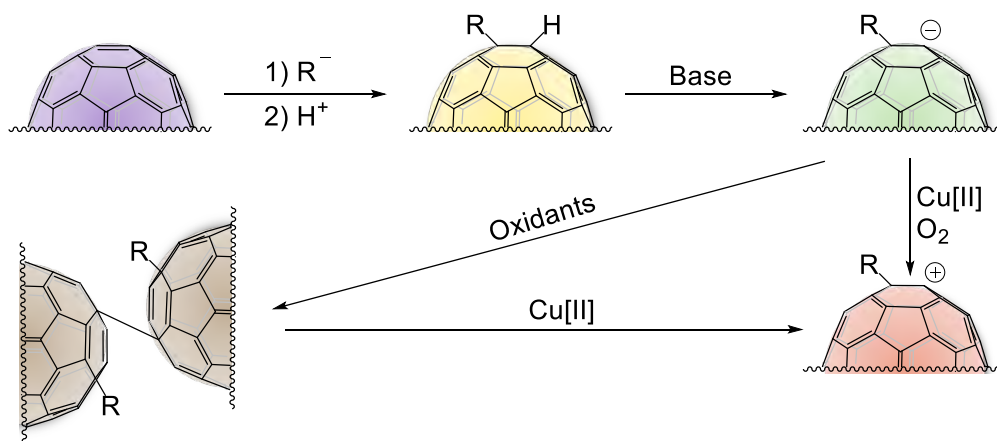


**Figure 1.2.2.3.**  $FeCl_3$ -mediated fullerene radical cation generation.

#### 1.2.2.4.Strategy for generation of fullerene cation

[60]Fullerene cation specie is the most popular and easy handled intermediate among all [60]fullerene cation intermediates. As we previously discussed, recent Cu[II]-mediated fullerene cation generation depicted many advantages, including facile synthesis, high selectivity, and high yields compared to other Lewis acid-mediated fullerene cation generation. Generally, Cu[II] mediated fullerene cation reaction mainly includes three steps: 1) the preparation of organohydro[60]fullerene precursors ( $\text{RC}_{60}\text{H}$ ) through nucleophilic addition; 2) the formation of organo[60]fullerene dimers ( $\text{RC}_{60}-\text{C}_{60}\text{R}$ ) through radical coupling dimerization; 3) the generation of *in situ* fullerene cation intermediate in the presence of Cu[II] salts (Figure 1.2.2.4). Owing to the impressively low LUMO energy level of the generated fullerene-cation,  $\text{RC}_{60}$  can immediately undergo three types of reactions: a) the intra-molecular rearrangements [46]; b) the intramolecular cyclization[68]; c) inter-molecular coupling reaction [69].

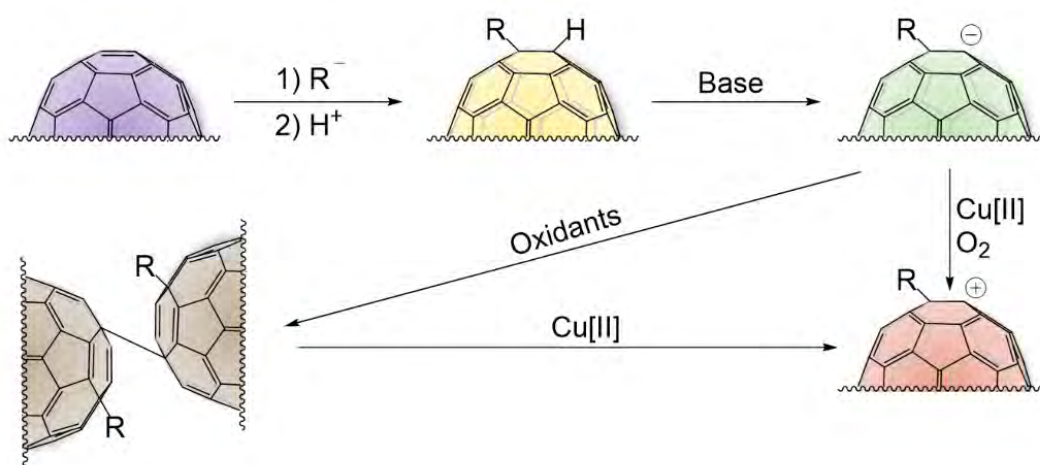


**Figure 1.2.2.4.** Cu[II]-mediated fullerene cations generation.

In sum, one of the main purposes of this thesis aims to provide a fullerene cation methodology for designing the new fullerene materials. Through applying newly produced materials, fullerenes application in PSCs can be explored and then give more insights for developing high-performance fullerene materials intended for PSCs.

### **1.3. Fullerenes in photovoltaics**

Fullerenes, one of the most applicable n-type organic semiconducting materials (with bandgap = 2.3 eV) [70], have demonstrated the highest feasibility in photovoltaics due mainly to their ultrafast photo-induced charge transfer property [10] and the low reorganization energy [11]. Accordingly, tremendous endeavors have been devoted to developing versatile fullerene materials for improving the performance of both organic solar cells (OSCs) and recently boosted perovskite solar cells (PSCs). Since the first fullerene derivative, namely phenyl-C<sub>61</sub>-butyric acid methyl ester (PC<sub>61</sub>BM), that applied as an electron acceptor integrated into the active layer in OSCs which showed a power conversion efficiency (PCE) of 3.2% [13], the performance has been dramatically improved to a PCE of 21.3% based on PSCs by using fullerene derivative as an over-coating electron-transport layer (ETL) [12]. Such impressively faster promotion of fullerene applied photovoltaics is doubtlessly benefited from high-pace development of fullerene synthetic chemistry, which renders versatile fullerene properties, so that enables related photovoltaics to achieve better performance. For fullerenes in OSCs, fullerene materials were applied as the electron acceptors mixed with the electron donors to fabricate the active layer for the device. Consequently, the energy level and the molecular packing of fullerenes were mostly concerned and investigated. Owing to the determined active layer materials adapted in PSCs, fullerenes were utilized as the electron-transport layers or dopant instead of the electron acceptors in OSCs. The design of fullerene materials refers to the energy level, and molecular packing sadly provided counterproductive outcomes when applied in PSCs. This thesis found there are three main factors, including the electron carrier mobility, interlayer morphology, and passivation effect, that significantly influence the performance of fullerenes applied PSCs. Therefore, this thesis aims to provide advanced knowledge regarding the design of fullerene materials applied in PSC for not only the scholars and scientists that currently engaged in this field, but also the prospective researchers.

### 1.3.1. Fundamentals of photovoltaics

Photovoltaics is clearly defined as devices converting the light into electricity by semiconducting materials, which are well accepted as one the most sustainable and environmentally friendly energy conversion devices because of its operation without pollution generation or greenhouse gas emissions [71]. This section briefly summarizes the fundamentals, including the device architecture and related photovoltaic parameters.

#### 1.3.1.1. Photovoltaic architecture

Typically, both lab-use and industry-use photovoltaics consist of three essential components, including an active layer, two charge-transport layers, and two conductive electrodes (Figure 1.3.1.1).

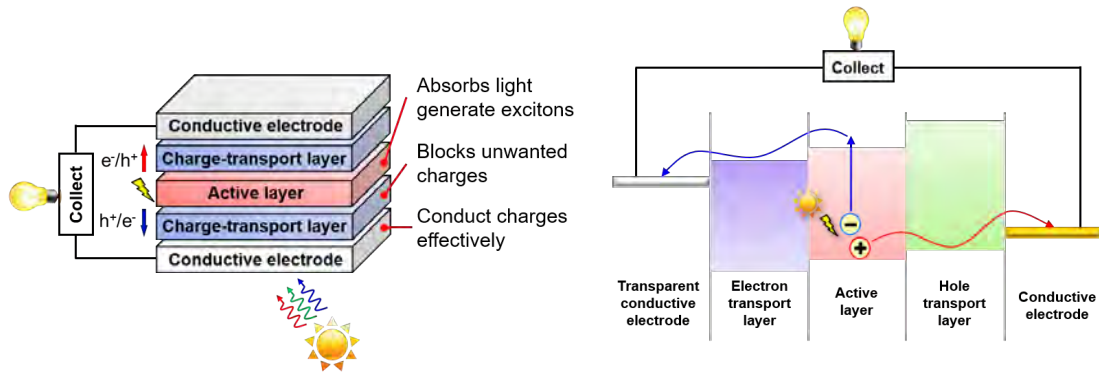


**Figure 1.3.1.1.** Illustrations of the structure and the working principle of photovoltaics.

The active layer, which can be regarded as the core engine in photovoltaics, is made up of the light-sensitive materials so that it can generate the excitons once it absorbs the light. Consequently, the performance of photovoltaics is mainly dependent on the selection of active materials, which also determines the type of photovoltaics. For instance, if the active layer is fabricated by using the organic electron acceptor/donor pair, this type of photovoltaics will be classified as organic solar cells (OSCs). When the active layer material is replaced by organic-inorganic perovskite materials, the type will be denoted as perovskite solar cells (PSCs). As the active layer



is the initial step to generate the excitons once it absorbs photons, tremendous research has been devoted to developing the active layer materials such as a) enhance the light absorption range and intensity to generate more excitons; b) tune the energy level of the conductive band (CB) and valence band (VB) to achieve high output voltage; c) using dopants or optimizing the device fabrication process to accelerate the charge dissociation and reduce the charge recombination. Then, generated excitons will dissociate to electrons and holes, which will produce the photocurrent when they move away from each other.

Owing to the recombination between electrons and holes that will diminish the photocurrent, the charge-transport layers are placed under and above the active layer, which is designed to filter out unwanted charges. Accordingly, the charge-transport layers are categorized into two different types. One is the hole-transport layer (HTL) that selectively transports the holes by blocking out the electron's movement, and the other is the electron-transport layer (ETL) that selectively transports the electrons through blocking out the hole's transports. Notably, although recent research has presented some novel device structures with a concept regarding HTL-free or ETL-free devices, this concept does not necessarily mean charge recombination can be free of consideration. These HTL-free PSCs can transport the electrons in extremely high efficiency and selectivity so that the remained holes can be collected directly by an electrode without the necessity of HTL. Otherwise, significant recombination can seriously undermine the device performance by using conventional ETL materials.

Finally, the structure will be ended up by two conductive electrodes, which are designed to collect the filtered charges to supply the external circuit. It should be mentioned that the conductive electrode used at the place where the light comes in should be transparent enough, which commonly named back electrode; otherwise, it hampers the active layer from efficiently absorbing the light. Accordingly, fullerene materials widely applied as electron-acceptors in the active layer of OSCs, or as ETLs in PSCs thanks to its excellent electrical properties.

### 1.3.1.2. Photovoltaic parameters

In order to reproducibly evaluate the device characteristics, current-voltage ( $J$ - $V$ ) curves with corresponding photovoltaic parameters were introduced as the characterization method of photovoltaics (Figure 1.3.1.2) [72].

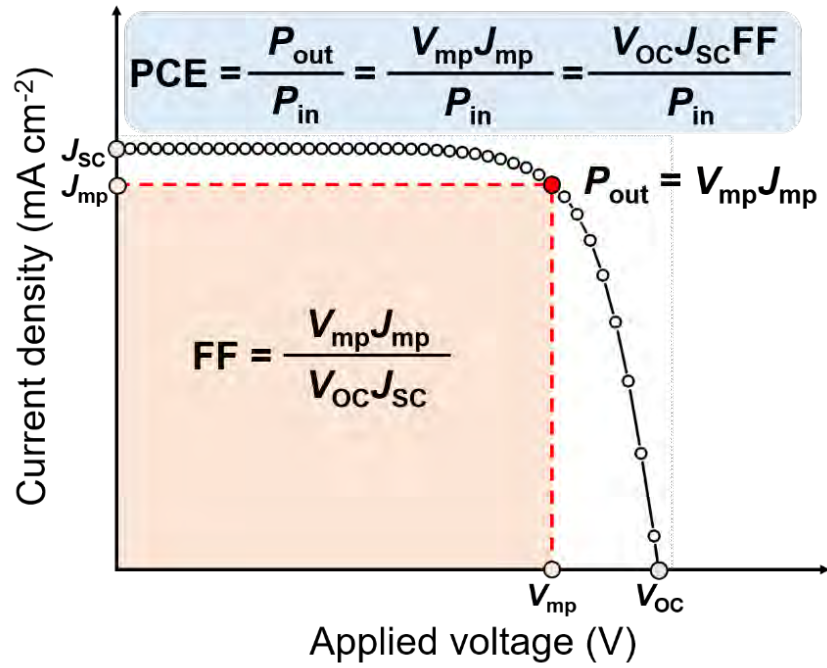


**Figure 1.3.1.2.** Illustrations of the  $J$ - $V$  curve with related photovoltaic parameters.

■ The open-circuit voltage ( $V_{oc}$ ):  $V_{oc}$  represents the maximum photovoltage in a photovoltaic, which is mainly depended on the materials applied in the active layer and the energy levels, such as the bandgap of the photosensitive materials. Empirically,  $V_{oc}$  of an OSC can be calculated theoretically according to the equation below:

$$V_{oc} = (E_{LUMO}^{acceptor} - E_{HOMO}^{donor} - 0.3) \times e^{-1} \text{ V}$$

where  $E$  is the energy level,  $e$  is the elementary charge, and 0.3 eV is an empirical value for charge separation [73].

■ The short-circuit current density ( $J_{sc}$ ):  $J_{sc}$  is derived from the short-circuit current ( $I_{sc}$ ) divided by the active area, which describes the maximum photocurrent in a

photovoltaic, relying on the device thickness, absorption coverage to the solar spectrum.

The current ( $I$ ) can be expressed by the following equation:

$$I = I_0 \times \left[ \exp \left( e \frac{U - IR_S}{nkT} \right) - 1 \right] + \frac{U \pm IR_S}{R_{SH}} - I_{PH}$$

where  $I_0$  is the dark current,  $e$  is the elementary charge,  $U$  is the applied voltage,  $R_S$  is the series resistance,  $n$  is the diode ideality factor,  $R_{SH}$  is the shunt resistance, and  $I_{PH}$  is the photocurrent. Accordingly, to achieve a high short-circuit current  $I_{SC}$  ( $U = 0$  V) value, photovoltaic should have large  $R_{SH}$  and small  $R_S$ .

■ The fill-factor (FF): FF is determined by the charge carrier recombination, charge transport, and impedance in a photovoltaic, which can be written as below:

$$FF = \frac{V_{mp}J_{mp}}{V_{OC}J_{SC}}$$

where  $P_{out}$  is the maximum power output, which is the product of the voltage ( $V_{mp}$ ) and current density ( $J_{mp}$ ) when the power output reaches the maximum, to the product of  $V_{OC}$  and  $J_{SC}$ .

■ The power conversion efficiency (PCE): PCE explains the useful output of the energy conversion of light energy to electricity, which is defined by the following equation:

$$PCE = \frac{P_{out}}{P_{in}} = \frac{V_{mp}J_{mp}}{P_{in}} = \frac{V_{OC}J_{SC}FF}{P_{in}}$$

where  $P_{out}$  denotes the maximum power output,  $P_{in}$  is the power of the incident light.

All mentioned photovoltaic parameters have been well-defined to evaluate the photovoltaic performance in any photovoltaic research, trying to explain the correlation between photovoltaic parameters and the material property such as the energy levels, absorption properties, solid-state packing, processing conditions [74].

### 1.3.2. Fullerenes in organic solar cells

#### 1.3.2.1. Introduction for organic solar cells

The organic solar cell is a type of photovoltaic that organic materials were utilized in the active layer for the light absorption to produce electricity from sunlight. The typical active layer in the OSC comprises a donor (p-type semiconductor) and an acceptor (n-type semiconductor). As fullerenes have been well demonstrated as the n-type semiconductor with excellent electron affinity and ultrafast charge separation, fullerenes have been widely applied in OSCs as the electron acceptor. Therefore, the donor/acceptor pair in the OSC can be regarded as a p-n junction to explain the photoelectric conversion mechanism (Figure 1.3.2.1.1).

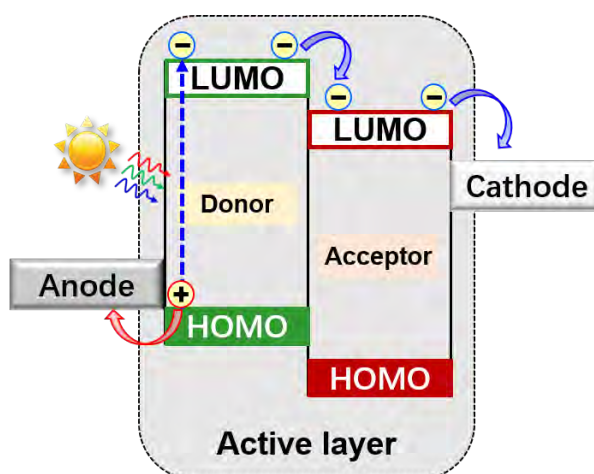


**Figure 1.3.2.1.** Illustrations of photoelectric conversion mechanism inside active layer.

In the beginning, the electron donor material in OSCs absorbs the most sunlight to generate tons of excitons, which are the electron-hole pair bound by Coulomb interactions. Then, the excitons diffuse to the interface between electron donor and electron acceptor. For the excitons that fail to reach the interface, it cannot contribute to the photocurrent because of charge recombination. Accordingly, the photovoltaic material, which can provide the excitons with a longer diffusion length, is generally believed to deliver a better performance in photovoltaics. The excitons at the interface then dissociate to electron-hole pair, promoting the electrons located at the highest

occupied molecular orbital (HOMO) of electron donor material to its lowest unoccupied molecular orbital (LUMO), which forms a charge separation state. Subsequently, electrons flow from the LUMO of electron donor to the LUMO of the electron acceptor at their interface. At this point, the  $V_{OC}$  of OSCs is determined by the gap between LUMO of the electron acceptor and HOMO of the electron donor, which can be roughly calculated by the difference of two energy levels as  $V_{OC} = \text{LUMO}_{\text{acceptor}} - \text{HOMO}_{\text{donor}}$ . Finally, electrons arrive at cathode through the electron-transport layer (ETL), with the holes flow directly to the anode via the hole-transport layer (HTL). Consequently, lots of research have been reported to increase the LUMO level of fullerene derivatives, which can effectively increase the PCE by increasing the  $V_{OC}$  paired with a given electron donor.

One of the typical strategies for efficiently tuning up the LUMO level of fullerenes is to break down the conjugate  $\pi$  system of pristine  $C_{60}$  ( $60\text{-}\pi$  system) to its lower stage through functionalization of fullerenes, such as  $58\text{-}\pi$  system ( $\text{PC}_{61}\text{BM}$ ) [13],  $56\text{-}\pi$  system (indene- $C_{60}$  bisadduct (ICBA) [39], methano-indene-[60]fullerene (MIF) [67]). However, further breaking down the conjugate  $\pi$  system failed to achieve better PCE, yet with a significant increase of  $V_{OC}$ , which was resulted from the dramatically decreased  $J_{SC}$  owing to the poor morphology for solid-state packing. In the past two decades, tremendous efforts have been devoted to the development of fullerene electron acceptors applied in OSCs, which successfully improved the PCE up to 6.4% [75] from a PCE of 2.9% [13] in 1995 based on poly(3-hexylthiophene) (P3HT): fullerenes as the active layer in OSCs. With the further optimization of electron donor materials and device fabrication, an up-to-date highest PCE of 11.2% using PffBT4T-2OD: $\text{PC}_{71}\text{BM}$  as active layer in a ternary OSC was achieved by the Wang group [76].

Herein, this section will demonstrate the development of fullerene electron acceptors using in OSCs based on the fullerene derivatives with different conjugated  $\pi$  system.

### 1.3.2.2.60- $\pi$ system acceptors

[60]Fullerene has 60 electrons located at its  $p$ -orbitals forming the 60- $\pi$  system with significant delocalization. The Heeger group reported the first [60]fullerene-applied OSC with a PCE of 2.9% by mixing MEH-PPV and  $C_{60}$  together to fabricate the active layer in OSCs (Figure 1.3.2.2) [13]. Owing to the poor solubility of  $C_{60}$  in conventional organic solvents such as xylene, 1,2-dichlorobenzene,  $C_{60}$  was tended to crystallize during the film formation, which prohibited  $C_{60}$  from applying in a high concentration for the active layer. Consequently, the first highly soluble fullerene derivative, namely  $PC_{61}BM$ , was obtained through breaking down  $\pi$ -conjugated system of  $C_{60}$ . Expectedly,  $PC_{61}BM$  applied OSCs presented a significantly improved PCE to 3.2% with mainly increased  $V_{OC}$  value because of the higher LUMO energy level of  $PC_{61}BM$ . Although  $PC_{61}BM$ -applied OSCs did not exhibit the best performance compared with later research work by similarly using  $PC_{61}BM$  as electron acceptor, which was attributed to the non-optimized device structure, this pioneering investigation undoubtedly paved a way for later research on the development of fullerene electron acceptors in OSCs.

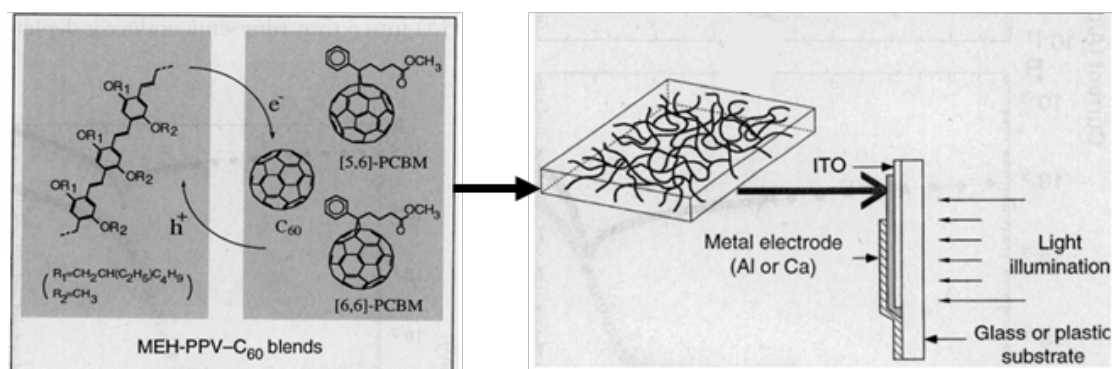
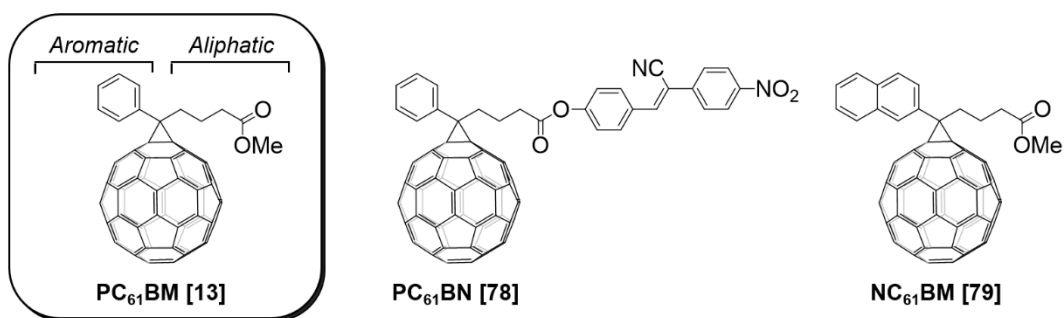


**Figure 1.3.2.2.** The first fullerene-applied OSCs with an illustration of device structure.

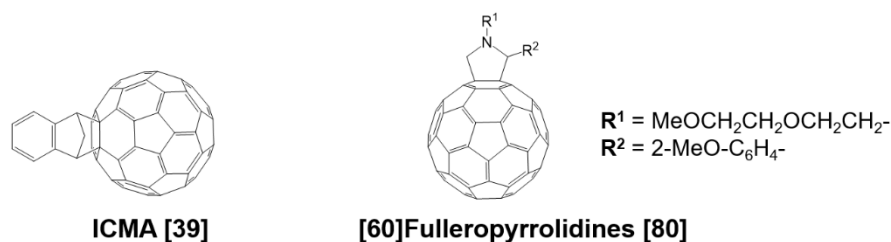
### 1.3.2.3.58- $\pi$ system acceptors

According to previously mentioned comparison between C<sub>60</sub>-applied OSCs and PC<sub>61</sub>BM-applied OSCs, it is easy to deduct that increased LUMO level of fullerene electron acceptor can significantly promote the PCE. Also, introducing the functional groups onto fullerene cage can be a facile way to efficiently bring down the  $\pi$ -system of fullerenes. Since then, tremendous research has been investigated on effectively increasing the  $V_{OC}$  to improve the output performance of OSCs. Accordingly, plenty of 58- $\pi$  system fullerene electron acceptors have been developed through the mono-addition of versatile functional groups onto the [60]fullerene cage (Figure 1.3.2.3).

#### □ PC<sub>61</sub>BM analogues



#### □ Cyclo[60]fullerene derivatives



#### □ 1,4-Adducts

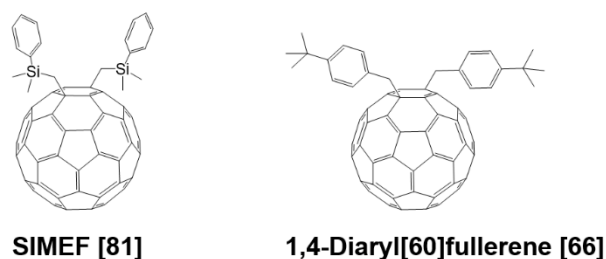


**Figure 1.3.2.3.** Fullerene electron acceptors with a 58- $\pi$  system.

So far, uncountable modifications of PC<sub>61</sub>BM have been investigated owing to its highly chemical modifiable potentials on the phenyl ring, the alkyl-ester, or even the whole fullerene cage [77]. However, most of PCBM analogues failed to achieve a significantly better performance than the PC<sub>61</sub>BM in OSCs, although a great deal of endeavor has been devoted to all aspects such as energy level, solubility, morphology, charge mobility. Herein, only the PCBM analogues that exhibited a better performance than PC<sub>61</sub>BM-applied OSCs will be discussed in this section. For the OSC that P3HT:PC<sub>61</sub>BM applied as the active layer, it typically presented a PCE around 3.8% although other photovoltaic parameters showing some differences because of processing variations always happened in any different circumstances. In 2011, Sharma's group successfully developed a PCBM analogue by using 4-nitro-4'-hydroxy- $\alpha$ -cyanostilbene (NHCS) unit to replace the methyl group of PC<sub>61</sub>BM [78]. The newly obtained PCBM analogue (PC<sub>61</sub>BN) was utilized as the electron acceptor in the OSC with P3HT as the electron donor, producing a PCE of 4.2% with all other photovoltaic parameters significantly promoted. The high  $V_{OC}$  of 0.86 V was benefited from an increased LUMO level of -5.9 eV. The high  $J_{SC}$  of 8.5 mA cm<sup>-2</sup> was reasonably attributed to the strong absorption by the PC<sub>61</sub>BN in a range of 250–900 nm, which helped the active layer generate more excitons to produce the photocurrent. The high FF of 0.58 was owing to the better film quality enabled by the improved solubility of PC<sub>61</sub>BN. Aside from the modification on aliphatic region of PCBM, the modifications on aromatic part have been also investigated. Hwang's group substituted the phenyl ring by naphthalene ring to afford naphthalene C<sub>61</sub>-butyric acid methyl ester (NC<sub>61</sub>BM) and successfully applied NC<sub>61</sub>BM as the electron acceptor in OSCs [79]. The P3HT:NC<sub>61</sub>BM OSCs exhibited a better performance than reference P3HT:PC<sub>61</sub>BM OSCs with a high PCE of 4.1% with significant improvement of all photovoltaic parameters ( $V_{OC}$  = 0.70 V,  $J_{SC}$  = 9.1 mA cm<sup>-2</sup>, and FF = 0.64). The higher  $V_{OC}$  value was derived from the higher LUMO energy level of NC<sub>61</sub>BM relate to the PC<sub>61</sub>BM. The higher FF was rationally ascribed to the well-balanced charge-carrier mobility of P3HT:NC<sub>61</sub>BM film, which presented a hole to electron mobility ratio ( $\mu_h/\mu_e$  = 1.34).



Compared with the  $\mu_h/\mu_e$  ratio of P3HT:PC<sub>61</sub>BM film ( $\mu_h/\mu_e = 1.41$ ),  $\mu_h/\mu_e$  ratio of P3HT:NC<sub>61</sub>BM film showed much closer to 1.0 which demonstrated a well-balanced charge-carrier mobility in OSCs. However, further modifications on phenyl ring by using anthracene or pyrene failed to give a better performance than PC<sub>61</sub>BM applied OSCs, which was resulted from the low LUMO energy levels of anthracene or pyrene derivatized PCBM analogues, and the poor morphology of the corresponding active layer film. The atomic force microscopy (AFM) demonstrated that the surface roughness for the P3HT:PC<sub>61</sub>BM and P3HT:NC<sub>61</sub>BM film are much smoother, which interpreted as a better interconnection between P3HT and fullerene electron acceptors. Understandably, the modifications on cage of PC<sub>61</sub>BM will bring down the conjugated  $\pi$ -system from 58- $\pi$  system to form the fullerene electron acceptors with a 56- $\pi$  system, which will be thusly discussed in following section of 56- $\pi$  system acceptors.

PCBM derivatives have a typical cyclopropane structure which are synthesized through the 1,3-dipole cycloaddition methodology. Enlightened by this point, other cyclic structures were thereafter installed to [60]fullerene cage by other cycloaddition reactions such as the Diels-Alder reaction, the Prato reaction, producing versatile fullerene electron acceptors with a 58- $\pi$  system. In 2010, Li and Hou *et al.* reported the indene-C<sub>60</sub> monoadduct (ICMA) electron acceptor synthesized by the Diels-Alder addition of the indene to C<sub>60</sub>. The synthesized ICMA was applied in OSCs with P3HT as the electron donor material, the P3HT:ICMA OSCs exhibited a PCE of 3.9% that is as good as the output of P3HT:PC<sub>61</sub>BM OSCs [39]. Compared with the PC<sub>61</sub>BM, although ICMA showed an enlarged  $V_{OC}$  value and an increased FF value, the decreased  $J_{SC}$  value resulted in an overwhelming performance than PC<sub>61</sub>BM applied OSCs'. Accordingly, considered the weak  $J_{SC}$  value of ICMA applied OSCs, they further introduced the indene onto ICMA to form the indene-C<sub>60</sub> bisadduct (ICBA). Although the  $J_{SC}$  value of P3HT:ICBA OSCs was expectedly weaker than that of P3HT:PC<sub>61</sub>BM OSCs, both  $V_{OC}$  and FF values were dramatically promoted and no further drop down of  $J_{SC}$  value compared with P3HT:ICMA OSCs. The PCE of P3HT:ICBA OSCs improved to 5.4% with an impressively high  $V_{OC}$  of 0.84 V and an

increased FF to 0.67. In addition to the Diels-Alder addition, the Prato reaction has been also widely applied to attach pyrrolidine ring onto the [60]fullerene cage, giving versatile [60]fulleropyrrolidine derivatives. Unfortunately, fullerene derivatives with heterocyclic ring commonly failed to produce a better performance than PC<sub>61</sub>BM applied OSCs. Herein, the best-performed fullerene derivative with heterocyclic ring was selected to illustrate, yet no better performance than PC<sub>61</sub>BM applied OSCs. In 2010, the Itoh group designed a series of fulleropyrrolidine-imidazolium hybrids, exhibiting the best performance among all other fulleropyrrolidine derivatives [80]. The P3HT:fulleropyrrolidine OSCs showed a moderate performance with a PCE of 3.4%, a  $V_{OC}$  of 0.66 V, a  $J_{SC}$  of 7.85 mA cm<sup>-2</sup> and an FF of 0.66. Although  $V_{OC}$  was significantly enlarged because of its higher LUMO energy level, other photovoltaic parameters did not have that much improvement. In particular,  $J_{SC}$  value of P3HT:fulleropyrrolidine OSCs was much smaller than  $J_{SC}$  value of P3HT:PC<sub>61</sub>BM. The reason why fulleropyrrolidine applied OSCs gave a poor performance was that the fulleropyrrolidine derivatives were incompatible to the conventional electron donor materials such as P3HT in OSCs. Such incompatible electron donor/acceptor pair turned out a poor active layer film quality, so that resulted in a smaller  $J_{SC}$  value. Accordingly, these findings could also explain why there were more fulleropyrrolidine derivatives applied in PSCs, as fulleropyrrolidine derivatives were applied as ETL or dopant in PSCs rather than an electron acceptor to fabricate the active layer in OSCs.

According to the fullerene derivative structure, fullerene derivatives have two different addition patterns, one is 1,2-addition pattern, and the other is 1,4-addition pattern. Cyclo[60]fullerene derivatives typically have a 1,2-addition pattern for their structure. Although there are fewer samples that applying fullerene derivatives with a 1,4-addition pattern in OSCs compared with cyclo[60]fullerene derivatives, the fullerene 1,4-adducts still have been investigated in OSCs as they are also regarded as 58- $\pi$  system electron acceptors. In 2009, Matsuo *et al.* successfully synthesized a fullerene derivative with a 1,4-addition pattern, namely SIMEF. They blended tetrabenzoporphyrin with SIMEF forming the electron donor/acceptor pair to fabricate

the active layer in OSCs [81]. The tetrabenzoporphyrin:SIMEF OSCs exhibited a PCE of 5.2%, a  $V_{OC}$  of 0.75 V, a  $J_{SC}$  of 10.5 mA cm<sup>-2</sup> and an FF of 0.65. This excellent device performance was contributed by the outstanding packing of SIMEF molecules, which have a columnar fullerene core array to bring about high electron mobility and undergo thermal crystallization for better phase separation with electron donors. However, when SIMEF was blended with conventional electron donor P3HT, it failed to give a better performance than P3HT:PC<sub>61</sub>BM OSCs [82]. Although the  $V_{OC}$  value was significantly increased thanks to the higher LUMO energy level that fullerene 1,4-adducts has, neither  $J_{SC}$  nor FF did any promotion to performance of OSCs, which could be attributed to the incompatible film formation by blending P3HT and SIMEF. In addition, other investigations that fullerene 1,4-adducts applied OSCs similarly showed poorer performance than PC<sub>61</sub>BM applied OSCs. The Nakamura group reported a 1,4-diaryl[60]fullerene derivative to function as electron acceptor in OSCs [66]. The P3HT:1,4-diaryl[60]fullerene OSCs gave a much low PCE of 1.6% compared to the performance of P3HT:PC<sub>61</sub>BM OSCs, yet  $V_{OC}$  significantly increased owing to the high LUMO energy level that fullerene 1,4-adduct has. Consequently, fullerene derivatives with a 1,4-addition pattern did not achieve better performance than fullerene derivatives with a 1,2-addition pattern, which could also empirically explain why there are few examples that fullerene 1,4-adducts applied in OSCs. As a matter of fact, the poor performance of fullerene 1,4-adducts applied OSCs could be attributed to the poor solid-state packing between fullerene 1,4-adducts and electron donor molecules, as fullerene 1,4-adducts generally are too bulky to have a nice interaction between themselves and electron donor molecules.

In short, tuning up the LUMO energy level of fullerene derivatives can predictably have an enlarged  $V_{OC}$ . However, the higher  $V_{OC}$  did not necessarily give a better overall performance if without consideration of corresponding influences on  $J_{SC}$  and FF through the related molecular packing or morphology. Accordingly, the later research was mostly devoted to balancing all photovoltaic parameters to achieve a valid enhancement of PCE.

### 1.3.2.4.56- $\pi$ system acceptors

It seems like the easiest way to establish fullerene electron acceptors with a 56- $\pi$  system is to introduce further functional groups onto the cage of fullerene electron acceptors with a 58- $\pi$  system.

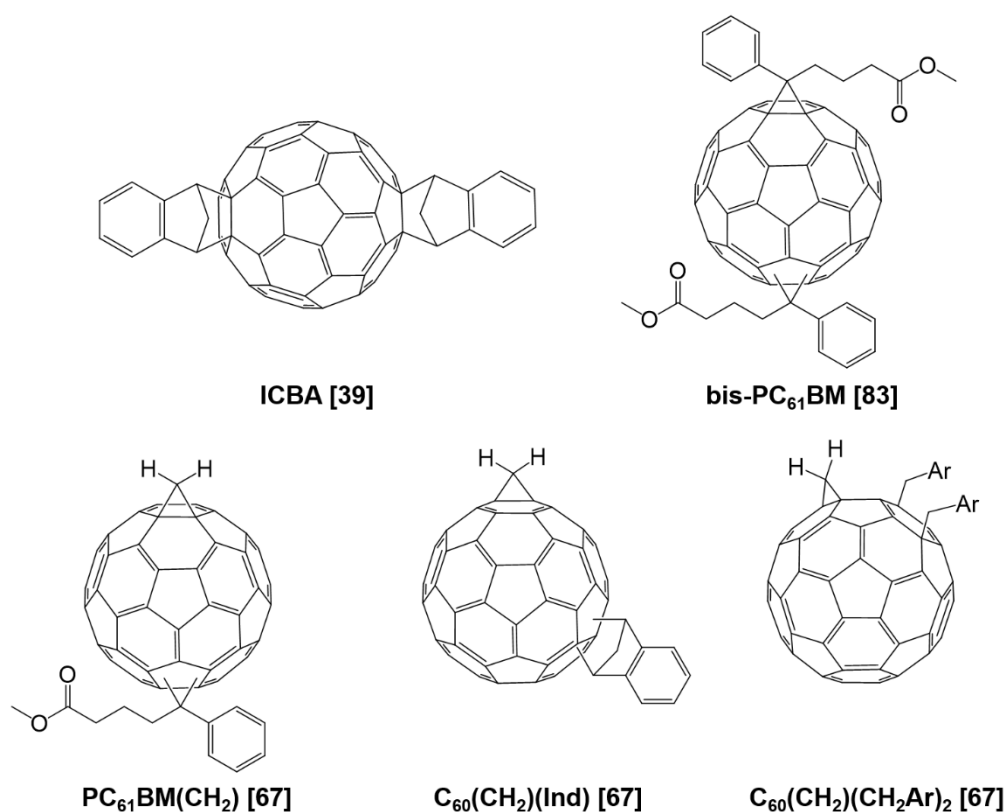


**Figure 1.3.2.4.** Fullerene electron acceptors with a 56- $\pi$  system.

For the example that previously demonstrated, further introduction of the indene onto ICMA (58- $\pi$  system) through the Diels-Alder addition produced ICBA (56- $\pi$  system), which promoted the efficiency up to 5.4% [39]. Nevertheless, simply tuning down the  $\pi$  system failed to obtain a better performance for the most cases. Accordingly, there were more considerations carried out on the molecular packing, and film morphology to achieve the better performance via well-balanced photovoltaic parameters. Enlightened by the merits by the PC<sub>61</sub>BM, Bolm and co-workers introduced an additional phenyl-butyrac acid methyl ester group onto the cage of PC<sub>61</sub>BM to produce the bis-PC<sub>61</sub>BM [83]. They fabricated the active layer by blending

P3HT with synthesized bis-PC<sub>61</sub>BM, and evaluated the performance of P3HT:bis-PC<sub>61</sub>BM OSCs. To their delight, the P3HT:bis-PC<sub>61</sub>BM OSCs delivered an excellent performance with an externally verified PCE of 4.5%, which was apparently better than the performance of P3HT:PC<sub>61</sub>BM OSCs. In agreement with the higher LUMO energy level of fullerene electron acceptors with a 56- $\pi$  system, the  $V_{OC}$  value of P3HT:bis-PC<sub>61</sub>BM OSCs was found to be increased to 0.73 V, which was 0.15 V higher than that of P3HT:PC<sub>61</sub>BM OSCs. Notably, although  $J_{SC}$  was decreased in some degree, its decrease did not significantly offset the contribution from the increased  $V_{OC}$  of P3HT:bis-PC<sub>61</sub>BM OSCs through further addition onto fullerene cage. Therefore, P3HT:bis-PC<sub>61</sub>BM OSCs can give a better performance than P3HT:PC<sub>61</sub>BM OSCs. However, it is obvious that the long aliphatic chain of PC<sub>61</sub>BM definitely has a large molecule size, which potentially hinders molecules from forming a compacted packing with the electron donor molecules.

Later on, Matsuo and co-workers designed a small building block to replace the phenyl-butyric acid methyl ester group of PC<sub>61</sub>BM for the fullerene synthetic precursor with a 58- $\pi$  system [67]. Such small building block for the 58- $\pi$  fullerene derivatives is fulfilled by introducing the methene group (-CH<sub>2</sub>-) onto fullerene cage, which produces cyclopropane fullerene, namely methano[60]fullerene (C<sub>61</sub>H<sub>2</sub>) as the precursor for synthesizing the fullerene electron acceptors with a 56- $\pi$  system. Finally, C<sub>61</sub>H<sub>2</sub> will be ended up by further introduction of versatile functional groups, producing a set of fullerene electron acceptors with a 56- $\pi$  system. For example, when install the phenyl-butyric acid methyl ester group onto C<sub>61</sub>H<sub>2</sub>, methano phenyl C<sub>61</sub> butyric-acid methyl ester, denoted as PC<sub>61</sub>BM(CH<sub>2</sub>), will be successfully obtained. Then, the synthesized PC<sub>61</sub>BM(CH<sub>2</sub>) was applied as the electron acceptor in the active layer of OSCs, which showed a slightly better performance with a PCE of 4.6%, a  $V_{OC}$  of 0.73 V, a  $J_{SC}$  of 9.0 mA cm<sup>-2</sup>, and an FF of 0.71 than P3HT:bis-PC<sub>61</sub>BM OSCs. Intriguingly, both  $J_{SC}$  and FF value of and P3HT:PC<sub>61</sub>BM(CH<sub>2</sub>) were significantly promoted compared to these of P3HT:bis-PC<sub>61</sub>BM OSCs, which perfectly complied to the concept that smaller substitution group can benefit a better solid-state packing of donor/acceptor pair. When

the less bulky functional group indene was installed onto  $C_{61}H_2$ , the methanoindene[60]fullerene (MIF), denoted as  $C_{60}(CH_2)Ind$ , was correspondingly obtained. Delightedly, the PCE of P3HT:MIF OSCs dramatically improved to 5.9% with a  $V_{OC}$  of 0.78 V, a  $J_{SC}$  of  $10.3\text{ mA cm}^{-2}$ , and an FF of 0.73. This impressively excellent performance can be conclusively attributed to the well-balanced of all photovoltaic parameters. The enlarged  $V_{OC}$  value was undoubtedly derived from the high LUMO energy level of MIF with a typical  $56-\pi$  system. Thanks to the small molecular size of both methene and indene, MIF can have a well solid-state molecular packing with electron donor, which is advantage to the formation of active layer with a high film quality.

However, when the methene group was introduced onto the cage of diaryl[60]fullerene with a 1,4-addition pattern, the produced derivative, denoted as  $C_{60}(CH_2)(CH_2Ar)_2$ , failed to exhibit a better performance than P3HT:PC<sub>61</sub>BM OSCs. The P3HT: $C_{60}(CH_2)(CH_2Ar)_2$  OSCs gave a poor PCE of 3.4% with a  $V_{OC}$  of 0.82 V, a  $J_{SC}$  of  $7.1\text{ mA cm}^{-2}$ , and an FF of 0.58. Although the  $V_{OC}$  value showed the highest among all other fullerene electron acceptors with a  $56-\pi$  system, the largely decreased  $J_{SC}$  and FF completely overwhelmed the contribution of the increased  $V_{OC}$  so that an extremely poor performance of P3HT: $C_{60}(CH_2)(CH_2Ar)_2$  OSCs was collected. This consequence apparently demonstrated that fullerene electron acceptors with a 1,4-addition pattern cannot be a good candidate for applications in OSCs, owing to its bulky molecule size as mentioned before. Therefore, it is easy to find that more attentions have been paid to the solid-state molecular packing of the donor/acceptor pairs, and morphology of fabricated active layer film when design fullerene electron acceptors with a lower conjugated system. This is due mainly to the difficulty in optimizing the well-balanced  $J_{SC}$  and FF values while a naturally increased  $V_{OC}$  value when substitution group attached onto fullerene cage.

### 1.3.2.5. Other $\pi$ system acceptors

Besides above-mentioned fullerene electron acceptors with a 58- $\pi$  or 56- $\pi$  system, currently most applicable fullerene electron acceptors in OSCs, other  $\pi$  system including the further decreased  $\pi$  system, higher fullerene  $\pi$  system, and endohedral fullerene  $\pi$  system were also investigated (Figure 1.3.2.5).

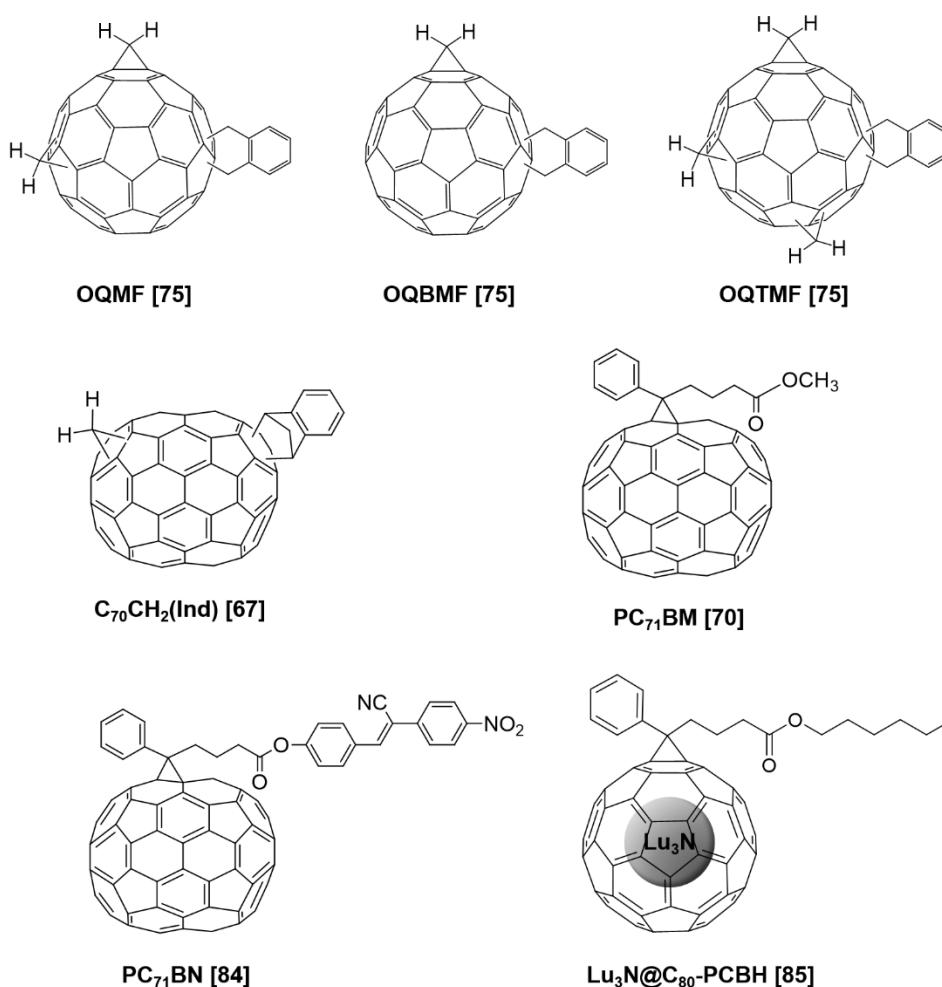


**Figure 1.3.2.5.** Fullerene electron acceptors with other  $\pi$  system.

Although further decrease the conjugated  $\pi$  system was commonly proved to be counterproductive because of dramatically decreased  $J_{SC}$  and FF values, several multi-adduct fullerenes exhibited enhanced performances when less bulky functional groups were installed. In 2014, Ding and co-workers reported a serial of fullerene electron

acceptors with a further decreased  $\pi$  system that can efficiently enhance the performance of OSCs [75]. Their work was started from methano[60]fullerene synthesis by the Bingel reaction, affording corresponding precursors  $C_{60}CH_2$  (58- $\pi$  system),  $C_{60}(CH_2)_2$  (56- $\pi$  system), and  $C_{60}(CH_2)_3$  (54- $\pi$  system) for the further derivatization. Finally, the target *o*-quinomethano[60]fullerene derivatives were synthesized by introducing the *o*-quino group onto the previously obtained methano[60]fullerenes. When the *o*-quino group was attached onto the  $C_{60}CH_2$ , *o*-quinomethane[60]fullerene (OQMF) with a 56- $\pi$  system was obtained. Owing to the similar structure between OQMF and MIF, the photovoltaic performance of P3HT:OQMF OSCs exhibited as good as the performance of P3HT:MIF OSCs with all similar photovoltaic parameters as a  $V_{OC}$  of 0.84 V, a  $J_{SC}$  of 9.96 mA cm<sup>-2</sup>, and an FF of 0.70. When the *o*-quino group was installed onto the  $C_{60}(CH_2)_2$ , *o*-quinobismethane[60]fullerene (OQBMF) with a 54- $\pi$  system was produced. The PCE of P3HT:OQBMF OSCs dramatically improved to 6.4% with a  $V_{OC}$  of 0.95 V, a  $J_{SC}$  of 9.67 mA cm<sup>-2</sup>, and an FF of 0.70. Although the  $J_{SC}$  was expectedly decreased because of additional addends enlarging the molecular size, the decreased  $J_{SC}$  did not significantly overshadow the contribution of increased  $V_{OC}$ . Moreover, the electron mobility of P3HT:OQBMF active layer film showed a comparable electron mobility of P3HT:OQMF active layer film. Such delight result was definitely resulted from the small substituents for tuning up the LUMO energy level of fullerene electron acceptors without damaging on other photovoltaic parameters, so that the methene building block can be established as an effective candidate for efficiently increasing the  $V_{OC}$  value to enhance the PCE. However, this strategy also has its ceiling, when the *o*-quino group was installed onto the  $C_{60}(CH_2)_3$ , *o*-quinotrimethane[60]fullerene (OQTMF) with a 52- $\pi$  system was obtained. The P3HT:OQTMF OSCs showed a dramatically low PCE of 3.0%, yet the  $V_{OC}$  value further improved to 1.00 V. This poor performance was majorly affected by the dramatically dropping down the  $J_{SC}$  ( $J_{SC} = 5.52$  mA cm<sup>-2</sup>) and FF values (FF = 0.54). Furthermore, the electron mobility of the P3HT:OQTMF film was much poorer which can be reasonably ascribed to the poor solid-state packing between P3HT



and OQTMF. Accordingly, although the  $V_{OC}$  values increased in accordance with the increased LUMO energy level of from OQMF to OQTMF by multi-addition, the multi-addition apparently increased molecular size so that negatively influenced the solid-state packing of donor/acceptor pairs. Therefore, it can also explain the reason why there are only limited examples for fullerene electron acceptors with a 52- $\pi$  system, and no any investigations on fullerene electron acceptors with further decreased conjugated  $\pi$  system.

It should be noted that there are more examples about [60]fullerene derivatives using as electron acceptors than other higher fullerenes such as [70]fullerene ( $C_{70}$ ), [80]fullerene ( $C_{80}$ ), *etc*, which is due mainly to abundant resources and easy synthesis of [60]fullerene derivatives. Optimistically, recent investigations have suggested that higher fullerene derivatives exhibit strong potentials in OSCs. Compared to  $C_{60}$ ,  $C_{70}$  has a much larger conjugated  $\pi$ -system owing to it has 70 electrons located at its  $p$ -orbitals. Although  $C_{70}$  has a much larger  $\pi$ -system than  $C_{60}$ , both the LUMO energy level and the energy band gap of  $C_{70}$  is very similar to these of  $C_{60}$  [70]. Intriguingly, for the most cases, the [70]fullerene derivatives having similar functional groups as [60]fullerene derivatives can even produce a better performance than their [60]fullerene functionalized forms, which could be explained by the high solubility and strong light absorption for [70]fullerene derivatives. For example, introducing the indene group to onto the methano[70]fullerene, the methanoindene[70]fullerene ( $C_{70}CH_2(Ind)$ ) with a 66  $\pi$ -system was obtained [67]. When replaced  $C_{60}CH_2(Ind)$  by  $C_{70}CH_2(Ind)$  in OSCs, the PCE of P3HT: $C_{70}(CH_2)(Ind)$  OSCs improved from 5.9% based on P3HT: $C_{60}(CH_2)(Ind)$  OSCs to 6.4% with a  $V_{OC}$  of 0.79 V, a  $J_{SC}$  of 11.1 mA cm<sup>-2</sup>, and an FF of 0.73. It should be noted that all photovoltaic parameters gave a similar performance exclude the significantly increased  $J_{SC}$ , which can be reasonably attributed to the strong absorption of  $C_{70}$  derivatives in the visible light range. As  $J_{SC}$  value is positively related to the amount of light that harvested by the active layer, strong absorption of  $C_{70}$  derivatives definitely contribute to the light absorption of active layer. By the same token, the synthesized PC<sub>71</sub>BN by introducing NHCS onto the fullerene

cage of C<sub>70</sub>, showed a better performance than its [60]fullerene derivatives form as PC<sub>61</sub>BN [84]. The P3HT:PC<sub>71</sub>BN OSCs achieved a high PCE of 5.8% with an obviously enlarged  $J_{SC}$  value of 11.8 mA cm<sup>-2</sup> compared with the  $J_{SC}$  value of P3HT:PC<sub>61</sub>BN OSCs in 10.3 mA cm<sup>-2</sup>. However, the phenyl-butyric acid methyl ester functionalized C<sub>70</sub> (PC<sub>71</sub>BM) did not exhibit a better performance than PC<sub>61</sub>BM when blended with P3HT to fabricate the active layer in OSCs. The P3HT:PC<sub>71</sub>BM OSCs gave a slightly poorer PCE of 3.2%, which was ascribed to incompatible solid-state packing between P3HT and PC<sub>71</sub>BM. Accordingly, when P3HT was replaced by other electron donor materials such as PffBT4T-2OD, the corresponding OSCs achieved the up-to-date highest performance by using fullerene electron acceptors with a PCE of 11.2% [76].

If the additional atoms, ions, or clusters enclosed within the inner spheres of fullerenes, another type fullerene namely endohedral fullerene could be obtained. Owing to the electrical properties of endohedral fullerenes are usually different to the empty fullerenes, several researches have been also devoted to investigating the applications of endohedral fullerenes in OSCs, although few examples exhibited superior performance than empty fullerenes applied OSCs. In 2009, the Dress group presented the first example that using the endohedral fullerene derivative in OSCs [85]. Dress and co-workers introduced phenyl-butyric acid hexyl ester onto the lutetium-nitride containing C<sub>80</sub> (Lu<sub>3</sub>N@C<sub>80</sub>) to enhance the solubility of the synthesized endohedral fullerene derivative (Lu<sub>3</sub>N@C<sub>80</sub>-PCBH). The P3HT:Lu<sub>3</sub>N@C<sub>80</sub>-PCBH OSCs gave a high PCE of 4.2% with a  $V_{OC}$  of 0.81 V, a  $J_{SC}$  of 8.6 mA cm<sup>-2</sup>, and an FF of 0.61. Such promoted efficiency was due mainly to the significantly increased  $V_{OC}$  value of P3HT:Lu<sub>3</sub>N@C<sub>80</sub>-PCBH OSCs, which was affected by the higher LUMO energy level of Lu<sub>3</sub>N@C<sub>80</sub>-PCBH compared to the PC<sub>61</sub>BM. Notably, Lu<sub>3</sub>N@C<sub>80</sub>-PCBH can form a well solid-state packing with P3HT, and Lu<sub>3</sub>N@C<sub>80</sub>-PCBH showed similar charge-carrier mobility to PC<sub>61</sub>BM. Accordingly, P3HT:Lu<sub>3</sub>N@C<sub>80</sub>-PCBH OSCs demonstrated a significant improvement on PCE without dropping down the  $J_{SC}$  and FF values.

### 1.3.2.6. Summary

In a short summary, the fullerene and its derivatives have been widely investigated as electron acceptors in OSCs. For given electron donors, which means the HOMO energy level of the electron donors is predetermined, tuning up the LUMO energy level of fullerene electron acceptors can thusly increase the  $V_{OC}$  so that enhance the PCE of corresponding OSCs. Therefore, plenty of functional groups were designed and introduced onto fullerenes to break down their conjugated  $\pi$  system. Empirically, fullerene electron acceptors with a 58- $\pi$  system such as PC<sub>61</sub>BM, ICMA, *etc.*, and fullerene electron acceptors with a 56- $\pi$  system such as bis-PC<sub>61</sub>BM, ICBA, MIF, *etc.* demonstrated the most excellent performance among fullerene acceptors in OSCs. Also, these fullerene derivatives are now the most commercially available fullerene electron acceptors owing to their facile synthesis and impressively excellent performance. Although further decrease the conjugated  $\pi$  system could theoretically give a better performance because of predictably increased  $V_{OC}$  value, the most cases failed to achieve a better performance than fullerene electron acceptors with a 58- $\pi$  system or a 56- $\pi$  system. This counterproductive outcome is due mainly to the poor molecular packing and poor electron mobility of the applied lower  $\pi$  system fullerene electron acceptors, and the complicated multi-steps synthesis seriously limited the applications of those materials in real photovoltaic industry. In addition, fullerene derivatives with a 1,2-addition pattern usually exhibit a better performance than their 1,4-adducts, which is reasonably ascribed to less bulky molecule size of 1,2-adducts compared to 1,4-adducts. Although there is no central theory to predict a good fullerene electron acceptor that improve the performance of OSCs, there does exist the semiempirical principle for designing a potentially good fullerene electron acceptor. For instance, effectively increase the LUMO energy level of fullerene derivatives by small size substituents, which sufficiently preserves the high  $J_{SC}$  and FF values for fullerenes applied OSCs. Accordingly, there should have a trade-off point among  $V_{OC}$ ,  $J_{SC}$  and FF to fulfill the best-performance OSCs. In addition, other higher fullerene derivatives such as [70]fullerene and its derivatives such as PC<sub>71</sub>BN, C<sub>70</sub>(CH<sub>2</sub>)(ind), PC<sub>71</sub>BM, *etc.* have

been proved to be a more better electron acceptor in OSC owing to their strong light absorption in visible light range and their excellent solubility compared to [60]fullerene derivatives. Apart from empty-fullerene electron acceptors, endohedral fullerenes such as  $\text{Lu}_3\text{N}@\text{C}_{80}\text{-PCBH}$ , have also demonstrated an excellent performance in OSCs. However, there are few examples that using endohedral fullerenes in OSCs, because the limited resource of endohedral fullerenes cannot match the bulk amount required in OSCs. At the end of this section, a summarized PCE record of fullerene electron acceptors using in P3HT electron donor applied OSCs was pictured in Figure 1.3.2.6.

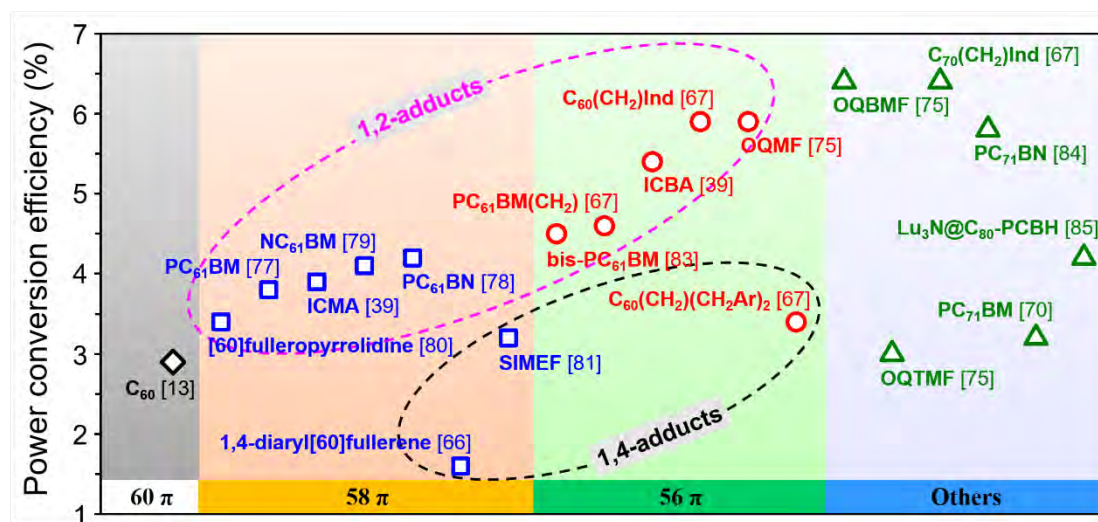


**Figure 1.3.2.6.** PCE record plot of OSCs with P3HT:fullerenes as active layer.

### 1.3.3. Fullerenes in perovskite solar cells

#### 1.3.3.1. Introduction for perovskite solar cells

Perovskite solar cells (PSCs), a currently fastest-advancing type of photovoltaics, that commonly include perovskite structured materials such as a hybrid organic-inorganic lead, tin halide-based material, etc. as the light-harvesting materials. Since the first PSC demonstrated in 2009 with a PCE of 3.8% by the Miyasaka group [86], tremendous efforts have been devoted to this area with an up-to-date National Renewable Energy Laboratory (NREL) certified highest PCE record of 25.2% in 2019. The impressively excellent performance of PSCs is thanks to many advantages that perovskite materials possesses such as high absorption coefficients, long charge carrier (electron-hole) diffusion lengths, tunable band gaps, and very low production costs. Different to the light-harvesting materials applied in OSCs, which commonly constitute of organic electron donor/acceptor pairs, the light-harvesting materials of PSCs are defined by perovskite materials.

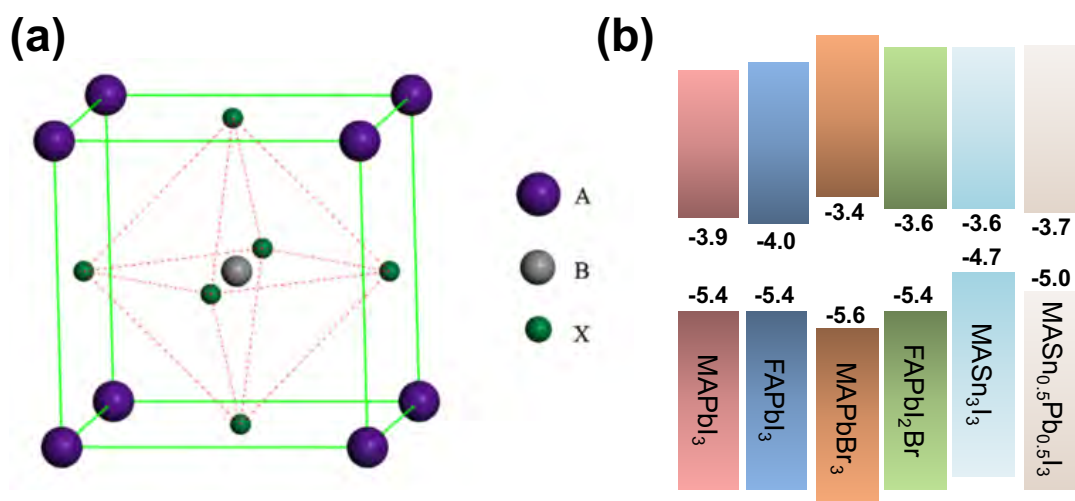


**Figure 1.3.3.1.** (a) The graphic illustration of octahedra structure of the perovskite material. (b) A summarize energy level diagram of representative organometal perovskite materials.

The perovskite materials have typical crystal octahedra structure that defined with a general formula as  $ABX_3$ , which is made up from corner-linked octahedral of X atoms with the B cation at their center, and the A cation between them (Figure 1.3.1.1 (a)) [87]. As the active layer is the core engine of photovoltaics, recent studies have successfully broadened the scope of perovskite materials with versatile energy band gaps (Figure 1.3.1.1 (b)) [88]. However, the most commonly investigated perovskite materials are still confined to methylammonium lead trihalide ( $MAPbI_3$ ) ( $CH_3NH_3PbX_3$ , where X is a halogen atom such iodine, bromine or chlorine), or formamidinium lead trihalide ( $FAPbI_3$ ) ( $H_2NCHNH_2PbX_3$ ), due mainly to their facile processing procedures and cheap costs. In addition, the device architecture of PSCs has also been optimized based on a view of device engineering. Generally, the device geometry structures have been classified as two major types, one is the normal-type structure which consists of n-i-p three layers from the bottom to top; the other is called the inverted-type device, which is made up from p-i-n layer by layer from the bottom to top. Depended by the materials used for PSCs and processing conditions of PSCs fabrication, both normal-type and inverted-type structures have been widely utilized.

Different to fullerenes functioning as the electron acceptor materials in OSCs, fullerene materials have been widely utilized as electron-transport layers (ETLs) in PSCs because of their remarkable charge-transfer ability. Compared to fullerenes in OSCs, fullerenes influence more leverage on  $J_{SC}$  and FF values of PSCs. According to the examples previously discussed in OSCs, although the more addends attached on fullerene cage can benefit a higher  $V_{OC}$  value of OSCs, the dramatically dropped  $J_{SC}$  and FF values seriously undermined the device performance, which could be attributed to a poor charge-transport ability. Consequently, there were more pristine  $C_{60}$  applied as ETLs in PSCs rather than fullerene multi-adducts. Besides using fullerenes as ETLs in PSCs, fullerenes have been also studied about the influence towards the perovskite layer. For example, during the formation of the perovskite layer, if the larger perovskite crystal size could be controlled, the grain boundaries and defects can be definitely reduced so that enhance the performance of PSCs. Consequently, fullerenes were

applied as an additive into perovskite active layer, which helps the reduction of grain boundaries and defects to improve the performance of PSCs. Similarly, fullerene derivatives also can be fabricated as a layer under the perovskite layer as a perovskite growth-template to help perovskite seeds grow with a larger crystal size to reduce the grain boundaries and defects. As such fullerene layers are placed underneath the perovskite layer and deposited above the other ELTs, usually are metal oxides ETLs, it is thusly denoted as fullerene over-coat layers in PSCs. More interestingly, there are more endohedral fullerenes applied examples reported in PSCs compared to the examples shown in OSCs. This is undoubtedly due to the trace amount of endohedral materials (usually less than 1.0 wt%) that required in PSCs through the doping methodology. As fullerene derivatives in PSCs usually demands low LUMO energy level to efficiently accommodate the photoelectrons generated from perovskite layer, fullerene derivatives in here usually equip with a higher  $\pi$  system such as 60- $\pi$  and 58- $\pi$  system, rather than further decreased  $\pi$  system. It should be noted that the perovskite materials such as  $\text{FAPbI}_3$ ,  $\text{MAPbI}_{3-x}\text{Cl}_x$ . commonly exhibit a better performance because of their strong absorption in the range of visible light and the wider energy band gaps. Herein, this section briefly summarizes the fullerene applications in PSCs, which is the starting point of the research in this thesis.

### 1.3.3.2. Fullerene as electron-transport layer

As same as the OSCs, the ETL is also the essential component for PSCs, which is placed to filter out the unwanted holes that may recombine with the electrons to decrease output current. The conventional electron-transport materials that utilized as ETLs in PSCs are metal oxides such as  $\text{TiO}_2$ ,  $\text{ZnO}$ ,  $\text{SnO}_2$ ,  $\text{Cs}_2\text{CO}_3$ , *etc.* Although metal oxide ETLs applied PSCs usually achieved a remarkably excellent performance, the use of metal oxides commonly results in many issues such as large hysteresis of PSCs, high sintering temperature and long time for ETL fabrication, *etc.*, which obviously limits their practical applications in PSCs. Promisingly, fullerene materials can be effectively applied as ETLs to solve these problems thanks to their low chemical capacitance and fast electron transfer. In addition, fullerenes can also function as a moisture insulator, which can enhance the long-term stability of PSCs. Herein, this section will discuss the fullerene ETLs that applied in PSCs by several selected symbolic examples (Figure 1.3.3.2).

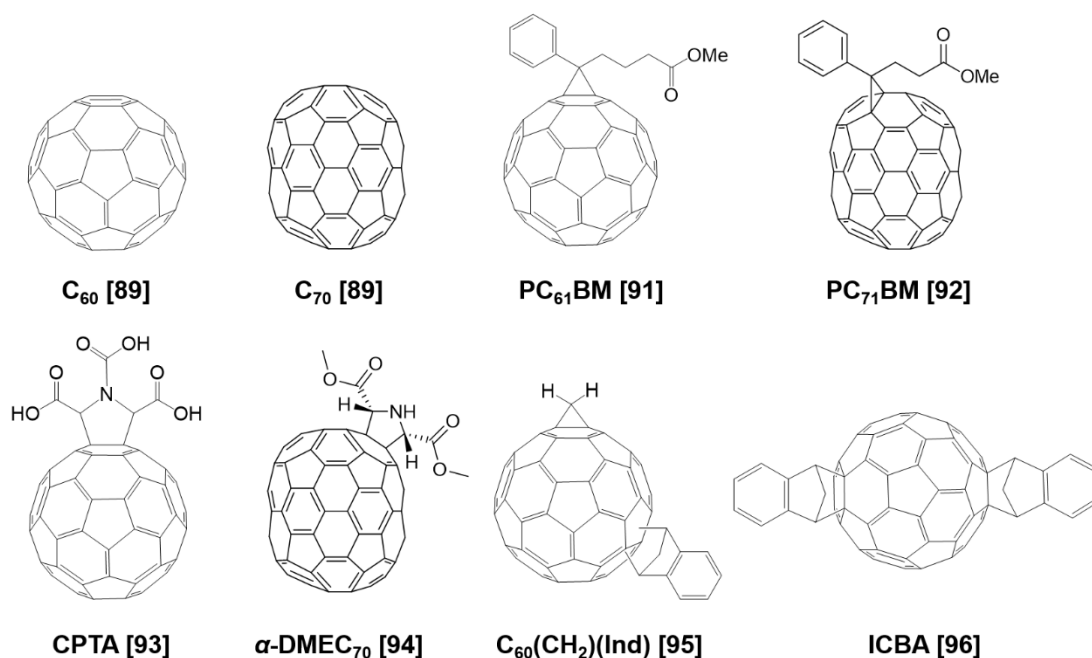


**Figure 1.3.3.2.** Fullerenes applied as electron-transport layer in PSCs.



In 2016, Yan's group reported the first thermally deposited C<sub>60</sub> as ETLs for normal-type PSCs with a configuration of fluorine doped tin oxide (FTO)/C<sub>60</sub>/MAPbI<sub>3</sub>/Spiro-OMeTAD/Au [89]. The thermally deposited C<sub>60</sub> ETLs applied PSCs showed the best-performance with a PCE of 15.7%, a  $V_{OC}$  of 1.10 V, a  $J_{SC}$  of 18.9 mA cm<sup>-2</sup>, and an FF of 0.75, which was benefited from the excellent electron-transport property of C<sub>60</sub> ETLs. Compared to solution-processed C<sub>60</sub> ETLs, the thermally deposited C<sub>60</sub> ETLs can reproducibly provide even and uniform ETLs so that a better performance of PSCs can be obtained. Nevertheless, when replaced C<sub>60</sub> ETLs by C<sub>70</sub> ETLs, the device performance was dramatically dropped down to a PCE of 14.9% ( $V_{OC}$  = 1.03 V,  $J_{SC}$  = 18.6 mA cm<sup>-2</sup>, and FF = 0.78). This was due mainly to C<sub>70</sub> has a much strong light absorption, which hampered the perovskite layer from adequately absorption the enough light to generate more excitons. Despite thermal deposition can produce a uniform ETL for having a better performance in PSCs, the thermal deposition is a slow and expensive process, which definitely limited its application in photovoltaic industry. Later on, the author *et al.* achieved the high efficiency by spin-coating mixed C<sub>60</sub>:C<sub>70</sub> in a weight ratio of 9:1 as ETLs [90]. A similar normal-type PSC with a device structure of indium tin oxide (ITO)/(C<sub>60</sub>:C<sub>70</sub>)/MAPbI<sub>3</sub>/Spiro-OMeTAD/Au was used, which demonstrated a high PCE of 16.7% with a  $V_{OC}$  of 1.02 V,  $J_{SC}$  of 22.9 mA cm<sup>-2</sup>, and an FF of 0.71 compared to a reference PSC that using thermally deposited C<sub>60</sub> ETLs (PCE = 16.7%,  $V_{OC}$  = 1.01 V,  $J_{SC}$  = 22.7 mA cm<sup>-2</sup>, and FF = 0.72). The reason why thermally deposited C<sub>60</sub> ETLs can provide PSCs with a better performance is majorly because of the even and uniform ETLs that can be formed. Intriguingly, 10 wt% addition of C<sub>70</sub> to C<sub>60</sub> ETLs by spin-coating not only inhibited the crystallinity of solution-processed C<sub>60</sub> ETLs, but also produced the ETLs as uniform as the thermally deposited ETLs. More interestingly, considered the remaining of solvent residue during the spin-coating process, a vacuum-dry process was studied to remove the solvent residue to further enhance the performance of solution-processed C<sub>60</sub>:C<sub>70</sub> ETLs-applied PSCs. With the vacuum-dry treatment, the solution-processed C<sub>60</sub>:C<sub>70</sub> ETLs became more condensed and less light sortition so that the PCE of PSCs improved to 18.0% with all other

photovoltaic parameters significantly improved ( $V_{OC} = 1.03$  V,  $J_{SC} = 24.3$  mA cm<sup>-2</sup>, and FF = 0.73). It should be highlighted that only pristine fullerenes such as C<sub>60</sub> and C<sub>70</sub> can be fabricated by thermal deposition, which is due to fullerene derivatives commonly decompose under the high temperature, which is a typical condition in thermally deposition chamber.

Apart from the pristine fullerenes have been tremendously applied as ETLs in PSCs, fullerene derivatives have also widely been investigated as ETLs in PSCs. Nevertheless, all examples that using fullerene derivatives as ETLs are demonstrated by using a solution-processed fabrication method because of the thermal instability of fullerene derivatives. For example, Han and Grätzel *et al.* reported using PC<sub>61</sub>BM as an ETL in an inverted-type PSC with an architecture of FTO/NiMgLiO/MAPbI<sub>3</sub>/PC<sub>61</sub>BM/Ti(Nb)O<sub>x</sub>/Ag, achieving a PCE of 16.2% with a  $V_{OC}$  of 1.07 V,  $J_{SC}$  of 20.6 mA cm<sup>-2</sup>, and an FF of 0.75 [91]. It is worth noting that the MAPbI<sub>3</sub>/PC<sub>61</sub>BM interface was very efficient for the electron extraction so that a higher FF can be observed in PSCs. Additionally, PC<sub>61</sub>BM is much soluble than C<sub>60</sub> in all conventional organic solvents, which allow PC<sub>61</sub>BM be formed in a condensed uniform film by simple spin-coating process. Similar to studies in OSCs, when PC<sub>61</sub>BM ETLs were replaced PC<sub>71</sub>BM ETLs in PSCs, the performance of PSCs was also further improved. Huang's group mixed three PC<sub>71</sub>BM stereoisomers together to form an integrated ETL in an inverted-type PSC with a device structure of ITO/PEDOT:PSS/MAPbI<sub>3</sub>/PC<sub>71</sub>BM/Ca/Al [92]. The PC<sub>71</sub>BM applied PSCs demonstrated a best-performance with a PCE of 20.1%, a  $V_{OC}$  of 1.03 V, a  $J_{SC}$  of 23.51 mA cm<sup>-2</sup>, and an FF of 0.83.

Although [60]fulleropyrrolidine derivatives have been demonstrated a poor performance in OSCs, they have been promisingly manifested as electron-transport materials in PSCs. Fang's group successfully synthesized carboxyl-functionalized fullerene, C<sub>60</sub> pyrrolidine tris-acid (CPTA) and applied CPTA as an ETL in a normal-type PSC with a conventional configuration of ITO/CPTA/MAPbI<sub>3</sub>/Spiro-OMeTAD/Au [93]. Solution-processed CPTA ETLs applied PSCs exhibited a

promising PCE of 18.4% with a  $V_{OC}$  of 1.10 V, a  $J_{SC}$  of 22.06 mA cm<sup>-2</sup>, and an FF of 0.76. Thanks to strong surface interaction between the carboxylic group of CPTA and the top surface of ITO substrate, the surface roughness of CPTA-coated ITO was significantly decreased so that an even smoother surface was available for following MAPbI<sub>3</sub> film deposition. In addition, despite the LUMO energy level of CPTA showed no significant difference to that of PC<sub>61</sub>BM with an LUMO energy level of -3.91 eV, the electron mobility ( $\mu_e$ ) of CPTA showed as twice high as that of PC<sub>61</sub>BM's electron mobility, which reasonably explained the better performance obtained when CPTA applied as ETLs in PSCs. Similar to the case that replaced PC<sub>61</sub>BM by PC<sub>71</sub>BM, the performance of PSCs could be further improved when replaced the [60]fulleropyrrolidine ETLs by [70]fulleropyrrolidines ETLs. In 2017, Echegoyen and co-workers utilized a pure *cis*- $\alpha$ -dimethoxy carbonyl [70]fulleropyrrolidine ( $\alpha$ -DMEC<sub>70</sub>) as the ETL in an inverted-type PSC with an device architecture of ITO/PEDOT:PSS/MAPbI<sub>3</sub>/ $\alpha$ -DMEC<sub>70</sub>/Al [94]. The pure  $\alpha$ -DMEC<sub>70</sub> ETLs-applied PSCs exhibited a substantially enhanced PCE of 18.6% with a  $V_{OC}$  of 1.02 V, a  $J_{SC}$  of 22.90 mA cm<sup>-2</sup>, and an FF of 0.80. Notably,  $\alpha$ -DMEC<sub>70</sub>-based PSCs showed the both higher  $J_{SC}$  and FF values, which can be associated with the higher electron mobility of  $\alpha$ -DMEC<sub>70</sub>. Also,  $\alpha$ -DMEC<sub>70</sub>-based PSCs showed a higher charge extraction efficiency even compared to PC<sub>71</sub>BM-based PSCs. Unlike to the limited fulleropyrrolidines applications in OSCs, there are more successful examples showing a better performance in PSCs. This is due mainly to the favorable low LUMO energy level of fulleropyrrolidine derivatives and their excellent electron-transport ability. Notably, [70]fullerene derivatives demonstrated both a better performance compared to their [60]fullerene form in both OSCs and PSCs. Accordingly, it could be regarded that [70]fullerene derivatives can potentially give more superiors in applications if their limited resource and expensive processing cost could be resolved.

Aside from the pristine fullerenes and fullerene monoadducts, fullerene bis-adducts have also been investigated although only limited examples demonstrated the delight results. For example, C<sub>60</sub>(CH<sub>2</sub>)(Ind), which indicated an impressively excellent

performance in OSCs [67], was also studied as the ETL in an inverted-type PSC with a configuration of ITO/NiO/DEA/MAPbI<sub>3</sub>/C<sub>60</sub>(CH<sub>2</sub>)Ind/PN4N/Ag by Yip and Matsuo *et al* [95]. C<sub>60</sub>(CH<sub>2</sub>)Ind-applied PSCs showed an increased PCE of 18.1% with a  $V_{OC}$  of 1.13 V, a  $J_{SC}$  of 20.4 mA cm<sup>-2</sup>, and an FF of 0.80. Although the C<sub>60</sub>(CH<sub>2</sub>)(Ind) showed a slightly lower electron mobility compared to PC<sub>61</sub>BM, both  $V_{OC}$  and FF values of C<sub>60</sub>(CH<sub>2</sub>)(Ind)-applied PSCs were significantly increased. This was mainly attributed to more effectively suppressed trap-assisted charge recombination by C<sub>60</sub>(CH<sub>2</sub>)(Ind) ETLs. ICBA, another popular fullerene material that widely applied in OSCs, was also investigated as an ETL in an inverted-type PSC with a device architecture of ITO/PTAA/(FA<sub>0.83</sub>MA<sub>0.17</sub>)<sub>0.95</sub>Cs<sub>0.05</sub>Pb(I<sub>0.6</sub>Br<sub>0.4</sub>)<sub>3</sub>/ICBA/C<sub>60</sub>/bathocuproine BCP)/Cu by Huang's group [96]. The ICBA ETL applied PSCs manifested a PCE of 18.3% with a significantly enhanced  $V_{OC}$  of 1.20 V, a  $J_{SC}$  of 19.7 mA cm<sup>-2</sup>, and an FF of 0.78. It is interesting to find that both two fullerene bis-adducts ETLs applied PSCs showed substantially higher  $V_{OC}$  values, which was ascribed to their high-lying LUMO energy level. Despite it seems like these satisfactory  $V_{OC}$  values of fullerene ETLs applied PSCs share the similar reason for  $V_{OC}$  enhancement in OSCs, it still remains uncertain why the  $V_{OC}$  values can be increased by an unmatched working function level. In addition, there is lack of subsequent research by using fullerene multi-adducts as ETLs in PSCs with as high PCE as presented examples. In addition, both presented fullerene multi-adducts ETLs demonstrated a lower electron mobility when applied as ETLs, which seriously limited the further enhancement of performance yet  $V_{OC}$  values were enhanced.

Accordingly, the backbone theory behinds the reason why fullerene multi-adducts ETLs can promote the performance of PSCs is highly demanded for further investigation. In a consequence, it is still better to give more leverage on fullerene monoadduct because of its high electron mobility for acting as ETLs in PSCs.

### 1.3.3.3. Fullerene as over-coat layer

Although tremendous efforts have been devoted to developing the fullerene ETLs for a high-performance PSC, it is still difficult to exceed the performance of metal oxide ETLs applied PSCs although the use of metal oxides inevitably faces with heavy hysteresis issue. Therefore, many groups anticipated that combined fullerene ETLs and metal oxide ETLs could achieve the hysteresis-free high-performance PSCs. Then, the over-coat methodology was designed and many fullerene derivatives were tested for achieving such purposes (Figure 1.3.3.3).

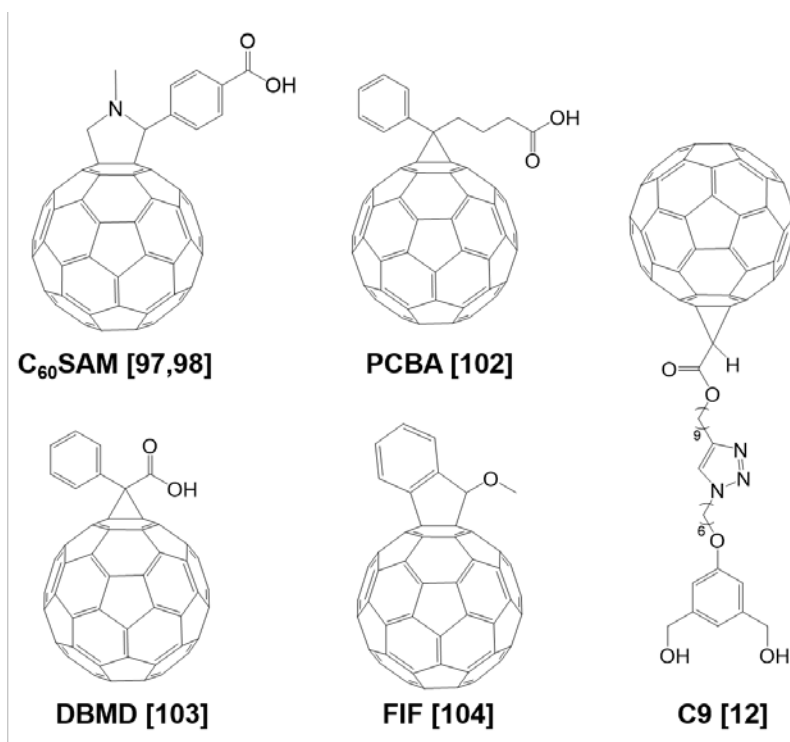


**Figure 1.3.3.3.** Fullerenes applied as over-coat on top of metal oxide layer in PSCs.

Considering the low electron mobility of the compact TiO<sub>2</sub> ETL triggers the charge recombination at the interface, Snaith's group firstly applied a [60]fulleropyrrolidine derivative as a fullerene over-coat layer on the top of TiO<sub>2</sub> ETL in a normal-type PSC [97]. The applied [60]fulleropyrrolidine was named as [60]fullerene self-assembled monolayer (C<sub>60</sub>SAM) owing to it can effectively functionalize the surface of mesoporous TiO<sub>2</sub> or ZnO to enhance the photoinduced electron transfer. They applied

a normal-type PSC with a device structure of FTO/TiO<sub>2</sub>/C<sub>60</sub>SAM/MAPbI<sub>3-x</sub>Cl<sub>x</sub>/Spiro-OMeTAD/Ag, which exhibited a pioneering PCE of 11.7% with a  $V_{OC}$  of 0.84 V, a  $J_{SC}$  of 19.6 mA cm<sup>-2</sup> and an FF of 0.72. Although the over-coat significantly improved the performance compared to the reference device, such performance was still far away to applied in PSCs, which was ascribed to the electron trapped in C<sub>60</sub>SAM over-coat film. Later on, Yan and Zhao *et al.* successfully achieved a best-PCE of 19.0% by using C<sub>60</sub>SAM over-coat in a normal-type PSC with a device architecture of FTO/SnO<sub>2</sub>/C<sub>60</sub>SAM/MAPbI<sub>3</sub>+Pb(SCN)<sub>2</sub>/Spiro-OMeTAD/Au [98]. Considered the electron trap in previous study, they applied C<sub>60</sub>SAM as a very thin fullerene over-coat layer onto the top surface of SnO<sub>2</sub>, which can not only passivate the surfaces of metal oxides, but also effectively enhance the charge transfer at metal oxide ETLs/perovskite interfaces. Accordingly, all photovoltaic parameters were significantly enhanced with a  $V_{OC}$  of 1.13 V, a  $J_{SC}$  of 21.35 mA cm<sup>-2</sup> and an FF of 0.79. The perovskite film on C<sub>60</sub>SAM/SnO<sub>2</sub> showed a much faster PL quenching efficiency than that on bare SnO<sub>2</sub>, which suggested that C<sub>60</sub>SAM over-coat definitely improve the electron extraction from perovskite layer. Delightedly, the C<sub>60</sub>SAM over-coat applied PSCs showed neglectable hysteresis, which was undoubtedly an obvious evidence to demonstrate the perfect combination of advantages of both fullerenes and metal oxides.

Apart from [60]fulleropyrrolidine derivatives that can be effectively applied as a fullerene over-coat in PSCs, PCBM analogues can be also used as a fullerene over-coat to enhance the performance of PSCs. Take the most commercially available PCBM analogue PC<sub>61</sub>BM as an example, the first PC<sub>61</sub>BM over-coat applied in PSC was successfully demonstrated by Lee's group in 2014 [99]. They deposited PC<sub>61</sub>BM onto sol-gel ZnO in a normal-type PSC with a device configuration of ITO/ZnO/PC<sub>61</sub>BM/MAPbI<sub>3</sub>/PTB7-Th/MoO<sub>3</sub>/Ag. The PC<sub>61</sub>BM over-coat applied PSC showed a promising PCE of 11.0% with a  $V_{OC}$  of 1.03 V, a  $J_{SC}$  of 15.10 mA cm<sup>-2</sup> and an FF of 0.71. Reasonably, both high  $V_{OC}$  and FF values were attributed to a more favorable energy-level alignment of PC<sub>61</sub>BM/ZnO exhibited at the interfaces, which effectively facilitating cascade charge extraction of PC<sub>61</sub>BM/ZnO film. Although the

first PC<sub>61</sub>BM over-coat PSCs showed a better performance than the first [60]fulleropyrrolidine over-coat applied PSC, such weak performance was still difficult to be applied in a real perovskite solar cell industry. Three years later, Yan and co-workers elegantly utilized Pb(SCN)<sub>2</sub> doped MAPbI<sub>3</sub> in a PC<sub>61</sub>BM over-coat applied PSC with an optimized device structure of FTO/SnO<sub>2</sub>/PC<sub>61</sub>BM/MAPbI<sub>3</sub>+Pb(SCN)<sub>2</sub>/Spiro-OMeTAD/Au [100]. The performance of PC<sub>61</sub>BM over-coat applied PSCs were further enhanced to a remarkably high PCE of 19.5% with a  $V_{OC}$  of 1.11 V, a  $J_{SC}$  of 22.44 mA cm<sup>-2</sup> and an FF of 0.77, which was reasonably attributed to the large perovskite crystal size and decreased grain boundaries that doped Pb(SNC)<sub>2</sub> provided. PC<sub>61</sub>BM can be easily used as a fullerene over-coat on top of metal oxide ETLs to further enhance the performance of PSCs, owing to its efficient electron extracting capability, and favorable energy-level alignment. Aside from the PC<sub>61</sub>BM, other PSCs target designed PCBM analogues were also elegantly reported. In 2015, Yang and Li *et al.* successfully synthesized one PCBM analogue, namely PCBB-2CN-2C8 [101]. They utilized a normal-type PSC with a device architecture of ITO/TiO<sub>2</sub>/PCBB-2CN-2C8/MAPbI<sub>3-x</sub>Cl<sub>x</sub>/Spiro-OMeTAD/Au to evaluate the performance of the PCBB-2CN-2C8 over-coat on TiO<sub>2</sub> ETL. The PCBB-2CN-2C8 applied device demonstrated a high PCE of 16.8% with a  $V_{OC}$  of 1.06 V, a  $J_{SC}$  of 20.68 mA cm<sup>-2</sup> and an FF of 0.79. By the same token as other fullerene over-coats, the PCBB-2CN-2C8 over-coat enhanced the charge extraction from the perovskite layer, and also improved the perovskite film quality with enlarged crystal size and reduced grain boundaries through the surface passivation effect. Intriguingly, when the methyl group in PC<sub>61</sub>BM hydrolyzed to its acid form, namely [6,6]-phenyl-C<sub>61</sub>-butyric acid (PCBA), can effectively bond to the surface of TiO<sub>2</sub> ETL [102]. The fabricated normal-type device with a structure of FTO/TiO<sub>2</sub>/PCBA/MAPbI<sub>3</sub>/Spiro-OMeTAD/Ag exhibited a substantially improved PCE of 17.8% a  $V_{OC}$  of 1.16 V, a  $J_{SC}$  of 21.38 mA cm<sup>-2</sup> and an FF of 0.72. The  $V_{OC}$  value of the PCBA-used device was much larger than that of the PC<sub>61</sub>BM-used device, which was obviously due to much strong interaction between PCBA and the top surface of TiO<sub>2</sub> so that effectively reduced the

recombination of holes at the  $\text{TiO}_2$ /perovskite interface. Additionally, PCBA also can improve the perovskite film quality, which allowed a better performance of total device.

Considered the key building block of  $\text{PC}_{61}\text{BM}$  is that 3-membered-carbon ring, many groups utilized that core building block to develop versatile promising fullerene materials for PSCs. In 2016, Bo's group reported a thermo-cleavable fullerene derivative di-*tert*-butyl methano[60]fullerene-61,61-dicarboxylate (DBMD) [103]. The DBMD was applied as a fullerene over-coat on the top surface of  $\text{TiO}_2$ , in a normal-type PSC with a geometry structure of  $\text{FTO}/\text{TiO}_2/\text{DBMD}/\text{MAPbI}_3/\text{Spiro-OMeTAD}/\text{Ag}$ . The DBMD-utilized device exhibited a PCE of 17.1% with a  $V_{\text{OC}}$  of 1.17 V, a  $J_{\text{SC}}$  of  $20.6 \text{ mA cm}^{-2}$  and an FF of 0.71. Notably, the  $V_{\text{OC}}$  value of DBMD was as high as other PCBM analogues-used devices, which obviously manifested that effectiveness of the methanene building block in PSCs. Later on, the Zhan group demonstrated the highest PCE record that using a fullerene over-coat in PSCs [12]. They designed a long chain fullerene derivative with two hydroxyl groups as anchors for surface modification of  $\text{SnO}_2$  layer. The synthesized long chain fullerene derivative, abbreviated as C9, possessed a suitable LUMO energy level and high electron affinity, which enhanced the extraction of electrons from perovskite layer and efficiently transferred to the  $\text{SnO}_2$  ETL. Thanks to the elegantly introduced hydroxyl groups, the oxygen vacancies on the top surface of  $\text{SnO}_2$  can be effectively passivated so that the electron-transport ability of  $\text{SnO}_2$  can be further improved. Meanwhile, the C9 over-coat layer efficiently enhanced interfacial charge extraction, thusly reducing the trap-assisted charge recombination. Moreover, the C9 also can function as the perovskite growth template for enlarging grain size, reduced grain boundaries and improved crystallinity in perovskite layer. Accordingly, the fabricated normal-type PSC with a device structure of  $\text{ITO}/\text{SnO}_2/\text{C9}/(\text{FAPbI}_3)_x(\text{MAPbBr}_3)_{1-x}/\text{Spiro-OMeTAD}/\text{Au}$  exhibited a highest PCE of 21.3% with  $V_{\text{OC}}$  of 1.12 V, a  $J_{\text{SC}}$  of  $24.1 \text{ mA cm}^{-2}$  and an FF of 0.79.

Although cyclo[60]fullerene derivatives with a full-carbon-ring, only 3-membered-ring and 5-membered-ring have been widely investigated, there is no any investigations by using a cyclo[60]fullerene with a 5-membered-carbon ring, which is



due mainly of lacking the accessible synthesis methodology. In 2019, the author *et al.* successfully developed a fullerene-cation mediated synthetic protocol to produce a series of cyclo[60]fullerenes with a 5-membered-carbon ring structure, which was denoted as full-carbon indene[60]fullerenes (FIFs) [104]. They demonstrated the applied FIF as an over-coat layer by using a normal-type of PSC with a device structure of ITO/SnO<sub>2</sub>/FIF/MAPbI<sub>3</sub>/Spiro-OMeTAD/Au, which expectedly produced a best PEC of 20.7% with a  $V_{OC}$  of 1.09 V, a  $J_{SC}$  of 23.7 mA cm<sup>-2</sup> and an FF of 0.79. Such high performance was manifested by the excellent properties that FIF has. For instance, the ether building block of FIF substantially facilitated the passivation of perovskite, which enhanced both electron extraction from the perovskite layer and also growth of large crystal perovskite with reduced grain boundaries and reduced electron-trap density. More importantly, although fullerene monoadduct definitely presented a weaker electron mobility compared to the pristine fullerenes owing to the increased LUMO energy level, FIF showed no significantly decrease in electron mobility compared to that of pristine [60]fullerene. Accordingly, it can be concluded that FIF not only can efficiently extract the electrons from the perovskite layer, but also fast enough to transfer the electron to the SnO<sub>2</sub> ETL.

In general, although only selected examples are discussed in this section, it still should be emphasized that all over-coating fullerene derivatives on metal oxides ETLs can reproducibly enhance the performance of PSCs with neglectable hysteresis. Compared to the fullerene derivatives were applied as single ETLs in PSCs, fullerene over-coat strategy does not require high solubility of fullerene derivatives because of only thin layer is applied. To the contrast, specific points such as functional groups (*e.g.* hydroxyl-, carboxylic-, amino-, *etc.*) owning the passivation ability and the electron extraction ability should be more considered. Therefore, there are more fullerene derivatives applied as fullerene over-coats in PSCs and more and more research appealing in this area.

### 1.3.3.4. Fullerene as dopant

Recently developed doping methodology further broadens the application scope of fullerene materials in PSCs. As fullerene materials are still limited in resource especially for the endohedral fullerenes, the doping method immediately attracted many attentions due to it requires only trace amount of fullerene materials for applications in PSCs. Unprecedentedly, only trace amount of fullerene dopant can dramatically enhance the performance of PSCs. Also, the doping methodology can be effectively applied among all three layers, the active layer, the electron-transport layer and the hole-transport layer. Herein, several symbolic examples were selected to demonstrate the fullerenes applied in PSCs by doping method (Figure 1.3.3.4).

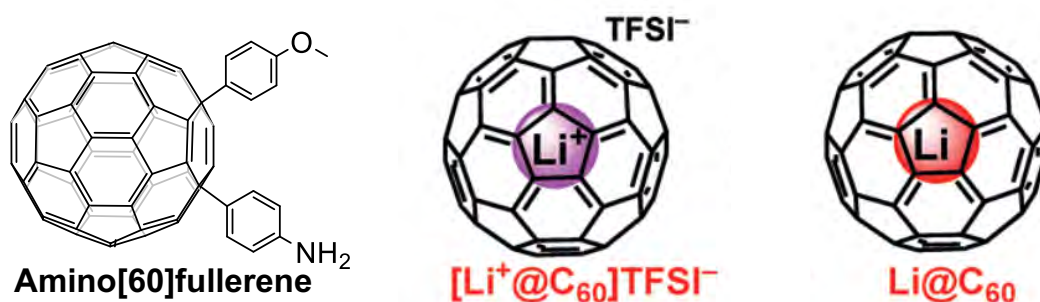


**Figure 1.3.3.4.** Fullerenes applied as dopant in PSCs.

In 2016, Wu and Chiang presented an inverted-type PC<sub>61</sub>BM-doped PSC with a device structure of ITO/PEDOT:PSS/PC<sub>61</sub>BM-CH<sub>3</sub>NH<sub>3</sub>PbI<sub>3</sub>/Ca/PC<sub>71</sub>BM/Al [105]. The 0.1 wt% of PC<sub>61</sub>BM doped PSCs demonstrated a significantly increased PCE of 16.0% with a  $V_{OC}$  of 0.97 V, a  $J_{SC}$  of 20.2 mA cm<sup>-2</sup> and an FF of 0.82 compared to the non-doped PSCs exhibiting a PCE of 11.4% with a  $V_{OC}$  of 0.95 V, a  $J_{SC}$  of 16.2 mA cm<sup>-2</sup> and an FF of 0.73. Apparently, all photovoltaic parameters showed substantially enhancement. The enhanced  $J_{SC}$  value was due mainly to the increased light-absorption of PC<sub>61</sub>BM-doped perovskite layer, which is resulted from the strong absorption of PC<sub>61</sub>BM in a range of 400–700 nm. The enhanced FF value was benefited from the enlarged perovskite crystal size and efficient electro-transporting. With the addition of 0.1 wt% of PC<sub>61</sub>BM in perovskite, the perovskite was formed with larger crystal size,

reduced grain boundaries and decreased electron-trap sites. In addition, the steady-state PL quenching spectra clearly depicted that the 0.1 wt% of PC<sub>61</sub>BM doped perovskite depicted a much better quenching efficiency than non-doped perovskite film, which proved that a better electron-transport that PC<sub>61</sub>BM doped perovskite film has. However, further increased doping concentration to 1.0 wt% of PC<sub>61</sub>BM dramatically undermined the device performance, which was ascribed to the poor solubility of PC<sub>61</sub>BM in perovskite precursor solution, and the over-concentrated PC<sub>61</sub>BM-doped perovskite precursor solution cannot afford a dense perovskite film, and perovskite even grew with larger grain boundaries. As the MAPbI<sub>3</sub> contains the amino residue in its structure, many amines have thusly been investigated as dopants in MAPbI<sub>3</sub>-used PSCs. Very recently, an amino[60]fullerene derivative was applied as a dopant in an inverted-type MAPbI<sub>3</sub>-used PSC with an device architecture of ITO/PEDOT:PSS/amino[60]fullerene-MAPbI<sub>3</sub>/C<sub>60</sub>/BCP/Ag by Matsuo's group [69]. The fabricated device exhibited a slightly higher PCE of 13.5% with a  $V_{OC}$  of 0.93 V, a  $J_{SC}$  of 20.2 mA cm<sup>-2</sup>, and an FF of 0.74. Similar to the study of PC<sub>61</sub>BM-doped PSCs, both  $J_{SC}$  and FF values have been promoted owing to an increased light absorption of amino[60]fullerene doped perovskite film. Therefore, doping the perovskite by a trace amount of fullerene derivatives can mostly render the perovskite film with enlarged crystal size and also enhanced light absorption of perovskite film to generate more photoelectrons.

Apart from empty fullerene dopant applied in the perovskite layer, the endohedral fullerenes could be also doped in an ETL to enhance the performance of PSCs. In 2019, Ueno *et al.* reported a Li@C<sub>60</sub> doped C<sub>60</sub> ETL applied in an inverted-type PSC with a device structure of ITO/PEDOT:PSS/MAPbI<sub>3</sub>/Li@C<sub>60</sub>-doped C<sub>60</sub>/Au [106]. The Li@C<sub>60</sub>-used PSC exhibited an improved PCE of 8.2% with a  $V_{OC}$  of 0.86 V, a  $J_{SC}$  of 16.7 mA cm<sup>-2</sup>, and an FF of 0.57 compared to a reference PSC with a PCE of 4.7%. However, the total device performance was too low to compare among such general system, which was attributed to a mismatched structure used in the device. Conventionally, the top electrode of a normal-type PSC is the Au electrode, which has

a lowest working function level to accommodate the holes from the HTL; the top electrode of an inverted-type PSC is made up from a BCP/Ag electrode, which possesses a highest working function level to accommodate the electrons from the ETL. Nevertheless, in this example, an Au electrode was mistakenly utilized in an inverted-type PSC, which resulted in a reasonably low performance. Comparison between the performance of Li@C<sub>60</sub>-doped C<sub>60</sub> ETL-used PSC and C<sub>60</sub> ETL-used PSC still provided some understandings, the  $V_{OC}$  value of Li@C<sub>60</sub>-doped C<sub>60</sub> ETL-used PSC was substantially increased, which was attributed to the better alignment between Fermi level of the C<sub>60</sub> ETL and the conductive band of the perovskite layer.

It is well known that fullerene is an electron acceptor that conventionally applied as the electron acceptor in OSCs or electron-transport material in PSCs. Notably, with the advent of endohedral metallic fullerenes, the electron property of fullerene is significantly influenced because of the inner metal. Accordingly, recent advance studies successfully utilized the endohedral fullerenes in hole-transport layer (HTL). Recently, the Matsuo group did the first investigation using Li@C<sub>60</sub>TFSI as a p-dopant in Spiro-OMeTAD to replace the conventional p-dopant LiTFSI in PSCs [107]. Although the tested PSC with a structure of FTO/C<sub>60</sub>/MAPbI<sub>3</sub>/Li@C<sub>60</sub>TFSI doped Spiro-OMeTAD/Au exhibited a low PCE of 13.1% compared to the conventional LiTFSI doped Spiro-OMeTAD with a PCE of 17.0%, the Li@C<sub>60</sub>TFSI-used PSCs achieved stability approximately 7-fold that of conventional LiTFSI-used PSCs. Moreover, when the perovskite layer was replaced by a mixed halide perovskite (FAPbI<sub>3</sub>)<sub>0.85</sub>(MAPbBr<sub>3</sub>)<sub>0.15</sub>, the performance substantially improved to a PCE of 16.8% with a  $V_{OC}$  of 1.01 V, a  $J_{SC}$  of 22.9 mA cm<sup>-2</sup>, and an FF of 0.72 yet still lower than a reference device with a PCE of 18.5%, but the stability of (FAPbI<sub>3</sub>)<sub>0.85</sub>(MAPbBr<sub>3</sub>)<sub>0.15</sub>-used PSCs was further enhanced to 10 times stable than that of reference devices. Therefore, endohedral metallic fullerenes can be used by doping strategy, which provided a potential solution to address the problem of perovskite solar cell stability.

### **1.3.3.5.Summary**

In a short summary, the fullerene and its derivatives also showed their remarkable superiors in recently fast-developed perovskite solar cell area. Different to the limited application in OSCs, fullerene exhibited a wide application range in PSCs such as the sing electron-transport layer, the fullerene over-coat on top of metal oxide ETL, and the dopant for improving the PSCs' performance. Among these applications, fullerene over-coat showed a dominant performance, owing to this strategy combined the both virtue of fullerene derivatives and metal oxides. Fullerene and its derivatives are famous for their high electron-affinity and extremely fast transport of electrons, which thusly provided hysteresis-free PSCs. Unlike to fullerene materials, metal oxides are typically used as ETLs in PSCs because of their impressively high capacitor of electrons, providing an extremely high PCE although commonly suffering the heavy hysteresis issue. Through the over-coating the fullerene materials on the top of metal oxides, the PSC exhibits a high PCE and neglectable hysteresis. In addition to the doping methodology, fullerenes are widely studied as the single ETL in PSCs. In particular, pristine fullerene such as C<sub>60</sub> and C<sub>70</sub>, and frequently used in an inverted-type PSC by thermal deposition, which is due mainly to match up the facile fabrication process. However, normal-type PSCs seldom use the fullerene materials as ETLs, which resulted from the low PCE that fullerene ETLs provided so that there is less attention that focus on fullerene ETLs compared to metal oxide ETLs. Notably, both the fullerene over-coat and the fullerene ETL are placed just below the perovskite layer, which definitely influences the perovskite crystal growth. Thanks to good molecular the design on passivating functional groups, working function level, electron extraction ability, etc. the perovskite crystal size can be further enlarged with reduced grain boundaries and electron-trap density so that a better performance of PSCs is correspondingly fulfilled. Apart from the above mentioned two methodologies, the doping methodology has been established owing to the highly development of device engineering. This methodology particularly broadens the application of endohedral fullerenes in PSCs, because only trace amount of materials that required by the experiment, which is definitely in favor

of the limited resources of endohedral fullerenes. Although the doping methodology can effectively enhance the performance of PSCs, it cannot increase the efficiency as much as previously mentioned two methods. This is because the core of PSCs is still predefined by active layer, electron-transport layer and hole-transport layer, the optimization by trace amount of materials is still limited within a narrow range. But there were still some interesting finds such as  $\text{Li}@\text{C}_{60}\text{TFSI}$  that could be well function in an HTL to improve the stability of PSCs. At the end of this part, a similarly summarized picture is provided for PCE record of fullerene materials applied in PSCs with illustration in different application methods (Figure 1.3.3.5).

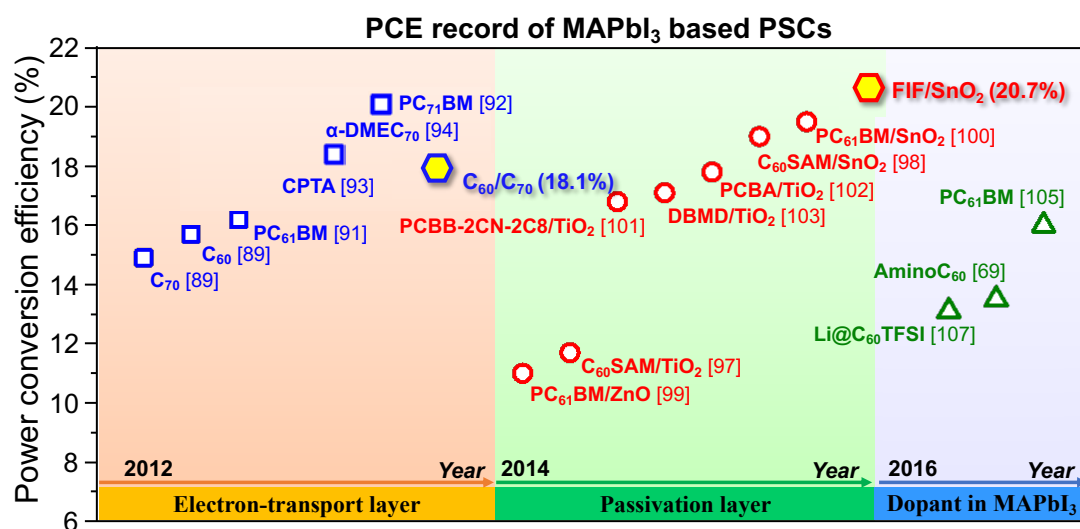


**Figure 1.3.3.5.** PCE record plot of fullerenes utilized MAPbI<sub>3</sub>-PSCs with different application methods.

## **Chapter 2.**

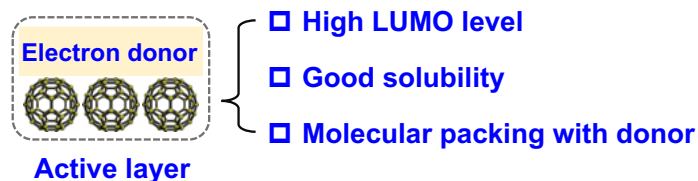
# **Purpose, Challenges and Structure of the Thesis**

## **2.1 How to design fullerenes for high-performance PSCs**

As discussed in Chapter 1, fullerene materials have been mostly demonstrated in photovoltaics because of their impressively excellent electric properties. Among all investigations in photovoltaics, fullerene materials in OSCs have been mostly exhibited so that tremendous materials have been achieved with excellent performance. However, the first fullerene applied PSCs was not achieved until 2013 by Wen's group with a PCE of 3.9% [15]. Consequently, there is still lack of deep research to discover the backbone theory behind how to design good fullerene materials for high-performance PSCs despite several examples successfully showing delighted performances. More sadly, the fullerene materials that designed through an OSC standpoint commonly showed poor performance even than non-functionalized pristine  $C_{60}$ , which severely frustrated the scientists for working in PSCs by using fullerene materials. Nevertheless, although inorganic metal oxide materials exhibited remarkable high PCE (>18%) than fullerene materials (PCE ~16%), the metal oxide applied PSCs always suffer from heavy hysteresis issue than a neglectable hysteresis of fullerene-applied PSCs. Therefore, the main purpose of this thesis is to provide knowledge and method for designing fullerene materials in high-performance PSCs, which can further propagate the PSCs' application in real industry.

Herein, preliminary principles for designing good fullerene materials for high-performance PSCs has been illustrated with comparing the design principle for fullerene materials in high-performance OSCs (Figure 2.1).

■ **Fullerenes in organic solar cells**



■ **Fullerenes in perovskite solar cells**

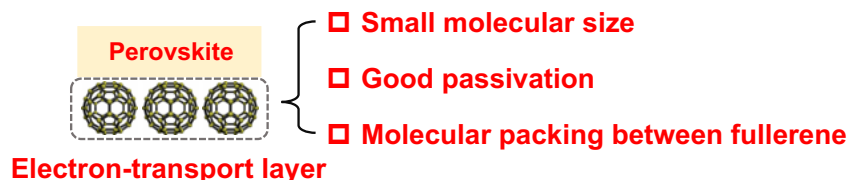


**Figure 2.1.** Principles for designing the fullerene materials for OSCs and PSCs.

Owing to fullerenes were applied as an electron acceptor and mixed with donor material in the active layer of OSCs, more attentions were concentrated on improving fullerene materials performance with consideration of active layer performance.

- **High LUMO level:** Decrease conjugated  $\pi$  system can increase the LUMO level so that achieve a higher  $V_{OC}$ . Thusly, more 56  $\pi$  system examples.
- **Good solubility:** Increase the solubility can form a condensed active layer so that generate more photocurrent  $J_{SC}$ .
- **Molecular packing with donor:** Forming a good packing with donor molecule can promote electron transfer and FF.

However, fullerenes were applied as a single layer for electron-transporting in the PSCs, the more attention should be considered for the electron-transport related parts.

- **Small molecular size:** Fullerene derivatives that having much smaller molecular size can contribute the efficient electron transfer between among fullerene cages, which leads a high  $J_{SC}$  value.
- **Good passivation:** Efficient coordinate the  $Pb^{2+}$  center can promote the stability of perovskite material and electron transfer from  $Pb^{2+}$  to ETL.
- **Molecular packing between fullerenes:** Uniformly amorphous fullerene film can help perovskite grow to large-crystal cell.



## **2.2 Challenges of designing and functionalizing fullerenes**

The major challenges that limited fullerene applications in OSCs can be reasonably attributed to the bottleneck happened in fullerene methodology development. As discussed in previous section, most fullerene materials that having good performance in OSCs unpredictably deliver poor performances in PSCs. And these materials are provided through the conventional fullerene anion or radical mediated chemistry, or pericyclic addition. Accordingly, without the development of new fullerene chemistry, it is much more difficult to develop new and promising fullerene materials for high-performance PSCs. Back to date during the development of fullerene materials in OSCs, the dramatic development of fullerene synthetic methods conclusively benefited tremendous generation of fullerene electron acceptors for high-performance OSCs, such as PC<sub>61</sub>BM, ICBA, MIF *etc.*

Therefore, referring to the knowledge from the development history between fullerene materials and fullerene chemistry, this thesis attributed the major challenges of fullerene materials in PSCs to the lack of further development of fullerene synthetic methodology. Accordingly, this thesis provides several highly promising fullerene materials through an unconventional fullerene-cation mediated synthetic methodology. Then, with the specifically PSC-targeted fullerene materials in hand, the backbone principle for applying the fullerene materials in PSCs can be systematically investigated.

## **2.3 Structure of the thesis**

The structure of the research in this thesis is mainly based on the three major findings that fullerene materials applied in PSCs from Chapter 3 to Chapter 6. In addition, several recently developed promising non-fullerene materials for high-performance PSCs are briefly introduced in Chapter 7.

**Chapter 3** describes how the morphology of fullerene ETL influences the performance of PSCs. This section unveiled that the thermal-deposited C<sub>60</sub> ETL can provide a uniform and amorphous film for achieving the high-performance PSCs.

However, the spin-coated C<sub>60</sub> ETL failed to obtain a high PCE, which is attributed to the difficulty of forming a nice perovskite layer on the top of highly-crystalline C<sub>60</sub> film that fabricated by this method. Moreover, a vacuum-dry process was established for decreasing the hydrophobicity of C<sub>60</sub> film to reach an even higher PCE.

**Chapter 4** discusses the how the molecular size of fullerenes influences the electron-transport ability of fullerenes using in PSCs. At the beginning, this chapter puts forward a fullerene-cation mediated synthetic method for producing unprecedented full-carbon indano[60]fullerenes. This chapter discovers that fullerene materials having small substituents can benefit a higher electron-transport ability, which also can explain why there is few fullerene multi-adducts using in PSCs compared with OSCs.

**Chapter 5** describes the how fullerene materials can passivate the perovskite Pb<sup>2+</sup> center with a reasonable design. Considered Pb<sup>2+</sup> can be typically regarded as the Lewis acid, which can be efficiently coordinated by the Lewis base species. Accordingly, the amino group (NH<sub>2</sub>-), ether group (RO-) were introduced according to our established fullerene-cation mediated synthetic methods. Thanks to the passivation effect, the perovskite can grow with an enlarged crystal size, which promotes both electron-transfer ability and stability of perovskite layer.

**Chapter 6** describes a recent developed evaporable fullerene-ketone that aims to combine the virtue of good morphology provided by thermally-deposition, excellent electron-transport ability enabled by small molecular size, and efficient passivation effect provided by the ketone group.

Finally, **Appendix** is created after the **Conclusion (Chapter 7)**, which presents several promising non-fullerene materials that can also effectively promote the performance of PSCs. One is the newly designed s-SWNT surfactant helps CNT applied as perovskite crystal bridge to improve the PSCs performance. The other is denatured M13 bacteriophage applied as large-crystal perovskite growth-template in high-performance PSCs.

## **Chapter 3.**

# **Interlayer morphology of fullerenes**

### **3.1 Research background**

Fullerenes, which have been mostly demonstrated in organic solar cells (OSCs) in the past two decades, currently attracted tremendous interest as electron transporting layers in PSCs owing to their highly efficient electron-transporting ability [108]. As discussed in Chapter 1.3, fullerenes have different functions in OSCs and PSCs, respectively. Notably, fullerene materials can function as ETLs in PSCs without the necessity of as high concentration of fullerene solution as fullerenes applied in OSCs. Moreover, there are examples that directly using pristine fullerenes, such as C<sub>60</sub> and C<sub>70</sub> in PSCs. Compared with fullerene derivatives, pristine fullerenes possess intrinsically higher electron mobility and conductivity, which renders fullerene can get rid of difficult and expensive chemical modification before using in PSCs [109–111]. At present, inorganic metal oxides electron-transport materials, such as SnO<sub>2</sub> and TiO<sub>2</sub>, are widely applied in PSCs. Nevertheless, the use of inorganic metal oxide ETLs commonly results in heavy hysteresis issue [112], which is now found to be originated from charge trapping [113,114] and accumulation [115]. Moreover, the high sintering temperature during the device fabrication also limits their applications in flexible and large-area application of PSCs [116]. Delightedly, thanks to low chemical capacitance and high electron affinity of fullerenes [117,118], fullerenes applied PSCs can avoid these problems [119,120]. Unfortunately, high PCEs were only fulfilled when fullerenes were thermally deposited. However, spin-coated fullerene ETL-applied PSCs cannot afford PCEs as high as those of thermal-deposited fullerene ETL-applied PSCs.

This chapter studied the reasons why the poor performance of spin-coated fullerene ETL-applied PSCs compared with that of thermal-deposited fullerene ETL-applied PSCs. Accordingly, a mixed fullerene method was designed for achieving high efficiency through spin-coating process. Through the comparison between thermal-deposited and spin-coated pristine fullerene ETLs in PSCs, we found that  $C_{60}$  is a better electron-transport material than  $C_{70}$  due mainly to its lower absorption. Moreover, thermal-deposited fullerene ETLs applied PSCs showed a better performance than that of spin-coated fullerenes ETL applied, which was benefited from the amorphous state of the thermal-deposited  $C_{60}$  films different to the crystalline state of the spin-coated  $C_{60}$  films. Considering that poor performance was resulted from the crystallinity of the fullerene films, the designed method showed that mixing  $C_{70}$  into  $C_{60}$  can effectively reduce the crystallinity of the fullerene film. Accordingly, the spin-coated mixed  $C_{60}/C_{70}$  ETL applied PSCs produced a PCE of 16.7%, which is as high as that of thermal-deposited  $C_{60}$  only ETL applied PSCs. Further enhancing the performance of the spin-coated  $C_{60}/C_{70}$  ETL applied PSCs can be achieved by a vacuum-dry process, which can remove the remaining hydrophobic solvents. The removal of the intercalated solvent from the fullerene layers further increased the optical transparency and electron-transport ability of the film. The vacuum-dried spin-coated  $C_{60}/C_{70}$  ETL-based PSCs afforded a PCE of 18.0%, which was significantly higher than that of the thermal-deposited  $C_{60}$  ETL applied PSCs. This research not only achieved a high PCE of the spin-coated fullerene ETL applied PSCs, but also provided further insights into understanding how fullerene ETLs influence the performance of PSCs through various analyses.

## 3.2 Mixed C<sub>60</sub>/C<sub>70</sub> ETL for high-performance PSCs

### 3.2.1 Investigation of pristine fullerene ETLs in PSCs

At first, we comprehensively compared pristine fullerenes C<sub>60</sub> and C<sub>70</sub> in both normal and inverted architectures using thermal-depositing and spin-coating method, respectively (Figure 3.2.1.1). The related photovoltaic parameters were summarized in Table 3.2.2.1.

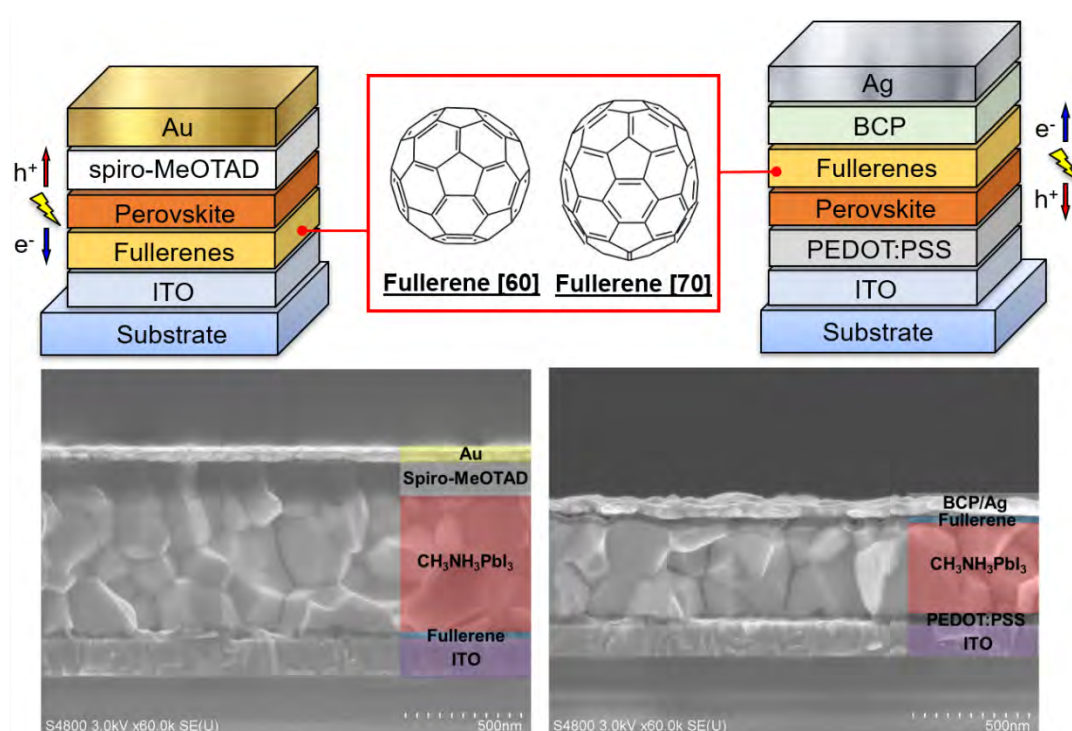


**Figure 3.2.1.1.** Illustration and cross-section SEM observations of PSC architectures used in this work.

**Table 3.2.1.1.** Photovoltaic parameters of the PSCs using thermal-deposited fullerenes as ETLs under one sun (AM 1.5 G, 100 mW cm<sup>-2</sup>).

Device Type	Fullerene	$J_{SC}$ [mA cm <sup>-2</sup> ]	$V_{OC}$ [V]	FF	$R_s$ [Ω cm <sup>2</sup> ]	$R_{SH}$ [Ω cm <sup>2</sup> ]	PCE <sub>Best</sub>	Hysteresis Index [121]
Normal	C <sub>60</sub>	22.7	1.01	0.72	37	3.7x10 <sup>4</sup>	16.7%	0.01
	C <sub>70</sub>	19.3	1.01	0.63	41	2.3x10 <sup>4</sup>	12.3%	0.03
Inverted	C <sub>60</sub>	22.9	0.90	0.77	9	1.1x10 <sup>4</sup>	15.8%	0.01
	C <sub>70</sub>	22.9	0.91	0.55	27	7.2x10 <sup>3</sup>	11.4%	0.02

The photovoltaic performance of both device types exhibited that the C<sub>60</sub>-applied PSCs afforded higher PCEs than the C<sub>70</sub>-applied devices, which is in accordance with the reported results [122,123]. Notably, The same  $V_{OC}$  values of the C<sub>60</sub>- and C<sub>70</sub>-applied PSCs indicate that C<sub>60</sub> ETL and C<sub>70</sub> ETL should have similar energy levels and energy disorders [124], which are also confirmed through ab initio computation. In addition, DFT calculations of C<sub>60</sub> and C<sub>70</sub> single molecules indicate that they possess similar LUMO energy levels. Accordingly, the energy diagram of each layers can be estimated for a comprehensive understanding of working function among each component (Figure 3.2.1.2).

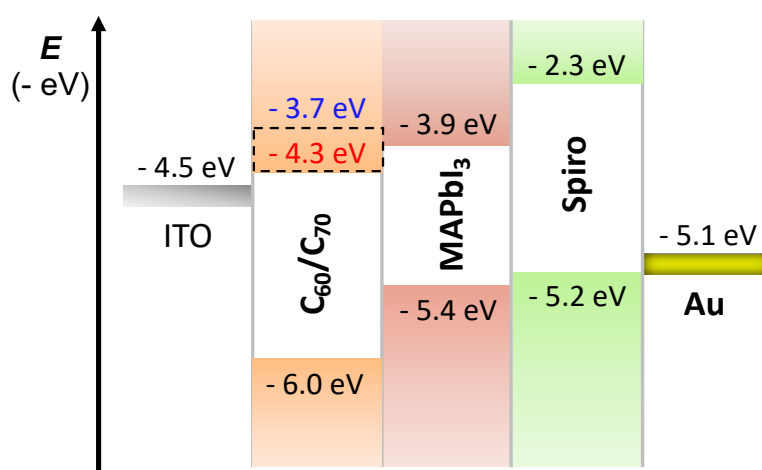


**Figure 3.2.1.2.** Computed energy band diagrams of pristine fullerenes and mixed C<sub>60</sub>/C<sub>70</sub>.

Notably, the  $J_{SC}$  value of C<sub>70</sub>-applied PSCs was lower than that of the C<sub>60</sub>-applied PSCs for the normal structure, but was similar for the inverted structure. The lower  $J_{SC}$  value can be reasonably attributed to higher absorption of C<sub>70</sub> among the visible-light range, which blocks the active from absorbing light to generate the photocurrent. Interestingly, the FF of the C<sub>60</sub>-applied PSCs was significantly higher than that of the C<sub>70</sub>-utilized PSCs for both device architectures. As shown in Table 3.2.1.1, the C<sub>70</sub>-applied PSCs depicted a higher series resistance ( $R_S$ ) and lower shunt resistance ( $R_{SH}$ ), which resulted in a lower FF value. Although some previous studies demonstrated that C<sub>70</sub> have higher conductivity [125], and electron affinity [126] than C<sub>60</sub>. Moreover, C<sub>70</sub>

is found to prevent the recombination of excitons more effective than  $C_{60}$ , owing to  $C_{70}$  possesses few circulating circuits, resulting in much efficient quantum current distributions inside the molecules [127]. However, photoluminescence (PL) measurement observed that the  $C_{60}$  films exhibited much efficient in quenching excitons from  $MAPbI_3$  than the  $C_{70}$  films (Figure 3.2.1.3). Moreover, the PL peak of  $MAPbI_3$  on  $C_{60}$  films shows slight blue-shift, which indicates that  $C_{60}$  can passivate the trap states of  $MAPbI_3$  as the trap states commonly trigger the spontaneous radiative recombination at the interface [128]. Moreover, the full width at half maximum (FWHM) was narrower for the perovskite on  $C_{60}$  than that on  $C_{70}$ , which indicates a reduction in the shallow trap density at the interface [129].

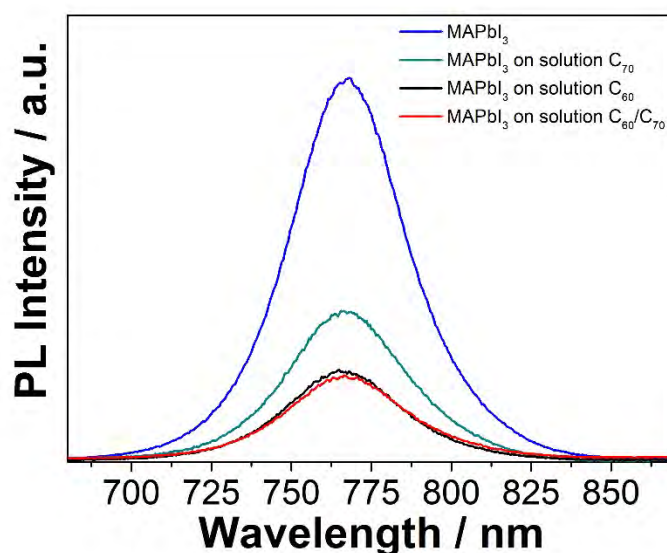


**Figure 3.2.1.3.** Photoluminescence of  $MAPbI_3$  on different fullerene ETL films with glass substrates.

It has been reported that the low molecular symmetry of  $C_{70}$  can provide smoother morphology of  $C_{60}$ , so that promotes electron transfer from perovskite [130,131]. Accordingly, it is easy to deduct that the higher FF can be fulfilled through the better interface morphology between  $C_{60}$  and  $MAPbI_3$ . Then, the  $C_{70}$  is thusly considered to be added to provide the  $C_{60}$  with a better morphology to achieve further higher PCEs.

### 3.2.2 Investigation of mixed fullerenes ETLs in PSCs

Subsequently, spin-coated  $C_{60}$  and  $C_{70}$  ETLs were only compared in the normal-type devices, as the normal-type PSCs commonly output higher performance than the inverted-type PSCs. Expectedly, the performance difference between the spin-coated  $C_{60}$ - and  $C_{70}$ -applied PSCs was as similar as that between the thermal-deposited  $C_{60}$ - and  $C_{70}$ -applied PSCs (Figure 3.2.2.1, Table 3.2.2.1); the  $C_{70}$ -applied PSCs indicated a lower  $J_{SC}$  and FF than the  $C_{60}$ -applied PSCs. Spin-coated fullerene ETLs- applied PSCs presented lower PCEs than the thermal-deposited fullerene ETLs-applied PSCs (compare between Table 3.2.1.1 and Table 3.2.2.1). Despite the spin-coated fullerene ETLs-applied PSCs showed lower efficiency, the spin-coating process is still preferred compared to thermal-depositing process because of its cheaper cost, facile fabrication technique, and simplicity. Consequently, it is important to figure out why the spin-coated fullerene ETLs-applied PSCs commonly give a lower performance, and then a solution could be provided.

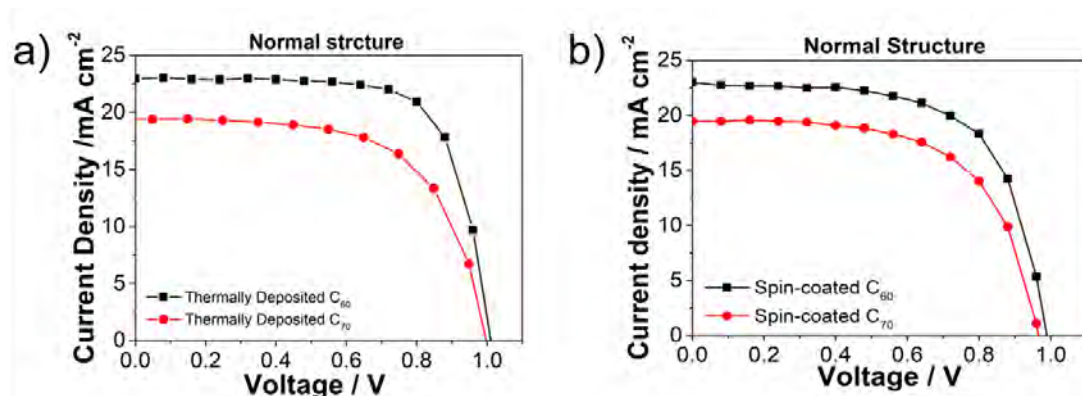


**Figure 3.2.2.1.**  $J$ - $V$  curves of the normal-type PSCs using a) thermal-deposited  $C_{60}$ - (black) and  $C_{70}$ - (red) as ETLs; b) spin-coated  $C_{60}$ - (black) and  $C_{70}$ - (red) as ETLs.

As the lower  $V_{OC}$  and FF resulted in the lower PCE of the spin-coated fullerene ETLs-applied PSCs (thermal-deposited  $C_{60}$ -applied PSCs:  $V_{OC} = 1.01$  V,  $J_{SC} = 22.7$  mA cm<sup>-2</sup>, FF = 0.72 from Table 3.2.1.1; spin-coated  $C_{60}$ -applied PSCs:  $V_{OC} = 0.99$  V,  $J_{SC} = 23.0$  mA cm<sup>-2</sup>, FF = 0.65 from Table 3.2.2.1), the lower performance is due mainly to the crystallinity of fullerene ETL films. Generally speaking, thermal-deposited



fullerene ETL films are found to be nearly amorphous [132,133], whereas spin-coated fullerene ETL films are found to have higher crystallinity [134,135].

**Table 3.2.2.1.** Photovoltaic parameters of the normal-type PSCs using spin-coated fullerenes as the ETLs under one sun (AM 1.5 G, 100 mW cm<sup>-2</sup>).

Fullerene	$J_{sc}$ [mA cm <sup>-2</sup> ]	$V_{oc}$ [V]	FF	$R_s$ [Ω cm <sup>2</sup> ]	$R_{sh}$ [Ω cm <sup>2</sup> ]	PCE <sub>Best</sub>	Hysteresis Index [121]
C <sub>60</sub>	23.0	0.99	0.65	42	1.7x10 <sup>4</sup>	14.8%	0.03
C <sub>70</sub>	19.5	0.97	0.62	36	6.8x10 <sup>4</sup>	11.7%	0.07
<b>C<sub>60</sub>/C<sub>70</sub> (9:1)</b>	<b>22.9</b>	<b>1.02</b>	<b>0.71</b>	<b>30</b>	<b>1.5x10<sup>5</sup></b>	<b>16.7%</b>	<b>0.04</b>
C <sub>60</sub> /C <sub>70</sub> (5:5)	21.2	1.02	0.55	65	5.7x10 <sup>3</sup>	11.8%	0.05
C <sub>60</sub> /C <sub>70</sub> (1:9)	20.4	1.00	0.55	60	6.8x10 <sup>3</sup>	11.1%	0.05

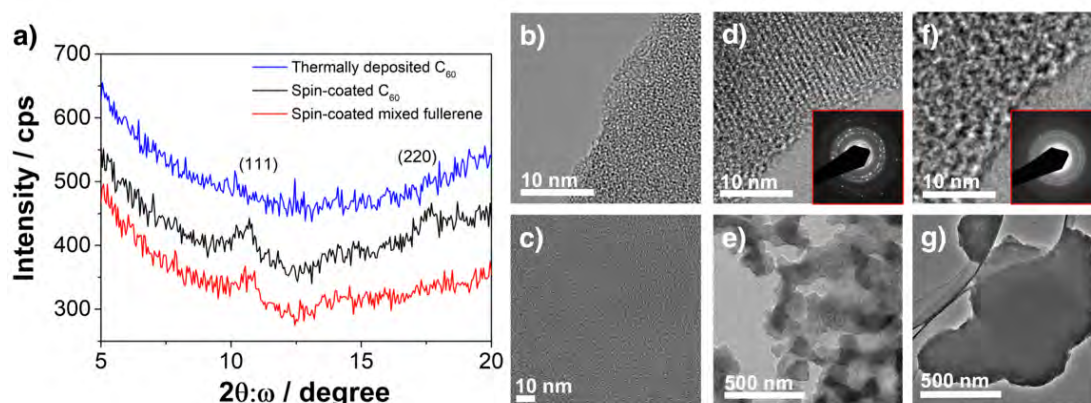


**Figure 3.2.2.2.** a) GIXRD 2θ scan of thermal-deposited C<sub>60</sub> film (blue line), spin-coated C<sub>60</sub> film (black line), and spin-coated mixed C<sub>60</sub>/C<sub>70</sub> film (red line). TEM images of b), c) thermal-deposited C<sub>60</sub> film; d), e) spin-coated C<sub>60</sub> film with an SAED as an inset; and f), g) spin-coated mixed C<sub>60</sub>/C<sub>70</sub> film with an SAED as an inset.

Accordingly, the grazing-incidence X-ray diffraction spectroscopy (GIXRD) was carried out to analyze the thermal-deposited C<sub>60</sub> ETL films and the spin-coated C<sub>60</sub> ETL films (Figure 3.2.2.2a). Figure 3.2.2.2a indicates that the XRD spectra of the thermal-deposited C<sub>60</sub> films do not depict any peaks, but those of the spin-coated C<sub>60</sub> films depict the (111) peak at 10° and the (220) peak at 18°. Further observation was conducted by the TEM images. The thermal-deposited C<sub>60</sub> films showed an amorphous state (Figure 3.2.2.2b) with no crystal domains (Figure 3.2.2.2c), while the spin-coated

C<sub>60</sub> films depicted high crystallinity (Figure 3.2.2.2d) with crystal domain sizes of 20 nm to 100 nm (Figure 3.2.2.2e). It is well-known that the grain boundaries between crystal domains can hinder the charge flow despite charge mobility may be high within a crystal domain. Accordingly, unless a film is formed in a predominately single crystalline phase, amorphous films should have better charge transport, which clearly explains the higher  $R_s$  and lower FF of the spin-coated C<sub>60</sub>-applied PSCs as compared with those of the thermal-deposited C<sub>60</sub>-applied PSCs. The lower charge transport suggests that more charge recombination; thus, lower  $V_{OC}$  value was obtained for the spin-coated fullerene-applied PSCs.

Considering that the crystallinity of the spin-coated C<sub>60</sub> films results in lower device performance, a small amount of C<sub>70</sub> was added into the C<sub>60</sub> solution to suppress the crystallinity of the spin-coated C<sub>60</sub> film, which is denoted as “mixed fullerene films” hereafter. It is worthwhile noting that the C<sub>60</sub> and C<sub>70</sub> mixtures are easily obtained from the fullerene production, which are considerably less expensive than the pure compounds [136]. GIXRD spectra in Figure 3.2.2.2a exhibits that the mixed fullerene film shows much weaker (111) and (220) peaks. Meanwhile, TEM observation also demonstrate that the mixed fullerene film (Figure 3.2.2.2f) exhibits suppressed crystallinity in contrast to the spin-coated C<sub>60</sub> film (Figure 3.2.2.2d). This is evident can be more clearly collected from the ring patterns SAED; the SAED pattern of the spin-coated C<sub>60</sub> film (Figure 3.2.2.2d inset) indicates stronger crystallinity than that of the mixed fullerene film (Figure 3.2.2.2f inset). Satisfactorily, crystal domains were not observed in the mixed fullerene films (Figure 3.2.2.2g).

The morphologies of the fullerene films were further investigated using the topography and adhesion modes of AFM. The mixed fullerene film exhibited an expectedly lower surface roughness with a roughness average ( $R_a$ ) of 2.43 nm in contrast to the spin-coated C<sub>60</sub> films with a  $R_a$  of 7.19 nm (Figure 3.2.2.3a and b). Subsequently, the crystal domain boundaries of the fullerene films were also detected by probing the adhesion of the film surface. According to the high adhesion force of the crystal boundaries, it can be concluded that the spin-coated C<sub>60</sub> films possessed many

domains of *ca.* 50 nm (Figure 3.2.2.3c). In the case of mixed fullerene films, the boundaries were much less defined (Figure 3.2.2.3d). Moreover, the 3D images indicate that the mixed fullerene films have much flatter topography.

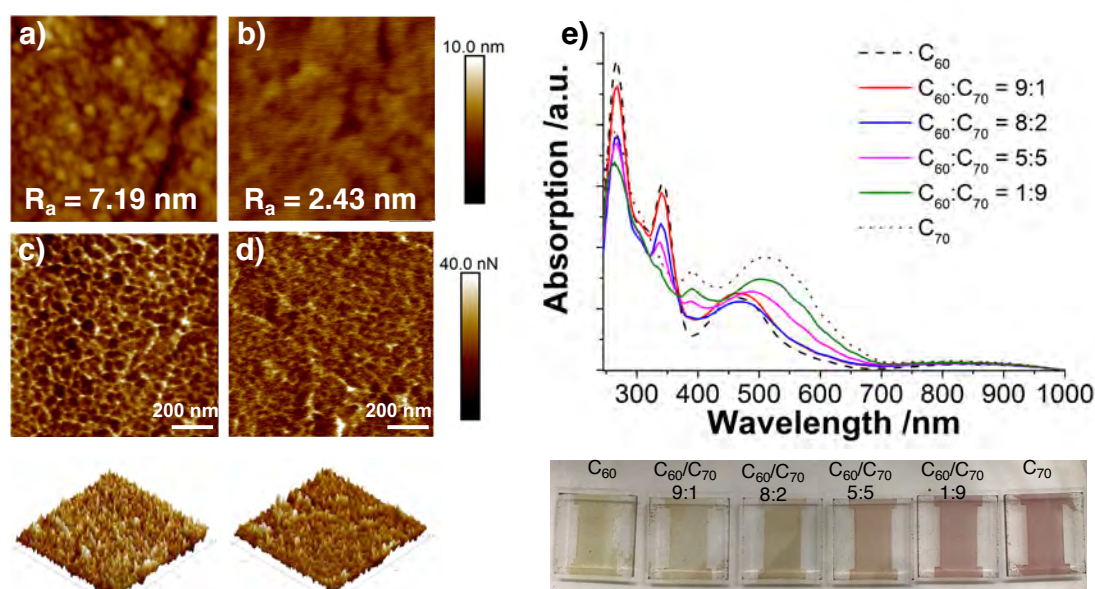


**Figure 3.2.2.3.** AFM topographic images of spin-coated a)  $C_{60}$  film and b) mixed  $C_{60}/C_{70}$  film with roughness average values. AFM adhesion images of spin-coated c)  $C_{60}$  film and d) mixed  $C_{60}/C_{70}$  film with the 3D images. e) Transmittance of fullerene ETL films with different  $C_{60}/C_{70}$  ratios along with their pictures.

Then PSCs with normal configuration were fabricated using the spin-coated mixed  $C_{60}/C_{70}$  ETLs with different  $C_{60}$  to  $C_{70}$  ratios (Table 3.2.2.2). The best PCE of 16.7% was achieved with the mixture of  $C_{60}/C_{70}$  in a 9:1 weight ratio, which shows a PCE as high as that of the thermal-deposited  $C_{60}$  ETL-applied PSCs (Table 3.2.1.1). However, the PSCs with greater  $C_{70}$  component gave lower  $J_{SC}$  and lower FF, which thusly resulted in a lower PCE (Table 3.2.2.2). As discussed above, the  $C_{70}$  has a stronger absorption than  $C_{60}$  in a visible light range, UV-vis was thereafter carried out to observe the transmittance of different  $C_{60}/C_{70}$  ratios. The UV-vis spectra indicated that the transmittance of the fullerenes film significantly reduced when increase in the amount of  $C_{70}$  in the film (Figure 3.2.2.3e), which results in the decreased  $J_{SC}$  value. Delightedly, the mixed  $C_{60}/C_{70}$  films with the weight ratio 9:1 exhibited almost the same

transmittance as that of the pure  $C_{60}$ , which showed the similar  $J_{SC}$  values. The observed lowering trend of FF is related to the poor charge transfer between  $C_{70}$  and the perovskite layer. In addition, PSCs where mixed  $C_{60}/C_{70}$  were showed higher  $V_{OC}$  than the pure  $C_{60}$ -applied or  $C_{70}$ -applied devices, which can be regarded as another evidence pointing to the lower recombination between the MAPbI<sub>3</sub> and the mixed  $C_{60}/C_{70}$  ETL film because of its amorphous nature, which exhibiting more efficient charge transfer than the pure pristine fullerene films.

To evaluate the feasibility of this mixed  $C_{60}/C_{70}$  ETL fabrication method, a statistical analysis was conducted to examine the reproducibility of the proposed method (Figure 3.2.2.4). Satisfactorily, all photovoltaic parameters collected from 10 devices in same batch showed high reproducibility.

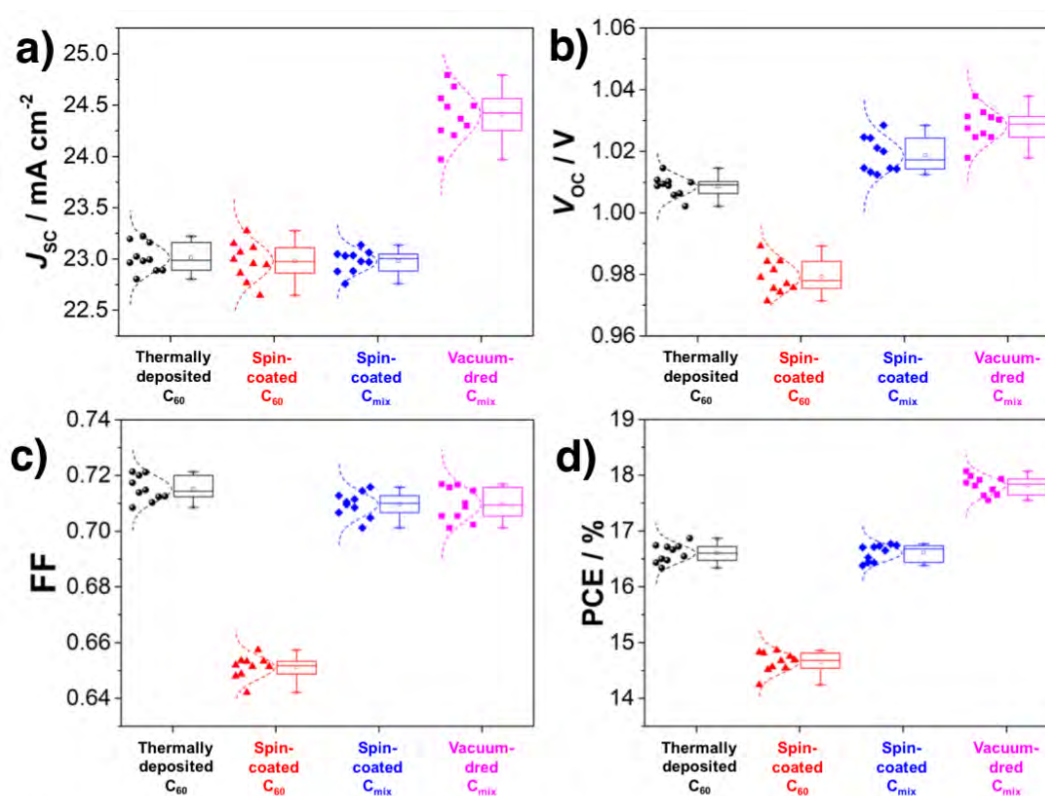


**Figure 3.2.2.4.** Photovoltaic parameters and statistical analysis of thermal-deposited  $C_{60}$ -applied PSCs (black circles), spin-coated  $C_{60}$ -applied PSCs (red triangles), spin-coated mixed  $C_{60}/C_{70}$ -applied PSCs (blue diamonds), and vacuum-dried mixed  $C_{60}/C_{70}$ -applied PSCs (purple squares), showing a)  $J_{SC}$ , b)  $V_{OC}$ , c) FF, and d) PCE.

### 3.2.3 Investigation of vacuum-dry process for fullerene ETLs in PSCs

Considering that the mixed C<sub>60</sub>/C<sub>70</sub> ETLs successfully achieved PCE as high as that of the thermal-deposited C<sub>60</sub> ETLs, a method to further improve the PCE of these mixed C<sub>60</sub>/C<sub>70</sub> ETLs applied PSCs. Apart from the amorphous state that thermal-deposited C<sub>60</sub> film provided, another favorable aspect of the thermal-deposited C<sub>60</sub> film is that it is solvent-free. Accordingly, removing the trapped solvents from the spin-coated mixed C<sub>60</sub>/C<sub>70</sub> films is expected to pack the fullerenes in a more compact manner, so that improving the charge transport because of eliminated solvent effects [137]. To remove the *ortho*-dichlorobenzene (*o*-DCB) effectively, three different treatments were applied to the spin-coated mixed C<sub>60</sub>/C<sub>70</sub> films: thermal annealing (TA) at 100 °C, TA at 200 °C, and TA at 100 °C under a vacuum chamber (0.01 MPa). Table 3.2.3.1 summarizes the photovoltaic parameters of the PSCs with different post-treatments applied to the spin-coated mixed C<sub>60</sub>/C<sub>70</sub> ETLs.

**Table 3.2.3.1.** Photovoltaic parameters of the normal-type PSCs using mixed C<sub>60</sub>/C<sub>70</sub> as the ETL with different post treatments under one sun (AM 1.5 G, 100 mW cm<sup>-2</sup>).

Fullerene	Treatment	$J_{sc}$ [mA cm <sup>-2</sup> ]	$V_{oc}$ [V]	FF	$R_s$ [Ω cm <sup>2</sup> ]	$R_{sh}$ [Ω cm <sup>2</sup> ]	PCE <sub>Best</sub>
Spin-coated C <sub>60</sub> /C <sub>70</sub> (9:1)	none	22.9	1.02	0.71	42	1.7x10 <sup>4</sup>	16.7%
	100 °C TA	23.2	1.04	0.71	33	1.7x10 <sup>3</sup>	16.9%
	200 °C TA	22.5	1.05	0.66	20	4.0x10 <sup>3</sup>	15.7%
	Vacuum-dry at 100 °C	24.3	1.03	0.73	28	1.5x10 <sup>4</sup>	18.0%

100 °C TA treatment of PSCs did not give a significant influence on the performance (Figure 3.2.3.1), which was attributed to the treating temperature is not sufficiently high to reach the boiling point of *o*-DCB. However, 200 °C TA treatment at 200 °C showed reduced device performance. According to the AFM morphology analysis in Figure 3.2.3.1, TA at 200 °C led to the severe aggregation of the fullerene films. Although such high enough temperature is effective for removing *o*-DCB, it results in strong crystallization, which seriously roughens the morphology as depicted

by the low FF [124,138]. To our delight, vacuum-dried the fullerene film at 100 °C for 10 min can effectively increase the PCE to 18.0% with the increased  $J_{SC}$  and  $V_{OC}$  values whereas FF stayed the same. The AFM roughness image and the corresponding  $R_a$  value indicate that the morphology of the  $C_{60}/C_{70}$  film further improved with the vacuum-dry process.

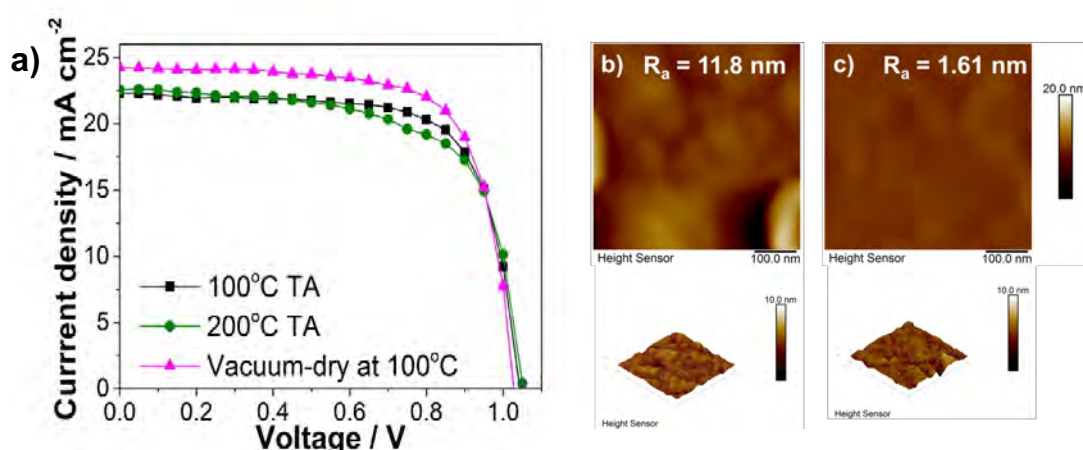


**Figure 3.2.3.1.** a)  $J$ - $V$  curves of PSCs with mixed  $C_{60}/C_{70}$  ETL by different post treatment. AFM images of spin-coated  $C_{60}/C_{70}$  films by b) 200 °C TA, and b) 100 °C vacuum-dry.

Then, XPS was applied to further confirm the removal of *o*-DCB by vacuum-dry process. The XPS data indicate that the chlorine from *o*-DCB solvent, which was detectable when treated with TA at 100 °C, was not detectable when treated with TA at 200 °C and vacuum-dry process (Figure 3.2.3.2a). Moreover, UV-vis absorption spectra exhibit that the vacuum-dry process further reduced the absorption, which contributes to the increased  $J_{SC}$  value (Figure 3.2.3.2b). This decrease in absorption can be reasonably attributed to the removal of ODCB increased the transmittance of the film through removing solvatochromism [124,138]. Cross-section SEM image of the spin-coated mixed  $C_{60}/C_{70}$  film shows that the fullerene film has a thickness of approximately 32 nm (Figure 3.2.3.2c), which has a similar optimized thickness *ca.* 35 nm as thermal-deposited  $C_{60}$  film. After the vacuum-dry process, the thickness of same mixed  $C_{60}/C_{70}$  film decreased to *ca.* 12 nm (Figure 3.2.3.2d). In addition, GIXRD



spectra indicated a decrease in the crystallinity of the spin-coated mixed  $C_{60}/C_{70}$  films upon vacuum-dry process, which is in accord with that the removal of solvent affected the packing and crystallinity of the fullerenes. Accordingly, the combination of enhanced transmittance and charge transport contribute to the increase in both  $J_{SC}$  and  $V_{OC}$ . Ultimately, the PCE of the vacuum-dry spin-coated  $C_{60}/C_{70}$ -applied PSC (18.0%) exceeded that of the thermal-deposited  $C_{60}$ -applied PSC (16.7%).

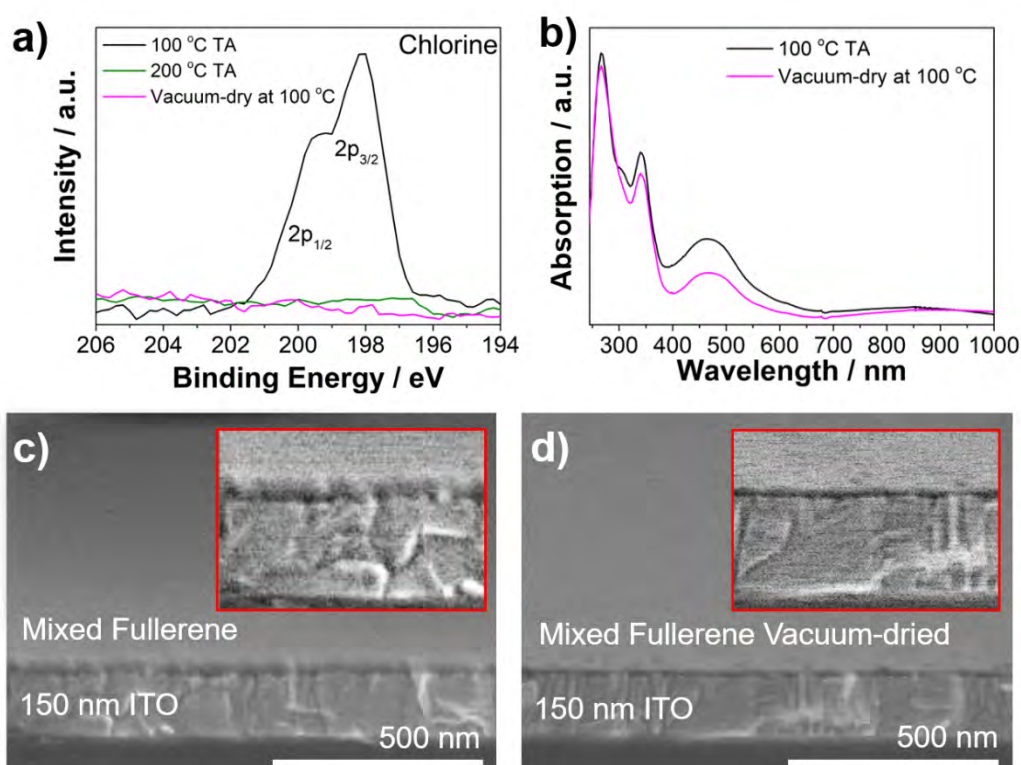


**Figure 3.2.3.2.** a) XPS chlorine spectra of a mixed  $C_{60}/C_{70}$  film with different post treatment. b) UV-vis absorption spectra of a mixed  $C_{60}/C_{70}$  film t with different post treatment. Cross-sectional SEM imagines of spin-coated c) mixed  $C_{60}/C_{70}$  film and d) the same film after vacuum-dry process on ITO substrates with magnified images as insets.

### **3.3 Materials and methods**

#### **3.3.1 Materials preparation**

##### **3.3.1.1 Mixed-fullerene solution preparation**

C<sub>60</sub> and C<sub>70</sub> were dissolved in a solution of *o*-DCB in different ratios with a mass concentration of 20.0 mg mL<sup>-1</sup>. The solution was filtered through a 0.45 µm polytetrafluoroethylene filter prior to use.

##### **3.3.1.2 Spiro-MeOTAD solution preparation**

A solution was prepared by mixing 85.8 mg Spiro-MeOTAD (Lumtech), 19.3 µL of a stock solution of 520 mg mL<sup>-1</sup> lithium bis(trifluoromethylsulphonyl)imide (Aldrich) in anhydrous acetonitrile, and 33.8 µL of 4-*tert*-butylpyridine (Aldrich) in 1 mL anhydrous chlorobenzene.

##### **3.3.1.3 PEDOT:PSS solution preparation.**

Poly(3,4-ethylenedioxythiophene) polystyrene sulfonate (PEDOT:PSS) solution was produced by adding 0.5 wt% polyoxyethylene tridecyl ether (Sigma-Aldrich Chemical Co., Inc.) to a PEDOT:PSS dispersion in water (Clevios P VP, Heraeus Precious Metals GmbH & Co.). The solution was filtered through a 0.45 µm polytetrafluoroethylene filter prior to use.

##### **3.3.1.4 Perovskite (MAPbI<sub>3</sub>) precursor solution preparation.**

CH<sub>3</sub>NH<sub>3</sub>I (TCI), PbI<sub>2</sub> (TCI), and anhydrous dimethyl sulfoxide (TCI) (molar ratio 1:1:1) were mixed in anhydrous *N,N*-dimethylformamide (TCI) with a concentration of 50 wt%. The solution was filtered through a 0.45 µm polytetrafluoroethylene filter prior to use.



### **3.3.2 Device fabrication**

#### **3.3.2.1 Fabrication of inverted type PSCs.**

Indium tin oxide (ITO) patterned glass substrates with a size of  $15 \times 15 \text{ mm}^2$  and sheet resistance of  $6 \Omega \text{ sq}^{-1}$  (Techno Print Co., Ltd.) were cleaned and sonicated with a detergent, distilled water, acetone, and isopropanol in an ultrasonic bath for 15 min. Subsequently, the substrates were treated with ultraviolet/ozone (UV/O<sub>3</sub>) for 15 min prior to use. Thereafter, 25  $\mu\text{L}$  of PEDOT:PSS solution was spin-coated on UV/O<sub>3</sub>-treated ITO substrates at 3000 rpm for 30 s. The coated ITO substrates were subsequently annealed at 105 °C for 10 min. Thereafter, 25  $\mu\text{L}$  of the perovskite precursor solution was spin-coated on the PEDOT:PSS layer at 3000 rpm for 30 s, and 0.5 mL of anhydrous diethyl ether was slowly dripped onto the substrate 10 s after the start of the spin-coating process. Subsequently, the film was annealed at 100 °C for 10 min to obtain a dense brown MAPbI<sub>3</sub> film. Subsequently, C<sub>60</sub> or C<sub>70</sub> was thermally deposited on the perovskite film to obtain a thickness of 30 nm at a constant evaporation rate of  $0.02 \text{ nm s}^{-1}$ . Similarly, bathocuproine was thermally deposited to obtain a thickness of 10 nm at the same evaporation rate. Finally, a 70-nm-thick Ag cathode was fabricated *via* thermal deposition at a constant evaporation rate of  $0.05 \text{ nm s}^{-1}$ .

#### **3.3.2.2 Fabrication of normal type PSCs.**

ITO patterned glass substrates were cleaned and sonicated with detergent, distilled water, acetone and isopropanol in an ultrasonic bath for 15 min, respectively. Subsequently, 25  $\mu\text{L}$  of mix-fullerene solution was spin-coated on ITO substrates at 3000 rpm for 30 s. The coated ITO substrates were used without any treatment or were followed by different processes, such as: 1) annealing at 100°C for 1 h; 2) annealing at 200 °C for 1 h; 3) drying up at 100°C under vacuum condition ( $\sim 1.0 \times 10^{-3} \text{ MPa}$ ) for 1 h. If thermal-deposited fullerene film was used, C<sub>60</sub> or C<sub>70</sub> was thermal-deposited on ITO substrates in a thickness of 30 nm at a constant evaporation rate of  $0.02 \text{ nm s}^{-1}$ . Then, 25  $\mu\text{L}$  of perovskite precursor solution was spin-coated on the fullerene layer at 3000 rpm for 30 s, with a dropping of 0.5 mL of anhydrous diethyl ether was slowly

dripped onto the substrate 10 s after the start of the spin-coating process. Next, the film was annealed at 100 °C for 10 min to obtain a dense brown MAPbI<sub>3</sub> film. The hole transporting layer was spin-coated from the Spiro-MeOTAD solution at 4000 rpm for 30 s. Finally, a 70-nm-thick of Au anode was fabricated by thermal deposition at a constant evaporation rate of 0.05 nm s<sup>-1</sup>.

### **3.3.3 Performance evaluation and characterization**

The  $J$ - $V$  characteristics were measured using a software-controlled source meter (Keithley 2400 SourceMeter) under dark conditions and the simulated sunlight irradiation of 1 sun (AM 1.5G; 100 mW cm<sup>-2</sup>) using a solar simulator (EMS-35AAA, Ushio Spax Inc.) with an Ushio Xe short arc lamp 500. The source meter was calibrated using a silicon diode (BS-520BK, Bunkokeiki). SEM analysis of the perovskite films was performed using an S-4800 (Hitachi). The TEM images are taken by JEM-2010F (JEOL Ltd.) with a thermal field emission gun operated at 200 keV. The Selected area electron diffraction (SAED) patterns are recorded by a Charge-coupled Device (CCD) at a camera length of 60 cm. Shimadzu UV-3150 was used for the UV-vis-NIR measurement. The PL measurements were performed using JASCO Spectrofluorometer (FP-8300). Topography images were recorded by using an atomic force microscope (AFM) operating in tapping mode (SPI3800N, SII). The grazing-incidence XRD 2 $\theta$  scans were performed on a Jordan Valley D1 diffractometer with copper K $\alpha$ 1 radiation and a parallel beam source. In the 2 $\theta$  scans, the scattering angle 2 $\theta$  between incident beam and diffracted beam changes while the incident angle  $\omega$  between incident beam and the sample surface is fixed at 1 degree. The valence band and Fermi levels measurements were performed using Riken Keiki PYS-A AC-2 and Kelvin probe spectroscopy in air (ESA), respectively. The photoemission measurements were performed using XPS (PHI5000, Versa Probe) with monochromatic Al K $\alpha$  radiation. The water contact angle measurements were performed using a contact angle meter (DMo-501, Kyowa Interface Science Co., Ltd.).

### 3.4 Summary

This work compared  $C_{60}$  and  $C_{70}$  in PSCs, which was further extended to thermal-deposited and spin-coated methods of fullerenes in normal and inverted structures of PSCs.  $C_{60}$  as ETL in PSC presented higher photovoltaic performance than  $C_{70}$ . The thermal-deposited  $C_{60}$ -applied normal-type PSCs exhibited a PCE of 16.7%. Through investigating the mechanism behind the efficiency enhancement, this work discovered that the high performance of the thermal-deposited  $C_{60}$ -applied PSCs is benefited from the low crystallinity of the fullerene and the absence of remnant solvents. By mixing a 10% weight ratio amount of  $C_{70}$  into a solution of  $C_{60}$ , the crystallinity of the spin-coated mixed  $C_{60}/C_{70}$  films decreased substantially, producing a PCE close to that of the thermal-deposited  $C_{60}$ -applied PSCs. Furthermore, by vacuum-dry process, the mixed  $C_{60}/C_{70}$  film, a PCE of 18% without hysteresis was achieved, which exceeds that of the thermal-deposited  $C_{60}$ -applied PSCs (Figure 3.4.1) [90].

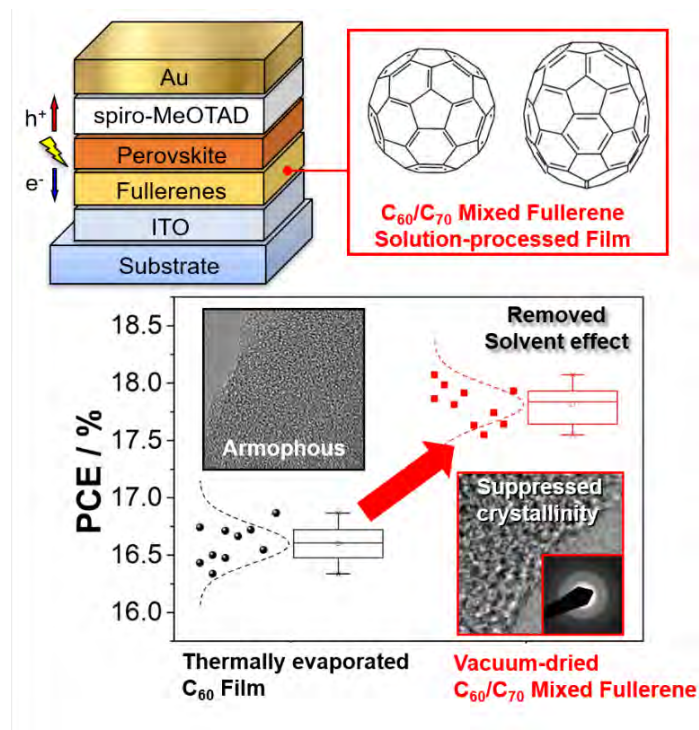


**Figure 3.4.1.** Graphic summary of using mixed  $C_{60}/C_{70}$  ETL for high-performance PSCs.



## **Chapter 4.**

# **Electron-transport mobility of fullerenes**

### **4.1 Research background**

As discussed in previous chapters, fullerene commonly functionalize as the ETL in PSCs other than electron acceptor in OSCs. Accordingly, the strategy for designing fullerene materials for OSCs usually failed to produce fullerene materials for high-performance PSCs. In a consequence, metal oxides such as titanium oxide ( $\text{TiO}_2$ ) and tin oxide ( $\text{SnO}_2$ ) are still currently most state-of-the-art ETLs that employed in PSCs [139–141]. Nevertheless, the fabrication of  $\text{TiO}_2$  ETL requires a long-time (*ca.* 2–5 h) and high-temperature (up to 500 °C) for sintering process [142,143], which results in more attraction toward  $\text{SnO}_2$  owing to its facile fabrication and its higher electron mobility, favorable energy level alignment, and comparatively wide bandgap. Although the PCEs of  $\text{SnO}_2$  applied PSCs have been achieved over 20.0%, the significant issues, such as large hysteresis of devices seriously limits its application, which is originated from the charge recombination [115], and charge trapping [113,114].

Fullerenes, n-type semiconducting materials, can be an effective solution to tackle with these hysteresis problems owing to its remarkably low chemical capacitance, high electron affinity, and energetically favorable deep-lying LUMO energy levels [118–120]. Although fullerenes ETLs can provide a hysteresis-free PSCs, PCEs still relatively lower than the champion records of metal oxides applied PSCs. Consequently, combining ETLs of the metal oxides and fullerenes have been rapidly investigated. For instance, modifying the interfacial surface of metal oxides ETLs by fullerene and its derivatives, namely the overcoating process, has been proved to be a practical method to reduce hysteresis and enhance the photovoltaic performance of PSCs [101,144–148].

Intriguingly, the most fullerenes that applied as interfacial modifier contain a cyclo-ring unit in their molecules, which can be reasonably attributed to two main aspects: 1) the LUMO level of [60]fullerenes ( $C_{60}$ ), 60- $\pi$  conjugation system, can be effectively tuned up to mono-cyclo[60]fullerenes with a 58- $\pi$  conjugation system [149,150]; 2) compared with other fullerene derivatives, such as 1,2- and 1,4-addition patterns, cyclo[60]fullerenes have a much compact molecular structure, which provides a highly-ordered packing in molecular assembling [12,100]. Among these cyclo[60]fullerene derivatives, only 3-membered-carbon-rings (e.g. PC<sub>61</sub>BM), 6-membered-carbon-rings (e.g. ICBA, MIF), and 5-membered-heteroatom-rings, have been presented, but their PCEs are relatively low (<20.0%). However, to the best of our knowledge, there has never been demonstrated any 5-membered-carbon-rings cyclo[60]fullerenes, namely full-carbon indano[60]fullerenes (FIFs), that applied in PSCs whether as fullerene-modified metal oxides or fullerene-passivated perovskite. This is mainly because the conventional fullerene synthetic chemistry, such as fullerene-anion (e.g. the Bingel reaction, the Prato reaction, *etc.*) or fullerene-radical chemistry requires an S<sub>N</sub>2 intramolecular cyclization pathway [151], which is unfavorable to produce the FIFs (Figure 4.1.1). In addition, previously mentioned cyclo[60]fullerenes commonly have a relatively large molecular size when they are designed to install the functional groups (e.g. -OH, -COOR, *etc.*) to modify the interfacial surface of metal oxides ETLs. This is another weak point of conventional fullerene synthetic chemistry that the bulky substituents are inevitable during molecular design. Promisingly, fullerene-cation chemistry can resolve aforementioned issues, and even produce scalable high yields owing to its unique high-reactivity of newly-generated LUMO.

In this work, we put forward a Cu[II]-promoted fullerene-cation-mediated strategy to access the full-carbon indano[60]fullerenes (FIFs) in scalable high yields up to 93% with versatile functional groups through an E2 intramolecular cyclization pathway (Figure 4.1.1). FIF has three superiors: 1) a suitable LUMO energy level and high electron carrier mobility, which benefits the extraction of photogenerated excitons from the perovskite film and transport to the SnO<sub>2</sub> ETL; 2) the Lewis base methoxy group at

the indano unit passivates the Pb center in perovskite through a coordinating interaction. Meanwhile, the methoxy group can similarly coordinate Sn of the tin oxide layer, where FIF can act as a bridge to improve the connection between ETL and the active layer; 3) the smallest molecular size allows it aligns much compactable so that improves the interfacial surface quality of film, which further benefits the pinhole-free film formation of perovskite. Therefore, the FIF applied perovskite exhibits a maximum PCE up to 20.7%, which is record-high among the reported fullerenes applied MAPbI<sub>3</sub>-type perovskite solar cells with reduced hysteresis.

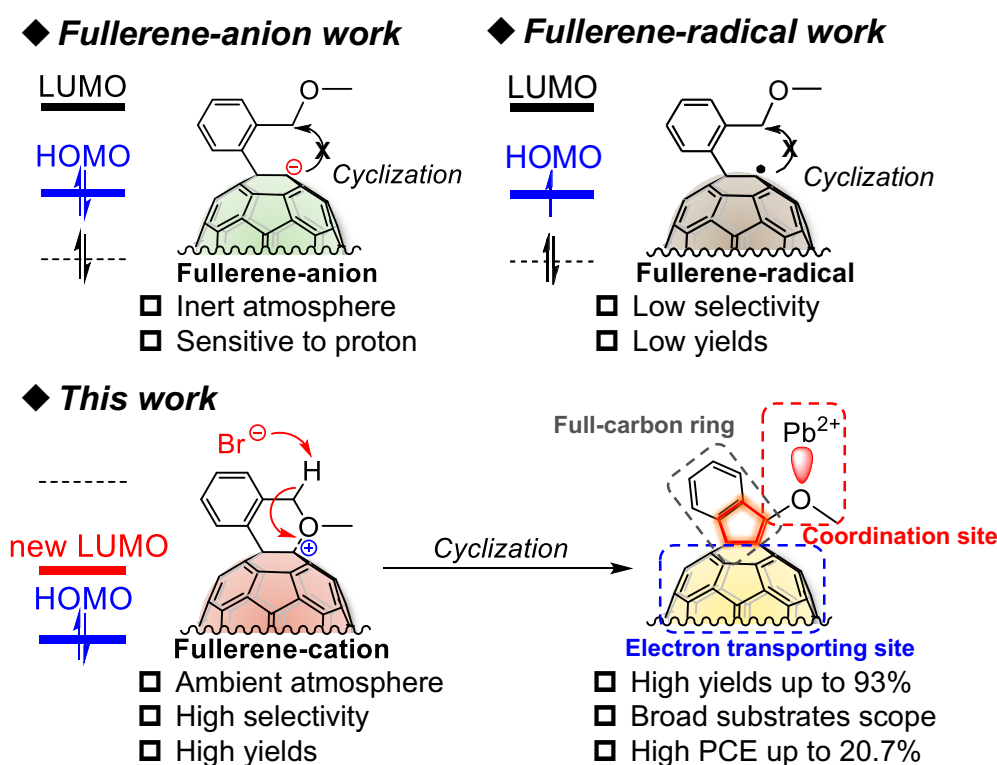


**Figure 4.1.1.** Concept of this work. The newly generated LUMO has unique reactivity, enabling the production of full-carbon indano[60]fullerene.

As this work contains both findings in electron mobility and passivation effect of FIFs, this chapter will mainly discuss how to apply the fullerene-cation chemistry to design a good fullerene material in PSCs, and how molecular size influences the electron mobility of fullerenes for high-performance PSCs. The passivation effect will thusly be discussed in the next chapter.

## 4.2 Fullerene-cation-mediated synthesis of FIFs

### 4.2.1 Synthesis of arylhydro[60]fullerenes

Arylhydro[60]fullerenes ( $\text{ArC}_{60}\text{H}$ , **3a–g**) were prepared by nucleophilic addition of functionalized Grignard reagents (**2a–g**) to pristine fullerene (Table 4.2.1).

**Table 4.2.1.** Synthesis of arylhydro[60]fullerenes **3a–g**<sup>a</sup>.

Entry	R <sub>1</sub>	R <sub>2</sub>	Products <b>3</b>	Yield (%) <sup>b</sup>
1	4-H-	CH <sub>3</sub> -		95
2	4-CH <sub>3</sub> -	CH <sub>3</sub> -		87
3	4-CH <sub>3</sub> O-	CH <sub>3</sub> -		84
4	4-F-	CH <sub>3</sub> -		80
5	4-H-	CH <sub>3</sub> (CH <sub>2</sub> ) <sub>5</sub> -		88
6	4-H-	CH <sub>3</sub> (CH <sub>2</sub> ) <sub>3</sub> CHCH <sub>2</sub> - CH <sub>2</sub> CH <sub>3</sub>		86
7 <sup>c</sup>	4-H-	CH <sub>3</sub> -		90

<sup>a</sup> Unless otherwise specified, all reactions were performed with 0.417 mmol of C<sub>60</sub>, 12.5 mmol of DMI, and 1.25 mmol of **2** ( $n = 0$ ) in 50.0 mL of *o*-DCB at 25 °C under an argon atmosphere, and quenched by 0.1 mL CH<sub>3</sub>COOH. <sup>b</sup> Isolated yield. <sup>c</sup>  $n = 1$ .



### 4.2.2 Synthesis of aryl[60]fullerenyl dimer precursors

The key precursors, aryl[60]fullerenyl dimers ( $\text{ArC}_{60}\text{-C}_{60}\text{Ar}$ , **4a–g**) were synthesized in high stoichiometric yield by using *N*-bromosuccinimide (NBS) in the presence of *t*-BuOK (Table 4.2.2).

**Table 4.2.2.** Synthesis of arylhydro[60]fullerenes **4a–g**<sup>a</sup>.

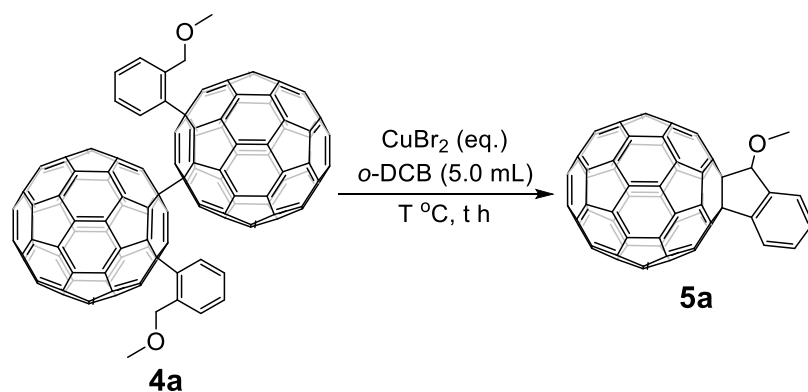
Entry	R <sub>1</sub>	R <sub>2</sub>	Products <b>4</b>	Yield (%) <sup>b</sup>
1	4-H-	CH <sub>3</sub> -		98
2	4-CH <sub>3</sub> -	CH <sub>3</sub> -		97
3	4-CH <sub>3</sub> O-	CH <sub>3</sub> -		99
4	4-F-	CH <sub>3</sub> -		97
5	4-H-	CH <sub>3</sub> (CH <sub>2</sub> ) <sub>5</sub> -		97
6	4-H-	CH <sub>3</sub> (CH <sub>2</sub> ) <sub>3</sub> CHCH <sub>2</sub> - CH <sub>2</sub> CH <sub>3</sub>		98
7 <sup>c</sup>	4-H-	CH <sub>3</sub> -		98

<sup>a</sup> Unless otherwise specified, all reactions were performed with 0.048 mmol of **3** and 0.05 mmol of *t*-BuOK in 5.0 mL of *o*-DCB at 25 °C under an argon atmosphere. After stirring for 15 min, 0.0192 mmol of NBS was added as oxidant. <sup>b</sup> HPLC yield. <sup>c</sup> n = 1.

### 4.2.3 Optimization for reaction conditions

Then, the reaction conditions were optimized for heating aryl[60]fullerenyl dimer (**4a**) at 100 °C in the presence of 4.0 equiv. CuBr<sub>2</sub> under an ambient atmosphere for 3.0 hours (Table 4.2.3). The optimized condition produced full-carbon indano[60]fullerene (**5a**, FIF) with a yield of 93% (Table 4.2.3, Entry 4).

**Table 4.2.3.** Optimization for reaction conditions for **5a**<sup>a</sup>.



Entry	CuBr <sub>2</sub> (eq.)	Temp. (°C)	Time (h)	Yield (%) <sup>b</sup>
1	0	100	3.0	—
2	2.0	25	3.0	N.R. <sup>c</sup>
3	2.0	100	3.0	70
<b>4</b>	<b>4.0</b>	<b>100</b>	<b>3.0</b>	<b>93</b>
5	6.0	100	3.0	82
6	4.0	80	3.0	66
7	4.0	120	3.0	88
8	4.0	100	2.0	75
9	4.0	100	4.0	76
10 <sup>d</sup>	4.0	100	3.0	91

<sup>a</sup> Unless otherwise specified, all reactions were performed with 0.03 mmol of **4a** and CuBr<sub>2</sub> in 5.0 mL of *o*-DCB under an argon atmosphere. <sup>b</sup> Isolated yield. <sup>c</sup> No reaction (N.R.). <sup>d</sup> Under an argon atmosphere.

#### 4.2.4 Substrate scope of FIFs

With the optimized reaction conditions in hand, the reaction scope was further explored and summarized in Table 4.2.4. 4-methyl substituted FIFs (**5b**) was synthesized and isolated in a yield of 90% (Table 4.2.4, Entry 2). To investigate the electronegativity influence of the substituents on fullerenes, electron-donating 4-methoxyl- (MeO-) and electron-withdrawing 4-fluoro moiety- (F-) attached fullerene derivatives were synthesized. The correspondingly produced FIFs **5c** and **5d** gave yields of 86% and 73%, respectively (Table 4.2.4, Entry 3 and 4). Although fullerenes with electron-donating groups generally give good yields, the yield of **5c** was lower than that of the non-substituted substrate, **5a**. This can be attributed to the poor solubility of methoxy-substituted fullerene derivatives [152]. In addition, fullerene derivatives with long carbon chains as the R<sup>2</sup> functional groups were synthesized, because long carbon chains on fullerenes are known to enhance the solubility [153]. Hexyl substituted derivative (**5e**) and 2-ethylhexyl substituted FIFs (**5f**) were produced in yields of 56% and 41%, respectively (Table 4.2.4, Entry 5 and 6). Expectedly, **5e** and **5f** possessed high solubilities that they could be dissolved in *o*-DCB with saturated concentrations of 22.8 mg mL<sup>-1</sup> and 28.6 mg mL<sup>-1</sup> at room temperature, respectively. Notably, the fullerene-cation-mediated cyclo[60]fullerene synthetic protocol can be extended to produce 6-membered ring derivatives. The 6-membered ring fullerene derivative (**5g**) was synthesized for comparison and its yield was 89% (Table 1, Entry 7). It should be highlighted that the total synthesis of FIF starting from the pristine C<sub>60</sub> gives a scalable high yield of 87%, which significantly outweighs the production of commercially available PC<sub>61</sub>BM in 55% yield [42].

**Table 4.2.4.** Fullerene-cation-mediated intramolecular cyclization with versatile substrates<sup>a</sup>.

Reaction scheme: **4a-g**  $\xrightarrow[\text{100 } ^\circ\text{C, 3 h}]{\text{CuBr}_2 \text{ (4.0 eq.)}, \text{o-DCB (5.0 mL)}}$  **Fullerene-cation**  $\rightarrow$  **5a-g**

Entry	R <sub>1</sub>	R <sub>2</sub>	Products 5	Yield (%) <sup>b</sup>
1	H-	CH <sub>3</sub> -	 <b>5a</b>	93
2	CH <sub>3</sub> -	CH <sub>3</sub> -	 <b>5b</b>	90
3	CH <sub>3</sub> O-	CH <sub>3</sub> -	 <b>5c</b>	86
4	F-	CH <sub>3</sub> -	 <b>5d</b>	73
5	H-	CH <sub>3</sub> (CH <sub>2</sub> ) <sub>5</sub> -	 <b>5e</b>	56
6	H-	CH <sub>3</sub> (CH <sub>2</sub> ) <sub>3</sub> CHCH <sub>2</sub> - CH <sub>2</sub> CH <sub>3</sub>	 <b>5f</b>	41
7	H-	CH <sub>3</sub> -	 <b>5g</b>	89

<sup>a</sup> Unless otherwise specified, all reactions were performed with 0.03 mmol of **4a–g** and 0.12 mmol of CuBr<sub>2</sub> in 5.0 mL of *o*-DCB solution at 100 °C for 3.0 h under an ambient atmosphere. <sup>b</sup> Isolated yield.

#### 4.2.5 Mechanistic studies of fullerene-cation mediated synthesis

To gain further insights into the reaction mechanism, two control experiments were conducted to explore the fullerene-cation mediated intramolecular cyclization. When aryl[60]fullerenyl dimer **4a** was heated at 100 °C in the absence of CuBr<sub>2</sub>, the reaction produced insoluble fullerene aggregations instead of the target molecule **5a**. Similarly, when the reaction was conducted in the presence of CuBr<sub>2</sub> and 2,2,6,6-tetramethylpiperidine-1-oxyl (TEMPO), the latter of which is a radical scavenger, there was no trace of **5a**. These additional experiments conclusively demonstrate that the fullerene-cation-intermediate is generated by the oxidation of fullerenyl radical in the presence of Cu[II]. Therefore, a plausible mechanism is proposed as following (Figure 4.2.5): First, the radical intermediate **I** is generated through thermolysis upon heating aryl[60]fullerenyl dimers **4a–g**. Then, the radical intermediate **I** is further oxidized by Cu[II] to form the key aryl[60]fullerenyl cation **II**. Finally, **II** undergoes an intramolecular cyclization triggered by the bromide with loss of one proton, producing the target molecule FIFs **5a–g**.

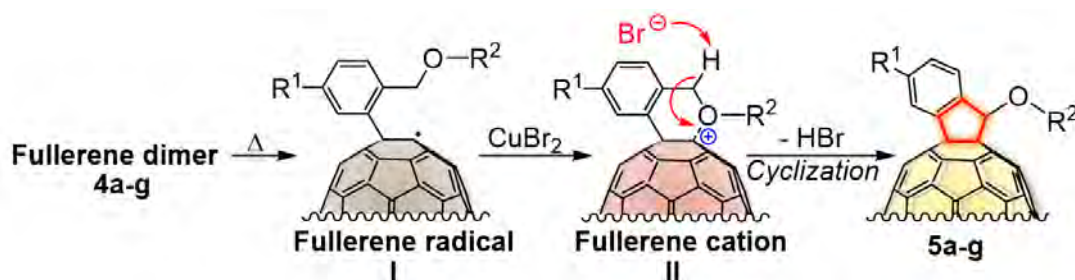


**Figure 4.2.5.** Mechanism of Cu[II]-promoted fullerene-cation-mediated synthesis for FIFs.

### 4.3 PSCs performance and electron mobility of FIFs

#### 4.3.1 Photovoltaic performance of FIFs applied PSCs

The normal planar PSCs with a structure of ITO/SnO<sub>2</sub>/Fullerenes/MAPbI<sub>3</sub>/Spiro-OMeTAD/Au were fabricated in this study (Figure 4.3.1.1). In this work, we applied FIFs as a passivation layer over-coating on SnO<sub>2</sub> to improve performance by 1) further increasing the electron-transport ability of metal oxides ETLs; 2) passivating the perovskite center to reduce the electron-trap site and facilitate the large-crystal growth of perovskite cell. As this chapter mainly focuses on how electron-transport ability influences the PSCs performance, the latter passivation effect will be discussed in the Chapter 5.

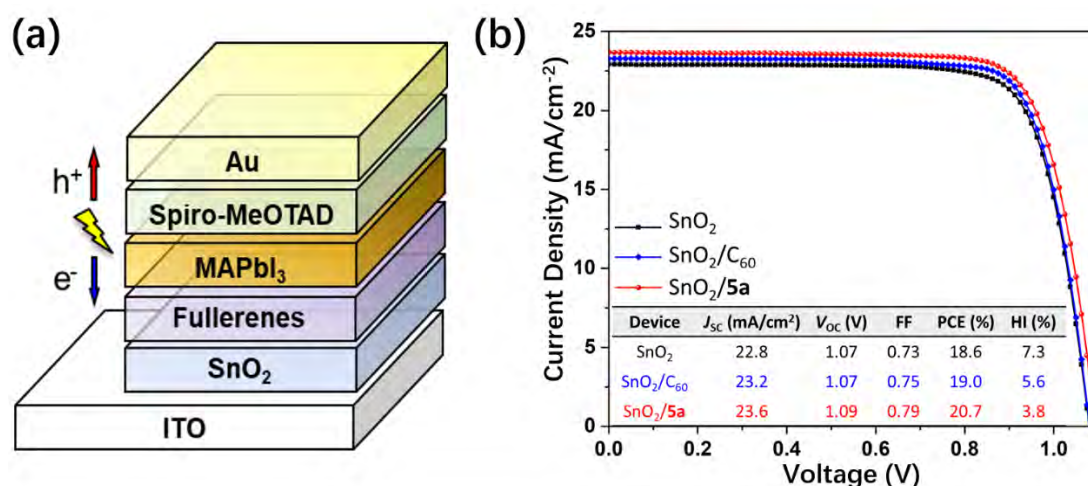


**Figure 4.3.1.1** (a) Illustration of a normal-type planar PSC structure in this study with fullerenes as passivation layers. (b)  $J$ - $V$  curves of the selected best-performing examples: control device on bare SnO<sub>2</sub> (black line), SnO<sub>2</sub>/C<sub>60</sub> (blue line) and SnO<sub>2</sub>/FIF **5a** (red line).

PSCs with FIF **5a** as the passivation layer showed the highest PCE of 20.7% with a  $J_{SC}$  of 23.8 mA cm<sup>-2</sup>, an  $V_{OC}$  of 1.09 V, and an FF of 0.79 (Figure 4.3.1.1b and Table 4.3.1.1: Entry 4). The PCE was significantly higher than those of the reference devices without fullerene (18.6%), with C<sub>60</sub> (19.0%), and PC<sub>61</sub>BM (16.5%) (Figure 4.3.1.1b; Table 4.3.1.1: Entry 1, 2, and 3). However, not all the cyclo[60]fullerene derivatives gave good performance. Spin-coating **5b** on SnO<sub>2</sub> resulted in poor film coverage (Table

4.3.1.1: Entry 5). In the case of **5c**, the fullerene could not be coated at all, due to the intrinsic low solubility as mentioned above. The **5d** film had a problem of being too hydrophobic, because of the attached F atom. As a result, perovskite films could not be coated uniformly on the fullerene layer (Table 4.3.1.1: Entry 6). Although **5e**- and **5f**-used devices exhibited high  $J_{SC}$  and  $V_{OC}$ , their FF values were also not as high as that of the **5a**-used devices. **5g** has a 6-membered-carbon-ring as opposed to the 5-membered-carbon-rings of other fullerene derivatives tested in this work. The device performance of the **5g**-based PSCs was not as high as the other fullerene-based perovskite solar cells (Table 4.3.1.1: Entry 9). Further, the cyclic voltammetry (CV) of **5g** showed an irreversible peak at its third redox potential, which suggests a possible cleavage of the 6-membered ring on **5g** under an operating condition. This points to the fact that cyclo[60]fullerenes with a 6-membered-ring are not feasible for the solar cell application, which is probably why there has not been a report on device application of cyclo[60]fullerenes with a 6-membered-ring.

**Table 4.3.1.1.** Photovoltaic parameters of the normal-type perovskite solar cells using fullerenes as the over-coating layer of ETL under 1 sun (AM 1.5 G, 100 mW cm<sup>-2</sup>). Average values with standard deviation are obtained from 20 devices in the same batch.

Entry	Fullerenes	$J_{SC}$ (mA cm <sup>-2</sup> )	$V_{OC}$ (V)	FF	$R_S$ ( $\Omega$ cm <sup>2</sup> )	$R_{SH}$ ( $\Omega$ cm <sup>2</sup> )	PCE <sub>best</sub>	PCE <sub>average</sub>	Hysteresis Index
1	–	22.8 ± 0.2	1.070 ± 0.004	0.73 ± 0.01	48.2	1.46x10 <sup>5</sup>	18.6%	18.1 ± 0.5%	0.073
2	C <sub>60</sub>	23.2 ± 0.3	1.070 ± 0.005	0.75 ± 0.02	34.2	7.58x10 <sup>5</sup>	19.0%	18.6 ± 0.4%	0.056
3	PC <sub>61</sub> BM	23.5 ± 0.3	1.040 ± 0.005	0.65 ± 0.01	44.1	5.21x10 <sup>5</sup>	16.5%	16.1 ± 0.3%	0.132
4	<b>5a</b>	<b>23.7 ± 0.2</b>	<b>1.089 ± 0.003</b>	<b>0.78 ± 0.01</b>	<b>29.7</b>	<b>8.03x10<sup>5</sup></b>	<b>20.7%</b>	<b>20.5 ± 0.2%</b>	<b>0.038</b>
5	<b>5b</b>	22.3 ± 0.3	1.064 ± 0.003	0.75 ± 0.01	46.9	1.09x10 <sup>5</sup>	18.5%	18.0 ± 0.5%	0.115
6	<b>5d</b>	22.8 ± 0.2	1.070 ± 0.004	0.71 ± 0.01	52.8	8.62x10 <sup>4</sup>	18.6%	18.1 ± 0.5%	0.114
7	<b>5e</b>	23.2 ± 0.3	1.074 ± 0.005	0.74 ± 0.01	32.8	1.38x10 <sup>5</sup>	18.7%	18.5 ± 0.2%	0.065
8	<b>5f</b>	23.6 ± 0.2	1.070 ± 0.004	0.73 ± 0.02	30.9	3.35x10 <sup>5</sup>	18.8%	18.4 ± 0.4%	0.067
9	<b>5g</b>	23.0 ± 0.2	1.058 ± 0.004	0.71 ± 0.02	53.2	2.65x10 <sup>5</sup>	17.6%	17.2 ± 0.4%	0.107

### 4.3.2 Energy levels of FIFs

As discussed in Chapter 1, the LUMO energy level of fullerenes leverages more influence on OSCs compared with PSCs. In PSCs, the electron-transport mobility is much more influential. Electron-transport consists of two steps, the first step is accepting the electrons produced from the active layer and then transferring electrons to next layer. Accordingly, fullerenes that designed for PSCs should be more considered about the electron-transport, rather than having high LUMO level by multi-addition on fullerenes. In order to illustrate this understanding, the CV then was conducted to evaluate the LUMO energy levels of produced FIFs (Figure 4.3.2).

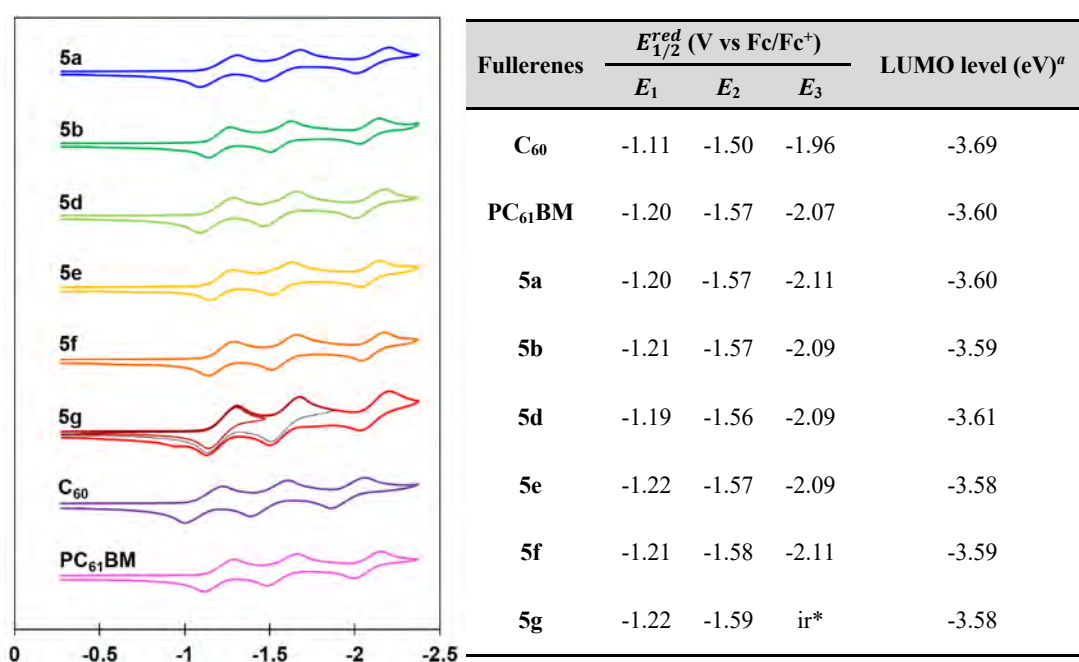


**Figure 4.3.2.** Potentials in eV vs a ferrocene/ferrocenium (Fc/Fc<sup>+</sup>) couple were recorded by cyclic voltammetry in *o*-DCB solution containing Bu<sub>4</sub>N<sup>+</sup>(CF<sub>3</sub>SO<sub>2</sub>)<sub>2</sub>N<sup>-</sup> (0.1 M) as supporting electrolyte at 25 °C with a scan rate of 0.05 V/s. Platinum disk, platinum wire, and Ag/Ag<sup>+</sup> electrodes were used as the working, counter, and reference electrodes, respectively. <sup>a</sup> Estimated LUMO levels using the following equation: LUMO level =  $-(4.8 + E_1)$  eV [154]. \* Irreversible wave.

According to the CV data, all FIFs possess comparable LUMO energy level



relative to PC<sub>61</sub>BM, which is a typical energy level for fullerene mono-adduct (Figure 4.3.2). Compared with pristine C<sub>60</sub>, all cyclo[60]fullerenes show a reasonably higher LUMO level and enlarged molecular size owing to the breaking down the conjugate system from 60- $\pi$  to 58- $\pi$  through mono-addition. The pristine C<sub>60</sub>, is the smallest molecule among fullerenes, demonstrates a lowest LUMO level but exceeds most fullerene derivatives applied in PSCs. Consequently, the higher LUMO energy level enabled by multi-addition strategy turns into ineffective when designing fullerenes for PSCs. Therefore, compared to pristine [60]fullerene, the smallest molecular size of fullerene derivatives is allowed by mono-addition. So, fullerene mono-adduct can perfectly match up the requirement of high enough electron-transport with versatile excellent properties such as good passivation and molecular packing state. Moreover, this result is in well accordance that FIF **5a** showed the best performance among other fullerenes.

In addition to the conjugated  $\pi$ -system of fullerenes, full-carbon cyclo[60]fullerene **5g** containing a 6-membered-ring unit shows an irreversible peak at its reductive wave, which demonstrates relatively poor electrochemical stability compared with FIFs or PC<sub>61</sub>BM. Consequently, such cyclo[60]fullerenes with a 6-membered-ring, such as MIF, ICBA failed to give a delighted results than PC<sub>61</sub>BM or FIFs.

Therefore, FIF successfully achieved the high-performance PSCs is not related to the LUMO energy level, is because of the small molecular size. Although the addition on fullerene inevitably increases the molecular size, which results in a decrease in electron-transport ability, the mono-addition can provide the possible passivation effect with the minimum sacrifice of electron-transport mobility.

### 4.3.3 Charge dynamics of FIF

In order to evaluate the electron mobilities of best-performed FIF **5a**, SCLC measurement using ETL only device structure is carried out to compare the electron mobilities of **5a** film and C<sub>60</sub> film, respectively (Figure 4.3.3 and Table 4.3.3). Expectedly, the **5a** film possesses a lower electron mobility ( $4.06 \times 10^{-6} \text{ cm}^2 \text{ Vs}^{-1}$ ) compared with C<sub>60</sub> ( $7.25 \times 10^{-6} \text{ cm}^2 \text{ Vs}^{-1}$ ), as **5a** has a smaller conjugated  $\pi$ -system compared with C<sub>60</sub> (Figure 4.3.3). Although C<sub>60</sub> shows much efficient electron-transport ability than FIFs, the strong passivation ability of FIF completely compensate the slightly decrease in electron-transport ability. Therefore, fullerene mono-adduct is the best stage to balance the electron-transport ability and other functions.

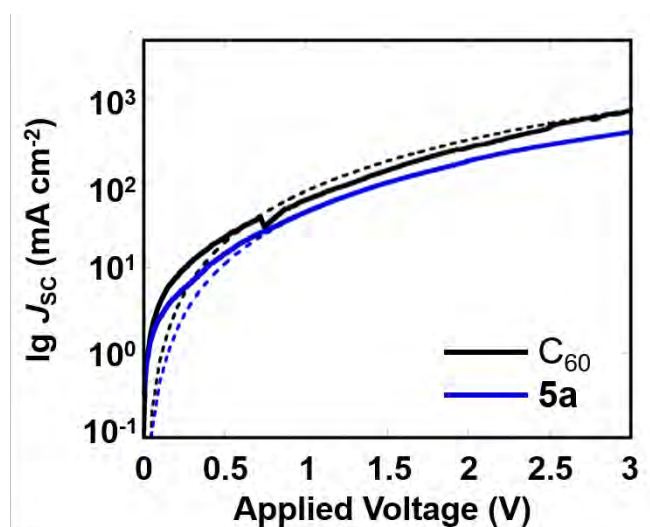


**Figure 4.3.3.** Electron mobility measurements based on space-charge limited current.

**Table 4.3.3.** Electron mobility of C<sub>60</sub> and **5a**.

Fullerenes	<i>R</i>	Electron mobility (cm <sup>2</sup> Vs <sup>-1</sup> )
C <sub>60</sub>	0.998	$7.254 \times 10^{-6}$
<b>5a</b>	0.999	$4.064 \times 10^{-6}$

#### 4.3.4 Hysteresis of FIF-applied PSCs

In order to evaluate device performance regarding the hysteresis, a mathematical equation is applied to quantitatively measure the degree of hysteresis as below:

$$\text{Hysteresis Index (HI)} = \frac{\int_{SC}^{OC} (J_{FS}(V) - J_{RS}(V)) dV}{\int_{SC}^{OC} J_{FS}(V) dV} \times 100\%$$

In equation,  $\int_{SC}^{OC} J_{FS}(V) dV$  and  $\int_{SC}^{OC} J_{RS}(V) dV$  stand for the area under  $J$ - $V$  curves measured from forward and reverse scans, respectively. Thus, a higher HI indicates more serious hysteresis (Figure 4.3.4). The control devices based on bare  $\text{SnO}_2$  indicates obvious hysteresis ( $\text{HI} = 7.3\%$ ). When **5a** is spin-coated on the top of  $\text{SnO}_2$ , the hysteresis is significantly reduced with a HI of 3.8%, which is mainly attributed to the high electron affinity of fullerenes that can reduce the charge recombination at the  $\text{SnO}_2$ /perovskite interface.

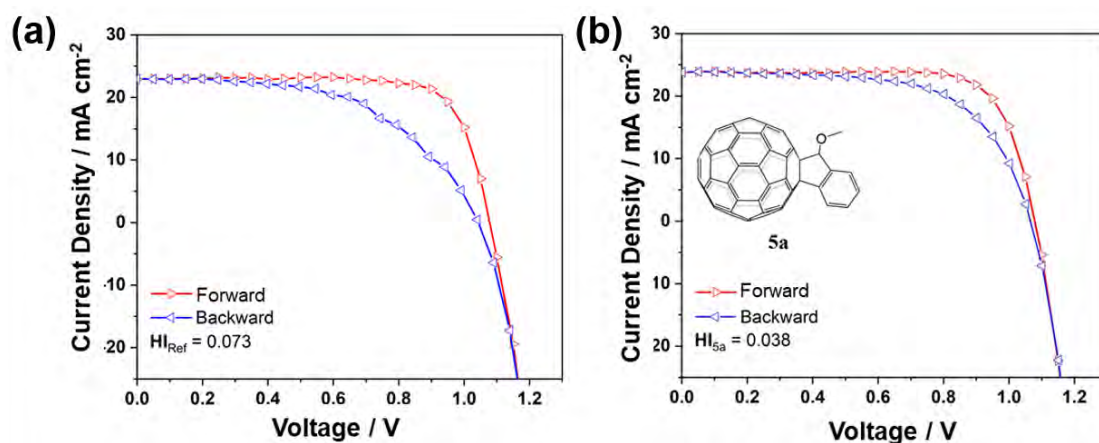


**Figure 4.3.4.**  $J$ - $V$  curves with hysteresis illustration of perovskite coated on (a) bare  $\text{SnO}_2$  and (b) on FIF **5a**/SnO<sub>2</sub>.

### 4.3.5 Computational studies of electron-transport ability of FIFs

The computational study was applied to further investigate the energy levels and bandgaps of FIFs. In all molecules, HOMO and LUMO are localized on the C<sub>60</sub> cage without appreciable density on the addends, indicating the fullerene cage plays a significant role in charge transport other than addends (Figure 4.3.5a). HOMO-5 and LUMO+7 that are closet in energy to frontier orbitals state with appreciable density on the addends, presenting significantly lower and higher in energy levels than HOMO and LUMO, respectively. Therefore, the addends can affect charge separation by their effect on packing and thereby on electronic coupling, which can also lead to shifts in HOMO/LUMO energy levels [155].

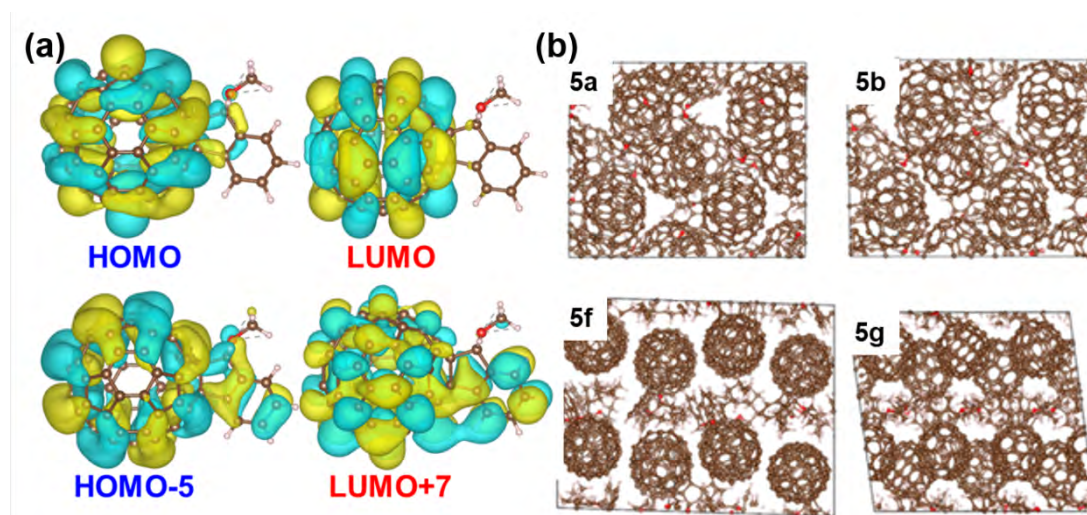


**Figure 4.3.5.** (a) Molecular orbitals of **5a** visualized by VESTA with isosurfaces at  $0.01 \text{ e}^{1/2} \text{ Å}^{-3}$ . (b) Solid state packing from molecular dynamic simulations.

As the thin fullerene passivation layer is applied in the device, the charge separation ability from the active layer is believed to play a significant role in the device performance. Therefore, a DFT computation was carried out to clarify the charge separation at the interface between fullerenes and perovskite by simulating the effective driving forces ( $\Delta G_{\text{sep}}$ ), and Marcus exponents for charge separation ( $\text{Exp}_{\text{sep}}$ ), respectively.  $\Delta G_{\text{sep}}$  can be approximated as the difference between the LUMO level of the fullerene and the CBM (conduction band maximum) of the perovskite. We used the

latest experimental electron affinity (EA) estimate of the methylammonium lead iodide to set  $E_{\text{CBM}} = -3.6$  eV and neglect reorganization of the perovskite which is small for inorganic semiconductors. To estimate  $\Delta G_{\text{sep}}$ , we adjusted the computed LUMO values by the difference between the experimental electron affinity (-4.3 eV) and computed LUMO (-3.68 eV) of  $\text{C}_{60}$ . As  $\Delta G_{\text{sep}}$  is negative and higher in magnitude than the reorganization energy ( $\lambda$ ), a larger  $\lambda$  value of **5a** is more favorable for charge separation at the interface than that of the other molecules. This is reflected in the values of the Marcus exponent  $\text{Exp}_{\text{sep}}$  of **5a** in  $4.3 \times 10^{-3}$ , which is 10 times larger than **5b**, and 100 times larger than **5f**, respectively (Table 4.3.5). Accordingly, the electronic coupling of **5a** with the perovskite is expected to be stronger than with the other molecules by the virtue of the smaller addends of **5a**, which conclusively demonstrate **5a** is advantageous from the charge separation perspective.

**Table 4.3.5.** Computed electrical parameters of FIFs.

Molecule	$\lambda$ (eV)	$\Delta G_{\text{sep}}$ (eV)	$\text{Exp}_{\text{sep}}$	$V$ (eV)	$\omega$ (s <sup>-1</sup> )
<b>5a</b>	0.186	-0.51	$4.3 \times 10^{-3}$	0.044	$5.7 \times 10^{10}$
<b>5b</b>	0.140	-0.49	$2.1 \times 10^{-4}$	0.030	$1.8 \times 10^{11}$
<b>5f</b>	0.143	-0.53	$4.0 \times 10^{-5}$	0.053	$5.0 \times 10^{11}$
<b>5g</b>	0.139	-0.54	$1.4 \times 10^{-5}$	0.045	$4.3 \times 10^{11}$

In addition, we also considered the effect of fullerene addends on charge transport within the fullerene film by assuming the hopping mechanism.  $\Delta G_t$  can be approximated from the difference in energies of occupied and unoccupied LUMO, which in turn can be approximated from the difference of redox potentials of neutral and anionic monomers:  $\Delta G_t = E_{\text{unoccLUMO}} - E_{\text{occLUMO}} \approx E_{\text{red}}^0 - E_{\text{red}}^{-1} \approx (E_0^{-1} - E_0^0) - (E_{-1}^{-1} - E_{-1}^0)$ , where  $E_{\text{unoccLUMO}}$  and  $E_{\text{occLUMO}}$  are energies of unoccupied and occupied LUMO,  $E_{\text{red}}^0$  and  $E_{\text{red}}^{-1}$  are reduction potentials of monomers at neutral and anionic geometries. As the reorganization energy  $\lambda$  is calculated as  $\lambda =$

$(E_0^{-1} - E_0^0) - (E_{-1}^{-1} - E_{-1}^0)$ , this estimate of  $\Delta G$  is equal to  $\lambda$ . Therefore, the equation can be simplified as:

$$\omega = \frac{V^2}{\hbar} \sqrt{\frac{\pi}{\lambda k_B T}} \exp \left[ -\frac{\lambda}{k_B T} \right]$$

The electronic coupling  $V$  is computed for dimers of closest molecular units. The mutual orientations of the molecules in the dimers were taken from solid state MD simulations. The solid-state packing obtained with MD is shown in Figure. 4.3.5b, which demonstrates that **5a** can form a better packing within the cell is consistent with our experimental results.

The estimates of electronic coupling between molecules and of resulting charge transport rates are also given in Table 4.3.5. The rates estimated by this model are higher than  $10^{10}$  for all selected molecules and can be considered sufficiently high; for example, experimental and computational estimates of the electron transport rate for the famous PCBM range  $10^9$ – $10^{12}$  s<sup>-1</sup>. The better solar cell performance with **5a** could, therefore, be rationalized from the ab initio perspective by improved charge separation while maintaining a high electron transport rate within the fullerene. We note that morphological and microstructural effects, not considered in the necessarily small-scale ab initio model, may also play a significant role.

## **4.4 Materials and methods**

### **4.4.1 Materials preparation**

Unless otherwise noted, all materials including dry solvents were obtained from commercial suppliers (Adamas-beta, TCI) and used without further purification. C<sub>60</sub> and PC<sub>61</sub>BM were purchased from American dye Inc. PbI<sub>2</sub> (99.9985%) and methylammonium iodide (MAI) was purchased from Sigma-Aldrich Inc. Anhydrous *N,N*-dimethylformamide (DMF), dimethyl sulfoxide (DMSO), *ortho*-dichlorobenzene (*o*-DCB), and chlorobenzene (CB) were purchased from Alfa Aesar. Spiro-MeOTAD was purchased from Luminescence Technology Corp. (Lumtec).

#### **4.4.1.1 SnO<sub>2</sub> precursor solution preparation**

27.1 mg SnCl<sub>2</sub>·2H<sub>2</sub>O (Aldrich, >99.995%) white powder was dissolved in 4.0 mL of anhydrous ethanol (TCI), which was filtered by 0.22 µm syringe filter before using.

#### **4.4.1.2 Fullerene solution preparation**

5.0 mg of fullerene, or FIFs was dissolved in 1.0 mL anhydrous *o*-DCB and then filtered by 0.22 µm syringe filter before using.

#### **4.4.1.3 MAPbI<sub>3</sub> precursor solution preparation**

355 mg of PbI<sub>2</sub>, 122 mg of CH<sub>3</sub>NH<sub>3</sub>I, and 54.7 µL of DMSO (molar ratio 1:1:1) were mixed in 490.5 µL of DMF solution at room temperature with stirring for 1 h. The solution was filtered through a 0.45 µm polytetrafluoroethylene filter prior to use.

#### **4.4.1.4 Spiro-MeOTAD solution preparation**

A solution was prepared by mixing 85.8 mg Spiro-MeOTAD, 19.3 µL of a stock solution of 520 mg mL<sup>-1</sup> lithium bis(trifluoromethylsulphonyl)-imide in anhydrous acetonitrile, and 33.8 µL of 4-*tert*-butylpyridine in 1.0 mL anhydrous chlorobenzene.

#### **4.4.2 Synthesis of full-carbon indano[60]fullerenes**

Unless otherwise noted, all reactions were performed with dry solvents under an atmosphere of argon in flame-dried glassware with standard vacuum-line techniques.

##### **4.4.2.1 Synthesis of aryl bromides (1a–g)**

MeOH (20.0 mL) was slowly added to sodium (517.5 mg, 22.5 mmol) at 0°C. After Na completely reacted with MeOH, different functionalized benzyl bromide (15 mmol) was added into the resulting solution at room temperature for 5 hours. Then, the resulting suspension was quenched by 10 mL H<sub>2</sub>O and extracted with CH<sub>2</sub>Cl<sub>2</sub> (10×3 mL). Combined organic layers were dried by MgSO<sub>4</sub>, and the solvent was removed under the reduced pressure to give a crude product. The further separation was carried on a silica gel column with n-hexane/ethyl acetate (10/1, v/v) as eluent, producing **1a–g** as a colorless oil.

##### **4.4.2.2 Synthesis of Grignard reagents (2a–g)**

An anhydrous tetrahydrofuran (THF) (10.0 mL) solution of aryl bromides **1a–g** (10 mmol) was slowly dropped into polished Mg powder (360.0 mg, 15 mmol) in a trace amount of I<sub>2</sub> as initiator under an argon atmosphere at 0 °C. After vigorously stirred 1 hour, the prepared Grignard solution (**2a–g**) was transferred by Schlenk operation and stocked in a Schlenk bottle. The concentration was confirmed before using through anhydrous titration by using menthol as titrant with a trace amount of 1,10-phenanthroline as indicator under an argon atmosphere.

##### **4.4.2.3 Synthesis of arylhydro[60]fullerenes (ArC<sub>60</sub>H, 3a–g)**

C<sub>60</sub> (300.0 mg, 0.417 mmol) was dissolved in anhydrous *o*-dichlorobenzene (*o*-DCB) (50.0 mL) containing 1,3-dimethyl-2-imidazolidinone (DMI) (1.4 mL, 12.5 mmol) as co-solvent. Then, previous synthesized Grignard reagent (**2a–g**) was added into the solution at 25 °C under an argon atmosphere. After stirring for 15 min, CH<sub>3</sub>COOH (0.1 mL, 1.75 mmol) was added to quench the reaction and then the solvent



was evaporated in *vacuo*. The residue was dissolved in CS<sub>2</sub> and purified through a silica gel column via CS<sub>2</sub>/CH<sub>2</sub>Cl<sub>2</sub> as the eluent to afford product **3a–g**.

#### 4.4.2.4 Synthesis of aryl[60]fullerenyl dimers (ArC<sub>60</sub>–C<sub>60</sub>Ar, **4a–g**)

Above synthesized monoadducts (**3a–g**) (0.048 mmol) was dissolved in 5.0 mL anhydrous *o*-DCB solution. Then, a solution of *t*-BuOK (58  $\mu$ L, 0.058 mmol, 1M) in THF was added and vigorously stirred at room temperature under an argon atmosphere for 15 min. Subsequently, *N*-bromosuccinimide (NBS) (34.2 mg, 0.192 mmol) was added. The reaction mixture was vigorously stirred for 12 hours at room temperature under the argon atmosphere. Then the resulting brownish suspension was quenched by 1.0 mL H<sub>2</sub>O and an excess amount of MeOH was added to precipitate the crude product. Finally, titled dimers (**4a–g**) were collected as a residue by filtration without necessities of further purifications.

#### 4.4.2.5 Synthesis of titled FIFs (**5a–g**)

0.030 mmol of dimers (**4a–g**) was dissolved in 10.0 mL of anhydrous *o*-DCB solution in the presence of CuBr<sub>2</sub> (26.8 mg, 0.120 mmol) as oxidant. After being vigorously stirred at 100 °C for 3 h, the resulting mixture was directly filtered through a silica gel plug to remove insoluble salt and then evaporated in *vacuo* to remove the solvent. Next, the residue was further separated on a silica gel column with CS<sub>2</sub> as eluent to afford products **5a–g**.

#### **4.4.2.6 Molecular characterization**

All NMR spectra were taken at 400 MHz (Bruker AVANCE III 400 spectrometer), 500 MHz (Bruker AVANCE III 500 spectrometer) or 600 MHz (Bruker AVANCE III 600 spectrometer). Unless otherwise specified, all the NMR spectra were recorded in parts per million (ppm, scale) with the proton of  $\text{CDCl}_3$  (7.260 ppm) or the proton of 1,1,2,2-tetrachloroethane- $d_2$  (TCE- $d_2$ ) (6.000 ppm) for  $^1\text{H}$  NMR and carbon of  $\text{CDCl}_3$  (77.16 ppm) or carbon of TCE- $d_2$  (73.78 ppm) for  $^{13}\text{C}$  NMR as internal reference, respectively. The data were presented as following order: chemical shift, multiplicity (s = singlet, d = doublet, t = triplet, hept = heptet, m = multiplet and/or multiplet resonances), coupling constant in hertz (Hz), and signal area integration in natural numbers, assignment (*italic*). High-resolution mass spectra (HRMS) were obtained by MALDI using a time-of-flight mass analyzer on a Bruker Ultra exTOF/TOF spectrometer. Potentials in V vs a ferrocene/ferrocenium ( $\text{Fc}/\text{Fc}^+$ ) couple were recorded by cyclic voltammetry in an *o*-DCB solution containing  $\text{Bu}_4\text{N}^+\text{CF}_3\text{SO}_2\text{N}^-$  (0.1 M) as supporting electrolyte at 25 °C with a scan rate of 0.05 V/s. Platinum disk, platinum wire, and  $\text{Ag}/\text{Ag}^+$  electrodes were used as the working, counter, and reference electrodes, respectively. The valence band and Fermi levels measurements were performed using Riken Keiki PYS-A AC-2 and Kelvin probe spectroscopy in the air (ESA), respectively.

### **4.4.3 Device fabrication and evaluation**

#### **4.4.3.1 Device fabrication of fullerene passivation layer applied PSCs**

Indium-doped tin oxide (ITO) patterned glass substrates were cleaned and sonicated with detergent, distilled water, acetone and isopropanol in an ultrasonic bath for 15 min, respectively. Next, the cleaned ITO substrates were treated with UV/O<sub>3</sub> for 15 min. Subsequently, 25  $\mu$ L of SnO<sub>2</sub> precursor solution was spin-coated on the cleaned ITO substrate at 3000 rpm for 30 s, which was annealed at 150 °C for 45 min. After cooling down to room temperature, the spin-coating process was repeated one more time followed by annealing at 180 °C for 1 h. Then, the SnO<sub>2</sub> coated ITO glass was further treated with UV/O<sub>3</sub> for 15 min before spin-coating of fullerene solution. 25  $\mu$ L of fullerene solution was spin-coated on the top of the SnO<sub>2</sub> layer at 4000 rpm for 30 s. Next, 25  $\mu$ L of perovskite precursor solution was spin-coated on the fullerene layer at 4000 rpm for 30 s, with slowly dropping 0.5 mL of anhydrous diethyl ether onto the substrate 10 s after the start of the spin-coating process, followed up with annealing at 100°C for 10 min. The hole transporting layer was spin-coated from the 20  $\mu$ L of Spiro-MeOTAD solution at 4000 rpm for 20 s. Finally, a 70-nm-thick of Au anode was fabricated by thermal deposition at a constant evaporation rate of 0.05 nm s<sup>-1</sup> under pressure of 10<sup>-6</sup> Torr.

#### **4.4.3.2 Photovoltaic characterization and measurement**

The current density vs voltage ( $J$ - $V$ ) characteristics were measured using a software-controlled source meter (Keithley 2400 SourceMeter) under dark conditions and the simulated sunlight irradiation of 1 sun (AM 1.5G; 100 mW cm<sup>-2</sup>) using a solar simulator (EMS-35AAA, Ushio Spax Inc.) with an Ushio Xe short arc lamp 500. The source meter was calibrated using a silicon diode (BS-520BK, Bunkokeiki). When evaluating, devices were masked with a black aperture to set the active area of the device to 0.1 cm<sup>2</sup>. Shimadzu IRAffinity-1s was used for the Fourier transform infrared spectroscopy (FT-IR) measurement. external quantum efficiency (EQE) spectra were measured using machine spectrometer with a wavelength ranging from 300 nm to 850

nm. Steady-state PL spectra were measured using a photoluminescence (PL) spectrometer (JASCO Spectrofluorometer FP-8300) with Xenon as the excitation source (excitation at 560 nm). The detected emission wavelength of the steady-state PL was from 675 nm to 875 nm. The water contact angle measurements were performed using a contact angle meter (DMo-501, Kyowa Interface Science Co., Ltd.). Scanning electron microscopy (SEM) measurements were carried out on an S-4800 scanning electron microscopy (Hitachi).

#### **4.4.3.3 Space-charge-limited current (SCLC) measurement**

The structure of the ETL-only device was ITO/Fullerenes(30 nm)/Al(80 nm). The mobility was determined by fitting the dark current to a model of a single-carrier SCLC, which is described by the equation,  $J_{\text{SCLC}} = 9\varepsilon_0\varepsilon_r\mu V^2/8L^3$ , where  $J_{\text{SCLC}}$  is the current density,  $\mu$  is the mobility,  $\varepsilon_0$  is the permittivity of free space,  $\varepsilon_r$  is the relative permittivity of the material,  $L$  is the thickness of the fullerenes layer, and  $V$  is the effective voltage. The thicknesses of the fullerene layer were measured using cross-sectional SEM images. Over-coating fullerene on SnO<sub>2</sub> ETL layers failed to give mobility data that can differentiate between the samples, due to the low thickness of the over-coating fullerene layers. Therefore, we measured a single layer of fullerene by using CS<sub>2</sub> (25 mg mL<sup>-1</sup>) as the solvent. The experimental dark current density was measured under an applied voltage swept from 0 to -5 V.

## 4.5 Summary

In summary, this work proposed a new synthetic strategy for cyclo[60]fullerenes with full-carbon ring unit through fullerene cation intermediates, which give by far greater yields than the conventional approach. We revealed the mechanism of how the *in situ* aryl[60]fullerene cations function as intermediates that enhance the selectivity of the reaction and enables a broad substrate scope. Using the new synthetic method, various designs of full-carbon indano[60]fullerenes (FIFs) were synthesized. Their device application as the passivation layer over-coating on the top of inorganic metal oxide ETLs in perovskite solar cells was demonstrated as well, which resulted in the extremely high PCE compared with the values reported in the literatures. In this section, we conclude that the design of fullerene derivatives using in PSCs should balance the electron-transport ability with other potential properties such as reorganization energy, and ability to passivate. Accordingly, fullerene derivatives with the mono-addition pattern exhibited its excellent application in PSCs compared with multi-adducts that mostly applied in OSCs. Moreover, passivation strategy that designed for applying the fullerene materials to PSCs show strong potential than single fullerene layer in PSCs, which will be detailed in the next chapter. Herein, this chapter mainly discussed how to balance a sacrifice in molecular size of fullerenes for having more efficient performance with good enough electron-transport ability.



## **Chapter 5.**

# **Passivation effect of fullerenes**

### **5.1 Research background**

In all kinds of photovoltaics, the performance mainly relies on the active layer, which is the core engine for generating the excitons. Although recently boosted development of PSCs successfully affording impressively excellent performances, the severe issues such as hysteresis [156], short longevity [157], unwanted charge recombination [158] sadly limit their practical use in real photovoltaic industry. Thanks to intensive studies attempted to solve those issues, the reason has now been clearly attributed to the surface defects that existed in the perovskite layer. Owing to the charge recombination at the defects of perovskite, the  $V_{oc}$  got significantly undermined. Moreover, as the perovskite layer is universally fabricated through the solution-processed strategy, the perovskite layer is much more likely to possess substantial disorders, including crystallographic defects and grain boundary defects. Therefore, many materials that containing the Lewis base structure such as carbonyl derivatives, amino derivatives *etc.* have been widely applied to passivate these defects to achieve an improved performance. In general, for all materials that designed for effectively passivating the perovskite, they usually are applied through two major methods. One is to position a single passivation layer underneath/above the perovskite layer to specifically passivate the bottom/top interface of perovskite layer; The other is to dope the perovskite layer by a trace amount (*ca.* 1.0 wt%) of materials, which aims to passivate the perovskite at their grain boundary. Technically speaking, despite the doping strategy is much easier to utilize compared with the fabricating the passivation layer, the doping strategy commonly encountered with the low reproducibility.

Consequently, single passivation layer method currently attracts more attentions, which demonstrates high reproducibility and extremely promising results. Notably, most materials that applied for passivating the perovskite are derived from the organic small molecules that possessing the Lewis base structure. There are few examples that demonstrating fullerene materials that designed for passivating the perovskite to improve the performance.

Herein, this chapter designed two fullerene materials that applying for the passivation of perovskite layer to improve the performance. One is the previously mentioned FIFs that applied as a single passivation layer for efficiently passivating the perovskite layer to reduce the hysteresis with all photovoltaic parameters significantly promoted, which afforded an excellent PCE in 20.7% with highly reproducible. However, fullerene materials were seldom applied as dopants inside a perovskite layer, which is due mainly to low solubility of fullerenes in polar solvent such as DMF, DMSO. To our delight, the developed fullerene-cation chemistry can also achieve the amino[60]fullerene derivatives, which allow fullerene dopant that using in perovskite layer to passivate the defects at the grain boundary. Therefore, in this chapter, the design principle and related performance that promoted by passivation will be deeply discuss and so that give a better understanding for designing a good fullerene material that applied for effectively passivating perovskite center.

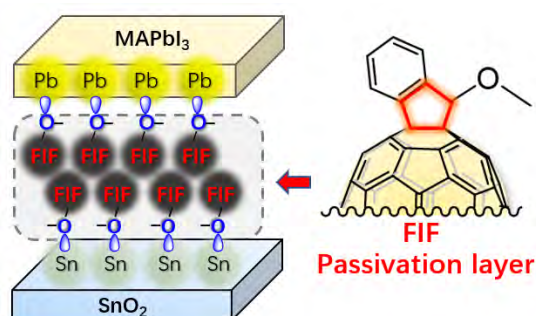


**Figure 5.1.** Molecular structure of FIF and the schematic mechanism of methoxy passivation.



## 5.2 FIFs as passivation layer in PSCs

Although introducing the Lewis base functional groups onto the cage of fullerene inevitably decreases the conjugated  $\pi$ -system, the obtained fullerene materials still can give excellent performance if the balance of electron-transport ability and passivation effect can be perfectly controlled. Accordingly, as discussed in Chapter 4, although FIFs indicated a lower electron-transport ability than pristine C<sub>60</sub>, it still exhibited excellent performance with PCE over than 20%, which was benefited from the excellent passivation effect provided by the ether group in FIFs other than its electron-transport ability. Considered that single fullerene layer can afford much reliable performance, the fullerene passivation layer was thusly positioned underneath the perovskite layer to promote the overall performance of PSCs. In this section, the mechanism how fullerene passivation work will be deeply discussed.

### 5.2.1 Influence of molecular hindrance

Comparing the performance of FIF **5a** and **5f** applied as passivation layer in PSCs, the **5a**-applied PSCs exhibited much excellent performance than **5f**-applied PSCs despite the **5f** showed a much excellent solidity than **5a**. The undermined performance of **5f**-applied PSCs was mainly resulted from the decreased the  $V_{OC}$  and FF values, which clearly reflects the poor passivation effect of the FIF **5f**.

In order to investigate the passivation effect of the ether structure designed in FIF, (FT-IR) was carried out on the selected FIFs as representative examples. Owing to the passivation effect is produced through the coordinating interaction between the lone electron pair of ether and Pb [157] (Figure 5.2.1). FT-IR spectra depicted that the **5a** and **5f** with and without the presence of PbI<sub>2</sub>. Apparently, the  $\nu_{C-H}$  at 2918 cm<sup>-1</sup> and  $\nu_{C-O}$  at 1097 cm<sup>-1</sup> of **5a** depicts a red-shift in the presence of PbI<sub>2</sub> (Figure 5.2.1. a and c). However, the  $\nu_{C-H}$  and  $\nu_{C-O}$  of **5f** does not present any shift at the same window-scale (Figure 5.2.1. b and d), which is mainly attributed to the bulky substituent as 2-ethylhexyl in the **5f** hampers the oxygen to form a Lewis coordinate with the Pb<sup>2+</sup>.

Through the passivation effect, charge recombination can be effectively reduced. Therefore, **5a**-based PSCs give a much better performance than **5g**-based PSCs due to the passivation. Moreover, this result also gives an explanation that why few fullerenes with good solubility commonly failed to give a better performance than conventional less bulky molecules.

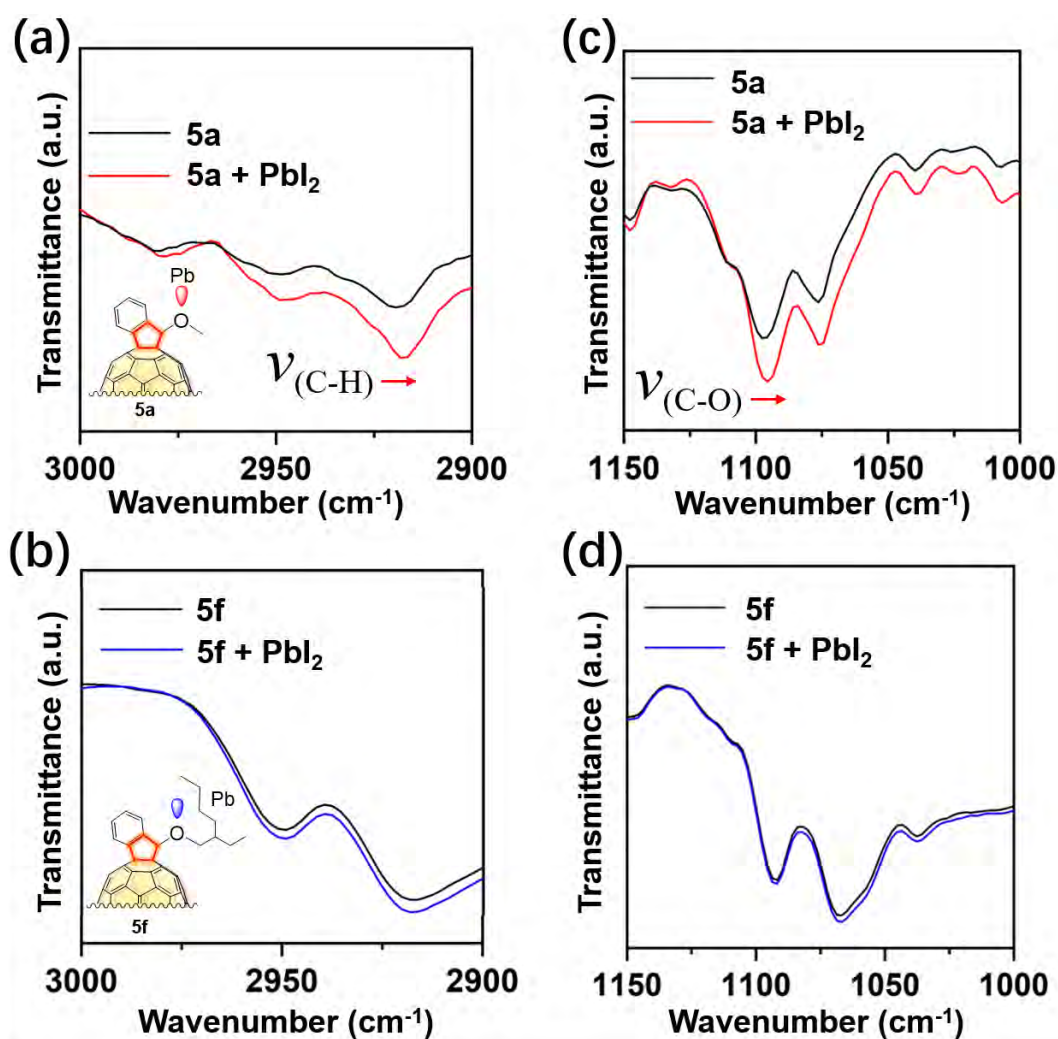


**Figure 5.2.1.** FTIR spectra of FIFs **5a** (red line) for (a)  $\nu_{(C-H)}$  and (c)  $\nu_{(C-O)}$ , **5f** (blue line) for (b)  $\nu_{(C-H)}$  and (d)  $\nu_{(C-O)}$  with and without the presence of PbI<sub>2</sub>.

### 5.2.2 Exciton quenching by passivation layer

The steady-state PL measurements are employed to investigate the charge extraction at the electron selective interface (Figure 5.2.2) The neat MAPbI<sub>3</sub> film exhibits the highest PL intensity with the PL peak at 775 nm. For the SnO<sub>2</sub>/MAPbI<sub>3</sub> film, a significant PL quenching of 52% is observed, which indicates the efficient electron extraction from the perovskite to the SnO<sub>2</sub> ETL. A further quenching (61%) is observed for the SnO<sub>2</sub>/C<sub>60</sub>/MAPbI<sub>3</sub> film with blue-shifted slightly, which is mainly attributed to the passivation of the trap states between MAPbI<sub>3</sub> and C<sub>60</sub>. A further quenching (75%) is observed for the SnO<sub>2</sub>/**5a**/MAPbI<sub>3</sub> film, which is mainly owing to smaller energy offset, provided by a higher LUMO level as previously mentioned, for the easy charge transfer. Meanwhile, the PL peak of this film is significantly further blue-shifted compared with C<sub>60</sub>-based MAPbI<sub>3</sub> film, indicating a strong passivation effect that **5a** gives. It should be mentioned that the full width at half-maximum (FWHM) is narrower for SnO<sub>2</sub>/**5a**/MAPbI<sub>3</sub> relate to that for SnO<sub>2</sub>/C<sub>60</sub>/MAPbI<sub>3</sub>, which demonstrates a reduction in the shallow trap density at the interface. Accordingly, the alkoxy group and small size of **5a** definitely demonstrate excellent passivation ability towards PSCs.

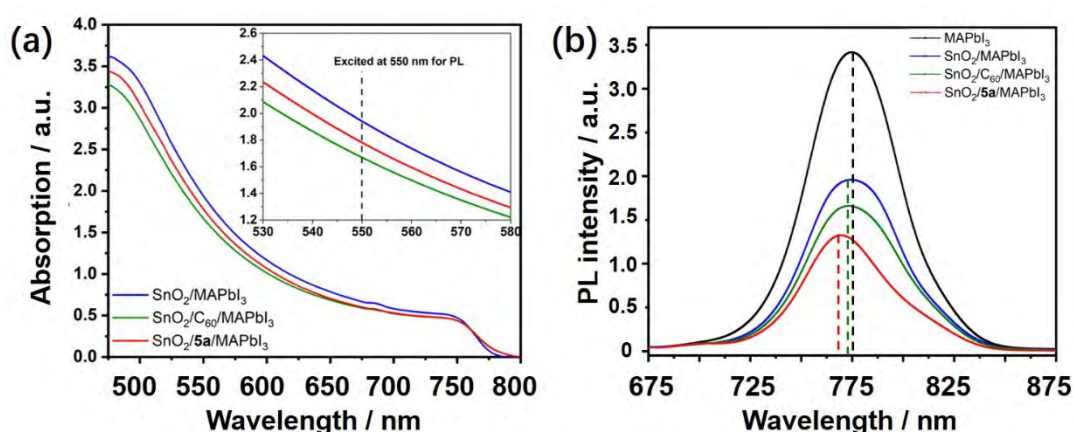


**Figure 5.2.2.** (a) UV-Vis spectra of glass/SnO<sub>2</sub>/MAPbI<sub>3</sub> (blue), glass/SnO<sub>2</sub>/C<sub>60</sub>/MAPbI<sub>3</sub> (green), glass/SnO<sub>2</sub>/**5a**/MAPbI<sub>3</sub> (red); (b) Steady-state PL spectra of glass/MAPbI<sub>3</sub> (black), glass/SnO<sub>2</sub>/MAPbI<sub>3</sub> (blue), glass/SnO<sub>2</sub>/C<sub>60</sub>/MAPbI<sub>3</sub> (green), and glass/SnO<sub>2</sub>/**5a**/MAPbI<sub>3</sub> (red) excited by a light source with a wavelength of 550 nm.

### 5.2.3 Film quality of perovskite layer

In order to have the investigation on the perovskite film quality, the water contact angles were carried out to demonstrate how the hydrophobicity influences the film formation (Figure 5.2.3). As the perovskite precursor solution is dissolved by using DMF as a solvent, the DMF is thusly applied in the water contact angles measurement. The contact angles of DMF on the  $C_{60}/SnO_2$ ,  $PC_{61}BM/SnO_2$ , and FIF **5a**/ $SnO_2$ , are measured to be  $69.8^\circ$ ,  $76.7^\circ$ , and  $67.4^\circ$ , respectively (Figure 5.2.3.a). Although pristine fullerene generally is hydrophobic, through the ether modification, the polarity of the molecule is increased and the methoxy group can effectively form a coordinate with both upper perovskite layer and down  $SnO_2$  ETL layer so that it provides a good interfacial surface for depositing the perovskite. Therefore, **5a** shows an intact coverage on  $SnO_2$  and provides a uniform perovskite film deposition (Figure 5.2.3. b and c).

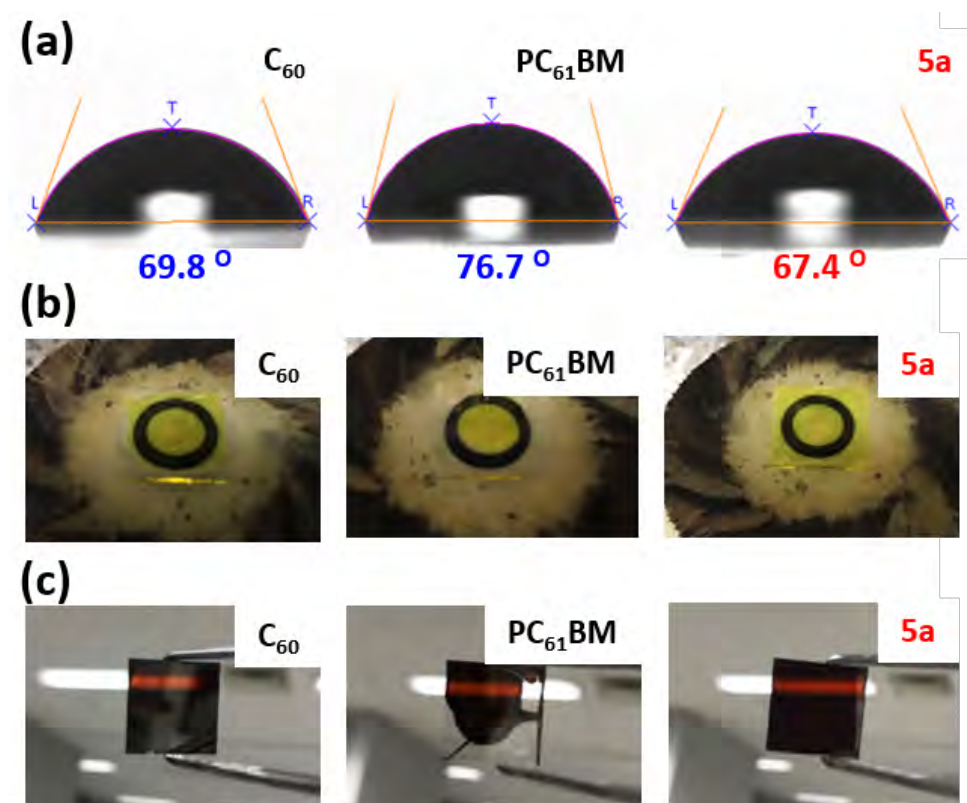


**Figure 5.2.3.** (a) Water contact angles of DMF on the  $C_{60}$ ,  $PC_{61}BM$ , FIF (**5a**), respectively. (b) Coverage images of corresponding fullerenes on the top of  $SnO_2$ . (c) The images of perovskite film on  $C_{60}$ ,  $PC_{61}BM$ , and FIF (**5a**), respectively.

#### 5.2.4 Large-size crystal growth of perovskite cell

Thanks to the hydrophilicity that passivation layer provided, the perovskite crystal can grow much smoothly with enlarged crystal size. Then, both the top-view SEM and cross-sectional images were taken to measure compare the average grain size of the perovskite coated on the  $\text{SnO}_2$  and **5a**/ $\text{SnO}_2$  substrates. Apparently, the average grain size of perovskite film on the **5a**/ $\text{SnO}_2$  is larger than that of the  $\text{SnO}_2$ , indicating that the grain boundary during grain growth can be enhanced by **5a** which benefits a larger grain size in the perovskite film (Figure 5.2.4.1). Notably, there is no void existed in the perovskite film deposited on **5a**, which can also explain a higher FF of **5a**-used PSCs. It can be deduced that the passivation effect of **5a** retarded the crystal growth, which is also reflected by the higher  $J_{\text{SC}}$  value of the **5a**-based devices compared with the reference.

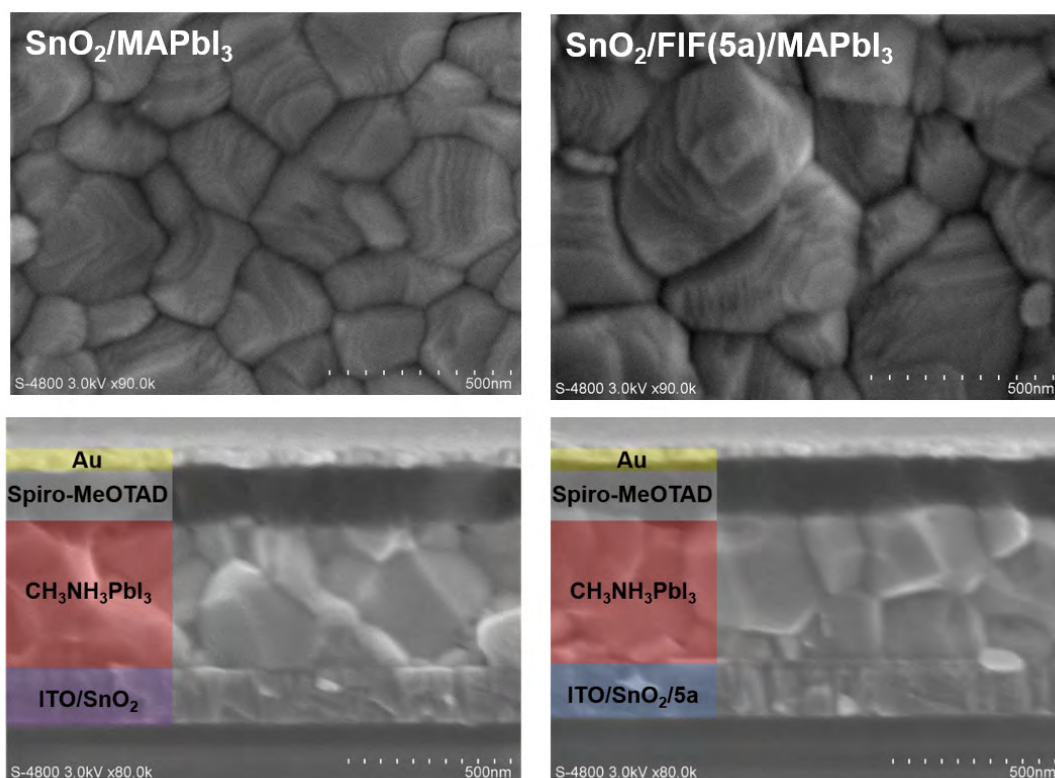


**Figure 5.2.4.1.** Top-view and cross-sectional SEM images of the perovskite films on **5a**-passivated and bare  $\text{SnO}_2$  substrates.

To ascertain this, XRD was conducted (Figure 5.2.4.2 and Table 5.2.4.1). The



tetragonal phase of perovskite films was depicted with a dominant peak (110) at  $14.0^\circ$ . The full-width at half-maximum (FWHM) of the (110) peaks was calculated through the Debye-Scherrer equation to estimate the crystal grain size [159]. The bare  $\text{SnO}_2/\text{MAPbI}_3$  film, the  $\text{SnO}_2/\text{C}_{60}/\text{MAPbI}_3$  film, and the  $\text{SnO}_2/\mathbf{5a}/\text{MAPbI}_3$  film showed (110) peaks with FWHM values of 0.467, 0.463, and 0.419, respectively, indicating that the crystal grain size of the  $\text{SnO}_2/\mathbf{5a}/\text{MAPbI}_3$  films is the largest. Moreover, the intensity ratio of the (110) peak to the (220) peak demonstrates the growth of the (110)-oriented grains, which indicates the favorable hole injection from the perovskite to hole-transporting layer [160]. The perovskite film on a  $\text{SnO}_2/\mathbf{5a}$  film presented the greatest ratio of 1.78 compared with 1.63 and 1.67 of the perovskite films on  $\text{SnO}_2$  and  $\text{SnO}_2/\text{C}_{60}$ , respectively.

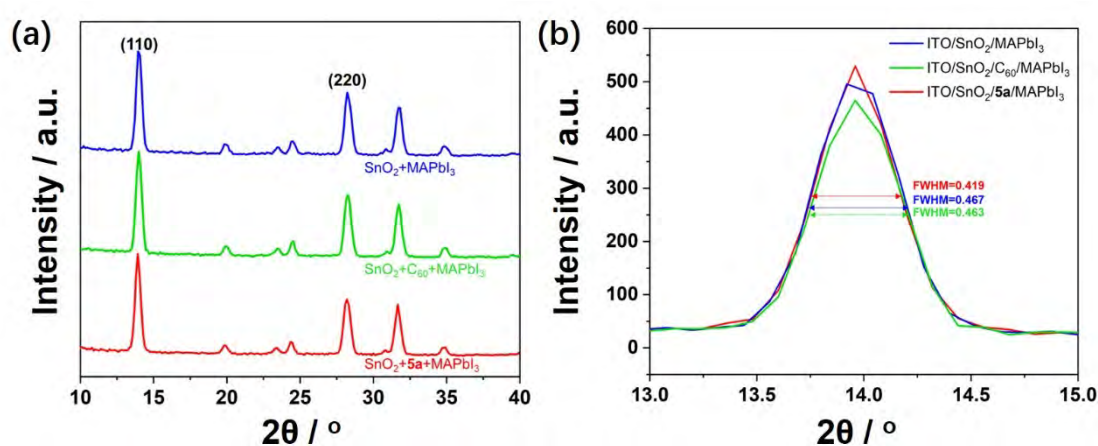


**Figure 5.2.4.2.** (a) XRD spectra of the reference  $\text{ITO}/\text{SnO}_2/\text{MAPbI}_3$  (blue),  $\text{ITO}/\text{SnO}_2/\text{C}_{60}/\text{MAPbI}_3$  (green),  $\text{ITO}/\text{SnO}_2/\mathbf{5a}/\text{MAPbI}_3$  (red). (b) (110) Peak showing the FWHM trend.

**Table 5.2.4.1.** XRD peak characterization and information.

Sample	Peak	Position ( $^\circ$ )	Intensity	Peak Area	FWHM	Peak Ratio
$\text{ITO}/\text{SnO}_2/\text{MAPbI}_3$	<110>	14.0	495.96	228.18	0.467	1.63
	<220>	28.2	303.62	160.18	0.541	
$\text{ITO}/\text{SnO}_2/\text{C}_{60}/\text{MAPbI}_3$	<110>	14.0	465.11	201.31	0.463	1.67
	<220>	28.2	279.16	146.26	0.541	
$\text{ITO}/\text{SnO}_2/\mathbf{5a}/\text{MAPbI}_3$	<110>	14.0	529.62	214.63	0.419	1.78
	<220>	28.2	296.73	157.16	0.559	

### 5.2.5 Trap density and trap-filling limit voltage

Trap density ( $n_t$ ) and trap-filling limit voltage ( $V_{TFL}$ ) were measured based on SCLC using charge carrier only devices with a structure of ITO/SnO<sub>2</sub>(30 nm)/Fullerenes(5 nm)/MAPbI<sub>3</sub>(400 nm)/PC<sub>61</sub>BM(30 nm)/Au(60 nm) (Figure 5.2.5). The  $n_t$  and  $V_{TFL}$  values are calculated from the equation,  $V_{TFL} = n_t e d^2 / 2 \epsilon_0 \epsilon_r$ , where  $e$  is electric charge ( $1.602 \times 10^{-19}$  V/m),  $d$  is thickness of the active layer,  $\epsilon_0$  is the vacuum permittivity ( $8.85 \times 10^{-14}$  F/cm) and  $\epsilon_r$  is the relative dielectric constant taken as 46.9. The experimental dark current density was measured under an applied voltage swept from 0 to -5 V. The **5a**- applied device showed lower  $V_{TFL}$  (0.31 V) and  $n_t$  ( $1.00 \times 10^{16}$  cm<sup>-3</sup>) compared with  $V_{TFL}$  (0.47 V) and  $n_t$  ( $1.52 \times 10^{16}$  cm<sup>-3</sup>) of the C<sub>60</sub>- applied device. Accordingly, the higher FF of the **5a**-based devices is not from the electron mobility, rather from the mentioned reduced surface trap-sites and the higher LUMO level of **5a**.

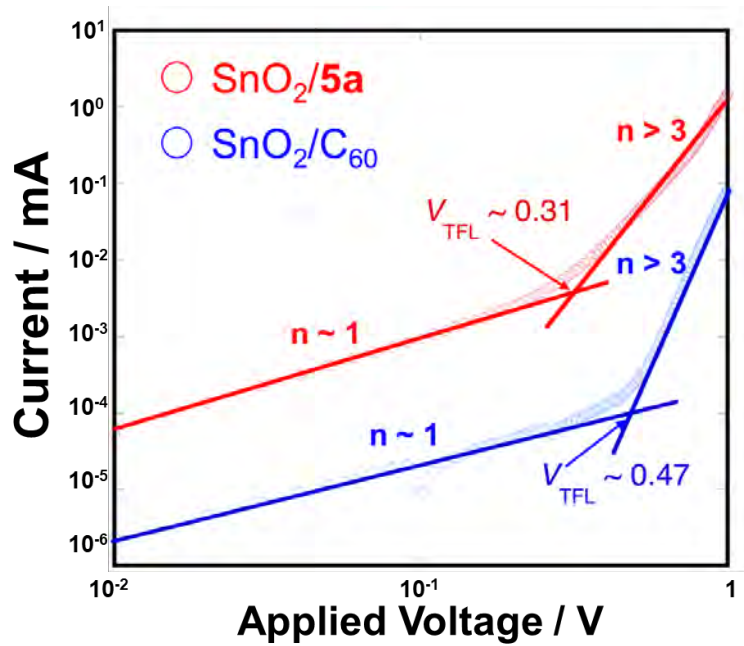


**Figure 5.2.5.** Trap density and trap-filling limit voltage measurement through SCLC curves.

### 5.2.6 Reproducibility of fullerene passivation layer applied PSCs

In order to have a reasonable evaluation of photovoltaic parameters, the statistical analyses were conducted from 20 devices in the same batch, which depicts that all devices were fabricated in high reproducibility (Figure 5.2.6). As vividly shown in the Figure, using fullerene as a single passivation layer demonstrate high reproducibility among all photovoltaic parameters.

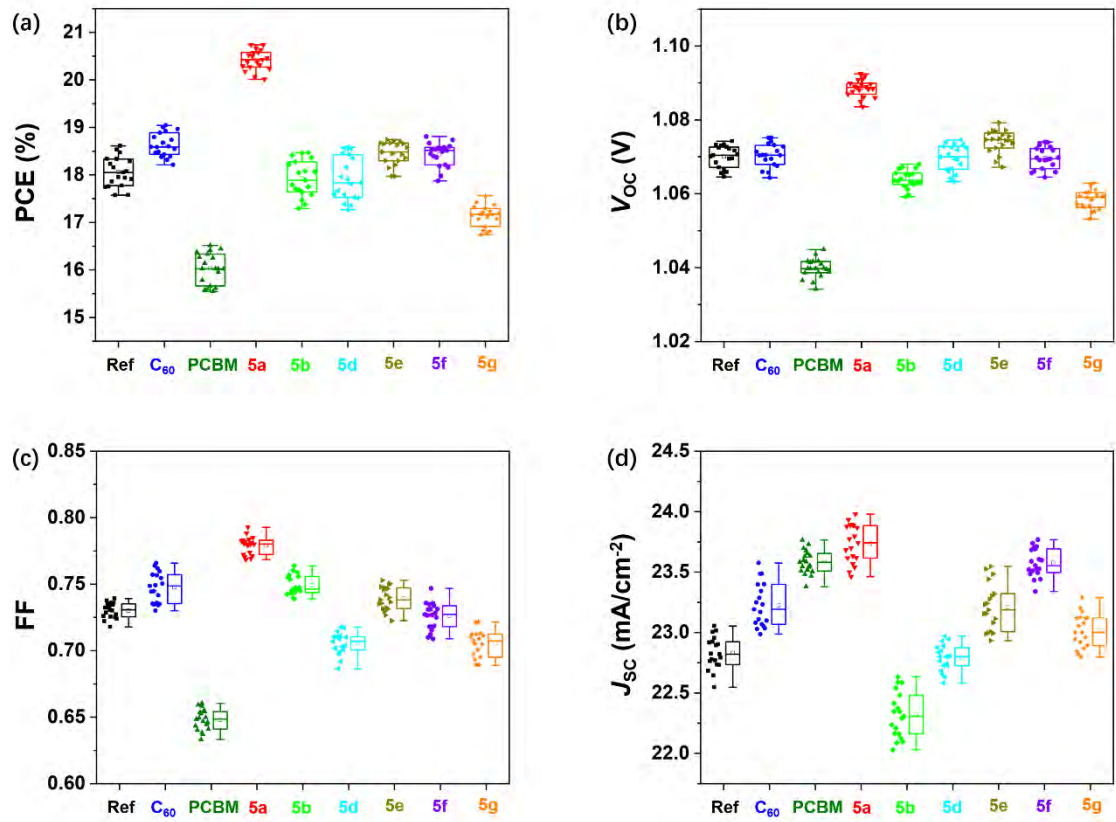


**Figure 5.2.6.** Statistical analyses and distribution of 20 devices in the same batch: (a) PCE, (b)  $V_{OC}$ , (c) FF, and (d)  $J_{SC}$ .



### 5.3 Amino[60]fullerene as passivation dopant in PSCs

Although small molecules containing the Lewis base structure such as hydroxyl (HO-), alkoxy (RO-), amino (NH<sub>2</sub>-) *etc.* have been applied as dopant for passivating the grain boundaries of perovskite crystal, the fullerene materials that having such potentials have never been reported. This issue mainly suffers from the inefficient synthesis of fullerene derivatives with such Lewis base structure. This section successfully synthesized the first amino[60]fullerenes through a fullerene-cation-mediated intermolecular coupling reaction. And then applied this amino[60]fullerene as a dopant inside perovskite layer to promote the performance. Although neither the performance or the reportability showed significant improvement compared with the single fullerene passivation layer applied PSCs, this work can serve as an example to demonstrate the possibility that using fullerene as dopant inside perovskite layer.

#### 5.3.1 Fullerene-cation-mediate synthesis of amino[60]fullerene

Aryl[60]fullerenyl cations ( $\text{ArC}_{60}^+$ ), which were generated by heating aryl[60]fullerenyl dimers ( $\text{ArC}_{60}\text{--C}_{60}\text{Ar}$ ) to generate aryl[60]fullerenyl radicals ( $\text{ArC}_{60}^\bullet$ ) followed by oxidation using Cu[II] salts ( $\text{Cu}(\text{BF}_4)_2(\text{aq.})$  or  $\text{CuBr}_2$ ), have extremely high reactivity as discussed in Chapter 4.2. This high reactivity is mainly initiated from the specific characteristics of their frontier orbitals. The abstraction of one electron from organofullerenyl anions to produce organofullerenyl radicals and the subsequent removal of one more electron to generate organofullerenyl cations can be regarded as abstraction of two electrons from the HOMO, which forms a new LUMO offering non-traditional reactivity for new fullerene modification reactions (Figure 5.3.1.1). Accordingly, the advantage of the present reaction is functional group and water tolerance due to the use of fullerenyl cation in-intermediates, which are not reactive toward them. Moreover, this reaction features novel reactivity of the newly generated LUMO of the fullerene cations toward aryl boronic acids bearing a partial negative charge. Therefore, the unprotected amino structure can be directly introduced even in

the presence of the H<sub>2</sub>O system.

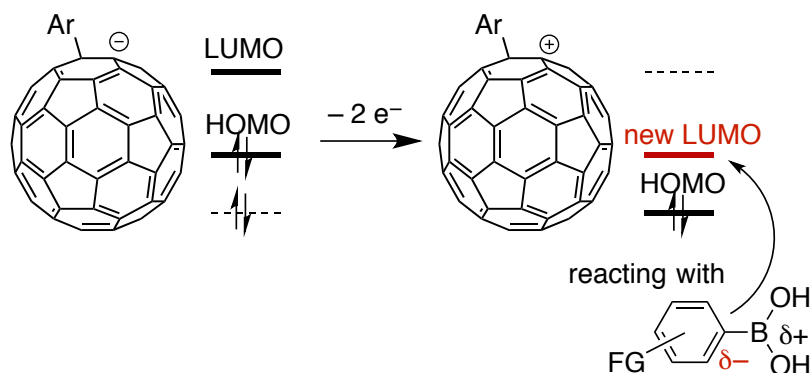


**Figure 5.3.1.1.** Fullerene-cation-mediated intermolecular coupling between fullerene-cation and weak nucleophiles.

With the optimal conditions in hand, the substrate scope was further investigated delightfully achieving high yields up to 93% with versatile functional groups (Figure 5.3.1.2). Notably, amino-group-functionalized boronic acid can directly react with the fullerenyl cation to produce amino[60]fullerene derivative in 50% and 53% yield in the presence of Cu(BF<sub>4</sub>)<sub>2</sub>(aq.) and CuBr<sub>2</sub>, respectively, without the use of protecting groups. It should be highlighted that this is the first fullerene derivative that have the unprotected amino group, which can be directly applied into perovskite precursor formation as the amino compounds are commonly used as cationic center in the perovskite center.

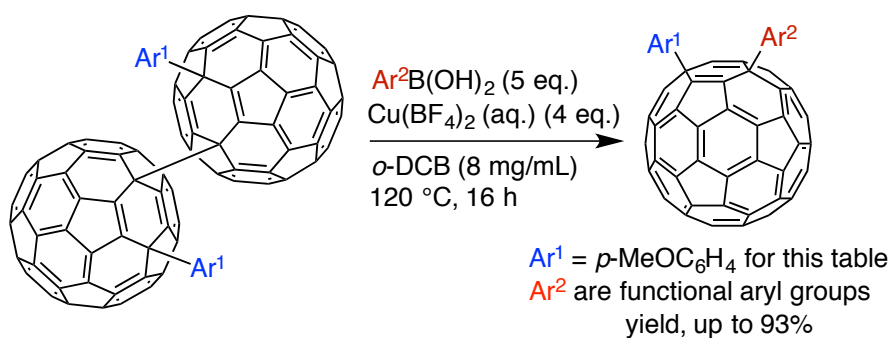


**Figure 5.3.1.1.** Fullerenyl-cation-mediated coupling reactions with functional aryl groups to obtain functionalized diaryl[60]fullerenes.

### 5.3.2 Amino[60]fullerene doped perovskite for PSCs

With the obtained amino[60]fullerene in hand, an inverted type PSC was fabricated to evaluate the performance of amino[60]fullerene dopant for perovskite. It has been reported that the amine group can interact with  $\text{CH}_3\text{NH}_3\text{PbI}_3$  to form a Lewis acid/base adduct, passivating trapping sites at grain boundaries. In addition, fullerene derivatives inside the photoactive layer are reported to enhance photovoltaic performance because of their intensive light-absorption among the visible light range. Therefore, the amino[60]fullerene can be effectively applied as a dopant inside perovskite layer. Expectedly, the PCE of control device increased from 12.7% to 13.5% upon addition of amino[60]fullerene, which is mainly contributed from the  $J_{\text{SC}}$  (Figure 5.3.2). However, this improvement was not as significant as previously reported fullerene single passivation layer applied in PSCs. This because of the dopant inside perovskite layer is much more difficult for providing an uniform growth of perovskite crystal.

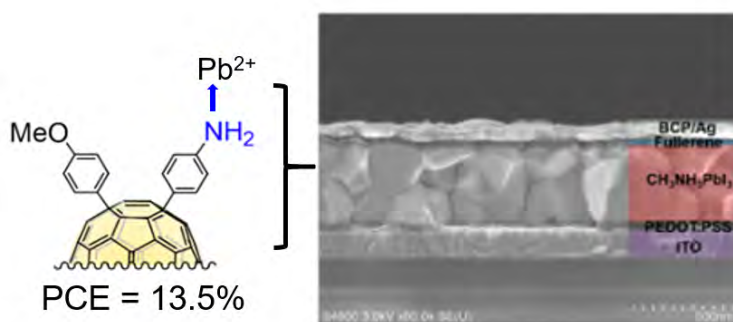


**Figure 5.3.2.** Amino[60]fullerene as an dopant for passivating the perovskite at grain boundaries.

Therefore, obtained fullerene derivatives with reactive functionalities are expected to be useful in various areas of research, such as energy-related studies, as shown in our demonstration of an amino-functionalized arylfullerene derivative as a dopant in a perovskite solar cell.

## 5.4 Materials and methods

### 5.4.1 Fullerene-cation-mediated synthesis of 1,4-diaryl[60]fullerenes

Unless otherwise noted, all materials including dry solvents were obtained from commercial suppliers and used without further purification. Unless otherwise noted, all reactions were performed with dry solvents under an atmosphere of argon in flame-dried glassware with standard vacuum-line techniques.

All NMR spectra were taken at 400 MHz (Bruker AVANCE III 400 spectrometer) or 600 MHz (Bruker AVANCE III 600 spectrometer). Unless otherwise specified, all the NMR spectra were recorded in parts per million (ppm, scale) with the proton of tetramethylsilane (TMS) (0.00 ppm) for  $^1\text{H}$  NMR and carbon of  $\text{CDCl}_3$  (77.16 ppm) or carbon of  $\text{TCE-}d_2$  (78.14 ppm) for  $^{13}\text{C}$  NMR as internal reference, respectively. The data were presented as following order: chemical shift, multiplicity (s = singlet, d = doublet, t = triplet, hept = heptet, m = multiplet and/or multiplet resonances), coupling constant in hertz (Hz), and signal area integration in natural numbers, assignment (*italic*). High-resolution mass spectra (HRMS) were obtained by MALDI using a time-of-flight mass analyzer on a Bruker Ultra exTOF/TOF spectrometer.

#### 5.4.1.1 Synthesis of organo(hydro)[60]fullerenes precursors

To a solution of  $\text{C}_{60}$  (100 mg, 0.139 mmol) in *ortho*-dichlorobenzene (*o*-DCB) (60 mL) containing anhydrous dimethyl sulfoxide (163 mg, 2.09 mmol) was added a tetrahydrofuran (THF) solution of different Grignard reagents ( $\text{Ar}^1\text{MgBr}$ ,  $\text{Ar}^1 = p\text{-CH}_3\text{OC}_6\text{H}_4$ ;  $= p\text{-}^t\text{BuC}_6\text{H}_4$ ) under the argon atmosphere at 25 °C. After vigorously stirring for 40 min, saturated aqueous  $\text{NH}_4\text{Cl}$  solution (0.1 mL) was added to quench the reaction for 1 hour at room temperature. The resulting dark red solution was filtrated through a pad of gel plug to remove the insoluble salts and then volatile components were removed under reduced pressure. The residue ( $\text{Ar}^1\text{C}_{60}\text{H}$ ,  $\text{Ar}^1 = p\text{-CH}_3\text{OC}_6\text{H}_4$ ) was further purified by a silica gel column with the  $\text{CS}_2$  as eluent, producing hydroaryl[60]fullerenes with an isolated yield of 73%. The residue ( $\text{Ar}^1\text{C}_{60}\text{H}$ ,  $\text{Ar}^1 = p\text{-}$

<sup>t</sup>BuC<sub>6</sub>H<sub>4</sub>) was further purified by a Buckyprep column with the toluene as eluent, producing hydroaryl[60]fullerenes with an isolated yield of 76%.

#### 5.4.1.2 Synthesis of aryl[60]fullerenyl dimers

To a solution of organo(hydro)[60]fullerenes precursors (Ar<sup>1</sup>C<sub>60</sub>H) (0.12 mmol, 1.0 eq.) in *o*-DCB (10 mL) was added a THF solution of *t*-BuOK (0.18 mmol, 1.5 eq., 1.0 mol/L) under the argon atmosphere at room temperature. After vigorously stirring for 20 min, I<sub>2</sub> (0.48 mmol, 4.0 eq.) was added under the argon atmosphere at room temperature for further 30 min. Later, the resulting mixture was quenched by 0.2 mL water, and then evaporated in vacuo to remove the volatile solvent. Finally, the residue was further separated on a silica gel column with CS<sub>2</sub> as the eluent to afford aryl[60]fullerenyl dimers in 58%. MALDI-TOF MS (+) for **2a** *m/z* calcd for C<sub>134</sub>H<sub>14</sub>O<sub>2</sub> [M<sub>1/2</sub>]<sup>+</sup>, 827.0, found 826.9; MALDI-TOF MS (+) for **2b** *m/z* calcd for C<sub>140</sub>H<sub>26</sub> [M<sub>1/2</sub>]<sup>+</sup>, 853.1, found 853.1.

#### 5.4.1.3 Synthesis of 1,4-diaryl[60]fullerenes

To a solution of aryl[60]fullerenyl dimer (Ar<sup>1</sup>C<sub>60</sub>–C<sub>60</sub>Ar<sup>1</sup>) (0.02 mmol, 1.0 eq.) in *o*-DCB (4 mL) was added aqueous Cu(BF<sub>4</sub>)<sub>2</sub> (0.08 mmol, 4.0 eq., 2.5 mol/L) or anhydrous CuBr<sub>2</sub> (0.08 mmol, 4.0 eq.) under the argon atmosphere. After stirring for 16 hours at 120 °C, the resulting mixture was filtrated through a silica gel plug to remove insoluble materials, and then evaporated in vacuo to remove the solvent. Finally, the residue was further separated on a silica gel column with CS<sub>2</sub>/CH<sub>2</sub>Cl<sub>2</sub> as eluent to afford 1,4-diaryl[60]fullerenes

#### **5.4.2 Fabrication procedures of inverted PSCs**

ITO substrates were cleaned with detergent, diluted water, and acetone and sonicated with isopropanol in an ultrasonic bath for 10 min, respectively. UV/O<sub>3</sub> was treated for 15 min prior to use. PEDOT:PSS (0.5 wt% of polyoxyethylene tridecyl ether in poly-(3,4-ethylenedioxythiophene)polystyrenesulfonic acid (PEDOT:PSS) dispersion in water) was spin coated at 3000 rpm for 30 s, which was followed by drying at 105 °C for 10 min. 355 mg of PbI<sub>2</sub>, 122 mg of CH<sub>3</sub>NH<sub>3</sub>I, and 54.7 μL of DMSO (molar ratio 1:1:1), and 1.0 mg of amino[60]fullerene (0.1 wt%) was mixed in 490.5 μL of DMF solution at room temperature with stirring for 1 h. The MAPbI<sub>3</sub> solution was spin-coated on the PEDOT:PSS layer at 4000 rpm for 30 s and 0.5 mL of diethyl ether was slowly dripped on the rotating substrate in 10 s before the surface changed to be turbid. The turbid film was followed by annealing at 100 °C for 10 min to obtain a dense MAPbI<sub>3</sub> film. The 30 nm C<sub>60</sub> film layer was thermally deposited on the perovskite film at a constant evaporation rate of 0.02 nm/s. Then, the 10 nm BCP layer was thermally deposited at a same evaporation rate. Device fabrication was finally completed by thermal evaporation of a 70-nm-thick film of Ag as the cathode.

## 5.5 Summary

In summary, this chapter deeply discusses how to design fullerene materials for effectively passivating the perovskite layer to improve the performance. Thanks to the fullerene-cation chemistry mediated synthesis, the fullerene can be installed with versatile Lewis base functional group such as alkoxy, amino. This chapter applied these synthesized fullerene materials by two main methodology as doping strategy and single fullerene passivation layer. When the FIF applied as fullerene passivation layer in PSCs, the performance significantly improved to a PCE of 20.7% with all photovoltaic parameters improved (Figure 5.5). However, the amino[60]fullerene doped perovskite did not exhibit significant improvement. The passivation effect can help perovskite grow with enlarged crystal size, and decrease the trap density at the interface. Moreover, this chapter found that when design fullerene passivation material, the less bulky moiety is much favorable because of the efficient coordination between Lewis base site and defect, yet the relatively poor solubility compared with long aliphatic chain substituted substrates.

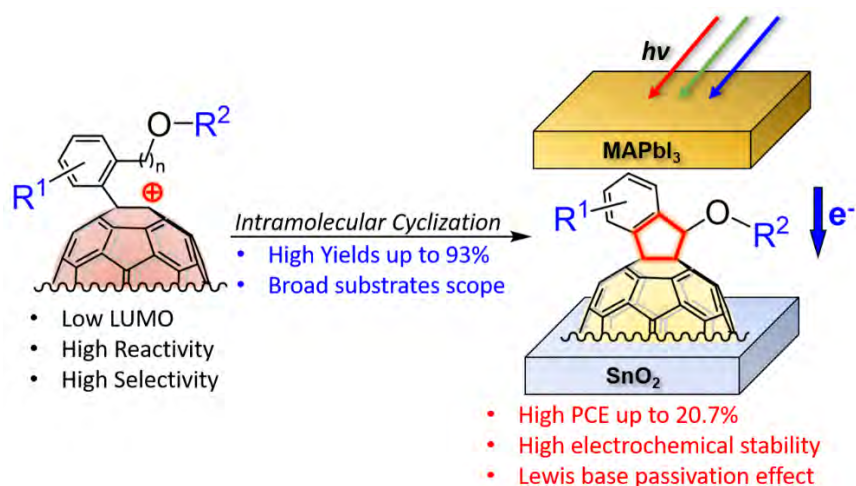


**Figure 5.5.** Graphic summary of FIF passivation layer using for high-performance PSCs.





## Chapter 6.

# Evaporable fullerene-fused ketone as ETL

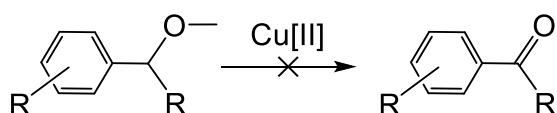
### 6.1 Research background

As discussed in the previous chapters, the key factors that influence the performance of fullerene applied PSCs are 1) the uniformly amorphous morphology; 2) enough high electron-transport ability by fullerene monoadduct; 3) good passivation effect allow by the Lewis base functional groups. Accordingly, it is easy to come up with an idea that if all above three aspects can be combined into one fullerene derivative, the designed fullerene is highly expected to exceed the current performance ceiling that fullerene applied PSCs. Although there are plenty of examples successfully combining the fullerene monoadduct with versatile Lewis base moiety, such fullerene materials immediately decomposed to pristine C<sub>60</sub> when processed by thermal deposition. Therefore, if the thermal stability of fullerene derivatives can be improved, the evaporable fullerene materials can be then achieved. According to the Bayer's strain theory, the five-membered ring should be the most stable ring structure as all carbon can match up with the orbital angle requirement of 109.3°. In addition, the homocyclic ring depicts a much strong stability than heterocyclic ring, which is directly related to the bond polarity. To our delight, the fullerene-cation-mediated synthesis can achieve this homocyclic ring structure with a five-membered ring. Although FIF indeed exhibited a much excellent thermal stability than PC<sub>61</sub>BM (3-membered-carbon ring) or cyclo[60]fullerenes with a 5-membered-hetero ring, it is still not stable enough to be processed by the thermal deposition process. Considered the carbon at benzene position of FIF is connected through a sp<sup>3</sup> orbital, the stable should be further increased if this sp<sup>3</sup> C can be converted to a sp<sup>2</sup> structure. Therefore, corresponding [60]fullerene-fused

ketones were then designed. However, there is no example that showing the direct conversion of the alkoyl to ketone structure, which thusly challenges the feasibility of the production of proposed fullerene-fused ketones (Figure 6.1.1.a). Notably, fullerene not only exhibits its excellent electrical property in photovoltaics, but it also presents its excellent superiors in electrochemistry.

Herein, this chapter utilizes the property that fullerene radical cation ( $C_{60}^{\bullet+}$ ) can be readily generated in the presence of metallic halides to fulfil the one-step oxidation of alkoxy to ketone. Accordingly, a highly efficient  $CuBr_2$  promoted one-step direct oxidation of alkoxy indano[60]fullerenes to [60]fullerene-fused ketones is showcased in this chapter (Figure 6.1.1.b). This chapter uncovers the new fullerene electrochemical property, namely electron-pool, for the direct oxidation: 1)  $C_{60}$  selectively transferred single electron to  $Cu[II]$  to afford  $C_{60}^{\bullet+}$ ; 2) generated  $C_{60}^{\bullet+}$  attracts electron density from the neighboring C–H bond, which is the key for initiating the direct oxidation of alkoxy. To our satisfactory, the obtained fullerene-fused ketones show expectedly high thermal stability, which was then investigated as the evaporable fullerene ETL in a normal type structure with promising high performance.

**(a) Previous Examples: without fullerene redox pendant**



**(b) This Work: one-step oxidation with the aid of fullerene redox pendant**

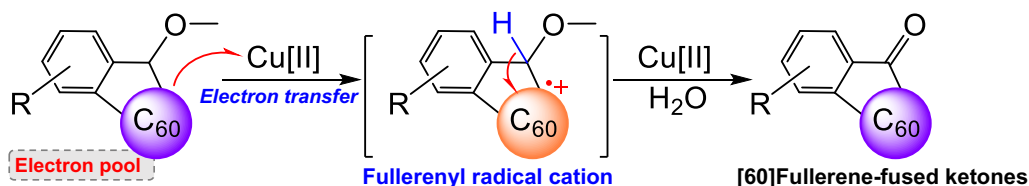


**Figure 6.1.1.** Concept of one-step direct oxidation of alkoxy group to ketones.



## 6.2.2 Mechanistic studies for the synthesis of fullerene-fused ketones

In order to gain deep insights to this unprecedented one-step oxidation, further experiments were carried out in this chapter.

### 6.2.2.1 $^{18}\text{O}$ Isotope-labeled experiments

The successful oxidation of alkoxy indano[60]fullerene **1a** under the argon atmosphere suggested that the oxygen source should not derive from the oxygen in air. Instead, the oxygen could directly retain from the methoxy group or come from the water residue in the system. Accordingly, the oxygen source of [60]fullerene-fused ketone **2a** was determined by performing the reaction in the presence of  $^{18}\text{O}$  isotope-labeled water ( $\text{H}_2^{18}\text{O}$ ) with the other conditions being the same (Figure 6.2.2.1).

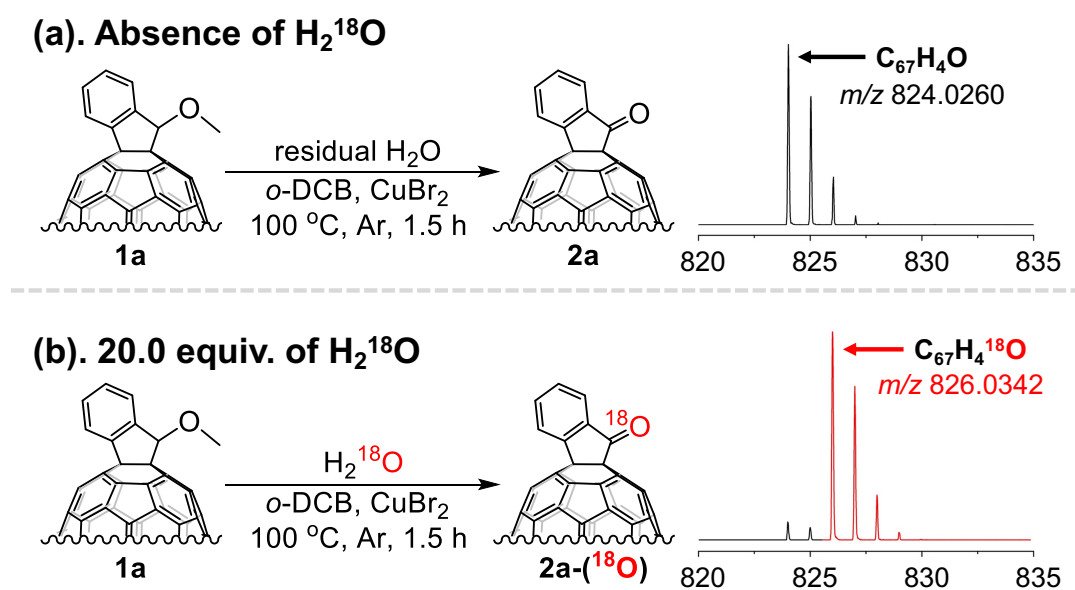


**Figure 6.2.2.1.**  $^{18}\text{O}$  isotope-labeled experiments. Reaction conditions: **1a** (3.0 mg, 3.6  $\mu\text{mol}$ ),  $\text{CuBr}_2$  (4.0 equiv.),  $o\text{-DCB}$  (3.0 mL) at  $100^\circ\text{C}$  for 1.5 hours in a sealed tube. (a) Absence of  $\text{H}_2^{18}\text{O}$ . (b) 20.0 equiv. of  $\text{H}_2^{18}\text{O}$ .

The control experiment was performed without the addition of  $\text{H}_2^{18}\text{O}$  under the optimized conditions. Then, the HRMS was applied to analyze the molecular weight of produced ketone **2a**, which indicates a mass-to-charge ratio ( $m/z$ ) of 824.0260 for the non- $^{18}\text{O}$  labeled **2a** (Figure 6.2.2.1.a). Subsequently, the experiment was conducted in

the presence of 20.0 equiv. of  $\text{H}_2^{18}\text{O}$  under the optimized conditions. A mass peak with an  $m/z$  of 826.0342 was clearly observed in HRMS, which conclusively proved that the obtained ketone contained  $^{18}\text{O}$  in its carbonyl group (Figure 6.2.2.1.b). Accordingly, the oxygen resource for the title oxidation reaction directly derives from the  $\text{H}_2\text{O}$  rather than from the methoxy or the atmosphere. Notably, although the excess amount of  $\text{H}_2^{18}\text{O}$  was used, the mass peak of non- $^{18}\text{O}$  labeled ketone **2a** still can be found in the HRMS of produced  $^{18}\text{O}$  labeled ketone **2a**-( $^{18}\text{O}$ ). Through calculation the mass intensity between **2a** and **2a**-( $^{18}\text{O}$ ), commercially anhydrous *o*-DCB was found to contain *ca.* 40 ppm  $\text{H}_2\text{O}$ , which adequately proceeded this direct oxidation (Table 6.2.2.1.1 and 6.2.2.1.2).

**Table 6.2.2.1.1.** HRMS data of non- $^{18}\text{O}$  labeled **2a**.

Molecular formula	Theoretical $m/z$	Found $m/z$	Absolute intensity (a.u.)	Normalized intensity (%) <sup>[a]</sup>
$\text{C}_{67}\text{H}_4\text{O}$	824.0262	824.0260	3798 <sup>[b]</sup>	100
	825.0296	825.0343	2705	71
	826.0329	826.0312	1006	26

[a] Calculated from the intensity of each peak divided by the intensity of the base peak.

[b] Selected as the base peak.

**Table 6.2.2.1.2.** HRMS data of  $^{18}\text{O}$  labeled **2a**-( $^{18}\text{O}$ ).

Molecular formula	Theoretical $m/z$	Found $m/z$	Absolute intensity (a.u.)	Normalized intensity (%) <sup>[a]</sup>
$\text{C}_{67}\text{H}_4\text{O}$	824.0262	824.0247	619	9
	825.0329	825.0318	426	6
$\text{C}_{67}\text{H}_4^{18}\text{O}$	826.0303	826.0342	7051 <sup>[b]</sup>	100
	827.0337	827.0346	5201	74
	828.0370	828.0368	1526	22

[a] Calculated from the intensity of each peak divided by the intensity of the base peak.

[b] Selected as the base peak.

### 6.2.2.2 Kinetic studies

The kinetic studies of the one-step direct oxidation of **1a** with CuBr<sub>2</sub> were carried out further to understand the reaction characteristics (Figure 6.2.2.2). All reactions were performed under the same conditions except varying the temperature. The concentration changes over time were monitored by the HPLC.

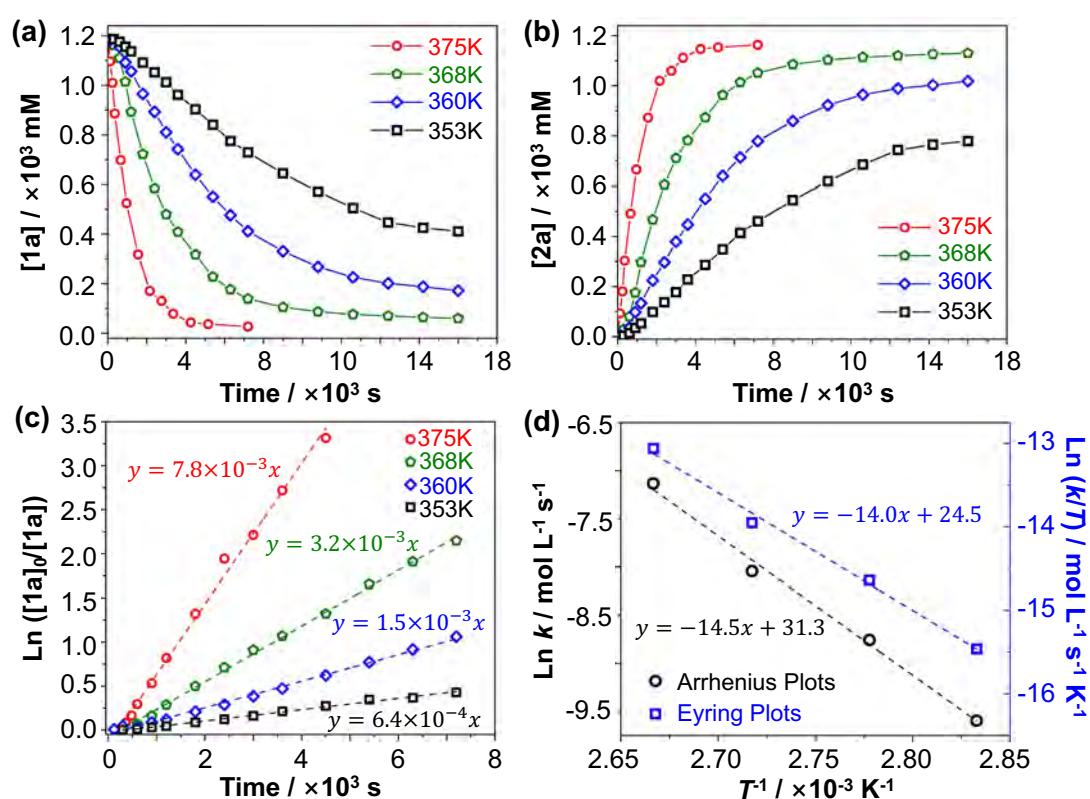


**Figure 6.2.2.2.** Reaction conditions: **1a** (3.0 mg, 3.6  $\mu\text{mol}$ ), CuBr<sub>2</sub> (4.0 equiv.), *o*-DCB (3.0 mL). (a) Concentration of **1a** varies over time at different temperature. (b) Concentration of **2a** varies over time at different temperatures. (c) Plots of  $\ln([1a]_0/[1a])$  varies over time at different temperature, where  $[1a]_0$  and  $[1a]$  stands for an initial concentration and the concentration at the time of **1a**, respectively. Reaction concentration varies over time at different temperature. (d) Arrhenius (black) and Eyring plots (blue) in this one-step oxidation reaction.

The change on concentration of reactant **1a** and product **2a** over time clearly indicated that this oxidation reaction reached the equilibrium faster and with higher yields when the reaction temperature increased (Figure 6.2.2.2.a and b). No by-product was formed during the transformation of concentration varies of **1a** and **2a**, which

conclusively confirmed that this oxidation route possessed high selectivity and efficiency. Logarithmic scale was used to determine the reaction order. The natural logarithm of **1a** consumption ratio exhibited a strong linear time dependence, which suggested this oxidation reaction presents a first-order reaction characteristic (Figure 6.2.2.2.c) [161]. Although this reaction involved three reactants, both CuBr<sub>2</sub> and H<sub>2</sub>O are in excess amounts relative to **1a**. Accordingly, this oxidation reaction is a pseudo-first order reaction. The rate constant ( $k$ ) dramatically increased from  $6.4 \times 10^{-4} \text{ mol}^{-1} \text{ L}^{-1} \text{ s}^{-1}$  to  $7.8 \times 10^{-3} \text{ mol}^{-1} \text{ L}^{-1} \text{ s}^{-1}$  when the reaction temperature increased from 353 K to 375 K (Table 6.2.2.2). Next, the activation energy  $E_a$ , activation enthalpy  $\Delta H^\ddagger$ , activation entropy  $\Delta S^\ddagger$ , and activation Gibbs free energy  $\Delta G^\ddagger$  was computed from Arrhenius plots ( $\ln k$  vs  $1/T$ ) and Eyring plots ( $\ln(k/T)$  vs  $1/T$ ) on the basis of following equations, respectively (Figure 6.2.2.2.d):

$$\ln k = -E_a/RT + \ln A$$

$$\ln (k/T) = -\Delta H^\ddagger/RT + [\ln (k_B/h) + \Delta S^\ddagger/R]$$

Where  $k$  is the rate constant,  $T$  is the temperature,  $R$  is the gas constant,  $\ln A$  is a constant,  $k_B$  is the Boltzmann constant,  $h$  is the Planck constant. The results summarized in Table 6.2.2.2 indicated that this one-step direct oxidation has an  $E_a$  of 120.6 kJ mol<sup>-1</sup>, and with an endothermic  $\Delta H^\ddagger$  of 116.4 kJ mol<sup>-1</sup>. The positive  $\Delta S^\ddagger$  of 6.2 J mol<sup>-1</sup> K<sup>-1</sup> indicated that this oxidation has an increase in disorder degree, which suggesting the products should have more components than the reactants.

**Table 6.2.2.2.** Activation parameters for the one-step direct oxidation of alkoxy indano[60]fullerene **1a**.

Temp. (K)	Rate constant (mol <sup>-1</sup> L <sup>-1</sup> s <sup>-1</sup> )	$E_a$ (kJ mol <sup>-1</sup> )	$\Delta H^\ddagger$ (kJ mol <sup>-1</sup> )	$\Delta S^\ddagger$ (J mol <sup>-1</sup> K <sup>-1</sup> )	$\Delta G^\ddagger$ [a] (kJ mol <sup>-1</sup> )
353	$6.4 \times 10^{-4}$	120.6	116.4	6.2	114.1
360	$1.5 \times 10^{-3}$				
368	$3.2 \times 10^{-3}$				
375	$7.8 \times 10^{-3}$				

[a] The activation free energy  $\Delta G^\ddagger$  was estimated from  $\Delta H^\ddagger$ ,  $\Delta S^\ddagger$  and temperature at 375 K according to the equation  $\Delta G^\ddagger = \Delta H^\ddagger - T\Delta S^\ddagger$ .

### 6.2.2.3 $^1\text{H}$ NMR investigations of the reaction

Additional experiments using  $^1\text{H}$  NMR were conducted to analyze other products formed in this reaction (Figure 6.2.2.3).

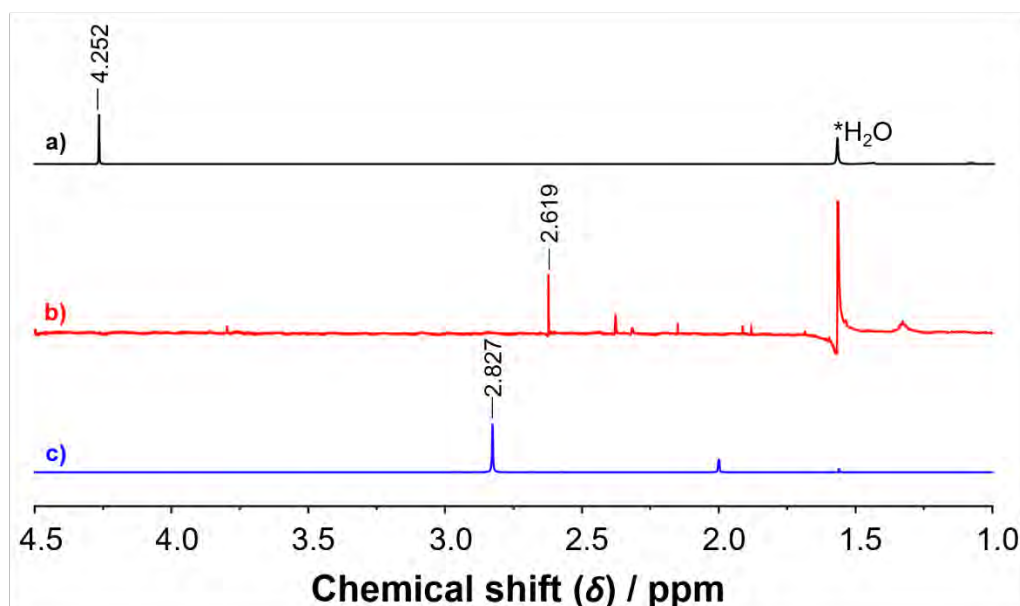


**Table 6.2.2.3.**  $^1\text{H}$  NMR with  $\text{H}_2\text{O}$  as internal reference ( $\delta = 1.560$  ppm) of (a) **1a**. (b) Reaction mixture. (c) Methanol.

$^1\text{H}$  NMR of **1a** clearly indicated a methoxy peak with a chemical shift ( $\delta$ ) at 4.25 ppm. After the oxidation reaction was finished, the  $^1\text{H}$  NMR indicated that the previous methoxy peak at  $\delta = 4.25$  ppm disappeared, while a new singlet peak appeared at  $\delta = 2.62$  ppm. However, compared with the  $^1\text{H}$  NMR of MeOH, showing the methoxy peak at  $\delta = 2.83$  ppm, the product was much up-field shifted. Notably, the reaction mixture was acidic when the reaction was finished, which suggested HBr should be generated during the reaction. Meanwhile, the reaction was performed at 100  $^\circ\text{C}$ , which is favorable for the formation of  $\text{CH}_3\text{Br}$  from the generated HBr and MeOH. Accordingly, a slightly up-field shift in  $^1\text{H}$  NMR can be found because of the formation of  $\text{CH}_3\text{Br}$ . More importantly, when  $\text{CH}_3\text{Br}$  was formed,  $\text{H}_2\text{O}$  was simultaneously generated and then it served back as oxygen resource for the oxidation. Accordingly, the methoxy of **1a** left as a methanol specie, suggesting that this oxidation reaction should involve a hemiketal intermediate.



#### 6.2.2.4 Radical scavenging experiments

As the formation of fullerenyl radical cation ( $C_{60}^{\bullet+}$ ) by  $CuBr_2$  was considered as the key specie for promoting the one-step oxidation of alkoxy, typical radical scavenger 2,2,6,6-tetramethyl-1-piperidinyloxy (TEMPO) was added to confirm the electron transfer from  $C_{60}$  to  $CuBr_2$  (Figure 6.2.2.4). When conducted the reaction in the presence of 4.0 equiv. of TEMPO, the yield of **2a** was dramatically decreased from 95% to 8%. A further increased amount of TEMPO to 10.0 equiv., the reaction was stopped, which indicated that the electron transfer process was suppressed. Therefore, the one-step direct oxidation of alkoxy is initiated from the electron transfer from  $C_{60}$  to  $CuBr_2$ , and  $C_{60}^{\bullet+}$  is the key specie to proceed the following oxidation steps.

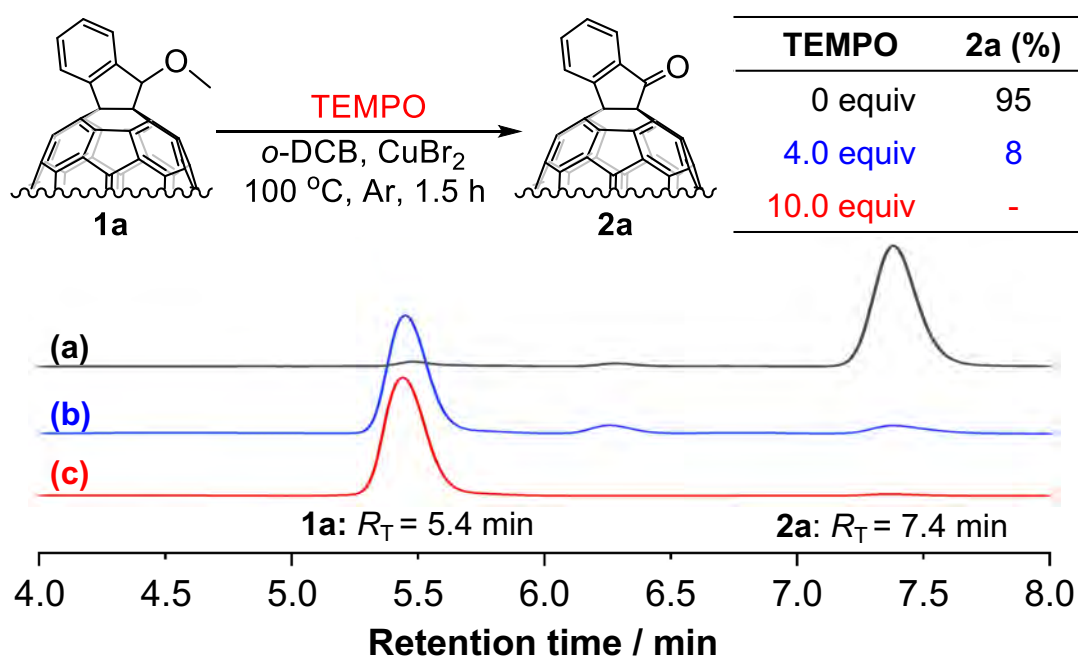


**Figure 6.2.2.4.** TEMPO experiments. Conditions: **1a** (3.0 mg, 3.6  $\mu$ mol),  $CuBr_2$  (4.0 equiv.), *o*-DCB (3.0 mL) at 100 °C for 1.5 hours. (a) Absence of TEMPO. (b) 4.0 equiv. of TEMPO. (c) 10.0 equiv. of TEMPO.

### 6.2.2.5 Proposed mechanism and computation studies

On the basis of the above experimental investigations and our previous research, a plausible reaction mechanism for  $\text{CuBr}_2$  promoted one-step direct oxidation of alkoxy to ketone was proposed (Figure 6.2.2.5.1).

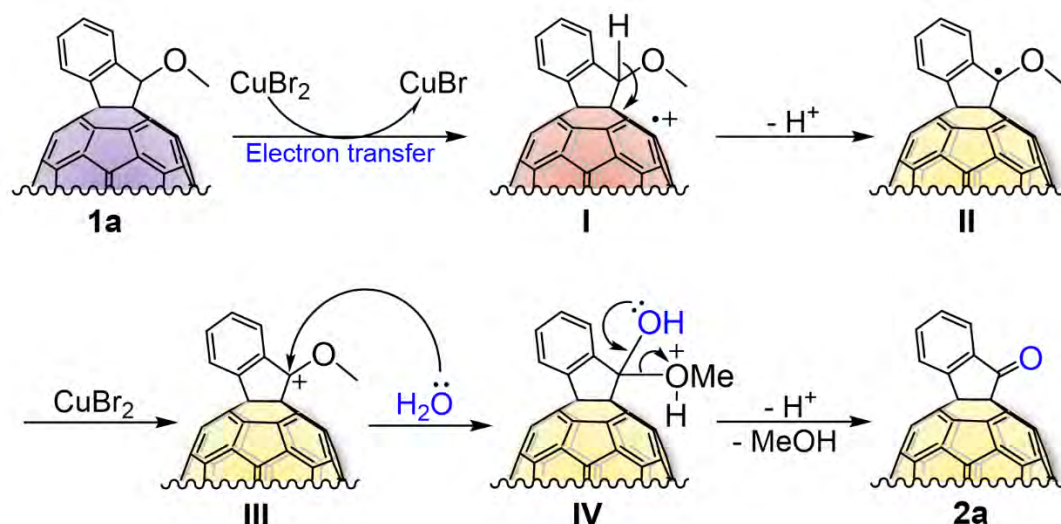


**Figure 6.2.2.5.1.** Plausible mechanism for  $\text{CuBr}_2$  promoted one-step direct oxidation of alkoxy to ketone.

At beginning, the fullerene moiety of indano[60]fullerene **1a** was oxidized by  $\text{CuBr}_2$  through electron transfer, producing the key active specie—indano[60]fullerenyl radical cation **I**. Owing to strong electron-deficiency of  $\text{C}_{60}^{+\bullet}$ , the neighbor C–H bond at benzene position was cleaved to generate neutral indano[60]fullerenyl radical **II** with releasing one molecule of proton, which then spontaneously formed HBr. Next,  $\text{CuBr}_2$  generated benzene-cation **III** was nucleophilic attacked by  $\text{H}_2\text{O}$ , producing the hemiketal intermediate **IV**. Finally, [60]fullerene-fused ketone **2a** was formed through the removal of methanol and proton.

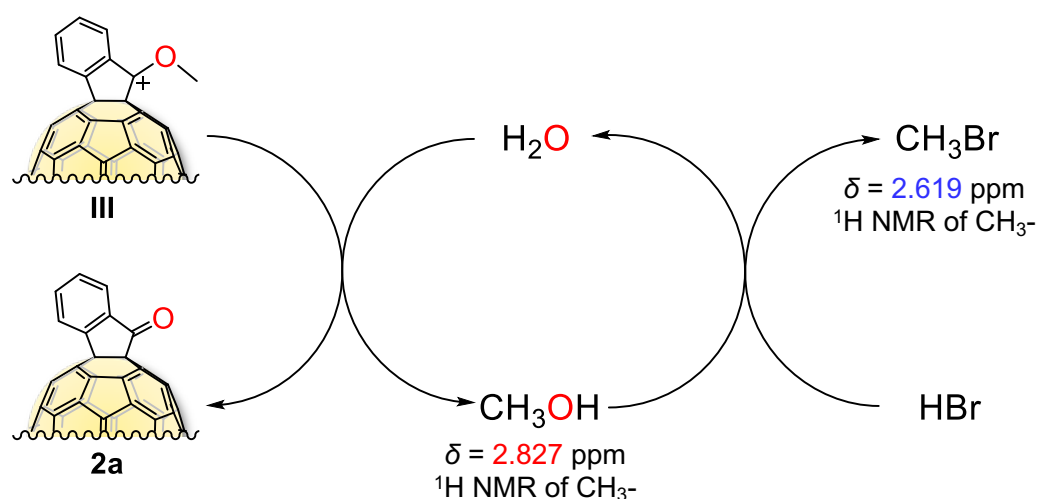


**Figure 6.2.2.5.2.** Plausible mechanism for  $\text{H}_2\text{O}$  involved cycle.  $^1\text{H}$  NMR with  $\text{H}_2\text{O}$  as internal reference ( $\delta = 1.560$  ppm).

Meanwhile, the produced methanol can react with  $\text{HBr}$  to generate  $\text{CH}_3\text{Br}$  and  $\text{H}_2\text{O}$ , which then quickly reacts with benzene-cation **III** (Figure 6.2.2.5.2). Therefore, [60]fullerene facilitated the one-step direct oxidation of alkoxy group to ketone by behaving as an electron-pool.

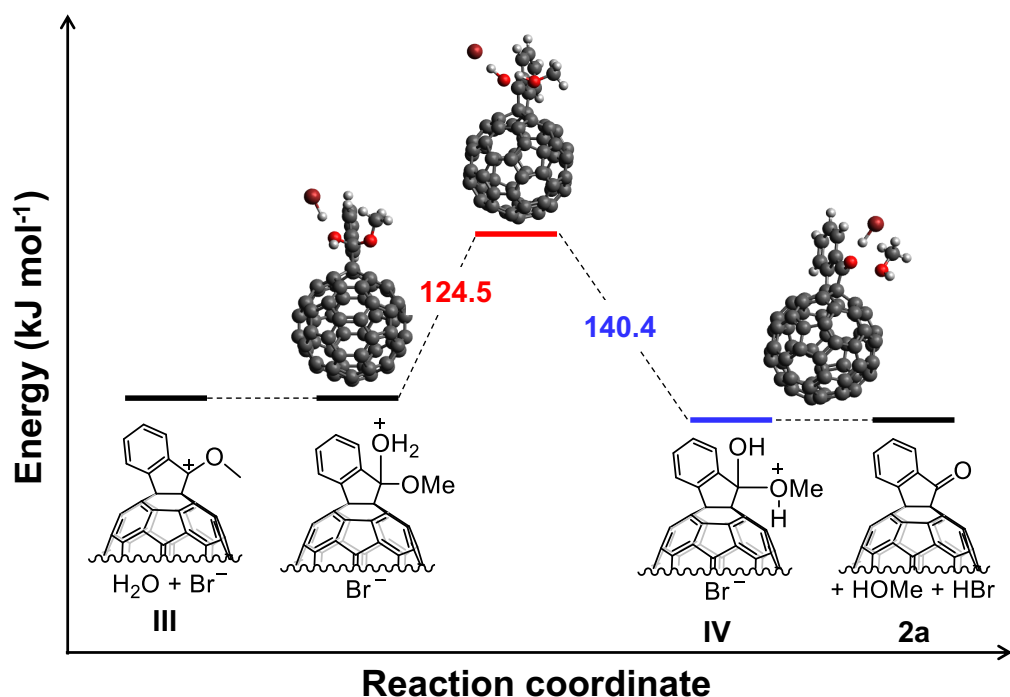


**Figure 6.2.2.5.3.** DFT computed energy change from **III** to **2a** in the presence of  $\text{Br}^-$ .

To confirm the proposed mechanism, the DFT calculations were performed to understand the key species and reaction barriers (Figure 6.2.2.5.3). The DFT results indicated that the key step is the proton transfer from H<sub>2</sub>O to methoxy with a computed potential energy barrier of 124.5 kJ mol<sup>-1</sup>, which is in decent agreement with the experiment value. It should be noted that bromide anion can efficiently accelerate this proton transfer according to the DFT computation in the absence of Br<sup>-</sup>. In addition, DFT calculations also showed facile oxidation of **1a** by Cu[II] and a relatively easy deprotonation of **I** to form HBr with a barrier on the order of 38.6 kJ mol<sup>-1</sup> (Figure 6.2.2.5.4). Accordingly, CuBr<sub>2</sub> plays two roles in this one-step oxidation reaction: a) electron transfer oxidation of fullerene by Cu[II]; b) proton transfer for formation of hemiketal by Br<sup>-</sup>.

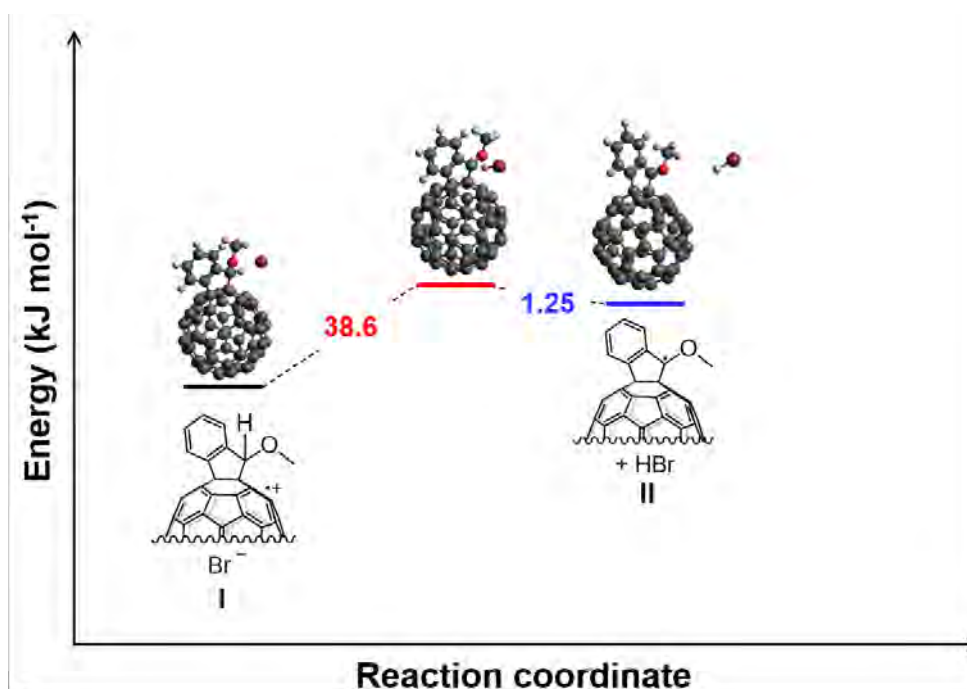
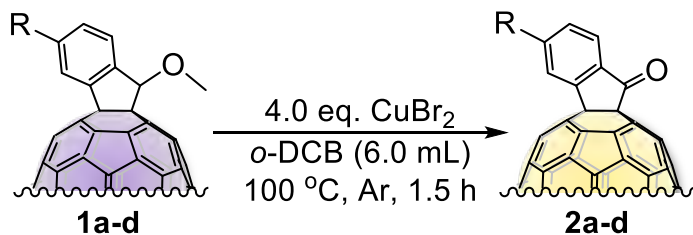
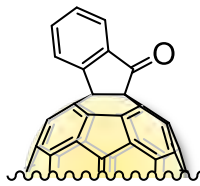
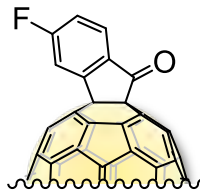
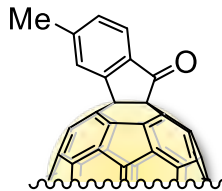
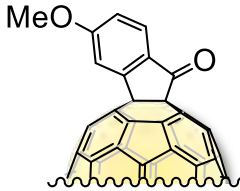


Figure 6.2.2.5.4. DFT computed energy change from **I** to **II** in the presence of Br<sup>-</sup>.

### 6.2.3 Extension of substrate scope

the substrate scope was further explored with selected representatives. As shown in Table 6.2.3, this one-step oxidation reaction proceeded smoothly to afford **2a–d** in extremely high yields. The optimized condition produced [60]fullerene-fused ketone **2a** with an isolated yield of 94% (Table 6.2.3, Entry 1). Then, a methyl substituted ketone **2b** was obtained in the same high yield of 93% (Table 6.2.3, Entry 2). To investigate the electron-negativity effect of the substituents on alkoxy indano[60]fullerenes, electron-withdrawing 4-fluoro- and electron-donating 4-methoxy moiety-functionalized indano[60]fullerene substrates were synthesized. The corresponding [60]fullerene-fused ketones **2c** and **2d** were successfully isolated in high yields of 92% and 94%, respectively (Table 6.2.3, Entry 3 and 4).

**Table 6.2.3.** CuBr<sub>2</sub> promoted one-step direct oxidation of alkoxy to ketone with versatile substrates<sup>[a]</sup>.

			
Entry	Products <b>2</b> (%) <sup>[b]</sup>	Entry	Products <b>2</b> (%)
1	 <b>2a</b> (94%)	3	 <b>2c</b> (92%)
2	 <b>2b</b> (93%)	4	 <b>2d</b> (94%)

<sup>[a]</sup> Unless otherwise specified, all the reactions were performed with 0.03 mmol of **1a–d**, 0.12 mmol of CuBr<sub>2</sub> in 10.0 mL of *o*-DCB solution at 100 °C for 1.5 h under an argon atmosphere. <sup>[b]</sup> Isolated yield.

## 6.3 Evaporable fullerene-fused ketone as ETL in PSCs

### 6.3.1 Thermal stability of fullerene-fused ketone

According to the Bayer's strain theory, the 5-membered-full-carbon ring show the most stable among other ring structures. Interestingly, the FIFs have the 5-membered-full-carbon ring. Then, the thermogravimetric analyses were carried out to compare the thermal stability of FIFs with PC<sub>61</sub>BM and C<sub>60</sub> (Figure 6.3.1).

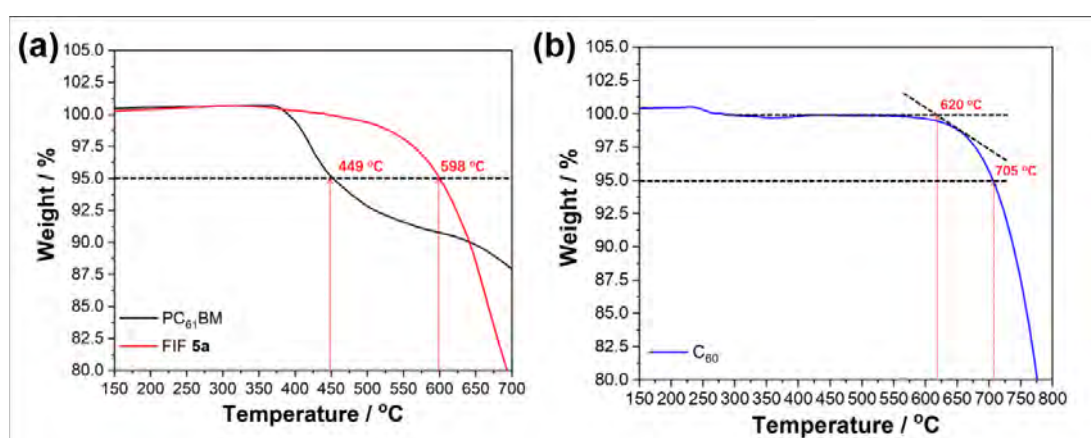


**Figure 6.3.1.** TGA analyses of (a) FIF **5a** and PC<sub>61</sub>BM, and (b) C<sub>60</sub> under the nitrogen atmosphere.

Herein, owing to the excellent performance the FIF **5a** achieved in PSCs, it thusly was selected to be further evaluate the thermal stability. FIF **5a** manifests strong thermal stability with a 5% weight loss temperature at 598 °C relative to PC<sub>61</sub>BM with a 5% weight loss at 449 °C, which is well accordance with the prediction based on Baeyer strain theory. Although **5a** did not show as high thermally stable as C<sub>60</sub>, it is still promising to be evaporated without thermal decomposition as it decomposing temperature is much ~150 °C higher than that of PC<sub>61</sub>BM. Accordingly, the 5-membered-full-carbon ring definitely opens a new gate for the fullerene materials applied in PSCs. If the thermal-deposition can be available for fullerene materials, the sever solubility issue could be no long in consideration for developing the fullerenes in photovoltaics. Therefore, the thermal-deposition of **5a** was then investigated.

### 6.3.2 Thermal-deposition of FIF and fullerene-fused ketone

As FIFs demonstrate an improved thermal stability compared with commercially available PC<sub>61</sub>BM, the selected FIF **5a** was then processed with the thermal-deposition procedure to fabricate ETLs for PSCs. In order to confirm whether the **5a** is tolerate towards thermal-deposition conditions, the HPLC was applied to analyze chemical components of **5a** before/after the thermal deposition process (Figure 6.3.2).

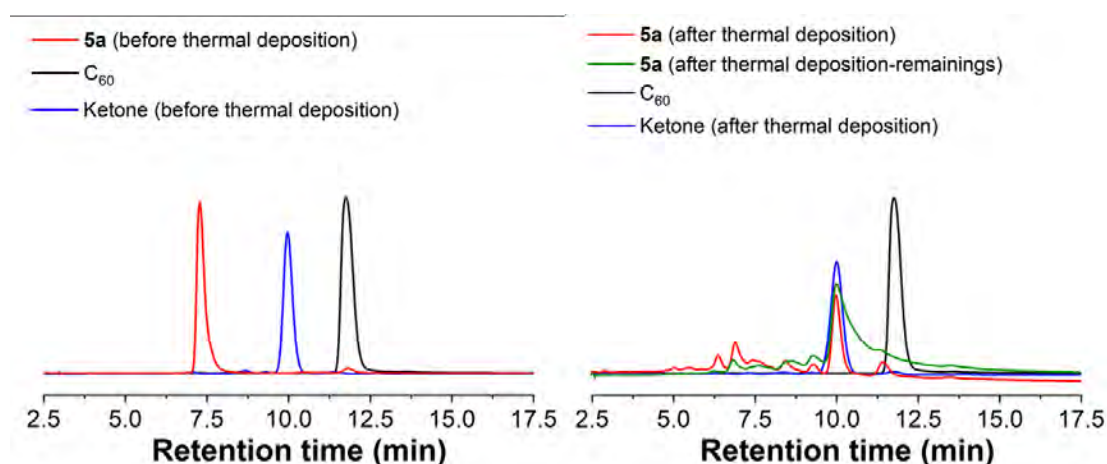


**Figure 6.3.2.** HPLC analyses of the fullerenes (a) before thermal deposition, and (b) after thermal-deposition under a vacuum chamber.

However, the HPLC of **5a** after the thermal-deposition indicated the significant decomposition of **5a** to form a set of complicated compounds. Among these complicated depositing compounds, there is still promising peak that appeared in the HPLC window, which gives a hope to fulfill the evaporable fullerenes. Through the NMR and HRMS, we confirmed the structure of the major decomposed compound after the thermal-deposition of **5a** is the [60]fullerene-fused ketone. It is interesting to find that the fullerene-fuse ketone can be directly synthesized from FIF **5a** through the thermal deposition process. Moreover, the fullerene-fused ketone demonstrates its high tolerance in thermal-deposition process, which gives a hope to apply such fullerene derivatives as evaporable fullerenes.



### 6.3.3 Device performance

With the evaporable fullerene-fused ketone **2a** in hand, then a normal type PSC with a configuration of ITO/Fullerene/MAPbI<sub>3</sub>/Spiro-MeOTAD/Au was fabricated to evaluate the performance of the evaporable fullerene as ETLs (Figure 6.3.3).

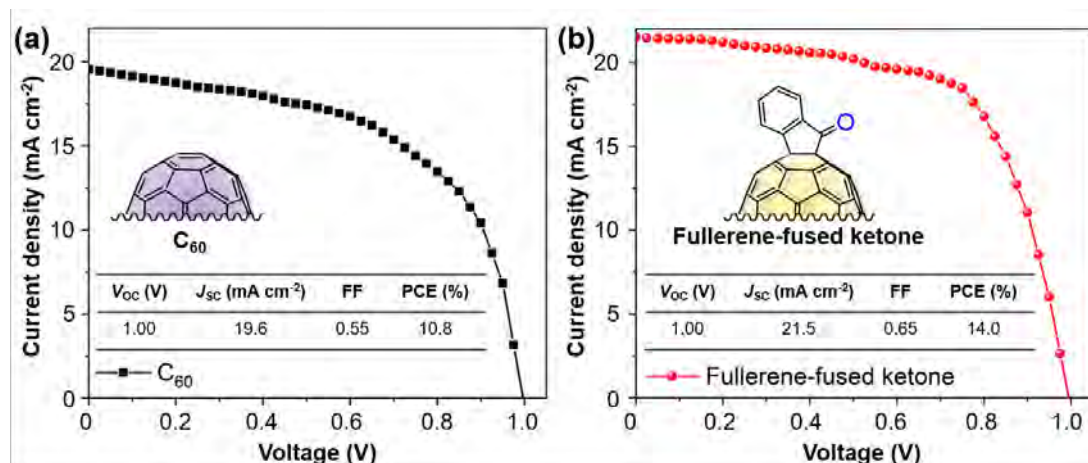


**Figure 6.3.3.**  $J$ - $V$  curves of (a)  $C_{60}$  as thermal-deposited ETL, and (b) Fullerene-fused ketone as thermal-deposited ETL.

As fullerene were applied as ETLs in the PSCs, both  $C_{60}$  reference and **2a** applied-PSCs indicated neglectable hysteresis. The evaporable **2a** applied PSCs showed significant improvement among all photovoltaic parameters with a PCE of 14.0%, a  $V_{OC}$  of 1.00 V, a  $J_{SC}$  of 21.5  $\text{mA cm}^{-2}$  and an FF of 0.65, compared with a  $C_{60}$ -reference PCE of 10.8%, a  $V_{OC}$  of 1.00 V, a  $J_{SC}$  of 19.6  $\text{mA cm}^{-2}$  and an FF of 0.55. Although this preliminary investigation showed the significant performance improvement, both relative low performances compared with reported  $C_{60}$  applied PSCs (PCE = 16.8%, in Chapter 4). Accordingly, investigation in mechanism and the reproducibility should be thereafter followed. Based on the design principle, the high  $J_{SC}$  value comes from the enlarged perovskite crystal and decreased light absorption of ETL. The increased FF can be reasonably ascribed from efficient passivation effect that carbonyl group afforded.



## 6.4 Materials and methods

### 6.4.1 Synthesis of fullerene-fused ketone

Unless otherwise noted, all materials including dry solvents were obtained from commercial suppliers (Sigma-Aldric, TCI, Wako) and used without further purification. Unless otherwise noted, all reactions were performed with dry solvents under an atmosphere of argon in flame-dried glassware with standard vacuum-line techniques or in a glove box. The reaction monitoring was conducted by an analytical HPLC, using a COSMOSIL Buckyprep-D column as solid state, toluene as eluent with a flow rate of 1.0 mL/min under the detection wavelength at 337 nm.

#### 6.4.1.1 <sup>18</sup>O isotope-labeled experimental procedure

3.0 mg (3.6 μmol) of **1a** and 1.5 μL of H<sub>2</sub><sup>18</sup>O (0.072 mmol, 20.0 equiv) were added to 3.0 mL of anhydrous *o*-DCB solution in the presence of CuBr<sub>2</sub> (3.2 mg, 14.4 μmol, 4.0 equiv). After being vigorously stirred at 100 °C for 1.5 h with a tiny sealed tube, resulting mixture was directly filtered through a silica gel plug to remove insoluble materials. Finally, the filtrate was condensed in vacuo for the following HRMS measurement.

#### 6.4.1.2 TEMPO experimental procedure

3.0 mg (3.6 μmol) of **1a**, 3.2 mg of CuBr<sub>2</sub> (14.4 μmol, 4.0 equiv), and 2,2,6,6-tetramethyl-1-piperidinyloxy (TEMPO) (2.3 mg, 4.0 equiv; 5.6 mg, 10.0 equiv) were added to 3.0 mL of anhydrous *o*-DCB solution. After being vigorously stirred at 100 °C for 1.5 h under the argon atmosphere, resulting mixture was directly filtered through a silica gel plug to remove insoluble materials. Finally, *ca.* 50 μL of filtrate was directly loaded on HPLC to analyze results.

#### **6.4.1.3 Synthesis of fullerene-fused ketones 2a–d**

The starting materials alkoxy indano[60]fullerenes **1a–d** were prepared according to methodology in Chapter 4. Without specifically notified, all reactions were performed by using 0.03 mmol of **1a–d**, 0.12 mmol anhydrous CuBr<sub>2</sub> (Sigma-Aldric) in 10.0 mL of anhydrous *o*-dichlorobenzene (*o*-DCB) under an argon atmosphere at 100 °C for 1.5 hours. After reaction was over, resulting mixture was directly filtered through a silica gel plug to remove insoluble salt, and then evaporated in vacuo to remove the solvent. Finally, the residue was further separated on a silica gel column with CS<sub>2</sub> or CS<sub>2</sub>/dichloromethane as eluents to afford products **2a–d**.

#### **6.4.2 Device fabrication**

ITO patterned glass substrates were cleaned and sonicated with detergent, distilled water, acetone and isopropanol in an ultrasonic bath for 15 min, respectively. Subsequently, fullerene was thermal-deposited on ITO substrates at a constant evaporation rate of 0.02 nm s<sup>-1</sup>. Then, 25 µL of perovskite precursor solution was spin-coated on the fullerene layer at 4000 rpm for 20 s, with a dropping of 0.5 mL of anhydrous diethyl ether was slowly dripped onto the substrate 5 s after the start of the spin-coating process. Next, the film was annealed at 100 °C for 10 min to obtain a dense brown MAPbI<sub>3</sub> film. The hole transporting layer was spin-coated from the Spiro-MeOTAD solution at 4000 rpm for 20 s. Finally, a 70-nm-thick of Au anode was fabricated by thermal deposition at a constant evaporation rate of 0.05 nm s<sup>-1</sup>.

## 6.5 Summary

In summary, this chapter combines the previously discussed factors, how fullerenes influence the high-performance PSCs, designed and successfully synthesized the first evaporable fullerene derivatives, namely [60]fullerene-fused ketones. Although fullerene-fused ketone is impossible obtained when conventional fullerene-anion or radical chemistry were applied, this chapter presented fullerene-radical cation-mediated one-step oxidation of alkoxy to ketone can smoothly access the fullerene-fused ketones (Figure 6.5). Meanwhile, this chapter unveiled the mechanism of *in situ* generated  $C_{60}^{*+}$  facilitates the one-step direct oxidation.  $C_{60}^{*+}$  can behave as an electron-pool: 1) initializing the oxidation by electron transfer to  $CuBr_2$  forming  $C_{60}^{*+}$ ; 2) activating neighbor C–H bond to cleave through dragging electrons from the bond and subsequently affording the key hemiketal intermediate. Accordingly, non-fullerene functionalized alkoxy understandably failed to undergo the one-step oxidation with weak oxidants, owing to failure of occurrence of the key radical cation specie at the beginning. Moreover, the obtained ketones were evaluated as the ETL in the PSCs through the thermal-deposition, which gave a significant improvement (PCE 14%) compared with the reference  $C_{60}$ -applied PSC in a PCE of 10.8%. Although current research did not demonstrate the reproducibility and other important parameters, the following research will be catch up immediately to uncover the backbone mechanism of how evaporable fullerene ETL influence the PSCs' performances.

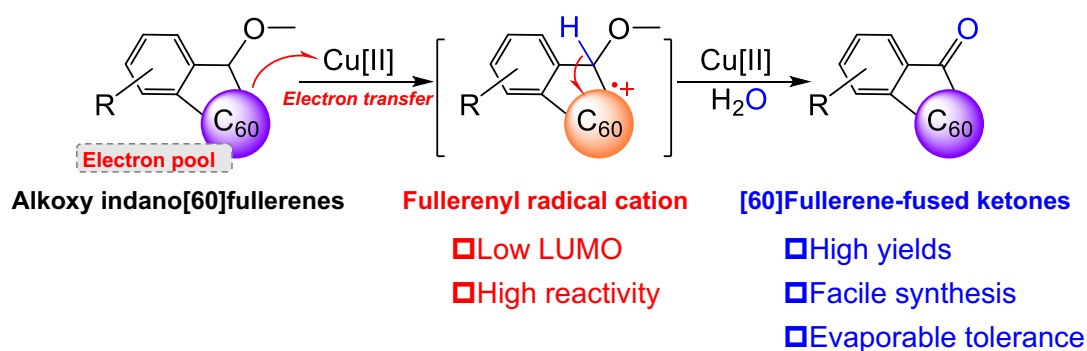


**Figure 6.5.** Graphic summary of one-step oxidation of alkoxy indano[60]fullerenes to [60]fullerene-fused ketones.



## Chapter 7.

# Conclusions

### 7.1 Conclusions

In conclusion, this thesis concluded three determinative factors that influenced the performance of fullerene materials applied PSCs, which clearly distinguishing from the conventional points that considered for OSCs. Typical fullerene materials applied in OSCs are mainly designed with considerable attentions among 1) high LUMO energy level, which gives a balanced level at 56  $\pi$ -system fullerene derivatives; 2) high solubility in non-polar solvent, which helps fullerene electron acceptors form into a condense active layer with electron donor materials; 3) good molecular packing between fullerenes and electron donor materials to accelerate the charge dissociation and transfer between at interface between electron donor and fullerene acceptors materials. However, all considerations for fullerene materials that tackled in OSCs turns in to ineffective once fullerenes were applied in PSCs. Significantly different to fullerenes in OSCs, this thesis found that fullerenes in PSCs should be more considered about 1) the interlayer morphology of fullerene ETL with a uniformly amorphous morphology can benefit a better performance in PSCs; 2) a small molecular size, which indicates a minimum sacrifice of electron mobility for additional functions; 3) passivation effect that enabled by the Lewis structure functionalized fullerenes.

In chapter 3, this thesis deeply discusses how interlayer morphology of fullerene ETL influences the performance of PSCs. Through the electron microscopy, typical thermal-deposited C<sub>60</sub> showed an amorphous morphology, which conclusively resulted in a highest performance among pristine fullerenes applied PSCs. On the basis of this finding, a mixed C<sub>60</sub>/C<sub>70</sub> with mass ratio of 9/1 was fabricated as ETL by spin-coating

process, which provided a PCE as high as thermal-deposited C<sub>60</sub> ETL. Moreover, a vacuum-dry treatment was specifically designed for the spin-coated C<sub>60</sub>/C<sub>70</sub> ETL, which further promoted the PCE up to 18.0%.

In chapter 4, this thesis focuses on finding the best fullerene molecular size for high-performance PSCs. Although C<sub>60</sub> can provide the best electron-transport ability thanks to its smallest molecular size for compacted packing, C<sub>60</sub> cannot provide other beneficiary functions if without chemical modifications. However, once pristine fullerenes are functionalized, the molecular size is inevitably enlarged. Through applying the designed full-carbon indano[60]fullerene in PSCs, this thesis concluded that the most favorable fullerene molecular size is the fullerene mono-adduct rather than fullerene multi-adduct in OSCs. Therefore, the fullerene mono-adduct can effectively provide many functions such as passivation site with the minimum compensation of electron-transport ability.

In chapter 5, this thesis comprehensively demonstrates the methodology how to introduce the Lewis base structures such as alkoxy, amino, into fullerene structure. To effectively passivate the perovskite, both dopant method and single passivation layer were investigated. The FIF passivation layer exhibited excellent passivation ability, enabling perovskite cell grow with enlarged crystal size, decreased grain boundaries, and reduced the trap sites at surface. Accordingly, a record-high PCE of 20.7% is achieved among fullerene-applied MAPbI<sub>3</sub> type PSCs. The amino[60]fullerene was applied as dopant in perovskite layer, achieving a slightly better performance. Therefore, the single passivation layer strategy is much more efficient compared with the doping strategy for high-performance PSCs.

In chapter 6, this thesis successfully combined all dominant points previously discussed, synthesizing [60]fullerene-fused ketones for being as ETL in PSCs. This fullerene ketone is the first fullerene derivative that tolerate the thermal-deposition process. ETL fabricated through the thermal-deposition can produce amorphous fullerene film for perovskite formation, which affords a significant improved performance compared with widely applied deposition C<sub>60</sub> ETLs. Moreover, the

synthesis of [60]fullerene-fused ketone also provide the breakthrough among the fundamental organic chemistry. This is the first example demonstrating the one-step direct oxidation of alkoxy groups to ketones, which is mainly thanks to the excellent electric property of fullerene. This thesis found that fullerene can function as an electron-pool to control the electron transfer so that facilitate the direct oxidation of alkoxy.

The ultimate purpose of this thesis, titled “Design and functionalization of fullerenes for high-performance perovskite solar cells”, is to provide 1) the efficient synthetic fullerene chemistry on the basis of unconventional fullerene-cation-mediated synthesis; 2) fundamental design and application knowledges for fullerene materials achieving high-performance PSCs to scholars and scientists that currently work in this area and will work in near future.

## 7.2 Prospects

At the end of this thesis, the author strongly believes that the fullerenes for PSCs will soon meet their prosperous future very soon. Owing to the limited research period during Doctoral course, deeper research cannot be carried for each mentioned point for fullerenes in PSCs. There are definitely many researches should be investigated in near future. For instance, the relations between fullerene derivatives and crystallinity, the influence of functional groups towards electron-transport ability in a fullerene mono-adduct system. In particular, the currently unfinished evaporable fullerene research doubtlessly created a bright future for fullerenes applying in PSCs. The evaporable fullerene can fully get rid of the considerations for solubility, which is still a tough issue for spin-coating processed fullerene ETL. Therefore, I would like spare my career in finding the new chemistry for fullerenes, and also the fine applications in a wide range beyond photovoltaics.

## *Conclusions*

---



## Appendix

As discussed in the main chapters in this thesis, it can be reasonably predicated that if similar functions could be achieved by other materials, the high-performance PSCs can be correspondingly reached. Therefore, besides the fullerene materials effectively designed for high-performance PSCs, this thesis will also briefly introduce several promising non-fullerene materials for high-performance PSCs. These promising materials are also highly expected to pave a new road for materials science and device engineering in PSCs.

### A.1 M13 bacteriophage-template for perovskite growth

The M13 bacteriophage has a structure of single-stranded DNA enclosed in a cylindrical capsid with 2700 copies of the pVIII protein on its body and five copies of the pIII protein on one end. The pVIII proteins are oriented in a way that the surface of the M13 bacteriophage has both peptide termini, *i.e.* amino ends and carboxyl ends. For this reason, the M13 bacteriophage has demonstrated metal template capability using the arms along the shaft of their body to bind to charged substances [162,163]. The flexible and filamentous nature of the M13 bacteriophage with the high aspect ratio of a diameter of *ca.* 6.5 nm to a length of *ca.* 880 nm indicates that they are excellent candidates for a crystal growth template [164]. As discussed in previous chapters, to improve the PCE of PSCs, the perovskite crystal size should be enlarged and their grain boundaries must be passivated.

Therefore, this work demonstrated the use of the M13 bacteriophage as the perovskite crystal growth template. The M13 bacteriophage has a uniform length of *ca.* 880 nm, which can surround the perovskite grains with a diameter of 300 nm to 1  $\mu$ m effectively. This is a crucial advantage as not only the size but also the homogeneity of

the perovskite grain is considered important for the perovskite film quality. Moreover, the synthesis of the M13 bacteriophage is organic solvent-free and significantly low-cost compared with the polymer and carbon nanotube additives. Such advantages make the M13 bacteriophage an excellent choice of additives for the organohalide metal perovskite films.

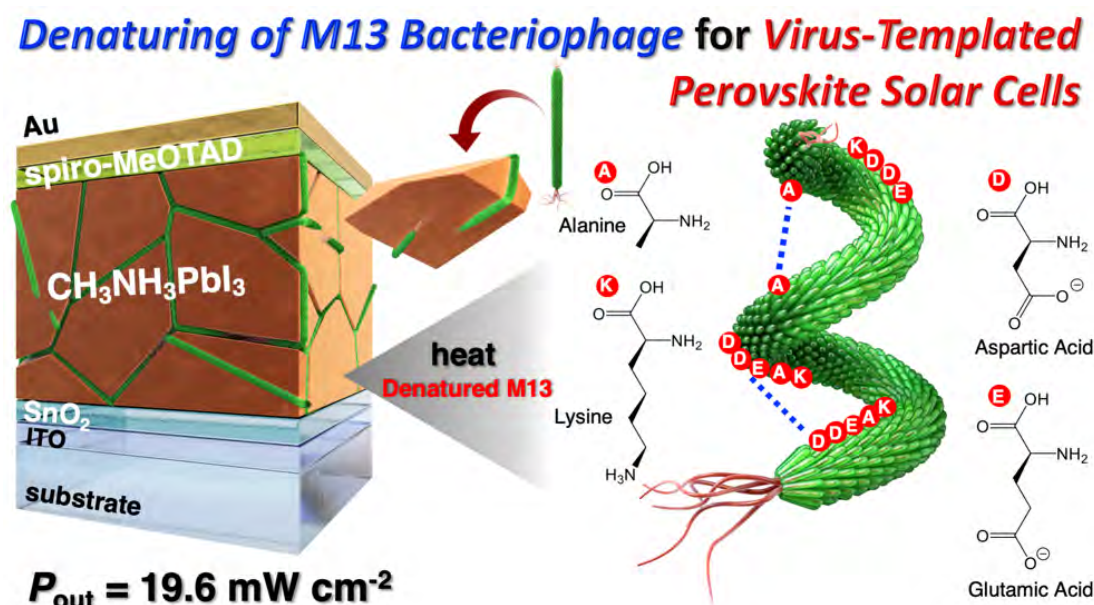


**Figure A.1.** The concept of applying denatured M13 bacteriophage for high-performance PSCs.

Herein, the wild-type M13 bacteriophage without any genetic engineering was mixed in the perovskite solution prior to spin-coating (Figure A.1). The carboxylic and the amino groups of the four types of amino acids on the surface of M13 bacteriophage formed a Lewis base coordination to  $\text{Pb}^{2+}$ . This is not surprising because amino acid in polypeptides are known to passivate perovskite grain boundaries and promote a favorable crystal orientation for charge transport. As the M13 bacteriophage in room temperature (r.t.) exists in tertiary and quaternary structures (4D structure), they had to be straightened by breaking the inter-and intra-molecular interactions using heat energy to maximize the crystal growth template effect. While the reference PSCs gave a PCE of 17.8%, the virus-added PSCs exhibited a PCE of 18.7%. When the virus-added perovskite precursor solution was heated at 65 °C before spin-coating, the PCE

increased to 19.7%. The efficiency further improved to 20.1% upon heating the virus-added perovskite precursor solution at 90 °C. Such high efficiency resulted from a high  $J_{SC}$  of 24.7 mA cm<sup>-2</sup>, a high  $V_{OC}$  of 1.09 V, and a high FF of 0.75. The high  $J_{SC}$  came from the increased incident photon-to-current efficiency attributed to the large crystal grains as well as the light scattering effect of the viruses. The high  $V_{OC}$  came from the passivation of the grain boundaries between perovskite crystals, which reduced the shallow trap sites and non-radiative recombination. The high FF came from the improved charge transport ascribed to both the favorable orientation of the perovskite crystals and the passivation effect of the crystal grains by the M13 bacteriophage. Within the best of our knowledge, this is the first bacteriophage application to PSCs and the first biomaterial to be used as the perovskite growth template and the passivator. This finding widens the material selection for the perovskite crystal growth template and the passivator.

## A.2 s-SWNT for growth and bridging perovskite crystals

Apart from passivating the perovskite at grain boundaries, and the perovskite crystal size control can effectively improve the performance of PSCs, the grain bridging can also access high-performance PSCs. Recently, our group reported that semiconducting single-walled carbon nanotubes (s-SWNTs) can function as effective crystal growth templates [165] as well as charge bridges between the grains owing to their compatible energy bandgap and high conductivity along the tube axis [166–168]. The seminal point of that work was, in fact, the role of chiral-selective sodium deoxycholate (DOC) surfactants, which is used in producing and dispersing the s-SWNTs. DOCs form the Lewis coordination complexes with the perovskite precursors to function as growth templates and passivators, inducing an increase in the crystal size and reduction in the number of trap sites, respectively. Despite the enhancement of PCE from 18.1% to 19.7% upon addition of the DOC-wrapped s-SWNTs(aq), the device PCE was limited by many factors and could potentially increase further. The FF was limited by the insulating nature of DOC and the limited solubility of the DOC-wrapped

s-SWNTs in DMF, the solvent used for perovskite precursors. Moreover, the  $V_{OC}$  of the device could potentially be improved further if other functional groups, such as urea and amine were used instead of the carboxylic group on DOC.

Polyaromatic nano-tweezer, which contains a bent polyaromatic group on one end and a functional group on the other end, has been reported to function as a nano-tweezer, clenching SWNTs. While the polyaromatic end induces strong  $\pi$ - $\pi$  interaction with the SWNTs, the functional end can be chemically modified with ease. Previously, we used modified polyaromatic nano-tweezer as charge-transporting layers in optoelectronics. Harnessing their suitable bandgaps and high mobility arising from the conjugated  $sp^2$  bonds, we demonstrated high optoelectrical performance in solar cells and organic light-emitting diodes.

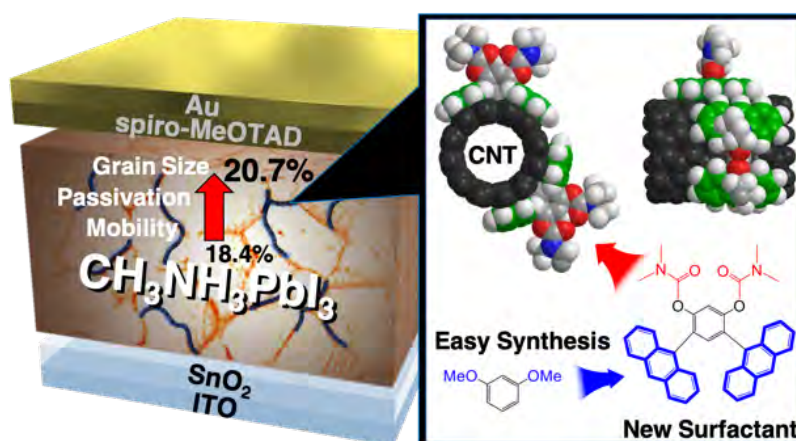


**Figure A.2.** The concept of applying denatured M13 bacteriophage for high-performance PSCs.

Hence, we designed and synthesized 4,6-di(anthracen-9-yl)-1,3-phenylene bis(dimethylcarbamate) (DPB), which is essentially a polyaromatic nano-tweezer with two urea-analogue functional groups. Subsequently, we used it as a new surfactant for s-SWNTs in PSCs. It was found that DPB could successfully replace DOC surfactants on s-SWNTs as confirmed by PL and UV-Vis. The DPB-clenched s-SWNTs showed much higher solubility in both DMF and DMSO than the conventional DOC-wrapped s-SWNTs. Accordingly, an effectively higher concentration of s-SWNTs could be added

to the perovskite precursor solution. The DPB on SWNTs expectedly manifested a stronger interaction with  $\text{Pb}^{2+}$  than DOC owing to the strong electron-donating nature of the lone pair electrons on the carbamate group enhanced by its configurational orientation facing away from SWNTs. The DPB-clenched s-SWNT-added perovskite films exhibited excellent charge-selectivity and reduced charge trap density. Moreover, the suitable molecular energy levels and higher mobility of DPB compared with DOC led to higher device performance as well. The DPB-clenched s-SWNTs-added PSCs exhibited a PCE of 20.7%, which is higher than those of the DOC-wrapped s-SWNT-added PSCs (19.7%) and pristine PSCs (18.4%). All of the three photovoltaic parameters, namely, high  $J_{\text{SC}}$ ,  $V_{\text{OC}}$ , and FF contributed to the high PCE of the DPB-clenched s-SWNTs-added PSCs. The high  $J_{\text{SC}}$  came from the large perovskite crystal size of over 500 nm. The high  $V_{\text{OC}}$  came from the strong passivation effect of the DPB-clenched s-SWNTs. The high FF came from the suitable bandgap, improved carrier mobility and charge selectivity of DPBs on s-SWNTs.



## Bibliography

- [1] H. W. Kroto, J. R. Heath, S. C. O'Brien, R. F. Curl, and R. E. Smalley, "C<sub>60</sub>: Buckminsterfullerene," *Nature* **318**, 162 (1985).
- [2] W. Krätschmer, L. D. Lamb, K. Fostiropoulos, and D. R. Huffman, "Solid C<sub>60</sub>: a new form of carbon," *Nature* **347**, 354 (1990).
- [3] J. Nelson, "Polymer: Fullerene bulk heterojunction solar cells," *Mater. Today* **14**, 462 (2011).
- [4] E. Castro, J. Murillo, O. Fernandez-Delgado, and L. Echegoyen, "Progress in fullerene-based hybrid perovskite solar cells," *J. Mater. Chem. C* **6**, 2635 (2018).
- [5] S. H. Friedman, D. L. DeCamp, R. P. Sijbesma, G. Srdanov, F. Wudl, and G. L. Kenyon, "Inhibition of the HIV-1 protease by fullerene derivatives: model building studies and experimental verification," *J. Am. Chem. Soc.* **115**, 6506 (1993).
- [6] Z. S. Martinez, E. Castro, C.-S. Seong, M. R. Cerón, L. Echegoyen, and M. Llano, "Fullerene Derivatives Strongly Inhibit HIV-1 Replication by Affecting Virus Maturation without Impairing Protease Activity," *Antimicrob. Agents Chemother.* **60**, 5731 (2016).
- [7] M. Lens, "Use of Fullerenes in Cosmetics," in *Recent Pat. Biotechnol.* **3**, 118 (2009).
- [8] M. Sawamura, K. Kawai, Y. Matsuo, K. Kanie, T. Kato, and E. Nakamura, "Stacking of conical molecules with a fullerene apex into polar columns in crystals and liquid crystals," *Nature* **419**, 702 (2002).
- [9] J. Lenoble, S. Campidelli, N. Maringa, B. Donnio, D. Guillon, N. Yevlampieva, and R. Deschenaux, "Liquid–Crystalline Janus-Type Fullerodendrimers Displaying Tunable Smectic–Columnar Mesomorphism," *J. Am. Chem. Soc.* **129**, 9941 (2007).

- [10] C. J. Brabec, N. S. Sariciftci, and J. C. Hummelen, "Plastic Solar Cells," *Adv. Funct. Mater.* **11**, 15 (2001).
- [11] I. Hiroshi, H. Kiyoshi, A. Tsuyoshi, A. Masanori, T. Seiji, O. Tadashi, S. Masahiro, and S. Yoshiteru, "The small reorganization energy of C<sub>60</sub> in electron transfer," *Chem. Phys. Lett.* **263**, 545 (1996).
- [12] K. Liu, S. Chen, J. Wu, H. Zhang, M. Qin, X. Lu, Y. Tu, Q. Meng, and X. Zhan, "Fullerene derivative anchored SnO<sub>2</sub> for high-performance perovskite solar cells," *Energy Environ. Sci.* **11**, 3463 (2018).
- [13] G. Yu, J. Gao, J. C. Hummelen, F. Wudl, and A. J. Heeger, "Polymer Photovoltaic Cells: Enhanced Efficiencies via a Network of Internal Donor-Acceptor Heterojunctions," *Science* **270**, 1789 (1995).
- [14] C. Yan, S. Barlow, Z. Wang, H. Yan, A. K.-Y. Jen, S. R. Marder, and X. Zhan, "Non-fullerene acceptors for organic solar cells," *Nat. Rev. Mater.* **3**, 18003 (2018).
- [15] J.-Y. Jeng, Y.-F. Chiang, M.-H. Lee, S.-R. Peng, T.-F. Guo, P. Chen, and T.-C. Wen, "CH<sub>3</sub>NH<sub>3</sub>PbI<sub>3</sub> Perovskite/Fullerene Planar-Heterojunction Hybrid Solar Cells," *Adv. Mater.* **25**, 3727 (2013).
- [16] P. J. Fagan, J. C. Calabrese, and B. Malone, "The Chemical Nature of Buckminsterfullerene (C<sub>60</sub>) and the Characterization of a Platinum Derivative," *Science* **252**, 1160 (1991).
- [17] S. I. Khan, A. M. Oliver, M. N. Paddon-Row, and Y. Rubin, "Synthesis of a rigid 'ball-and-chain' donor-acceptor system through Diels-Alder functionalization of buckminsterfullerene (C<sub>60</sub>)," *J. Am. Chem. Soc.* **115**, 4919 (1993).
- [18] P. J. Fagan, P. J. Krusic, D. H. Evans, S. A. Lerke, and E. Johnston, "Synthesis, chemistry, and properties of a monoalkylated buckminsterfullerene derivative, tert-BuC<sub>60</sub> anion," *J. Am. Chem. Soc.* **114**, 9697 (1992).
- [19] Y. Matsuo and E. Nakamura, "Selective Multiaddition of Organocopper Reagents to Fullerenes," *Chem. Rev.* **108**, 3016 (2008).
- [20] Y. Murata, K. Motoyama, K. Komatsu, and T. S. M. Wan, "Synthesis, properties, and reactions of a stable carbanion derived from alkynyldihydrofullerene: 1-octynyl-C<sub>60</sub> carbanion," *Tetrahedron* **52**, 5077 (1996).



- [21] C. Bingel, "Cyclopropanierung von Fullerenen," *Chem. Ber.* **126**, 1957 (1993).
- [22] M. Keshavarz-K, B. Knight, G. Srdanov, and F. Wudl, "Cyanodihydrofullerenes and Dicyanodihydrofullerene: The First Polar Solid Based on C<sub>60</sub>," *J. Am. Chem. Soc.* **117**, 11371 (1995).
- [23] F. Wudl, A. Hirsch, K. C. Khemani, T. Suzuki, P.-M. Allemand, A. Koch, H. Eckert, G. Srdanov, and H. M. Webb, "Survey of Chemical Reactivity of C<sub>60</sub>, Electrophile and Dieno—polarophile Par Excellence," in *Fullerenes* **481**, 11 (1992).
- [24] A. Naim and P. B. Shevlin, "Reversible addition of hydroxide to the fullerenes," *Tetrahedron Lett.* **33**, 7097 (1992).
- [25] A. M. Benito, A. D. Darwish, H. W. Kroto, M. F. Meidine, R. Taylor, and D. R. M. Walton, "Synthesis and characterisation of the methanofullerenes, C<sub>60</sub>(CHCN) and C<sub>60</sub>(CBr<sub>2</sub>)," *Tetrahedron Lett.* **37**, 1085 (1996).
- [26] L. Echegoyen and L. E. Echegoyen, "Electrochemistry of Fullerenes and Their Derivatives," *Acc. Chem. Res.* **31**, 593 (1998).
- [27] J. W. Bausch, G. K. S. Prakash, G. A. Olah, D. S. Tse, D. C. Lorents, Y. K. Bae, and R. Malhotra, "Considered novel aromatic systems. 11. Diamagnetic polyanions of the C<sub>60</sub> and C<sub>70</sub> fullerenes: preparation, <sup>13</sup>C and <sup>7</sup>Li NMR spectroscopic observation, and alkylation with methyl iodide to polymethylated fullerenes," *J. Am. Chem. Soc.* **113**, 3205 (1991).
- [28] K. Holczer, O. Klein, S. Huang, R. B. Kaner, K. Fu, R. L. Whetten, and F. Diederich, "Alkali-Fulleride Superconductors: Synthesis, Composition, and Diamagnetic Shielding," *Science* **252**, 1154 (1991).
- [29] K. Tanigaki, T. W. Ebbesen, S. Saito, J. Mizuki, J. S. Tsai, Y. Kubo, and S. Kuroshima, "Superconductivity at 33 K in Cs<sub>x</sub>Rb<sub>y</sub>C<sub>60</sub>," *Nature* **352**, 222 (1991).
- [30] G. K. Wertheim, D. N. E. Buchanan, and J. E. Rowe, "Electronic structure of barium fullerides," *Chem. Phys. Lett.* **206**, 193 (1993).
- [31] J. R. Morton, K. F. Preston, P. J. Krusic, S. A. Hill, and E. Wasserman, "ESR studies of the reaction of alkyl radicals with fullerene (C<sub>60</sub>)," *J. Phys. Chem.* **96**, 3576 (1992).

- [32] J. R. Morton, K. F. Preston, P. J. Krusic, S. A. Hill, and E. Wasserman, "The dimerization of fullerene  $\text{RC}_{60}$  radicals [ $\text{R} = \text{alkyl}$ ]," *J. Am. Chem. Soc.* **114**, 5454 (1992).
- [33] M. A. Cremonini, L. Lunazzi, G. Placucci, and P. J. Krusic, "Addition of alkylthiyl and alkoxy radicals to  $\text{C}_{60}$  studied by ESR," *J. Org. Chem.* **58**, 4735 (1993).
- [34] R. Borghi, B. Guidi, L. Lunazzi, and G. Placucci, "ESR Detection of the Regioisomers Due to Addition of Methoxy and Methylthio Radicals to Fullerene  $\text{C}_{70}$ ," *J. Org. Chem.* **61**, 5667 (1996).
- [35] K.-F. Liou and C.-H. Cheng, "Photoinduced reactions of tertiary amines with [60]fullerene; addition of an  $\alpha\text{-C-H}$  bond of amines to [60]fullerene," *Chem. Commun.*, 1423 (1996).
- [36] S. Zhang, T. L. Brown, Y. Du, and J. R. Shapley, "Metalation of fullerene ( $\text{C}_{60}$ ) with pentacarbonylrhenium radicals. Reversible formation of  $\text{C}_{60}\{\text{Re}(\text{CO})_5\}_2$ ," *J. Am. Chem. Soc.* **115**, 6705 (1993).
- [37] M. Nambo, R. Noyori, and K. Itami, "Rh-Catalyzed Arylation and Alkenylation of  $\text{C}_{60}$  Using Organoboron Compounds," *J. Am. Chem. Soc.* **129**, 8080 (2007).
- [38] M. D. Tzirakis and M. Orfanopoulos, "Acyl Radical Reactions in Fullerene Chemistry: Direct Acylation of [60]Fullerene through an Efficient Decatungstate-Photomediated Approach," *J. Am. Chem. Soc.* **131**, 4063 (2009).
- [39] Y. He, H.-Y. Chen, J. Hou, and Y. Li, "Indene- $\text{C}_{60}$  Bisadduct: A New Acceptor for High-Performance Polymer Solar Cells," *J. Am. Chem. Soc.* **132**, 1377 (2010).
- [40] M. Prato and M. Maggini, "Fulleropyrrolidines: A Family of Full-Fledged Fullerene Derivatives," *Acc. Chem. Res.* **31**, 519 (1998).
- [41] Y. Nakamura, N. Takano, T. Nishimura, E. Yashima, M. Sato, T. Kudo, and J. Nishimura, "First Isolation and Characterization of Eight Regioisomers for [60]Fullerene-Benzzyne Bisadducts," *Org. Lett.* **3**, 1193 (2001).
- [42] J. C. Hummelen, B. W. Knight, F. LePeq, F. Wudl, J. Yao, and C. L. Wilkins, "Preparation and Characterization of Fulleroid and Methanofullerene Derivatives," *J. Org. Chem.* **60**, 532 (1995).

- [43] E. K. Campbell, M. Holz, D. Gerlich, and J. P. Maier, "Laboratory confirmation of  $C_{60}^+$  as the carrier of two diffuse interstellar bands," *Nature* **523**, 322 (2015).
- [44] H.-S. Lin and Y. Matsuo, "Functionalization of [60]fullerene through fullerene cation intermediates," *Chem. Commun.* **54**, 11244 (2018).
- [45] A. Iwashita, Y. Matsuo, and E. Nakamura, "AlCl<sub>3</sub>-Mediated Mono-, Di-, and Trihydroarylation of [60]Fullerene," *Angew. Chemie Int. Ed.* **46**, 3513 (2007).
- [46] Y. Zhang, Y. Matsuo, and E. Nakamura, "Regiocontrolled Synthesis of 1,2-Di(organo)fullerenes via Copper-Assisted 1,4-Aryl Migration from Silicon to Carbon," *Org. Lett.* **13**, 6058 (2011).
- [47] Y. Zhang, Y. Matsuo, C.-Z. Li, H. Tanaka, and E. Nakamura, "A Scalable Synthesis of Methano[60]fullerene and Congeners by the Oxidative Cyclopropanation Reaction of Silylmethylfullerene," *J. Am. Chem. Soc.* **133**, 8086 (2011).
- [48] G. A. Olah, I. Bucsi, D. S. Ha, R. Aniszfeld, C. S. Lee, and G. K. S. Prakash, "Friedel-Crafts Reactions of Buckminsterfullerene," *Fuller. Sci. Technol.* **5**, 389 (1997).
- [49] G. A. Olah, I. Bucsi, C. Lambert, R. Aniszfeld, N. J. Trivedi, D. K. Sensharma, and G. K. S. Prakash, "Polyarenefullerenes,  $C_{60}(H-Ar)_n$ , obtained by acid-catalyzed fullerenation of aromatics," *J. Am. Chem. Soc.* **113**, 9387 (1991).
- [50] A. G. Avent, P. R. Birkett, H. W. Kroto, R. Taylor, and D. R. M. Walton, "Stable [60]fullerene carbocations," *Chem. Commun.*, 2153 (1998).
- [51] T. Kitagawa, Y. Lee, M. Hanamura, H. Sakamoto, H. Konno, K. Takeuchi, and K. Komatsu, "Nucleophilic substitution of alkylchlorodihydro[60]fullerenes: thermodynamic stabilities of alkylated  $C_{60}$  cation intermediates," *Chem. Commun.*, 3062 (2002).
- [52] T. Kitagawa, H. Sakamoto, and K. Takeuchi, "Electrophilic Addition of Polychloroalkanes to  $C_{60}$ : Direct Observation of Alkylfullerenyl Cation Intermediates," *J. Am. Chem. Soc.* **121**, 4298 (1999).
- [53] Y. Murata, F. Cheng, T. Kitagawa, and K. Komatsu, "Generation of Fullereny Cation  $(EtO)_2P^+(OH)CH_2-C_{60}^+$  from  $RC_{60}-H$  and from  $RC_{60}-C_{60}R$  ( $R = CH_2P(O)(OEt)_2$ )," *J. Am. Chem. Soc.* **126**, 8874 (2004).

- [54] S. G. Kukolich and D. R. Huffman, "EPR spectra of C<sub>60</sub> anion and cation radicals," *Chem. Phys. Lett.* **182**, 263 (1991).
- [55] C. A. Reed, K.-C. Kim, R. D. Bolskar, and L. J. Mueller, "Taming Superacids: Stabilization of the Fullerene Cations. *Science* **289**, 101 (2000).
- [56] G. A. Olah, I. Bucsi, R. Aniszfeld, and G. K. Surya Prakash, "Chemical reactivity and functionalization of C<sub>60</sub> and C<sub>70</sub> fullerenes," *Carbon N. Y.* **30**, 1203 (1992).
- [57] Q. Xie, F. Arias, and L. Echegoyen, "Electrochemically-reversible, single-electron oxidation of C<sub>60</sub> and C<sub>70</sub>," *J. Am. Chem. Soc.* **115**, 9818 (1993).
- [58] C. Bruno, I. Doubitski, M. Marcaccio, F. Paolucci, D. Paolucci, and A. Zaopo, "Electrochemical Generation of C<sub>60</sub><sup>2+</sup> and C<sub>60</sub><sup>3+</sup>," *J. Am. Chem. Soc.* **125**, 15738 (2003).
- [59] H. S. Shin, H. Lim, H. J. Song, H.-J. Shin, S.-M. Park, and H. C. Choi, "Spontaneous electron transfer from C<sub>60</sub> to Au ions: oxidation of C<sub>60</sub> and hole doping," *J. Mater. Chem.* **20**, 7183 (2010).
- [60] T. Kitagawa, H. Sakamoto, K. K. Takeuchi, Y. Lee, M. Hanamura, H. Sakamoto, H. Konno, K. K. Takeuchi, and K. Komatsu, "Electrophilic Addition of Polychloroalkanes to C<sub>60</sub>: Direct Observation of Alkylfullerenyl Cation Intermediates," *J. Am. Chem. Soc.* **121**, 3062 (1999).
- [61] S. H. Hoke II, J. Molstad, G. L. Payne, R. J. Cotter, B. Kahr, D. Ben-Amotz, and R. G. Cooks, "Aromatic hydrocarbon derivatives of fullerenes," *Rapid Commun. Mass Spectrom.* **5**, 472 (1991).
- [62] M. Hashiguchi, K. Watanabe, and Y. Matsuo, "Facile fullerene modification: FeCl<sub>3</sub>-mediated quantitative conversion of C<sub>60</sub> to polyarylated fullerenes containing pentaaryl(chloro)[60]fullerenes," *Org. Biomol. Chem.* **9**, 6417 (2011).
- [63] M. Hashiguchi, N. Obata, M. Maruyama, K. S. Yeo, T. Ueno, T. Ikebe, I. Takahashi, and Y. Matsuo, "FeCl<sub>3</sub>-Mediated Synthesis of Fullerenyl Esters as Low-LUMO Acceptors for Organic Photovoltaic Devices," *Org. Lett.* **14**, 3276 (2012).
- [64] M. Hashiguchi, H. Inada, and Y. Matsuo, "Solution-phase synthesis of dumbbell-shaped C<sub>120</sub> by FeCl<sub>3</sub>-mediated dimerization of C<sub>60</sub>," *Carbon N. Y.* **61**, 418 (2013).

- [65] M. Hashiguchi, T. Ueno, and Y. Matsuo, "FeCl<sub>3</sub>-Mediated Retro-Reactions of Fullerene Derivatives to C<sub>60</sub>," *Fullerenes, Nanotub. Carbon Nanostructures* **22**, 845 (2014).
- [66] Y. Zhang, Y. Matsuo, C. Z. Li, H. Tanaka, and E. Nakamura, "A scalable synthesis of methano[60]fullerene and congeners by the oxidative cyclopropanation reaction of silylmethylfullerene," *J. Am. Chem. Soc.* **133**, 8086 (2011).
- [67] Y. Matsuo, J. Kawai, H. Inada, T. Nakagawa, H. Ota, S. Otsubo, and E. Nakamura, "Addition of dihydromethano group to fullerenes to improve the performance of bulk heterojunction organic solar cells," *Adv. Mater.* **25**, 6266 (2013).
- [68] Y. Matsuo, K. Ogumi, Y. Zhang, H. Okada, T. Nakagawa, H. Ueno, A. Gocho, and E. Nakamura, "Fullerene cation-mediated demethylation/cyclization to give 5- and 7-membered cyclo[60]fullerene derivatives," *J. Mater. Chem. A* **5**, 2774 (2017).
- [69] X.-Y. Yang, H.-S. Lin, I. Jeon, and Y. Matsuo, "Fullerene-Cation-Mediated Noble-Metal-Free Direct Introduction of Functionalized Aryl Groups onto [60]Fullerene," *Org. Lett.* **20**, 3372 (2018).
- [70] T. Rabenau, A. Simon, R. K. Kremer, and E. Sohmen, "The energy gaps of fullerene C<sub>60</sub> and C<sub>70</sub> determined from the temperature dependent microwave conductivity," *Zeitschrift für Phys. B Condens. Matter* **90**, 69 (1993).
- [71] S. Lo Piano and K. Mayumi, "Toward an integrated assessment of the performance of photovoltaic power stations for electricity generation," *Appl. Energy* **186**, 167 (2017).
- [72] A. Mishra and P. Bäuerle, "Small molecule organic semiconductors on the move: Promises for future solar energy technology," *Angew. Chemie - Int. Ed.* **51**, 2020 (2012).
- [73] M. C. Scharber, D. Mühlbacher, M. Koppe, P. Denk, C. Waldauf, A. J. Heeger, and C. J. Brabec, "Design Rules for Donors in Bulk-Heterojunction Solar Cells—Towards 10 % Energy-Conversion Efficiency," *Adv. Mater.* **18**, 789 (2006).
- [74] W. J. Potscavage, A. Sharma, and B. Kippelen, "Critical Interfaces in Organic

- Solar Cells and Their Influence on the Open-Circuit Voltage,” *Acc. Chem. Res.* **42**, 1758 (2009).
- [75] D. He, X. Du, Z. Xiao, and L. Ding, “Methanofullerenes,  $C_{60}(CH_2)_n$  ( $n = 1, 2, 3$ ), as building blocks for high-performance acceptors used in Organic Solar Cells,” *Org. Lett.* **16**, 612 (2014).
- [76] W. Li, J. Cai, F. Cai, Y. Yan, H. Yi, R. S. Gurney, D. Liu, A. Iraqi, and T. Wang, “Achieving over 11% power conversion efficiency in PffBT4T-2OD-based ternary polymer solar cells with enhanced open-circuit-voltage and suppressed charge recombination,” *Nano Energy* **44**, 155 (2018).
- [77] P. A. Troshin, H. Hoppe, J. Renz, M. Egginger, J. Y. Mayorova, A. E. Goryachev, A. S. Peregodov, R. N. Lyubovskaya, G. Gobsch, N. S. Sariciftci, and V. F. Razumov, “Material Solubility-Photovoltaic Performance Relationship in the Design of Novel Fullerene Derivatives for Bulk Heterojunction Solar Cells,” *Adv. Funct. Mater.* **19**, 779 (2009).
- [78] J. A. Mikroyannidis, A. N. Kabanakis, S. S. Sharma, and G. D. Sharma, “A Simple and Effective Modification of PCBM for Use as an Electron Acceptor in Efficient Bulk Heterojunction Solar Cells,” *Adv. Funct. Mater.* **21**, 746 (2011).
- [79] H. U. Kim, J.-H. Kim, H. Kang, A. C. Grimsdale, B. J. Kim, S. C. Yoon, and D.-H. Hwang, “Naphthalene-, Anthracene-, and Pyrene-Substituted Fullerene Derivatives as Electron Acceptors in Polymer-based Solar Cells,” *ACS Appl. Mater. Interfaces* **6**, 20776 (2014).
- [80] K. Matsumoto, K. Hashimoto, M. Kamo, Y. Uetani, S. Hayase, M. Kawatsura, and T. Itoh, “Design of fulleropyrrolidine derivatives as an acceptor molecule in a thin layer organic solar cell,” *J. Mater. Chem.* **20**, 9226 (2010).
- [81] Y. Matsuo, Y. Sato, T. Niinomi, I. Soga, H. Tanaka, and E. Nakamura, “Columnar structure in bulk heterojunction in solution-processable three-layered p-i-n organic photovoltaic devices using tetrabenzoporphyrin precursor and silylmethyl[60]fullerene,” *J. Am. Chem. Soc.* **131**, 16048 (2009).
- [82] Y. Matsuo, A. Ozu, N. Obata, N. Fukuda, H. Tanaka, and E. Nakamura, “Deterioration of bulk heterojunction organic photovoltaic devices by a minute amount of oxidized fullerene,” *Chem. Commun.* **48**, 3878 (2012).
- [83] M. Lenes, G.-J. A. H. Wetzelaer, F. B. Kooistra, S. C. Veenstra, J. C. Hummelen,

- and P. W. M. Blom, "Fullerene Bisadducts for Enhanced Open-Circuit Voltages and Efficiencies in Polymer Solar Cells Advanced Materials Volume 20, Issue 11," in *Adv. Mater.* **20**, 2116 (2008).
- [84] S. P. Singh, C. P. Kumar, G. D. Sharma, R. Kurchania, and M. S. Roy, "Synthesis of a modified PC<sub>70</sub>BM and its application as an electron acceptor with poly(3-hexylthiophene) as an electron donor for efficient bulk heterojunction solar cells," *Adv. Funct. Mater.* **22**, 4087 (2012).
- [85] R. B. Ross, C. M. Cardona, D. M. Guldi, S. G. Sankaranarayanan, M. O. Reese, N. Kopidakis, J. Peet, B. Walker, G. C. Bazan, E. Van Keuren, B. C. Holloway, and M. Drees, "Endohedral fullerenes for organic photovoltaic devices," *Nat. Mater.* **8**, 208 (2009).
- [86] A. Kojima, K. Teshima, Y. Shirai, and T. Miyasaka, "Organometal halide perovskites as visible-light sensitizers for photovoltaic cells," *J. Am. Chem. Soc.* **131**, 6050 (2009).
- [87] L. Lang, J. H. Yang, H. R. Liu, H. J. Xiang, and X. G. Gong, "First-principles study on the electronic and optical properties of cubic ABX<sub>3</sub> halide perovskites," in *Phys. Lett. Sect. A Gen. At. Solid State Phys.* **378**, 290 (2014).
- [88] C. C. Chueh, C. Z. Li, and A. K. Y. Jen, "Recent progress and perspective in solution-processed Interfacial materials for efficient and stable polymer and organometal perovskite solar cells," *Energy Environ. Sci.* **8**, 1160 (2015).
- [89] D. Zhao, W. Ke, C. R. Grice, A. J. Cimaroli, X. Tan, M. Yang, R. W. Collins, H. Zhang, K. Zhu, and Y. Yan, "Annealing-free efficient vacuum-deposited planar perovskite solar cells with evaporated fullerenes as electron-selective layers," *Nano Energy* **19**, 88 (2016).
- [90] H.-S. Lin, I. Jeon, R. Xiang, S. Seo, J.-W. Lee, C. Li, A. Pal, S. Manzhos, M. S. Goorsky, Y. Yang, S. Maruyama, and Y. Matsuo, "Achieving High Efficiency in Solution-Processed Perovskite Solar Cells Using C<sub>60</sub>/C<sub>70</sub> Mixed Fullerenes," *ACS Appl. Mater. Interfaces* **10**, 39590 (2018).
- [91] W. Chen, Y. Wu, Y. Yue, J. Liu, W. Zhang, X. Yang, H. Chen, E. Bi, I. Ashraful, M. Grätzel, L. Han, † Liyuan Han, and L. Han, "Efficient and stable large-area perovskite solar cells with inorganic charge extraction layers," *Science* **350**, 944 (2015).

- [92] C. H. Chiang, M. K. Nazeeruddin, M. Grätzel, and C. G. Wu, “The synergistic effect of H<sub>2</sub>O and DMF towards stable and 20% efficiency inverted perovskite solar cells,” *Energy Environ. Sci.* **10**, 808 (2017).
- [93] Y. C. Wang, X. Li, L. Zhu, X. Liu, W. Zhang, and J. Fang, “Efficient and Hysteresis-Free Perovskite Solar Cells Based on a Solution Processable Polar Fullerene Electron Transport Layer,” *Adv. Energy Mater.* **7**, 1 (2017).
- [94] E. Castro, G. Zavala, S. Seetharaman, F. D’Souza, and L. Echegoyen, “Impact of fullerene derivative isomeric purity on the performance of inverted planar perovskite solar cells,” *J. Mater. Chem. A* **5**, 19485 (2017).
- [95] Q. Xue, Y. Bai, M. Liu, R. Xia, Z. Hu, Z. Chen, X. F. Jiang, F. Huang, S. Yang, Y. Matsuo, H. L. Yip, and Y. Cao, “Dual Interfacial Modifications Enable High Performance Semitransparent Perovskite Solar Cells with Large Open Circuit Voltage and Fill Factor,” *Adv. Energy Mater.* **7**, 1 (2017).
- [96] Y. Lin, B. Chen, F. Zhao, X. Zheng, Y. Deng, Y. Shao, Y. Fang, Y. Bai, C. Wang, and J. Huang, “Matching Charge Extraction Contact for Wide-Bandgap Perovskite Solar Cells,” *Adv. Mater.* **29**, 1 (2017).
- [97] A. Abrusci, S. D. Stranks, P. Docampo, H.-L. Yip, A. K.-Y. Jen, and H. J. Snaith, “High-Performance Perovskite-Polymer Hybrid Solar Cells via Electronic Coupling with Fullerene Monolayers,” *Nano Lett.* **13**, 3124 (2013).
- [98] C. Wang, D. Zhao, C. R. Grice, W. Liao, Y. Yu, A. Cimaroli, N. Shrestha, P. J. Roland, J. Chen, Z. Yu, P. Liu, N. Cheng, R. J. Ellingson, X. Zhao, and Y. Yan, “Low-temperature plasma-enhanced atomic layer deposition of tin oxide electron selective layers for highly efficient planar perovskite solar cells,” *J. Mater. Chem. A* **4**, 12080 (2016).
- [99] J. Kim, G. Kim, T. K. Kim, S. Kwon, H. Back, J. Lee, S. H. Lee, H. Kang, and K. Lee, “Efficient planar-heterojunction perovskite solar cells achieved via interfacial modification of a sol–gel ZnO electron collection layer,” *J. Mater. Chem. A* **2**, 17291 (2014).
- [100] W. Ke, C. Xiao, C. Wang, B. Saparov, H.-S. Duan, D. Zhao, Z. Xiao, P. Schulz, S. P. Harvey, et al., “Employing Lead Thiocyanate Additive to Reduce the Hysteresis and Boost the Fill Factor of Planar Perovskite Solar Cells,” *Adv. Mater.* **28**, 5214 (2016).



- [101] Y. Li, Y. Zhao, Q. Chen, Y. Yang, Y. Liu, Z. Hong, Z. Liu, Y. T. Hsieh, L. Meng, Y. Li, and Y. Yang, “Multifunctional Fullerene Derivative for Interface Engineering in Perovskite Solar Cells,” *J. Am. Chem. Soc.* **137**, 15540 (2015).
- [102] Y. Dong, W. Li, X. Zhang, Q. Xu, Q. Liu, C. Li, and Z. Bo, “Highly Efficient Planar Perovskite Solar Cells Via Interfacial Modification with Fullerene Derivatives,” *Small* **12**, 1098 (2016).
- [103] Q. Xu, Z. Lu, L. Zhu, C. Kou, Y. Liu, C. Li, Q. Meng, W. Li, and Z. Bo, “Elimination of the J–V hysteresis of planar perovskite solar cells by interfacial modification with a thermo-cleavable fullerene derivative,” *J. Mater. Chem. A* **4**, 17649 (2016).
- [104] H.-S. Lin, I. Jeon, Y. Chen, X.-Y. Yang, T. Nakagawa, S. Maruyama, S. Manzhos, and Y. Matsuo, “Highly Selective and Scalable Fullerene-Cation-Mediated Synthesis Accessing Cyclo[60]fullerenes with Five-Membered Carbon Ring and Their Application to Perovskite Solar Cells,” *Chem. Mater.* **31**, 8432 (2019).
- [105] C. H. Chiang and C. G. Wu, “Bulk heterojunction perovskite-PCBM solar cells with high fill factor,” *Nat. Photonics* **10**, 196 (2016).
- [106] H. Ueno, I. Jeon, H. Lin, A. Thote, T. Nakagawa, H. Okada, S. Izawa, M. Hiramoto, H. Daiguji, S. Maruyama, and Y. Matsuo, “Li@C<sub>60</sub> endohedral fullerene as a supraatomic dopant for C<sub>60</sub> electron-transporting layers promoting the efficiency of perovskite solar cells,” *Chem. Commun.* **55**, 11837 (2019).
- [107] I. Jeon, H. Ueno, S. Seo, K. Aitola, R. Nishikubo, A. Saeki, H. Okada, G. Boschloo, S. Maruyama, and Y. Matsuo, “Lithium-Ion Endohedral Fullerene (Li<sup>+</sup>@C<sub>60</sub>) Dopants in Stable Perovskite Solar Cells Induce Instant Doping and Anti-Oxidation,” *Angew. Chemie - Int. Ed.* **57**, 4607 (2018).
- [108] T. Gatti, E. Menna, M. Meneghetti, M. Maggini, A. Petrozza, and F. Lamberti, “The Renaissance of fullerenes with perovskite solar cells,” *Nano Energy* **41**, 84 (2017).
- [109] P.-W. Liang, C.-C. Chueh, S. T. Williams, and A. K.-Y. Jen, “Roles of Fullerene-Based Interlayers in Enhancing the Performance of Organometal Perovskite Thin-Film Solar Cells,” *Adv. Energy Mater.* **5**, 1402321 (2015).
- [110] E. von Hauff, V. Dyakonov, and J. Parisi, “Study of field effect mobility in

- PCBM films and P3HT:PCBM blends,” *Sol. Energy Mater. Sol. Cells* **87**, 149 (2005).
- [111] Y. Xie, Y. Li, L. Xiao, Q. Qiao, R. Dhakal, Z. Zhang, Q. Gong, D. Galipeau, and X. Yan, “Femtosecond Time-Resolved Fluorescence Study of P3HT/PCBM Blend Films,” *J. Phys. Chem. C* **114**, 14590 (2010).
- [112] J. Wei, Y. Zhao, H. Li, G. Li, J. Pan, D. Xu, Q. Zhao, and D. Yu, “Hysteresis Analysis Based on the Ferroelectric Effect in Hybrid Perovskite Solar Cells,” *J. Phys. Chem. Lett.* **5**, 3937 (2014).
- [113] T. Leijtens, G. E. Eperon, S. Pathak, A. Abate, M. M. Lee, and H. J. Snaith, “Overcoming ultraviolet light instability of sensitized TiO<sub>2</sub> with meso-superstructured organometal tri-halide perovskite solar cells,” *Nat. Commun.* **4**, 2885 (2013).
- [114] S. Ito, S. Tanaka, K. Manabe, and H. Nishino, “Effects of Surface Blocking Layer of Sb<sub>2</sub>S<sub>3</sub> on Nanocrystalline TiO<sub>2</sub> for CH<sub>3</sub>NH<sub>3</sub>PbI<sub>3</sub> Perovskite Solar Cells,” *J. Phys. Chem. C* **118**, 16995 (2014).
- [115] H. J. Snaith, A. Abate, J. M. Ball, G. E. Eperon, T. Leijtens, N. K. Noel, S. D. Stranks, J. T.-W. Wang, K. Wojciechowski, and W. Zhang, “Anomalous Hysteresis in Perovskite Solar Cells,” *J. Phys. Chem. Lett.* **5**, 1511 (2014).
- [116] I. Jeon, T. Chiba, C. Delacou, Y. Guo, A. Kaskela, O. Reynaud, E. I. Kauppinen, S. Maruyama, and Y. Matsuo, “Single-Walled Carbon Nanotube Film as Electrode in Indium-Free Planar Heterojunction Perovskite Solar Cells: Investigation of Electron-Blocking Layers and Dopants,” *Nano Lett.* **15**, 6665 (2015).
- [117] N. Ahn, I. Jeon, J. Yoon, E. I. Kauppinen, Y. Matsuo, S. Maruyama, and M. Choi, “Carbon-sandwiched perovskite solar cell,” *J. Mater. Chem. A* **6**, 1382 (2018).
- [118] N. Ahn, K. Kwak, M. S. Jang, H. Yoon, B. Y. Lee, J.-K. Lee, P. V Pikhitsa, J. Byun, and M. Choi, “Trapped charge-driven degradation of perovskite solar cells,” *Nat. Commun.* **7**, 13422 (2016).
- [119] C. Tao, S. Neutzner, L. Colella, S. Marras, A. R. Srimath Kandada, M. Gandini, M. De Bastiani, G. Pace, L. Manna, M. Caironi, C. Bertarelli, and A. Petrozza, “17.6% stabilized efficiency in low-temperature processed planar perovskite

- solar cells,” *Energy Environ. Sci.* **8**, 2365 (2015).
- [120] W. Ke, D. Zhao, C. R. Grice, A. J. Cimaroli, J. Ge, H. Tao, H. Lei, G. Fang, and Y. Yan, “Efficient planar perovskite solar cells using room-temperature vacuum-processed C60 electron selective layers,” *J. Mater. Chem. A* **3**, 17971 (2015).
- [121] J.-W. Lee, S.-G. Kim, S.-H. Bae, D.-K. Lee, O. Lin, Y. Yang, and N.-G. Park, “The Interplay between Trap Density and Hysteresis in Planar Heterojunction Perovskite Solar Cells,” *Nano Lett.* **17**, 4270 (2017).
- [122] S. Collavini, I. Kosta, S. F. Völker, G. Cabanero, H. J. Grande, R. Tena-Zaera, and J. L. Delgado, “Efficient Regular Perovskite Solar Cells Based on Pristine [70]Fullerene as Electron-Selective Contact,” *ChemSusChem* **9**, 1263 (2016).
- [123] K. Zhang, H. Yu, X. Liu, Q. Dong, Z. Wang, Y. Wang, N. Chen, Y. Zhou, and B. Song, “Fullerenes and derivatives as electron transport materials in perovskite solar cells,” *Sci. China Chem.* **60**, 144 (2017).
- [124] T. Heumueller, T. M. Burke, W. R. Mateker, I. T. Sachs-Quintana, K. Vandewal, C. J. Brabec, and M. D. McGehee, “Disorder-Induced Open-Circuit Voltage Losses in Organic Solar Cells During Photoinduced Burn-In,” *Adv. Energy Mater.* **5**, 1500111 (2015).
- [125] M. Hosoya, K. Ichimura, Z. H. Wang, G. Dresselhaus, M. S. Dresselhaus, and P. C. Eklund, “Dark conductivity and photoconductivity in solid films of C<sub>70</sub>, C<sub>60</sub>, and K<sub>x</sub>C<sub>70</sub>” *Phys. Rev. B* **49**, 4981 (1994).
- [126] R. C. Haddon, “C<sub>70</sub> Thin Film Transistors,” *J. Am. Chem. Soc.* **118**, 3041 (1996).
- [127] X. Xi, W. Li, J. Wu, J. Ji, Z. Shi, and G. Li, “A comparative study on the performances of small molecule organic solar cells based on CuPc/C<sub>60</sub> and CuPc/C<sub>70</sub>,” *Sol. Energy Mater. Sol. Cells* **94**, 2435 (2010).
- [128] J. Xu, A. Buin, A. H. Ip, W. Li, O. Voznyy, R. Comin, M. Yuan, S. Jeon, Z. Ning, J. J. McDowell, P. Kanjanaboos, J.-P. Sun, X. Lan, L. N. Quan, D. H. Kim, I. G. Hill, P. Maksymovych, and E. H. Sargent, “Perovskite–fullerene hybrid materials suppress hysteresis in planar diodes,” *Nat. Commun.* **6**, 7081 (2015).
- [129] D. W. de Quilettes, S. M. Vorpahl, S. D. Stranks, H. Nagaoka, G. E. Eperon, M. E. Ziffer, H. J. Snaith, and D. S. Ginger, “Impact of microstructure on local carrier lifetime in perovskite solar cells,” *Science* **348**, 683 (2015).

- [130] J. Pascual, I. Kosta, E. Palacios-Lidon, A. Chuvilin, G. Grancini, M. K. Nazeeruddin, H. J. Grande, J. L. Delgado, and R. Tena-Zaera, "Co-Solvent Effect in the Processing of the Perovskite:Fullerene Blend Films for Electron Transport Layer-Free Solar Cells," *J. Phys. Chem. C* **122**, 2512 (2018).
- [131] X. Zhang, X. Ai, R. Zhang, Q. Ma, Z. Wang, G. Qin, J. Wang, S. Wang, K. Suzuki, T. Miyazaki, and S. Mizukami, "Spin conserved electron transport behaviors in fullerenes (C<sub>60</sub> and C<sub>70</sub>) spin valves," *Carbon N. Y.* **106**, 202 (2016).
- [132] J. H. Weaver, J. L. Martins, T. Komeda, Y. Chen, T. R. Ohno, G. H. Kroll, N. Troullier, R. E. Haufler, and R. E. Smalley, "Electronic structure of solid C<sub>60</sub>: Experiment and theory," *Phys. Rev. Lett.* **66**, 1741 (1991).
- [133] J. C. Petersen and S. E. Choi, "Infrared-infrared double-resonance spectra involving fermi perturbed levels and CO stretch band transitions of CD<sub>3</sub>OH," *Appl. Phys. B* **56**, 185 (1993).
- [134] K. Ahn, J. Beom Kim, H. Park, H. Kim, M. Hyung Lee, B. Joon Kim, J. Ho Cho, M. Sung Kang, and D. Ryeol Lee, "Enhancing crystallinity of C<sub>60</sub> layer by thickness-control of underneath pentacene layer for high mobility C<sub>60</sub>/pentacene ambipolar transistors," *Appl. Phys. Lett.* **102**, 43306 (2013).
- [135] Q. Meng, H. Dong, W. Hu, and D. Zhu, "Recent progress of high performance organic thin film field-effect transistors," *J. Mater. Chem.* **21**, 11708 (2011).
- [136] L. M. Andersson, Y.-T. Hsu, K. Vandewal, A. B. Sieval, M. R. Andersson, and O. Inganäs, "Mixed C<sub>60</sub>/C<sub>70</sub> based fullerene acceptors in polymer bulk-heterojunction solar cells," *Org. Electron.* **13**, 2856 (2012).
- [137] S. M. Gorun, K. M. Creegan, R. D. Sherwood, D. M. Cox, V. W. Day, C. S. Day, R. M. Upton, and C. E. Briant, "Solvated C<sub>60</sub> and C<sub>60</sub>/C<sub>70</sub> and the low-resolution single crystal X-ray structure of C<sub>60</sub>," *J. Chem. Soc. Chem. Commun.*, 1556 (1991).
- [138] T. D. Anthopoulos, B. Singh, N. Marjanovic, N. S. Sariciftci, A. Montaigne Ramil, H. Sitter, M. Cölle, and D. M. de Leeuw, "High performance n-channel organic field-effect transistors and ring oscillators based on C<sub>60</sub> fullerene films," *Appl. Phys. Lett.* **89**, 213504 (2006).
- [139] N. J. Jeon, J. Lee, J. H. Noh, M. K. Nazeeruddin, M. Grätzel, and S. Il Seok, "Efficient Inorganic–Organic Hybrid Perovskite Solar Cells Based on Pyrene

- Arylamine Derivatives as Hole-Transporting Materials,” *J. Am. Chem. Soc.* **135**, 19087 (2013).
- [140] J. M. Ball, M. M. Lee, A. Hey, and H. J. Snaith, “Low-temperature processed meso-superstructured to thin-film perovskite solar cells,” *Energy Environ. Sci.* **6**, 1739 (2013).
- [141] J.-W. Lee, Z. Dai, T.-H. Han, C. Choi, S.-Y. Chang, S.-J. Lee, N. De Marco, H. Zhao, P. Sun, Y. Huang, and Y. Yang, “2D perovskite stabilized phase-pure formamidinium perovskite solar cells,” *Nat. Commun.* **9**, 3021 (2018).
- [142] J. H. Noh, S. H. Im, J. H. Heo, T. N. Mandal, and S. Il Seok, “Chemical Management for Colorful, Efficient, and Stable Inorganic–Organic Hybrid Nanostructured Solar Cells,” *Nano Lett.* **13**, 1764 (2013).
- [143] M. Saliba, S. Orlandi, T. Matsui, S. Aghazada, M. Cavazzini, J.-P. Correa-Baena, P. Gao, R. Scopelliti, E. Mosconi, K.-H. Dahmen, F. De Angelis, A. Abate, A. Hagfeldt, G. Pozzi, M. Graetzel, and M. K. Nazeeruddin, “A molecularly engineered hole-transporting material for efficient perovskite solar cells,” *Nat. Energy* **1**, 15017 (2016).
- [144] L. Zuo, Z. Gu, T. Ye, W. Fu, G. Wu, H. Li, and H. Chen, “Enhanced Photovoltaic Performance of CH<sub>3</sub>NH<sub>3</sub>PbI<sub>3</sub> Perovskite Solar Cells through Interfacial Engineering Using Self-Assembling Monolayer,” *J. Am. Chem. Soc.* **137**, 2674 (2015).
- [145] C. Liu, K. Wang, P. Du, T. Meng, X. Yu, S. Z. D. Cheng, and X. Gong, “High performance planar heterojunction perovskite solar cells with fullerene derivatives as the electron transport layer,” *ACS Appl. Mater. Interfaces* **7**, 1153 (2015).
- [146] Y.-C. Wang, J. Chang, L. Zhu, X. Li, C. Song, and J. Fang, “Electron-Transport-Layer-Assisted Crystallization of Perovskite Films for High-Efficiency Planar Heterojunction Solar Cells,” *Adv. Funct. Mater.* **28**, 1706317 (2018).
- [147] X. Zhao, L. Tao, H. Li, W. Huang, P. Sun, J. Liu, S. Liu, Q. Sun, Z. Cui, L. Sun, Y. Shen, Y. Yang, and M. Wang, “Efficient Planar Perovskite Solar Cells with Improved Fill Factor via Interface Engineering with Graphene,” *Nano Lett.* **18**, 2442 (2018).
- [148] C. Tao, J. Van Der Velden, L. Cabau, N. F. Montcada, S. Neutzner, A. R.

- Srimath Kandada, S. Marras, L. Brambilla, M. Tommasini, W. Xu, R. Sorrentino, A. Perinot, M. Caironi, C. Bertarelli, E. Palomares, and A. Petrozza, “Fully Solution-Processed n–i–p-Like Perovskite Solar Cells with Planar Junction: How the Charge Extracting Layer Determines the Open-Circuit Voltage,” *Adv. Mater.* **29**, 1604493 (2017).
- [149] G. Zhao, Y. He, and Y. Li, “6.5% Efficiency of Polymer Solar Cells Based on poly(3-hexylthiophene) and Indene-C<sub>60</sub> Bisadduct by Device Optimization,” *Adv. Mater.* **22**, 4355 (2010).
- [150] Y. Matsuo, J. Kawai, H. Inada, T. Nakagawa, H. Ota, S. Otsubo, and E. Nakamura, “Addition of Dihydromethano Group to Fullerenes to Improve the Performance of Bulk Heterojunction Organic Solar Cells,” *Adv. Mater.* **25**, 6266 (2013).
- [151] D. M. Guldi, B. M. Illescas, C. M. Atienza, M. Wielopolski, and N. Martín, “Fullerene for organic electronics,” *Chem. Soc. Rev.* **38**, 1587 (2009).
- [152] Y.-T. Su, Y.-L. Wang, and G.-W. Wang, “Palladium-catalyzed heteroannulation of [60]fullerene with N-(2-arylethyl) sulfonamides via C–H bond activation,” *Org. Chem. Front.* **1**, 689 (2014).
- [153] K. Gao, L. Li, T. Lai, L. Xiao, Y. Huang, F. Huang, J. Peng, Y. Cao, F. Liu, T. P. Russell, R. A. J. Janssen, and X. Peng, “Deep Absorbing Porphyrin Small Molecule for High-Performance Organic Solar Cells with Very Low Energy Losses,” *J. Am. Chem. Soc.* **137**, 7282 (2015).
- [154] W.-Y. Wong, X.-Z. Wang, Z. He, A. B. Djurišić, C.-T. Yip, K.-Y. Cheung, H. Wang, C. S. K. Mak, and W.-K. Chan, “On the efficiency of polymer solar cells,” *Nat. Mater.* **6**, 704 (2007).
- [155] A. Pal, L. K. Wen, C. Y. Jun, I. Jeon, Y. Matsuo, and S. Manzhos, “Comparative density functional theory–density functional tight binding study of fullerene derivatives: effects due to fullerene size, addends, and crystallinity on band structure, charge transport and optical properties,” *Phys. Chem. Chem. Phys.* **19**, 28330 (2017).
- [156] S. A. L. Weber, I. M. Hermes, S.-H. Turren-Cruz, C. Gort, V. W. Bergmann, L. Gilson, A. Hagfeldt, M. Graetzel, W. Tress, and R. Berger, “How the formation of interfacial charge causes hysteresis in perovskite solar cells,” *Energy Environ.*

- Sci.* **11**, 2404 (2018).
- [157] R. Wang, M. Mujahid, Y. Duan, Z.-K. Wang, J. Xue, and Y. Yang, “A Review of Perovskites Solar Cell Stability,” *Adv. Funct. Mater.* **29**, 1808843 (2019).
- [158] G.-J. A. H. Wetzelaer, M. Scheepers, A. M. Sempere, C. Momblona, J. Ávila, and H. J. Bolink, “Trap-Assisted Non-Radiative Recombination in Organic–Inorganic Perovskite Solar Cells,” *Adv. Mater.* **27**, 1837 (2015).
- [159] B. D. Hall, D. Zanchet, and D. Ugarte, “Estimating nanoparticle size from diffraction measurements,” *J. Appl. Crystallogr.* **33**, 1335 (2000).
- [160] Q. Wang, M. Lyu, M. Zhang, J.-H. Yun, H. Chen, and L. Wang, “Transition from the Tetragonal to Cubic Phase of Organohalide Perovskite: The Role of Chlorine in Crystal Formation of  $\text{CH}_3\text{NH}_3\text{PbI}_3$  on  $\text{TiO}_2$  Substrates,” *J. Phys. Chem. Lett.* **6**, 4379 (2015).
- [161] T. Oshima, H. Kitamura, T. Higashi, K. Kokubo, and N. Seike, “Kinetic Substituent and Solvent Effects in 1,3-Dipolar Cycloaddition of Diphenyldiazomethanes with Fullerenes C60 and C70: A Comparison with the Addition to TCNE, DDQ, and Chloranil,” *J. Org. Chem.* **71**, 2995 (2006).
- [162] Y. J. Lee, H. Yi, W.-J. Kim, K. Kang, D. S. Yun, M. S. Strano, G. Ceder, and A. M. Belcher, “Fabricating Genetically Engineered High-Power Lithium-Ion Batteries Using Multiple Virus Genes,” *Science* **324**, 1051 (2009).
- [163] K. T. Nam, D.-W. Kim, P. J. Yoo, C.-Y. Chiang, N. Meethong, P. T. Hammond, Y.-M. Chiang, and A. M. Belcher, “Virus-Enabled Synthesis and Assembly of Nanowires for Lithium Ion Battery Electrodes,” *Science* **312**, 885 (2006).
- [164] C. Mao, D. J. Solis, B. D. Reiss, S. T. Kottmann, R. Y. Sweeney, A. Hayhurst, G. Georgiou, B. Iverson, and A. M. Belcher, “Virus-Based Toolkit for the Directed Synthesis of Magnetic and Semiconducting Nanowires,” *Science*. **303**, 213 (2004).
- [165] S. Seo, I. Jeon, R. Xiang, C. Lee, H. Zhang, T. Tanaka, J.-W. Lee, D. Suh, T. Ogamoto, R. Nishikubo, A. Saeki, S. Chiashi, J. Shiomi, H. Kataura, H. M. Lee, Y. Yang, Y. Matsuo, and S. Maruyama, “Semiconducting carbon nanotubes as crystal growth templates and grain bridges in perovskite solar cells,” *J. Mater. Chem. A* **7**, 12987 (2019).

- [166] S. Berson, R. de Bettignies, S. Bailly, S. Guillerez, and B. Jousselme, “Elaboration of P3HT/CNT/PCBM Composites for Organic Photovoltaic Cells,” *Adv. Funct. Mater.* **17**, 3363 (2007).
- [167] S. Chaudhary, H. Lu, A. M. Müller, C. J. Bardeen, and M. Ozkan, “Hierarchical Placement and Associated Optoelectronic Impact of Carbon Nanotubes in Polymer-Fullerene Solar Cells,” *Nano Lett.* **7**, 1973 (2007).
- [168] R. Ihly, A.-M. Dowgiallo, M. Yang, P. Schulz, N. J. Stanton, O. G. Reid, A. J. Ferguson, K. Zhu, J. J. Berry, and J. L. Blackburn, “Efficient charge extraction and slow recombination in organic–inorganic perovskites capped with semiconducting single-walled carbon nanotubes,” *Energy Environ. Sci.* **9**, 1439 (2016).